**FAN-BEAM MULTIPLEXED
COMPTON SCATTER TOMOGRAPHY FOR
SINGLE-SIDED NONINVASIVE INSPECTION**

DISSERTATION

Brian L. Evans, Captain, USAF

AFIT/DS/ENP/99-1

**DEPARTMENT OF THE AIR FORCE
AIR UNIVERSITY
AIR FORCE INSTITUTE OF TECHNOLOGY**

Wright-Patterson Air Force Base, Ohio

Approved for Public release; distribution unlimited

FAN-BEAM MULTIPLEXED COMPTON
SCATTER TOMOGRAPHY FOR SINGLE-SIDED
NONINVASIVE INSPECTION

DISSERTATION

Brian L. Evans, Captain, USAF

AFIT/DS/ENP/99-1

Disclaimer:

The views expressed in this dissertation are those of the author and do not reflect the official policy or position of the Department of Defense or the U.S. Government.

REPORT DOCUMENTATION PAGE

Form Approved
OMB No. 0704-0188

1. AGENCY USE ONLY (Leave blank)	2. REPORT DATE	3. REPORT TYPE AND DATES COVERED
	April 1999	Doctoral Dissertation

4. TITLE AND SUBTITLE
FAN-BEAM MULTIPLEXED COMPTON SCATTER TOMOGRAPHY FOR SINGLE-SIDED NONINVASIVE INSPECTION

5. FUNDING NUMBERS

6. AUTHOR(S)
Brian L. Evans, Captain, USAF

7. PERFORMING ORGANIZATION NAME(S) AND ADDRESS(ES)
Air Force Institute of Technology
2950 P. Street
Wright-Patterson AFB, OH 45433-7765

8. PERFORMING ORGANIZATION REPORT NUMBER

AFIT/DS/ENP/99-1

9. SPONSORING/MONITORING AGENCY NAME(S) AND ADDRESS(ES)
Air Force Research Laboratory -- Metals, Ceramics & Nondestructive Evaluation Div.
AFRL / MLL
2230 10th Street, Room 123
Wright-Patterson AFB, OH 45433

10. SPONSORING/MONITORING AGENCY REPORT NUMBER

11. SUPPLEMENTARY NOTES

12a. DISTRIBUTION AVAILABILITY STATEMENT
Approved for public release; distribution unlimited.

12b. DISTRIBUTION CODE

13. ABSTRACT (Maximum 200 words)
Multiplexed Compton scatter tomography (MCST) is explored as a method of nondestructively generating cross-sectional images of a sample's electron density. MCST is viable when access is available to only one side of the sample because it registers scattered gamma radiation. Multiplexing in scattered photon energy and in detector position allows simultaneous interrogation of many voxels with comparatively wide collimation. Primary components include a radioisotope source, fan beam collimators, and energy-discriminating detectors. The application of MCST to inspecting aluminum airframes for corrosion is considered. This application requires source gammas near 100 keV where the scattered gamma energy is severely broadened by the momentum of electrons in the target. A deterministic system model is developed to map the sample's voxel densities to the instrument's measurements. The model incorporates advanced features to avoid using a detector response function. Two image reconstruction methods are developed and investigated: filtered backprojection and iterative reconstruction. A demonstration MCST system is assembled from components available commercially. It is used to image several aluminum phantoms and to validate the system model and iterative image reconstruction algorithm. A next-generation MCST system is modeled. Issues are considered such as efficiency, counting time, and contrast recovery in various samples.

14. SUBJECT TERMS
Nondestructive Testing, Nondestructive Evaluation, Tomography, Computerized Tomography, Gamma Ray Scattering, Compton Scattering, Compton Scatter Imaging, Radiation Imaging, Radiological Imaging, Radiation Measuring Instruments, Gamma Spectrometers

15. NUMBER OF PAGES
168

16. PRICE CODE

17. SECURITY CLASSIFICATION OF REPORT	18. SECURITY CLASSIFICATION OF THIS PAGE	19. SECURITY CLASSIFICATION OF ABSTRACT	20. LIMITATION OF ABSTRACT
Unclassified	Unclassified	Unclassified	UL

Standard Form 298 (Rev. 2-89) (EG)
Prescribed by ANSI Std. 239.18
Designed using Perform Pro, WHS/DIOR, Oct 94

FAN-BEAM MULTIPLEXED COMPTON SCATTER TOMOGRAPHY FOR SINGLE-SIDED
NONINVASIVE INSPECTION

DISSERTATION

Presented to the Faculty of the Graduate School of Engineering

of the Air Force Institute of Technology

Air University

Air Education and Training Command

In Partial Fulfillment of the Requirements for the Degree of

Doctor of Philosophy

Brian L. Evans, B.S., M.S.
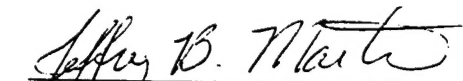
Captain, USAF

April 1999

FAN-BEAM MULTIPLEXED COMPTON SCATTER TOMOGRAPHY FOR SINGLE-SIDED NONINVASIVE INSPECTION

Brian L. Evans, B.S., M.S.
Captain, USAF

Approved: Date

Jeffrey B. Martin
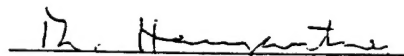
Jeffrey B. Martin (Chairman)   18 Mar 99

Paul I. King

Paul I. King (Dean's Representative)   2 Apr 99

Larry W. Burggraf

Larry W. Burggraf   19 Mar 99

R L Crane

Robert L. Crane   19 MAR 99

Thomas N. Hangartner
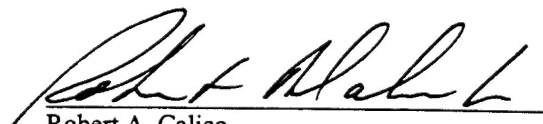
Thomas N. Hangartner   19 March 99

Michael C. Roggemann

Michael C. Roggemann   3/24/99

Accepted:

Robert A. Calico

Robert A. Calico
Dean, Graduate School of Engineering

Table of Contents

List of Figures

Abstract

As many Air Force weapons systems become older, their airworthiness can be degraded by environmental corrosion of aluminum airframes and control surfaces. The aircraft require nondestructive inspection of certain structural components to ascertain their integrity. Frequently access is available to only one side of the aircraft component needing inspection, so transmission radiography is not possible and scattered radiation must be used. There is a need for a reliable and practical instrument that can noninvasively detect and image the density loss that is indicative of corrosion.

This research develops, investigates, and demonstrates a novel single-sided radiological imaging technique called multiplexed Compton scatter tomography (MCST). Scanning systems now used for airframe inspection isolate small volumes of the sample for individual interrogation. MCST uses spatial and energy multiplexing to provide a truly tomographic inspection mode that interrogates comparatively large regions of the sample simultaneously. This new imaging modality may provide an advantage in efficiency and practicality. MCST uses a radionuclide gamma ray source and multiple energy-discriminating detectors. Collimators restrict the inspection region to a tomographic slice that is defined by the intersection of the source illumination fan beam and the detector acceptance fan beam. The detectors record the energy spectra of gamma rays scattered in the sample. MCST exploits the relationship between a Compton scattered gamma ray's energy shift and scattering angle to localize each recorded event to any number of curved projections.

The airframe inspection application presents a thin, low-Z target that requires source photons in the energy range near 100 keV to provide reasonable system efficiency. Planar high-purity germanium (HPGe) detectors are well suited for this energy regime and are available in linear arrays to provide simultaneous spatial sampling. At these energies, the scattered gamma ray spectra are significantly influenced by the momentum distribution of the electrons in the target, a phenomenon known as Doppler broadening. This broadening is energy-variant and the shape is a function of scattering material.

A deterministic system model is developed that implements advanced features such as Doppler broadening, extended source and detector sizes, and the spatially-variant and energy-variant aspects of detector response. These features allow direct simulation without convolving an idealized model with an

experimentally-measured detector response function. Likewise, it allows the direct use of measured spectra for image reconstruction without deconvolving the detector response function.

Two novel approaches to image reconstruction are developed, one based on filtered backprojection and another based on an iterative technique. The filtered backprojection method requires unfolding a scattering angle distribution from each measured energy distribution. Several iterative methods are described to perform this unfolding step. The iterative image reconstruction method is based on a penalized weighted least-squares (PWLS) linear system solution, but implements a two-level iteration to account for nonlinear implicit dependencies in the system.

A demonstration MCST system was assembled from components available commercially. This system includes a 6-element array of HPGe detectors, a ^{109}Cd radionuclide that emits 88 keV gammas, and fan beam collimators developed specifically for this system. It is used to produce the first one-sided MCST images from several aluminum phantoms. This validates the system model and iterative image reconstruction algorithm, and demonstrates the feasibility of the one-sided MCST technique.

The response of a next-generation MCST system is simulated. The simulations address such issues as the contrast recovered from various samples, system efficiencies, and counting times.

FAN-BEAM MULTIPLEXED COMPTON SCATTER TOMOGRAPHY
FOR SINGLE-SIDED NONINVASIVE INSPECTION

I. Introduction

1.1. Research Objectives

The objective of this project is to investigate and demonstrate the principles of a multiplexed Compton scatter tomography (MCST) system for nondestructive inspection of low-Z materials, particularly aluminum. The research effort consists of analytical modeling and an experimental MCST system that verifies the computer models and demonstrates MCST imaging with experimental data.

Primary components of the Compton scatter tomography system include a radionuclide source, an array of high-purity germanium detectors, radiation collimators, and the sample under investigation. Additional components include signal processing electronics, data acquisition system, and image reconstruction software. Gamma radiation from the source Compton scatters in the sample, and the detectors record the resulting scattered energy spectrum. A cross-sectional image into the depth of the sample is then reconstructed from the set of measured spectra. The use of scattered radiation allows applications where access is limited to only one side of the inspected object so that conventional transmission tomography is impractical or impossible. An example of such an application is inspection of aircraft wings, fuselages, and fuel tanks.

Other one-sided Compton scatter imaging methods simply use narrow collimation of source and detector fields-of-view to isolate the volume under inspection. The energy-discriminating detectors in MCST allow fan-beam collimation of the source and detectors so that comparatively large volumes of the sample are interrogated simultaneously. This wide field-of-view approach coupled with multiple energy channels in multiple detectors constitutes the multiplexing which sets this technique apart from the systems relying on narrow collimation

The analytical modeling consists primarily of a deterministic gamma-ray transport code and two image reconstruction codes. The transport code is a deterministic model developed to simulate the energy distribution of scattered gamma rays collected by an MCST instrument. The code differs from previously

published work with the inclusion of some important phenomena that influence the signal in an MCST system. Some important examples include Doppler broadening of Compton scattered photons, detector resolution, and the finite sizes of sources and detectors. Thus the model allows for an evaluation of particular MCST designs without costly construction and measurement. The image reconstruction codes unfold a cross-sectional image of the sample from the energy spectral data.

A demonstration MCST system validates the modeling by collecting actual energy spectra for comparison against the deterministic model. Furthermore, data collected with the demonstration system are used to reconstruct rudimentary electron density images of the inspected phantoms. This validates the image reconstruction techniques.

One may envision many applications of Compton scatter tomography, but one application of interest to the project sponsor, The Air Force Research Laboratory, is given particular consideration -- the detection of corrosion in aluminum aircraft sheet metal. This application is particularly challenging due to one-sided geometry constraints, low contrast, and demanding resolution requirements. The viability and reliability of detecting corrosion defects with a hypothetical full-scale multiplexed Compton scatter tomography system is assessed. However, the generality of the results obtained will be preserved whenever possible.

Another noteworthy MCST application that has been the subject of recent research at AFIT is the measurement and quantification of bone density (Sands, 1999). Such measurements are important for the diagnosis of osteoporosis and represent a possible medical application of an MCST system.

1.2. Scope of the Research

The ultimate objective is to demonstrate a new method for single-sided nondestructive inspection of low-Z materials. Much of the method development and assessment is based on computer modeling. However the project includes a demonstration MCST system which will validate the gamma-ray transport code and reconstruction algorithms by collecting actual data for comparison. The demonstration MCST system is built from off-the-shelf components and is consequently not optimal. It is only intended as a proof-of-principal device, not a full-scale inspection system. Nevertheless, test images of rudimentary phantoms are reconstructed using real data obtained with the demonstration system.

The scope of this work is restricted to inspection of aluminum samples due to the principal application of interest, noninvasive airframe inspection. Experimental samples are composed of pure aluminum, but the presence of aluminum corrosion products containing hydrogen and oxygen is considered in the modeling. Other materials that will surely be present in any field sample are not considered. Examples of such materials are paint, primer, steel rivets, and alloying metals. These factors are indeed worthy of consideration, but the feasibility of this technique must first be demonstrated and established with simplified phantoms.

1.3.   Why MCST?

The Air Force Research Laboratory hopes to develop advanced systems for noninvasive inspection of aluminum aircraft components such wings and fuselage sections where hidden corrosion of metal may threaten airworthiness. In many situations, immediate access is restricted to only one side of the part needing inspection, making conventional transmission tomography impossible. Examples of such situations include inspection of wings, fuel tanks, and fuselage lap joints. Disassembly of the aircraft for inspection of these areas is impractical and expensive. The situation calls for a one-sided inspection system that can be used with the inspected parts in place on the aircraft. Ideally, this system should generate cross-sectional images of the inspected region for easy interpretation by technicians. Composition changes, reduction of density, or the thinning and even loss of structural material would indicate corroded regions. Several techniques are available for one-sided inspection, each of which has its particular pros and cons for the airframe inspection application.

Ultrasound imaging is used successfully in the aircraft industry for inspection of aerospace components. In the pulse-echo technique both the acoustic transmitter and receivers are positioned on the same side of the inspected object, providing one-sided inspection capability. (Bray and McBride, 1992) General Electric, for instance, uses ultrasound for inspection of critical bearings in their commercial jet engines. Problems arise with ultrasound when the acoustical properties of the object change abruptly. Such is the case in aircraft lap joints, where two pieces of aluminum sheet metal may be separated by a small gap of air that makes a very poor acoustic coupling. The sonic pulse is reflected from the inside surface of the first layer, so signal from the deeper sheet is lost. Aircraft lap joints are particularly prone to

corrosion because they can trap the moisture that acts as the corrosion catalyst, so ultrasound may not be ideally suited for this application.

Low-frequency eddy current inspection can penetrate aluminum to a depth of approximately 10 mm and allows detection of second-layer cracking or the thinning of material that accompanies corrosion. It has been successfully applied for airframe inspection, but is most useful in inspection of large, uniform surfaces for which the response of clean material is well-characterized (Bray and McBride, 1992). Structure may present problems because the resulting changes in eddy current response may be difficult to interpret, particularly because eddy current testing does not provide an image for rapid evaluation by human operators. Inspection of large areas requires scanning over numerous positions to test small areas independently.

Compton scatter inspection systems penetrate the depth of the sample with x-rays or gamma rays, and measure the radiation scattered back toward the surface. Compton scatter is essentially a collision between an electron and photon, so the probability of such an event in an incremental volume is proportional to the number of electrons in that volume. This concept is demonstrated by Figure 1-1, which shows that for a photon energy of 100 keV, the Compton scattering cross section per atom is very nearly linear with the atomic number Z and thus with the number of electrons in the atom. Measuring the intensity of radiation scattered from a small volume, therefore, gives a measure of that volume's electron density. The intensity measurement may need to be corrected for attenuation within the sample of the incident and scattered radiation. Some information concerning the mass density and composition of the sample may be inferred from the electron density measurements. For instance, if the sample is known to be
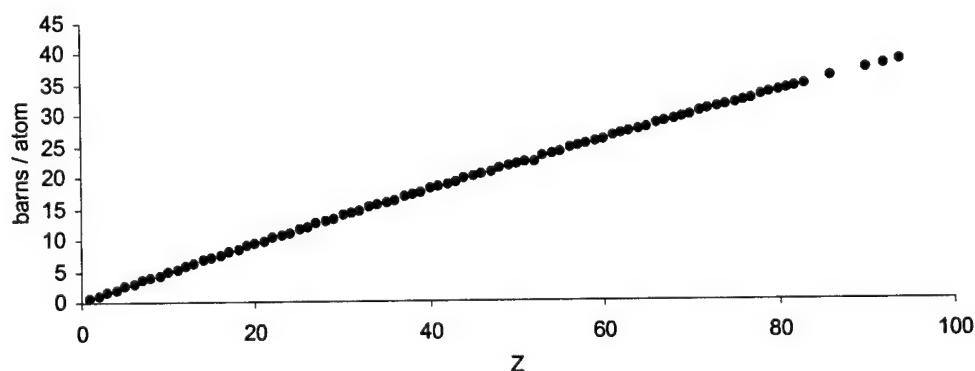
Figure 1-1. Compton Scatter Cross Sections of the Elements for 100 keV Photons. Cross sections from (Berger, 1987).

composed entirely of one substance, the electron density is directly proportional to the mass density. However, when there are multiple materials in the sample, it may be difficult to couple properly the attenuation correction with the electron density, resulting in qualitative, rather than quantitative, measures.

Some Compton scatter imaging systems have been developed and have found operational use. Notable examples are the COMSCAN system (Harding, 1997; Lawson, 1995) and ARACOR BIT system. Others have demonstrated results on similar laboratory systems (Zhu, 1996; Thoe, 1996). These devices are variations on the type of scanner first developed by Lale in 1959 (Lale, 1959). They accomplish x-ray backscatter depth profiling (x-ray BDP) by using narrow collimation of the source and detectors (Harding, 1997; Zhu, 1996) or narrow collimation of the source and somewhat wider collimation of detectors (Thoe, 1996). The purpose of the collimation is to select for inspection only the volume formed by the intersection of the source collimator and detector collimator. Figure 1-2 illustrates the essential features of an x-ray BDP system. Use of multiple detectors such as in the ARACOR BIT system provides sampling of the incident x-ray beam at multiple depths along its path. The scattered x-ray fluence registered in the detectors is taken as a measure of the electron density in the selected volume. Each measurement will be modified by attenuation of the incident and scattered beam, so attenuation correction is sometimes required.

This technique is sometimes referred to as Compton scatter tomography, but differs from most tomographic techniques in the sense that image reconstruction is not built from projections as in, for example, Computed Tomography (CT), Positron Emission Tomography (PET), or Single Photon Emission Tomography (SPECT). Modern tomographic techniques usually reconstruct a two-dimensional function
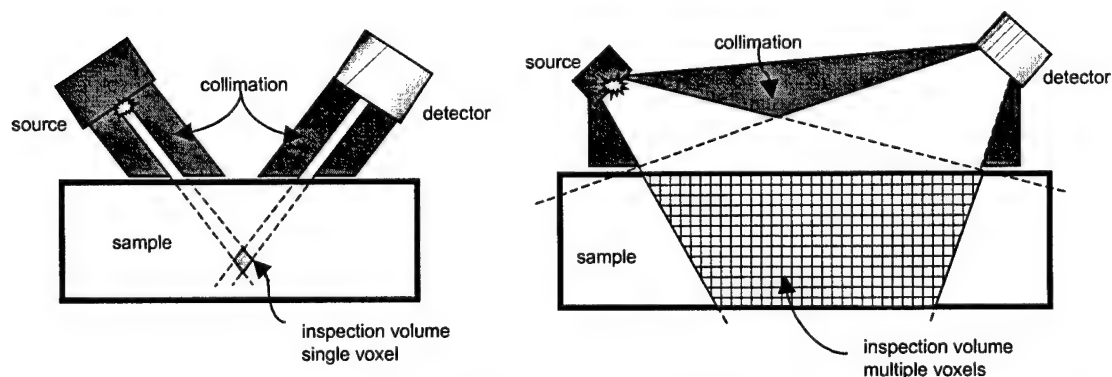
Figure 1-2. Comparison of x-ray BDP to MCST. Left: x-ray BDP where the measurement volume is the intersection of the incident beam and the detector acceptance cone. Right: single-detector MCST where wide-angle collimation interrogates many voxels simultaneously.

from a set of line integrals (Cho, 1993). X-ray BDP, on the other hand, creates an image of the sample by compiling the results from many independently measured volume elements or voxels. Because each voxel is inspected independently, it is necessary to scan the apparatus over the volume of interest. Although this process seems cumbersome and less elegant than reconstructing from projections, the advantage of the narrowly collimated system is that resolution is limited only by the diameter of the collimation. Efficiency falls off rapidly as the collimation becomes narrower, however high-intensity x-ray tubes may be used because the energy of the incident photons need not be well defined. This feature allows for good data throughput (Harding, 1989).

Multiplexed Compton Scatter Tomography (MCST), like x-ray BDP, uses Compton scattered radiation to inspect within the depth of the sample, but much wider source and detector fields-of-view allow simultaneous inspection of multiple voxels, as illustrated in Figure 1-2. Consequently, the number of scan positions needed to image a given volume may be significantly reduced from that of x-ray BDP. Simultaneous inspection is possible because image reconstruction proceeds from projections not unlike the reconstructions used in CT, SPECT and PET. The projections are not defined by physical collimation, but rather from the energy shift of the scattered photons detected. Therefore, MCST requires an energy-sensitive detector (or set of detectors) and a radioisotope source. Multiplexed Compton scatter tomography refers to the use of multiple energy channels in multiple detectors to inspect multiple voxels simultaneously. This is an important distinction that sets this technique apart from x-ray BDP which is sometimes referred to as Compton scatter tomography.

While Figure 1-2 suggests a wide field-of-view for both source and detectors, they are both confined to a planar fan beam slice of the sample as in conventional transmission CT. This simplifies backprojection and image reconstruction to a single image plane and reduces noise problems associated with unwanted scatters.

1.4.   MCST Background & Literature Review

The principle underlying multiplexed Compton scatter tomography was first developed by Kondic (Kondic, 1983) who proposed exploiting the relationship between the energy E' of a Compton scattered gamma ray with initial energy E_0 and its scattering angle θ to extract information about the scattering

location. The scattering angle θ is defined as the angle between the initial and deflected photon wave vectors. The relationship is given to first order by the Compton equation.

$$E' = \frac{E_0}{1 + \frac{E_0}{m_0 c^2}(1 - \cos\theta)} \qquad (1\text{-}1)$$

Under ideal conditions, the Compton equation can be used to localize possible scattering locations to a circular isogonic arc.

To demonstrate, assume that a point source of gamma radiation with a single energy E_0 is located at the origin of a Cartesian coordinate system and that an ideal point detector is located at position x_{det} on the x-axis. Restrict consideration to a single x-z plane and to photons that travel initially from the source into the portion of coordinate space below the z-axis. If the detector records a singly-scattered photon of energy E' then the scattering angle θ is known through Equation (1-1). The locus of possible scattering locations is an isogonic arc passing through both the source and detector as shown in Figure 1-3. The radius R of the circle is given by (Norton, 1994)

$$R = \frac{x_{det}}{2} \frac{1}{\sin\theta} \qquad (1\text{-}2)$$

and the circle is centered at
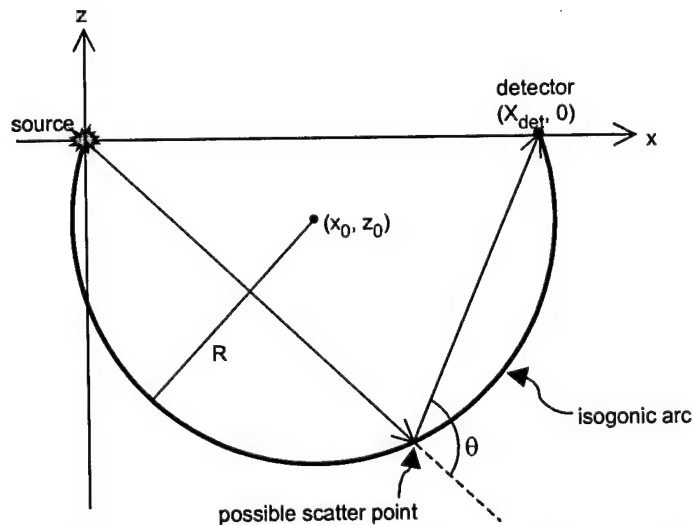
Figure 1-3. An Isogonic Arc Defined by Source Position, Detector Position, and Scattering Angle.

$$(x_0, z_0) = \left(\frac{x_{det}}{2}, \frac{-x_{det}}{2} \frac{1}{\tan \theta} \right)$$

(1-3)

If multiple detector positions are used, each registering counts at multiple energies, the result is a mesh of isogonic arcs in the imaging plane as illustrated in Figure 1-4. Each arc corresponds uniquely to a particular scattered gamma-ray energy E′ recorded in a particular detector. The shorter and shallower arcs correspond to small θ and thus to E′ near E_0. Conversely the larger and deeper arcs correspond to larger θ and thus to lower E′. Sampling through the object may be improved by adding more detectors, changing the source location, or both. These isogonic curves are analogous to the straight line projections acquired in CT. Whereas the data set in CT represents integrals of attenuation coefficient along straight lines through the object, the data set here represents integrals of the object's electron density along curved paths. However, factors such as geometry and attenuation of incident and scattered radiation make the actual projections much less straightforward than the analogy suggests.

To consider a more realistic case, finite sizes must be assigned to the source and detector aperture. In this case isogonic regions replace the idealized isogonic arcs. Any singly-scattered photon at energy E′ recorded in a detector may have scattered from any point in the corresponding isogonic region of the image plane. An illustration of such a region is also shown in Figure 1-4. Early modeling performed in this research made it clear that treating the sources and detectors as finite-sized objects is necessary to develop truly realistic models of the imaging system, particularly when those sizes are comparable to the size of the sample features which must be resolved.
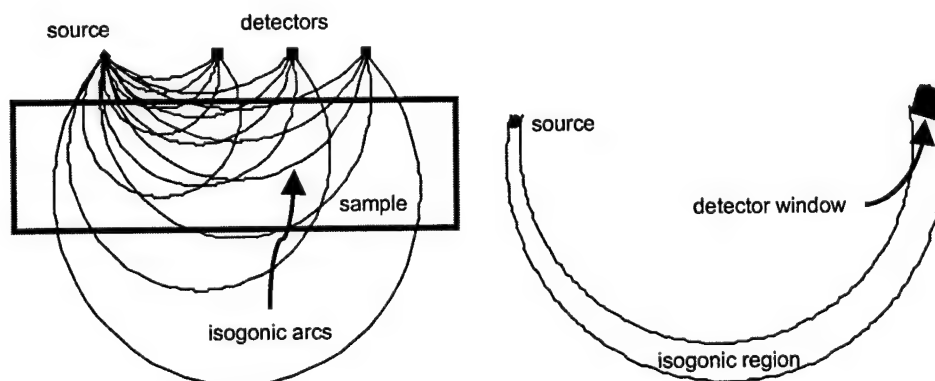
Figure 1-4. Isogonic Curves. Left: Multiplexing in energy and detector position creates a mesh of isogonic curves through the sample. Right: Considering non-point sources and detector apertures replaces each isogonic curve with an isogonic region.

The two pieces of work which most closely parallel this research are those of N.V. Arendtsz (Arendtsz, 1995a; Arendtsz, 1995b) and T.H. Prettyman (Prettyman, 1991; Prettyman, 1993).

Prettyman developed a tomography technique that combines information collected simultaneously with a transmission tomographic scanner and a projective scatterometer. The projective scatterometer consists of a fan-beam-field-of-view high-purity germanium (HPGe) detector that measures scattered energy spectra. A ^{137}Cs source provides 662 keV source gammas. Rotating the cylindrical sample relative to the source and detectors increases the number of projections. Figure 1-5 provides an illustration of this dual mode concept. Prettyman's work uses primarily Monte Carlo simulations to establish the viability of the dual mode technique, but he performs experimental measurements to validate the Monte Carlo code. Images are reconstructed from Monte Carlo data. The combined transmission/scatter mode has certain advantages over dual energy CT for imaging industrial samples. For one-sided applications such as airframe inspection, geometry limitations preclude the use of transmission measurements, and the sample cannot be rotated 360 degrees relative to the detectors. Rather than sample rotation, the MCST must rely on multiple source and detector positions to increase the number of projections. Nevertheless, Prettyman's projective scatterometer has the same function as the MCST system's detectors.

N.V. Arendtsz's body of work in Energy spectral Compton scatter tomography (ESCST) is more closely related to the work presented here. Arendtsz reconstructed 2-D images on a 10 x 10 grid of phantoms from experimentally measured scattering spectra. Her system consists of a ^{137}Cs source, and a coaxial HPGe detector positioned at various locations surrounding the phantom as illustrated in Figure 1-6. It should be evident from Figure 1-6 that the geometry used by Arendtsz cannot be applied to the one-sided
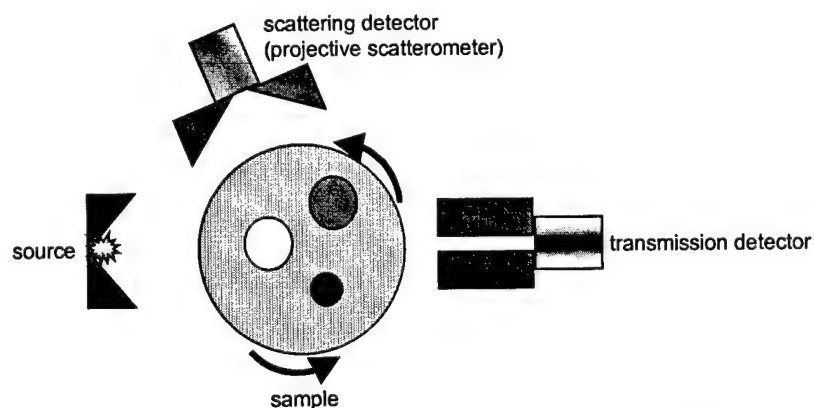
Figure 1-5. The Dual-Mode Concept of Prettyman. Author's interpretation.
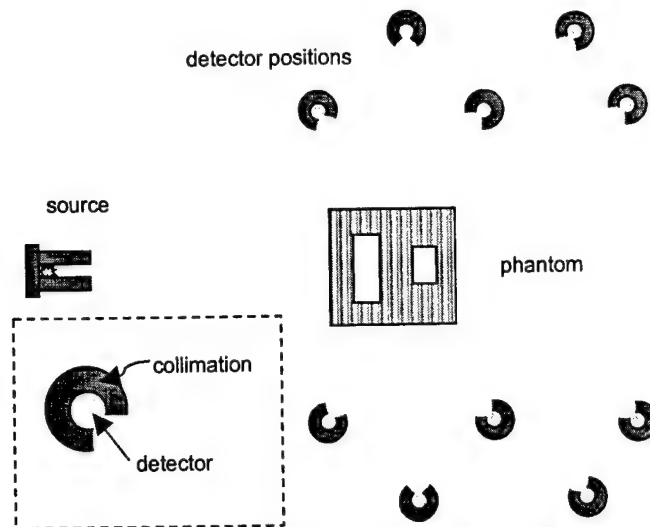
Figure 1-6. The ESCST Demonstration of Arendtsz. Author's interpretation.

inspection problem. Arendtsz developed a system model to simulate the physics of ESCST based on modeling a point source and ideal point detector. To use experimental data for image reconstruction, she deconvolved an experimentally-measured detector response function from the measured spectra to make the spectra more consistent with the idealized assumptions of the system model. This approach required measuring the energy spectra collected by the detector from several small phantoms and interpolating intermediate values. For image reconstruction Arendtsz investigated several iterative methods.

Norton showed that the image reconstruction problem for Compton scattering tomography has an analytical solution that is very similar to the filtered backprojection algorithm widely used in conventional transmission CT. The analytical solution is based on some ideal assumptions concerning attenuation and assumes continuous and idealized sampling in both position and energy. A discretized version is investigated here.

1.5. MCST Application: Aluminum Airframe Inspection

1.5.1. Aluminum Corrosion

Pure aluminum exposed to air rapidly oxidizes and forms a thin protective film of aluminum oxide, alumina, which tends to resist further oxidation and thereby gives aluminum its good anti-corrosive qualities. This film is typically only about 25 Angstroms thick, and takes the form of amorphous aluminum oxide Al_2O_3 covered by aluminum oxyhydroxide, AlOOH (Godard, 1967; Marcus, 1995). The film is brittle and cannot elongate under stress that may be applied to the metal, which may cause damage to the

protective layer (Dix, 1946). The film may also contain points of weakness due to the presence of either normal metal impurities or intentional alloying elements that do not form a protective oxide film as readily. The important point is that in all naturally formed films there are points of weakness where corrosion may start (Dix, 1946).

Electrochemical corrosion of aluminum takes place in the presence of an electrolyte such as an aqueous medium when the electrolyte penetrates to the metal surface, and there exists a difference in electrochemical potential forming an anode and a cathode. The amount of metal dissolved at the anode is proportional to the current caused by the potential difference. In the case of galvanic corrosion the potential difference arises when aluminum is in contact with a dissimilar metal such as copper or steel. This type of corrosion is much more prevalent in marine atmospheres than in rural or industrial atmospheres (Godard, 1967). Aluminum corrosion should be signaled by a loss of metal thickness and pitting and possibly accompanied by the presence of corrosion products. The principal corrosion products expected are the hydrated aluminum oxides of gibbsite, $Al(OH)_3$, or boehmite, $AlO(OH)$ (Godard, 1967). Gibbsite is a clay mineral, whose crystalline form has an electron density similar to that of aluminum. However, studies of aircraft corrosion have shown that the actual corrosion product has a density of about half that of aluminum. The difference is due to the formation of pores in the amorphous corrosion product as it dehydrates. The pores are volumes that were filled with electrolyte (water) during the corrosion process. The relative volume of pores in corrosion product is about 40 percent (Lawson, 1995). This reduced electron density may be exploited to signal the presence of anomalies in the sample. In moist environments the corrosion product may even be washed away from repeated exposure to water. In this case a void in the sample may appear that provides an even higher contrast anomaly with virtually zero electron density.

The Air Force Research Laboratory would like to develop a system with adequate resolution to detect millimeters-sized corrosion defects in an aircraft's aluminum sheet metal. Defects that lie hidden on the unexposed side of a sample or within some structure such as a lap joint pose the biggest challenge for detection, but are very important to detect. Attenuation of both the incident and scattered radiation means that the deeper sections of the sample produce less signal than those near the exposed surface. Corrosion may also be present on the exposed surface of the aluminum, but obscured from visual inspection by paint

and primer. The thickness of aluminum sheet metal used in airframes ranges in thickness from 3mm – 10 mm but may be as much as 10 – 15 mm in areas such as lap joints where the structure consists of several layers of sheet (Lawson, 1995).

X-ray backscatter depth profiling (x-ray BDP) has already been demonstrated to be an effective tool for detection of the metal loss and corrosion product which accompanies the corrosion of aircraft sheet metal (Lawson, 1995; Harding, 1997). These techniques have more than adequate resolution to detect millimeter-sized defects. The MCST technique is being considered for the potential advantages it may provide in this application, in particular the ability to image extended sections without scanning voxel-by-voxel.

1.5.2.   Choice of Radioisotope and Detector System

The MCST system requires a radioisotope gamma ray source so that the energy shift of scattered photons can be detected. X-ray tubes produce a spectrum of energies, so they are not suited to this application. Measuring the energy shift with limited ambiguity calls for radioisotope that emits a single gamma ray line at an energy E_0. The energy range of interest is the range of singly-scattered photon energies limited at the upper end by E_0 and at the lower end by $E_0/(1-(2E_0/511))$, where energies are in keV. The source may be acceptable if it emits additional x-rays or gamma rays considerably below the energy range of interest, but emissions higher than E_0 are troublesome because photons downscattered from the higher-energy line will pollute the desired spectrum. It is also important for measurement efficiency to select a source energy at which Compton scatter is the dominant mode of interaction.

Figure 1-7 shows the various photon interaction cross sections (barns/atom) in aluminum as a function of energy. The XCOM Photon cross section code (Berger, 1987) produces the values shown. The figure reveals that Compton scatter is the most likely interaction above 55 keV, and dominates above 100 keV. Photoelectric interactions are of some concern as they will cause absorption of a photon and thereby reduce the intensity of scattered radiation, particularly from deeper regions of the sample. Coherent scattering may be a source of trouble because it will contribute to the multiple scatter background. A single coherent scatter is very likely to scatter at a small angle (Evans, 1965), so the chances of observing many single coherent scatter events in the MCST system are low since it observes larger angles. Additionally, a single coherent scatter event will be recorded at the source energy, so those counts may be discarded. More
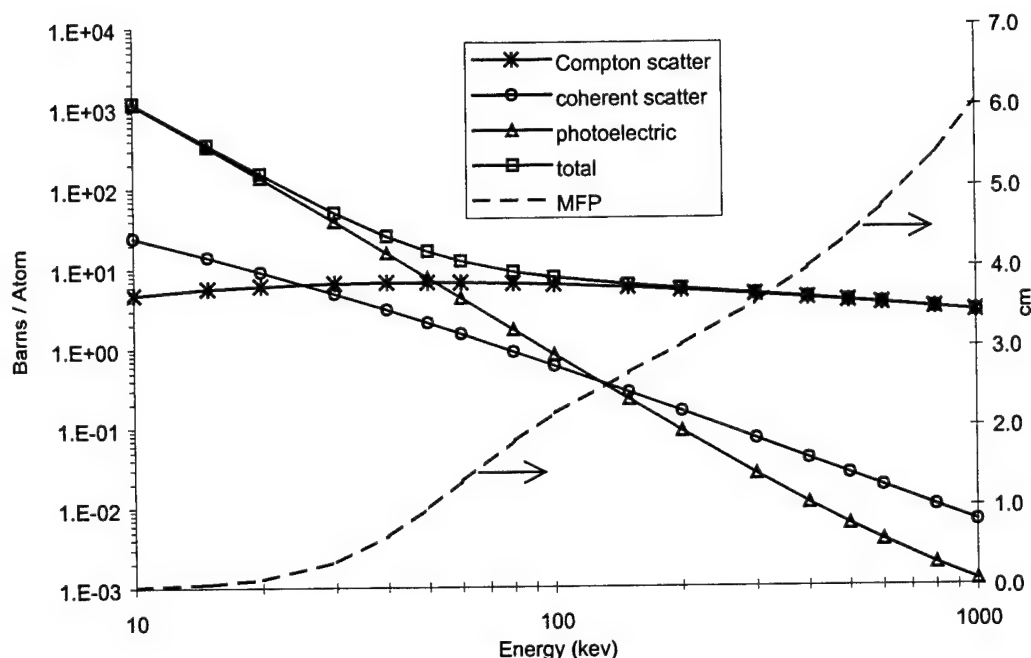
Figure 1-7. Partial Interaction Cross-Sections and Mean Free Path (MFP) in Aluminum.

troubling is the possibility of coherent scatter followed by Compton scatter, resulting in a count that carries a viable energy but incorrect scattering angle information. Such events will be considered part of the multiple scatter contamination of the signal, and will be investigated in Chapter 2.

Another consideration for choosing a source is the penetrating power of the photons into the sample material. Attenuation of incident and scattered photons must be considered. Enough penetration is desired to illuminate the deepest portions of the sample and then recover photons that scatter there. A source with low energy will illuminate only the closest surface of the sample, and recover little data from the deeper portions of the sample. On the other hand, an overly energetic source will pass most photons straight through a thin sample without interacting. In applications like airframe inspection, these photons may scatter back from components or structure installed behind the sample. Based on these concerns, a possible rule of thumb is to select a source energy that has a mean free path in the target of about twice the target thickness, thereby avoiding excessive absorption or unwanted transparency of the sample.

A source energy near 100 keV fits the requirements for application to aluminum airframe inspection well. The mean free path is around 2 cm, and it is energetic enough that Compton scatter dominates. The desire for quasi-monoenergetic sources eliminates from consideration some popular

isotopes with emissions near 100 keV such as [57]Co (122 keV, 136 keV), [133]Ba (81 keV, 302 keV, 355 keV), 153Gd (69 keV, 83 keV, 97 keV, 103 keV) and [152]Eu (122 keV, 344 keV, 778 keV, 964 keV, 1085 keV, 1112 keV, 1408 keV). An isotope with a reasonably long half-life is desired to avoid the expense of repeated replacement and because there are no on-site production capabilities. Several commercially available candidate radioisotopes with single emission lines near 100 keV are listed in Table 1-1 (Isotope Products Laboratories, 1995; Amersham Corp., 1994; North American Scientific, Inc., 1994). [109]Cd was selected for this project largely because of its immediate availability in a sealed capsule form. The solid cadmium metal deposits provide a higher specific activity than the solutions or gasses, making possible a smaller, more point-like source. The other isotope readily available in sealed capsule, [241]Am, provides a 59.5 keV gamma which was judged too low in energy to image a 1-cm thick aluminum target. The xenon gas is available in concentrations only up to 100 μCi/cm^3 (North American Scientific, Inc., 1994) and the short half-life would mean frequent replacement. The obvious disadvantage to [109]Cd is the low intensity of 88 keV gammas, requiring a higher activity source than would otherwise be needed.

Table 1-1. Candidate Isotopes for MCST System

Isotope	Gamma Emission		Other Emissions		Half Life	Available Form
	Energy	Intensity	Energy	Intensity		
[109]Cd	88.0 keV	3.60%	22-26 keV	99.80%	1.27 y	capsule
[123]Te^m	159.0 keV	84.0%	27-32 keV	50.30%	119.7 d	solution
[133]Xe	81.0 keV	37.0%	30-36 keV	48.90%	5.254 d	gas ampoule
[144]Ce	133.5 keV	10.8%			284 d	solution
[241]Am	59.5 keV	35.7%	11-21 keV	39.50%	432.7 y	capsule
[243]Am	74.6 keV	60.0%	43.54 keV	5.10%	7380 y	solution

The choice of radioisotope and detector system should not be considered independently. To maximize the data throughput, the detector should be very efficient at the source energy. The detector should also have high intrinsic peak efficiency and a low peak-to-total ratio across the energy range considered so the signal collected is not corrupted with extensive counts that register only a fraction of the true gamma ray energy. In other words, the Compton continuum should be negligible. Good energy resolution is also desired to pinpoint photon energies with minimal error. The best energy resolution is achieved with high-purity germanium (HPGe) detectors (Knoll, 1989). The p-type planar variety is available in sizes ranging from 6mm to 36mm diameter and 5mm to 15mm thickness. They typically have a resolution of about 550 eV at 122 keV (EG&G Ortec, 1997). Larger detectors have better efficiency, but

poorer energy resolution. Use of smaller detectors can increase the spatial sampling rate, as more detectors may be positioned in a given space. Figure 1-8 is a scan of a graph provided by one manufacturer, EG&G Ortec. It shows their reported intrinsic full-energy efficiency as a function of energy for p-type planar HPGe detectors. At energies below 10 keV, the efficiency is affected by the beryllium window thickness, while at energies above 50 keV the efficiency is affected by the detector thickness. At the energies of interest here, the efficiency is reported as 85 to 100 percent for a 10 mm thick detector.
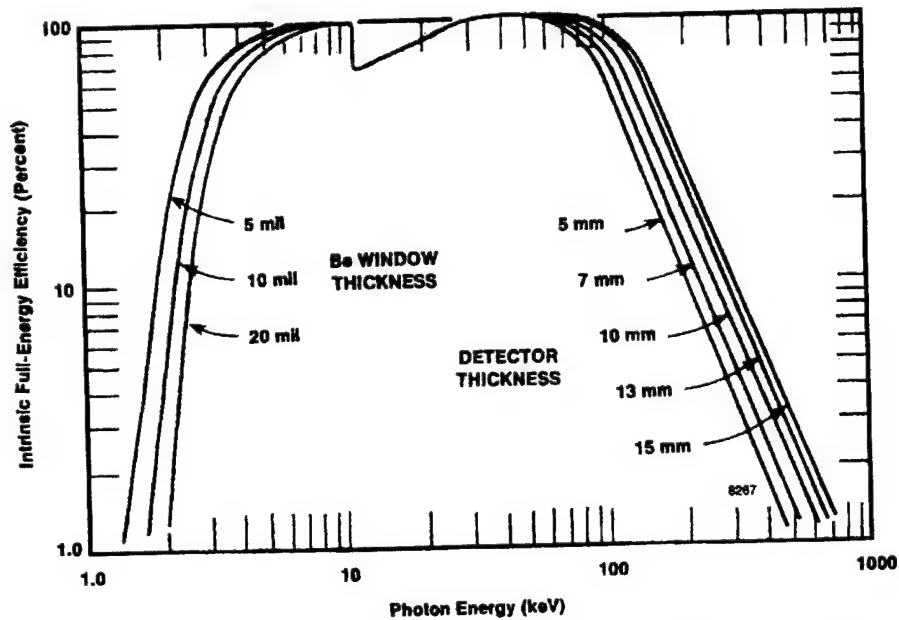
Figure 1-8. Intrinsic Peak Efficiency of P-Type Planar HPGe Detectors. (EG&G Ortec, 1997). Used with permission.

1.6. Physics of Compton Scattering

Compton scattering occurs when an x-ray or gamma ray with an initial energy E_0 collides with an atomic electron and is deflected from its initial trajectory through some angle θ. A shift in energy occurs resulting in a deflected photon with energy E'. This phenomenon was first described by A.H. Compton, who showed that the energy E' may be derived from a classical model to be (recalling Equation (1-1)),

$$E' = \frac{E_0}{1 + \frac{E_0}{m_0 c^2}(1 - \cos\theta)} \cdot \tag{1-1}$$

In low-Z materials Compton scatter is the predominant photon interaction over most the range of energies (40-120 keV) used in diagnostic x-rays. This fact stands in contrast to the preponderance of diagnostic techniques which use the photoabsorption interaction to characterize low-Z samples (Cho,

1993), the most familiar of which are the many methods developed for x-ray transmission imaging of body tissue.

The Klein-Nishina relation provides the differential cross section for Compton scattering at angle θ per unit solid angle $d\Omega$. It is given here per free electron for unpolarized radiation.

$$\left(\frac{d\sigma}{d\Omega}\right)_{KN} = \frac{1}{2}r_0^2\left(\frac{E'}{E_0}\right)^2\left(\frac{E'}{E_0} + \frac{E_0}{E'} - \sin^2\theta\right) \tag{1-4}$$

Equations (1-1) and (1-4) were derived on the assumption that the scattering electron is a free electron -- unbound and at rest. When scattering from atomic electrons these assumptions are clearly not valid, but the equations are still widely used because they represent good approximations for many applications. The simplest approximation to the atomic electron Compton scattering cross section consists of a modification to the free-electron Klein-Nishina cross section called the incoherent scattering function approximation (Hubbell, 1975; Hubbell, 1997). The incoherent scattering function $S(x, Z)$ is defined as the ratio of differential Compton-scattering cross sections of electrons bound to an atom of atomic number Z and that of a free electron (Namito, 1995). Therefore,

$$\left(\frac{d\sigma}{d\Omega}\right)_{bound} = \left(\frac{d\sigma}{d\Omega}\right)_{KN} S(x, Z) \tag{1-5}$$

where

$$x = \frac{\sin\left(\frac{\theta}{2}\right)}{\lambda_0} \tag{1-6}$$

and λ_0 is the wavelength of incident radiation. $S(x, Z)$ is unitless. The effect of the incoherent scattering function is to diminish the Compton scattering cross section in the forward direction. It is here that the binding energy of the electrons has the greatest effect, since the momentum transfer from photon to electron is smallest. In the limiting case as θ approaches zero, the incoherent scattering function gives zero probability for Compton scatter and the Klein-Nishina cross section is non-zero. The incoherent scattering function provides a more appreciable correction for higher Z and for lower E_0. Figure 1-9 shows how the aluminum incoherent scattering function changes with angle for an 88 keV and 662 keV source. Note that at the higher energy the correction is only appreciable at small angles. Figure 1-9 also shows a comparison
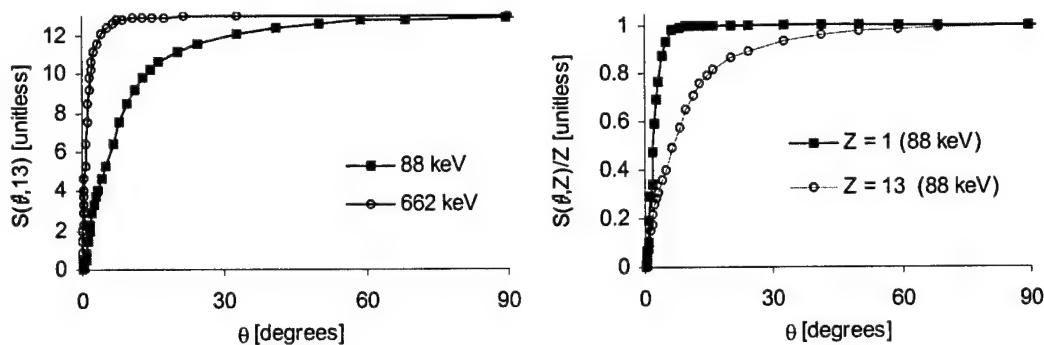
Figure 1-9. Incoherent Scattering Functions. Left: Aluminum functions at E_0 = 88 keV, 662 keV. Right: Comparison of hydrogen and aluminum. Data from (Hubbell, 1975).

of the incoherent scattering functions for hydrogen (Z=1) and aluminum (Z=13) that demonstrates how the correction is more appreciable in higher-Z materials.

Another important effect not predicted by the first order scattering model (Equation (1-5) and (1-6)) is the energy distribution of scattered photons that results from the momentum of bound electrons. For any precisely defined θ, the scattered energy E' is not precisely known as Equation (1-1) suggests. Instead, the momentum distribution of the bound electrons gives rise to a distribution of possible energies for any θ (Cooper, 1971; Cooper, 1977; Cooper, 1997; Biggs, 1978; Urban, 1978; Ribberfors, 1975). This phenomenon is referred to as Compton broadening, or more commonly as Doppler broadening. The distribution of E' is material dependent because it is a function of the momentum distribution of electrons in the scattering atom. The electron momentum distribution is described by the material's Compton profile. Doppler broadening is also θ dependent. The severity of Doppler broadening increases with scattering angle θ because at larger values of θ more of the electron's momentum may be imparted to the photon. Doppler broadening is also E_0 dependent. The width of the E' distribution relative to E_0 decreases for higher E_0 (Matschenko, 1989). For a current compilation of articles concerning Doppler broadening, the reader is referred to Volume 50, No. 1 of *Radiation Physics and Chemistry* (Berstrom, 1997; Kane, 1997; Cooper, 1997; Harding, 1997; Hubbell, 1997).

To describe Doppler-broadened incoherent scattering, the impulse approximation is often invoked (Berstrom, 1997; Matschenko, 1997; Namito, 1994) to compute a double-differential cross section for scattering at angle θ per differential solid angle $d\Omega$ per differential energy dE' (Ribberfors, 1975).

$$\left[\frac{d^2\sigma_s}{d\Omega dE'}\right]_{IA} = \frac{m_0 r_0^2}{2\sqrt{E_0^2 + E'^2 - 2E_0 E' \cos\theta}} \cdot \left(\frac{E'}{E_0}\right)\left(\frac{E_C}{E_0} + \frac{E_0}{E_C} - \sin^2\theta\right) \cdot J(p_z) \qquad (1\text{-}7)$$

Here m_0 and r_0 are the classical electron rest mass and radius, respectively and E_C is the energy given by

Equation (1-1). $J(p_z)$ is the scattering material's Compton profile, which is available in the literature

(Biggs, 1978). The variable p_z is a scalar value that represents the projection of the change in photon

direction onto the electron's pre-collision momentum vector. If $\mathbf{p}_0$ is the pre-collision electron momentum

vector, and $\mathbf{k}_1$ and $\mathbf{k}_2$ are the initial and final photon wave vectors then (Eisenberger, 1970)

$$p_z = \frac{\mathbf{p}_0 \cdot (\mathbf{k}_2 - \mathbf{k}_1)}{|\mathbf{k}_2 - \mathbf{k}_1|} \qquad (1\text{-}8)$$

or if E_0 and E' are expressed in keV then p_z is given in atomic units as (Urban, 1978)

$$p_z = \frac{137}{511}\frac{E_0 E'(1 - \cos\theta) - 511(E_0 - E')}{\sqrt{E_0^2 + E'^2 - 2E_0 E' \cos\theta}} \cdot \qquad (1\text{-}9)$$

The impulse approximation is valid only when the recoil energy of the electron exceeds its binding energy

(Kane, 1997). It is therefore unsuitable for use with forward-directed small-angle scattering. Fortunately

these small angles are the ones at which Doppler broadening is least severe.

It is important to understand that integrating the impulse approximation with respect to E' removes

the E' dependence and recovers the Klein-Nishina relationship (Cooper, 1997).

$$\int_{-\infty}^{\infty}\left[\frac{d^2\sigma_s}{d\Omega dE'}(\theta, E', Z)\right]_{IA} dE' = \left[\frac{d\sigma}{d\Omega}(\theta, Z)\right]_{KN} \qquad (1\text{-}10)$$

Figure 1-10 demonstrates this point. The curves are evaluated for $E_0 = 88$ keV. The figure shows

both the Klein-Nishina curve and the Klein-Nishina curve corrected with the incoherent scattering function

for aluminum. As expected they are similar at large scattering angles and diverge only at smaller angles

where the electron binding energy is comparable to that of the collisional energy transfer. For the range of

scattering angles where the impulse approximation is considered valid (Kane, 1997) the integral of

Equation (1-10) was evaluated with Mathematica to integrate the impulse approximation over E'. The data

clearly shows how the integration recovers the Klein-Nishina curve.
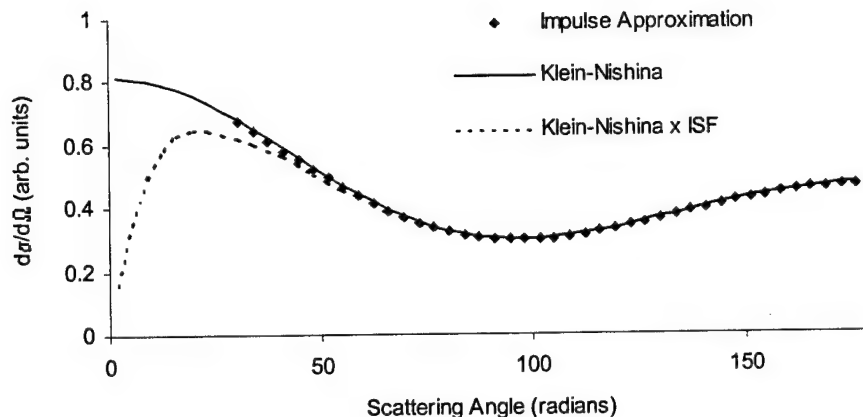
Figure 1-10. Comparison of Scattering Angle Distributions. Energy-integrated impulse approximation, Klein-Nishina, and Klein-Nishina with incoherent scattering function correction.

Figure 1-11 compares the Compton profiles for hydrogen and aluminum. Both curves are normalized per electron for better comparison. The aluminum profile is broader than that of hydrogen because contributions from the outer 2p, 3s and 3p orbitals contribute the sharp central peak which is superimposed on the broad, flatter contributions of the core 1s and 2s electrons (Biggs, 1978). Hydrogen has the narrowest profile of all the elements. Thus as Z increases so does the width of the Compton profile. Figure 1-11 also shows the energy distribution of 88 keV gammas scattered from aluminum at two precise angles as computed from the impulse approximation. Note that the width of the Doppler broadening is considerably shift-variant as it increases with larger scattering angle (lower energy). For most angles the FWHM of the broadening is on the order of keV. Considering that HPGe detectors typically have resolutions of several hundred eV in this energy regime, Doppler broadening is clearly a significant contribution to the scattered energy spectra. As the incident energy E_0 increases, so does the width of the
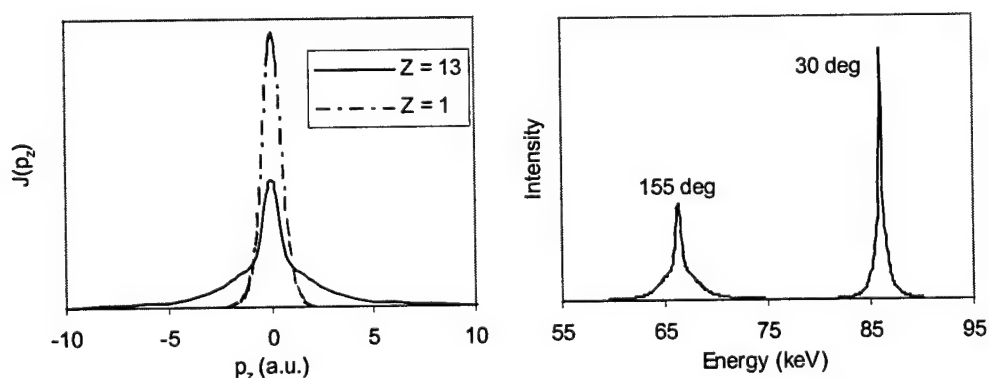
Figure 1-11. The Compton Profile of Aluminum. Left: Compared to that of hydrogen. Right: The Doppler broadening from 88 keV gammas at two scattering angles.

1-19

Doppler broadening.

The important implication of Doppler broadening for the MCST system is that it nullifies the one-to-one relationship between θ and E′ embodied in Equation (1-1). Even if E′ were measured with absolute certainty, Doppler broadening still causes ambiguity in θ.

Although the Compton profiles are not Gaussian, it is instructive to quantify the amount of Doppler broadening by calculating the full width at half-maximum (FWHM) of the E′ distribution resulting from scattering at a given θ as a function of the incident energy E_0. This quantity is labeled $\Delta C(E_0)$. Using the function derived by Matschenko, Figure 1-12 shows $\Delta C(E_0)$ for 90 degree aluminum scatter (Matschenko, 1989). Also shown is the FWHM resolution of a typical HPGe detector such as the ones used in this research. If the Doppler broadening were too narrow to be resolved by the detector, then it would not contribute substantially to the spectroscopy of scattered photons. Figure 1-12 clearly shows that this is not the case. Although the severity Doppler broadening increases rapidly with E_0 in absolute units, when considered relative to the available range of single-scatter photon energies, the broadening actually becomes less severe with increasing E_0. Consider the range of scattering energies ΔE predicted by Equation (1-1)

$$\Delta E(E_0) = E_0 - \frac{E_0}{1 + 2\dfrac{E_0}{m_0 c^2}} \tag{1-11}$$

and define $R(E_0) = \Delta C(E_0) / \Delta E(E_0)$ as the ratio of the Doppler broadening FWHM ΔC to the range of scattering energies ΔE. It turns out that R decreases rapidly with increasing E_0 up to about 200 keV, as shown in Figure 1-12. This implies that at higher energies, the Doppler broadening will have a lesser impact than it will have at lower energies on the system's ability to resolve adjacent scattering angles from the raw energy spectrum.

1.7.   The Central Equation of MCST

The fundamental premise of MCST is that one can reconstruct the density distribution in a cross-sectional slice of an unknown sample from a set of energy spectral measurements. To do this the MCST system must exploit the relationship between the set of pixel densities and the energy distributions of
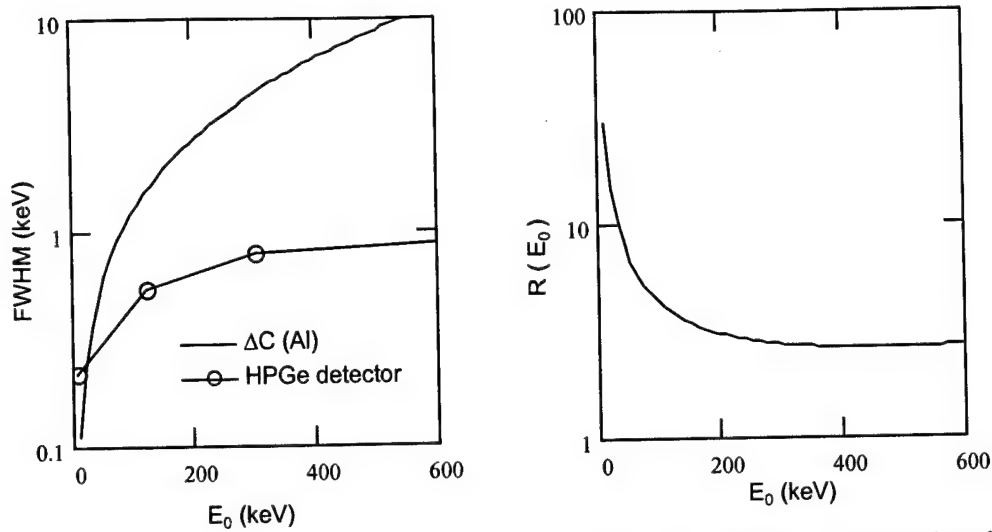
Figure 1-12. Aluminum Doppler Broadening Versus Energy. Left: The FWHM of Doppler broadening increases more quickly than typical HPGe detector resolution. Data shown is for $\theta=90°$ in Al. Right: The ratio $R = \Delta C / \Delta E$ improves at energies above 200 keV.

scattered photons that converge on a set of detectors. Arendtsz writes this relationship as the mathematical system (Arendtsz, 1995b).

$$\Psi = A(\rho)\cdot \rho \qquad (1\text{-}12)$$

where the vector Ψ is the discretized set of energy spectral measurements from the detectors and the vector ρ is the discretized set of densities in the sample. The term scattergram is adopted here when referring to Ψ; a term that acknowledges its similarites to the sinogram data encountered in transmission computed tomography (Barrett and Swindell, 1981). The matrix A represents a mapping of the densities ρ to the measurements Ψ. This mapping is written as an implicit function of ρ because it is dependent on the attenuation of radiation within the sample. The attenuation is an exponential path integral involving the sample density. Thus the system is implicit and nonlinear. The system is known precisely only if the presumably unknown quantity ρ is precisely known.

Deterministic computer codes are developed in Chapter 2 to perform the forward mapping – to simulate Ψ given a known ρ and to calculate the system mapping $A(\rho)$. The central equation is implemented as an algorithm in a code called ScatGram. The inverse mapping is the subject of Chapter 3 – to estimate the unknown ρ given the recorded spectral data Ψ. Performing the inverse mapping is the essence of image reconstruction.

1.8. Summary

Multiplexed Compton scatter tomography (MCST) is a new radiological imaging technique that reconstructs cross-sectional electron density images. Unlike conventional computed tomography (CT or CAT scan), MCST is viable when access is available to only one side of the sample because it registers scattered radiation rather than transmitted radiation.

Compton scatter is a photon-electron collision resulting in an energy and trajectory shift of the photon. Previous Compton scatter inspection devices relied on narrow collimation of a radiation source and detectors to isolate incremental volumes, or voxels, for individual interrogation. Compiling an image required scanning the apparatus over each voxel to interrogate it independently. In contrast, MCST uses comparatively wide fields-of-view for both source and detectors to create a fan beam inspection volume. MCST uses multiplexing in energy and detectors to allow simultaneous interrogation of many voxels within its fan beam. It exploits the relationship between a Compton-scattered photon's energy shift and its scattering angle to reconstruct an image from a mesh of curved projections. Primary components of an MCST system include a radioisotope gamma ray source, fan beam collimators, and an array of energy-discriminating detectors.

This research examines for the first time whether MCST may be used for single-sided inspection of thin aluminum samples. The eventual application of this technique to noninvasive inspection of aluminum airframes is considered. This application presents several new challenges never addressed previously. Constraints on the physical access to airframe components means the inspection must be conducted from a single side of the sample. Gamma rays in the 100 keV energy region are required to ensure that a significant portion interact in the thin, low-Z target. Gamma rays in this energy regime are strongly influenced by the momentum distribution of atomic electrons, a phenomenon known as Doppler broadening. These gammas are detected with good photopeak efficiency in planar high-purity germanium (HPGe) detectors that provide state-of-the-art energy resolution. They are available in multiple-element arrays to provide spatial sampling and simultaneous acquisition.

Chapter 2 describes the advanced deterministic system model developed for this research. The advanced model provides a flexible tool for evaluating potential MCST designs. To do so, it incorporates system features not previously considered in analytical MCST modeling (Arendtsz, 1995a; Arendtsz,

1995b; Prettyman, 1993) such as the extended sizes of source and detector, energy-variant detector energy resolution and efficiency, energy-variant Doppler broadening, and spatially-variant detector response. Incorporating these features avoids the cumbersome step of measuring and interpolating a detector response function that must be deconvolved from measured spectra, a step that can introduce appreciable error. The deterministic model was benchmarked with good results against the widely accepted MCNP Monte Carlo transport code.

Chapter 3 describes how cross-sectional electron density images are reconstructed from scattered gamma ray energy spectra. Two novel reconstruction techniques are developed based on filtered backprojection (FBP) and on penalized weighted least-squares iterative reconstruction (PWLS). The equations developed by Norton for filtered backprojection with a highly idealized system are adapted to a realistic system with coarse position sampling, extended source and detector sizes, and realistic energu spectra. The PWLS algorithm for iterative image reconstruction in positron emission tomography (PET) (Fessler, 1994) is adapted for reconstruction in MCST, but an additional layer of iteration is added to account for attenuation.

Chapter 4 describes the components of the first single-sided MCST system. The system was constructed for this research to demonstrate the principles of MCST and to verify the advanced system model and iterative image reconstruction algorithm. Major components of the system include a 6-element array of HPGe detectors, fan beam collimators, and a ^{109}Cd radionuclide source. The detector response was carefully characterized for incorporation into the system model.

Chapter 5 provides experimental results from the demonstration MCST system, and shows images reconstructed from gamma ray spectra measured from several aluminum phantoms. These represent the first-ever one-sided MCST images. The results serve to validate the deterministic model and the iterative reconstruction code, and they demonstrate the general legitimacy of the MCST technique.

Chapter 6 describes the modeling of a next-generation MCST system. The image contrast recovered from various features is investigated. Critical issues such as efficiency, collection time, and availability of gamma ray sources are addressed.

Chapter 7 gives conclusions and recommendations for future work.

II. MCST Modeling

Computer models developed to simulate the response of the MSCT system form the foundation of the system's ability to transform recorded energy spectra into a cross-sectional image of the sample. The central piece of code is the ScatGram deterministic photon transport code developed in Fortran 90. This code was benchmarked against the widely-accepted MCNP Monte Carlo radiation transport code. Several critical aspects of the MCST response that are beyond the scope of ScatGram were modeled with Monte Carlo simulation.

2.1. Introduction To The ScatGram Code

The purpose of the scattergram generation code ScatGram is to model the physics behind Equation (1-12) to predict a distribution of scattered gamma rays, the scattergram, given a user-specified scattering sample. The model also forms the basis of the image reconstruction code. The output is useful for investigating the response of the imaging system under various geometries and for constructing images to approximate those that would result from processing of actual MCST signals. The code is deterministic in nature. It uses an algorithm that divides the scattering object, the sample, into many small cells or voxels, and calculates the analytical probability of scattering a source gamma ray from each voxel into each energy channel in each detector. Integration over all cells yields the set of probabilities per source particle of observing a singly-scattered gamma ray in a given energy channel of a given detector.

Although the voxels within the fan beam are assigned a volume for the purpose of computing the scattering probabilities, the algorithm is really spatially 2-dimensional because only a 2-dimensional array of voxels is considered.

Arendtsz developed a similar analytical model called the forward model (Arendtsz, 1995a). The ScatGram code incorporates several important differences that are necessary to model MCST signals with greater fidelity. Whereas this forward model computes the energy spectrum of scattered radiation converging on a point detector, the ScatGram code computes the energy spectrum of the flux integrated over multiple circular surfaces. These surfaces represent finite-sized detector entrance windows. This treatment is important for the MCST system because the physical sizes of the detectors cause their response to depart greatly from ideal point detectors. Second, the model developed by Arendtsz and Hussein

assumes that photon scattering physics follows the Compton angle-energy relationship of Equation (1-1) and the Klein-Nishina relationship for differential scattering cross section of Equation(1-4). It was shown earlier how these assumptions are largely invalid at the energies of interest for the MCST. Consequently, ScatGram incorporates Doppler broadening of scattered photons and detector energy resolution. It also has the capability to model a spatially extended source, rather than a point source. This simply involves treating the extended source as a collection of point sources.

Both Arendtsz and Prettyman rely on a point source and ideal point detector model, but compensate for the effects of these assumptions using experimentally measured detector response functions (Arendtsz, 1995b; Prettyman, 1991). The pulse height distribution of the actual detector at several energies is measured by scattering from small targets, and the response at intermediate energies is interpolated from the results. Their use of 662 keV ^{137}Cs sources creates a significant Compton continuum. Convolving the ideal point response with the detector response function compensates for the effects of aperture size, and the non-ideal detector pulse height distribution. Although Doppler broadening is not explicitly mentioned, its effects would also be included in the detector response function. In contrast, the scattergram code includes these effects within the integration kernel. With this approach reliable and flexible modeling may be accomplished with the need for minimal laboratory measurements. It will also become evident in Chapter 3 how inclusion of these effects into the mathematical modeling will simplify image reconstruction by avoiding the need to deconvolve the detector response function from measured data.

The primary advantages of the ScatGram scattergram generation code to other techniques such as discrete ordinates or Monte Carlo are computational speed and ease of implementation (Arendtsz, 1995b). The liabilities of this technique stem mainly from ignoring the higher-order scatters and other particle interactions that the other techniques do not ignore. The ScatGram code presumes that the flux reaching the detector window is comprised of singly-scattered gamma rays that scattered in the sample. Other types of photon interactions (photoelectric absorption, coherent scatter, and pair production) are treated only by inclusion in the total attenuation cross sections, so that the effects of any resulting particles are ignored. These assumptions can only remain viable if Compton scattering is the dominant mode of photon interaction in the target and careful fan beam collimation curtails the effects of multiple scattering.

Another of ScatGram's important assumptions is that of full-energy photon detection. The model assumes that any photon incident on a detector window will be counted at the full energy, or not counted at all. This approach ignores the scatter and escape within the detector crystal that gives rise to the Compton continuum and a peak-to-total ratio less than one (Knoll, 1986). Although the planar HPGe detectors in the MCST system have good full energy efficiency at the energies used, some photons will deposit only a fraction of their energy, resulting in erroneous low-energy counts. Clearly this assumption is dependent on the detectors and energies used. It proved to be adequate for the demonstration MCST system described in Chapter 4.

To produce realistic spectral data, the ScatGram code must incorporate the response characteristics of the modeled detectors. Examples of such characteristics include the detector full-energy efficiency and energy resolution. The ScatGram code is organized so that these detector characteristics reside in Fortran 90 module subroutines and may be changed and compiled separately without disturbing the rest of the source code.

The deterministic nature of the algorithm does not account for the random nature of photon detection that is embodied in counting statistics. Instead it calculates the expectation value of the intensity of counts in each channel. Measurement noise is simulated by superimposing random values that are selected according to counting statistics as discussed below in Section 2.4.4.

2.2.   ScatGram Interface

2.2.1.   Model Output

Suppose the problem includes N_d detector positions and the energy spectrum is discretized into N_E energy bins of equal width δE. Each energy channel may be characterized by its central energy E_k ($k = 1,2,\ldots, N_E$) but encompasses all energies within $\delta E/2$ of E_k. The program outputs a formatted file listing the probabilities per source photon of scattering from the target into energy bin k of detector j ($j = 1,2,\ldots, N_d$). This set of probabilities is denoted $I(j, E_k)$ ($k = 1,2,\ldots,N_E$; $j = 1,2,\ldots,N_d$). The N_d detector positions can be subdivided into N positions of a detector array with M detectors in the array ($N_d = N*M$) so the discretized energy spectrum (in the form of a probability distribution) for the mth detector in the nth array position is contained in row $j = (n-1) + m$. It is expected that any sample will be inspected with an array at

multiple positions to enhance the sampling in both position and scattering angle. Each array position has an associated source position which may or may not change.

2.2.2. Model Input Parameters

Given a set of input parameters, the ScatGram code must map these parameters into a set of estimated scattergram measurements, the single-scatter energy distribution recorded in each detector.

Geometry Parameters. As the code was developed specifically with the demonstration MCST system in mind, the geometry parameters describe the positions of a linear array of equally-spaced, similarly-sized detector elements. The position of the sample and source remains fixed in Cartesian space, but the N-element linear array can be positioned at up to 8 different locations each with a corresponding source location.

The user supplies a text file in the Fortran 90 namelist I/O format that allows the code to read in all the parameters needed to specify the geometry of the problem. Table 2-1 lists the parameters read from the geometry file, with a description of each. All positions and measurements are in centimeters. All angles are in radians. Figure 2-1 should clarify the meanings of some parameters.

Table 2-1. Geometry Parameters in the ScatGram Code

NAMELIST	PARAMETER	DESCRIPTION
PixelData	minx, maxx	x coordinate of leftmost, rightmost cells
	minz, maxz	z coordinate of topmost, bottommost cells
	NX, NZ	number of cells in the x-direction, z-direction
	wd	the width of the inspection volume in y-direction (fan-beam tomographic slice width)
	wColl	width of the slit in the detector collimator plate
SourceLocation	xsrc1...xsrc8	x coordinate of the source center in positions 1 - 8
	zsrc1...zsrc8	z coordinate of the source center in positions 1 - 8
SourceSpecs	DXsrc, DZsrc	width and height of the source active volume
	NXsrc, NZsrc	number of source subpositions to compute in the x- and z-directions (to simulate an extended source)
	thetasrc1...thetasrc8	angle of inclination, relative to x-axis, of source active volume in positions 1 - 8
DetectorData	DeltaXDet	center-to-center spacing of detector windows
	rdet	radius of detector windows
	Ndet	number of detectors in the array
	theta1...theta8	angle of inclination, relative to x-axis, of detector array in positions 1 - 8
DetectorPosit	xdet1...xdet8	x coordinate: center, first detector window in positions 1 - 8
	zdet1...zdet8	z coordinate: center, first detector window in positions 1 - 8
Collimation	mcoll1, bcoll1	slope and intercept of field-of-view boundary 1
	mcoll2, bcoll2	slope and intercept of field-of-view boundary 2
CountTimes	count1 ... count8	counting times in seconds at positions 1 - 8
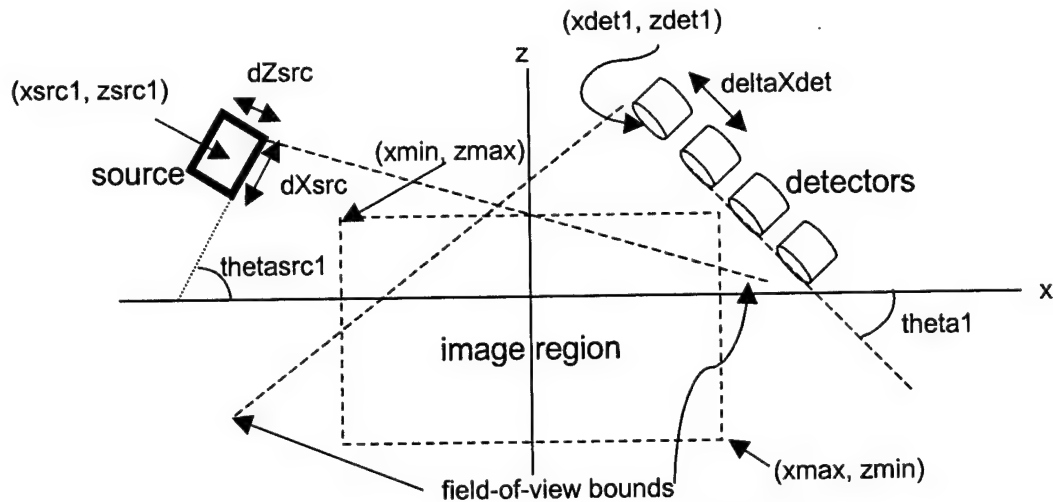
Figure 2-1. Geometry Parameters in the ScatGram Code.

Field-of-view boundaries limit the contributing cells to those lying within the field-of-view of the detectors and the source. This feature is useful because the image region is always rectangular. Because of collimation, only a portion of this region may be visible to the detectors, and only a portion may be illuminated by the source. The user must ensure all cells in the detector field-of-view containing scattering material are included in the image region, or are shielded from the source, and that all cells illuminated by the source are included in the image region or are shielded from the detectors. Cells not within the field-of-view boundaries are still included in attenuation calculations where necessary.

Material Properties. The current version of the code handles three different materials in the inspection volume. It would require only minor modifications to add more, but only three were chosen to model an inspection volume composed of aluminum, the corrosion product gibbsite, and air. Two user-supplied input files define the distribution of these materials within the inspection volume. The code reads the type of material in each cell from a formatted file composed of N_x x N_z integer numbers. The entries simply specify which material is in the corresponding cell: 1 for aluminum, 2 for corrosion, and 0 for air. The user also supplies a file composed of N_x x N_z floating-point numbers representing the mass densities of each cell. Therefore, the density of any type of material may be varied within the inspection volume. The total attenuation and Compton scattering cross sections for these three materials are contained within the code. Their values are polynomial interpolations of cross section data obtained from the XCOM code (Berger, 1987). These cross sections are relatively featureless and vary smoothly over the energy range 40 keV – 88 keV so the polynomials provide very good fits. The Compton profiles of aluminum, gibbsite, and

air are precomputed and stored in external files that are loaded when the program starts. Each material in the problem has a separate array of floating point numbers representing its Compton profile.

Compton Profile Matrices. Consider the case of a known angular distribution $f(\theta)$ in one detector element of singly-Compton-scattered photons from a monoenergetic source. Assume $f(\theta)$ is continuous on the interval $\theta = [0, \pi]$ and consists of photons singly scattered from a homogeneous material. Now we seek to estimate the scattered photon energy distribution resulting from this scattering angle distribution. To incorporate Doppler broadening the angular spectrum must be blurred with a shift-variant point spread function, properly redistributing the values $f(\theta)$ over all energies to produce a blurred spectrum $w_{out}(E')$. This operation is a linear superposition integral of the form

$$w_{out}(E') = \int_0^\pi p(E';\theta) \cdot f(\theta) d\theta.$$ (2-1)

The integration kernel $p(E'; \theta)$ describes the mapping from θ to E', the Compton profile, which correctly spreads the value of $f(\theta)$ across E'. Like Compton broadening, the mapping $p(E', \theta)$ is truly two-dimensional and shift-variant so that $p(E_1-\Delta E, \theta_1) \neq p(E_2-\Delta E, \theta_2)$ where E_1 and E_2 are the mean energy of the distribution for θ_1 and θ_2 respectively. To extend Equation (2-1) to the case of a discretized energy spectrum with N_E finite-width energy bins, replace the continuous mapping $p(E', \theta)$ with a discretized bin-to-bin mapping $h(E_i, \theta_j)$.

$$w_i^{out} = \sum_{j=1}^{N_\theta} h(E_i, \theta_j) \cdot f_j^{in}$$ (2-2)

The mapping embodied in $h(E_i, \theta_j)$ is a linear operator that can be represented by an $N_E \times N_\theta$ matrix $\mathbf{H}$. Any entry $\mathbf{H}_{ij}$ represents the probability, computed from the impulse approximation, for scattering into the range of energies characterized by the energy bin E_i (with bin width $\delta E'$) given that the scattering angle is within the range of angles characterized by θ_j.

$$\mathbf{H}(E_i, \theta_j, Z) = \frac{\left[\dfrac{d^2\sigma_s}{d\Omega dE'}(E_i, \theta_j, Z)\right]_{IA} \delta E'}{\left[\dfrac{d\sigma_s}{d\Omega}(\theta_j, Z)\right]_{KN}} \qquad i \in \{1,2,...,N_E\}, j \in \{1,2,...,N_\theta\}$$ (2-3)

The atomic number Z is included to acknowledge that the Compton profile changes with the scattering material. Now Equation (2-2) can be written

$$\mathbf{w}_{out} = \mathbf{Hf} \, . \tag{2-4}$$

The denominator of Equation 2-3 is a normalization that makes each column sum to 1. Recall from Chapter 1 that integrating the impulse approximation with respect to E′ results in the Klein-Nishina relationship, so every column of $\mathbf{H}$ is normalized by the differential cross section for scattering into angle bin θ_j at any energy. That makes $\mathbf{H}$ consistent with Equation 2-4 and the definition of $\mathbf{f}$ as an angular distribution that already embodies the Klein-Nishina angular probabilities. It also preserves the number of counts so that

$$\sum_{i=1}^{N_E} w^{out}(i) = \sum_{i=1}^{N_E} f(i) \, . \tag{2-5}$$

In the ScatGram algorithm this normalization is required because the impulse approximation is not used to calculate an absolute cross section. Instead, the probability for scatter in any particular cell comes from interpolations on tabulated cross section data, giving the Compton scatter probability integrated over all directions (Berger, 1987). This probability is distributed over all scattering directions according to the Klein-Nishina equation. The Compton profile operates on the resulting angular distribution, spreading the values in energy with the linear operator $\mathbf{H}$. This approach is completely equivalent to using unnormalized impulse approximation to calculate the probabilities for scattering into E_i and θ_j. In both cases the incoherent scattering function should be used to account for the reduced forward-scatter probability brought on by the binding energy effects. The methodology was chosen because it is more convenient computationally, especially when ScatGram calculates spectra for benchmarking against production codes that do not include the Doppler broadening. Furthermore, Chapter 3 will explain how the $\mathbf{H}$ matrix is used to invert Equation (2-4) for one mode of image reconstruction. The methodology parallels the technique used by Namito to incorporate Doppler broadening into the EGS4 code. His results agree very well with experimentally measured data (Namito, 1994).

Every material in the problem requires a unique profile matrix. The profiles of non-elemental materials are computed by superposition of the profiles of elements within the substance. Each element is weighted by its atomic ratio and total Compton scattering cross section (Namito, 1994). A weighted sum is

also used to calculate the incoherent scattering function of a non-elemental material (Yuasa, 1997). Such an approach should be considered a first-order approximation, as molecular binding effects will perturb the profiles. However, the approximation is all that is available, since true molecular Compton profiles are not well understood or well tabulated.

2.3.   ScatGram Computational Algorithm

Simulation of the scattergram signal collected in the MCST system begins with calculation of the intensity of scattered photons in energy bin k of detector j, which is denoted $I(j, E_k)$. These values represent a relative energy distribution of scattered photons and will be the starting point for simulation of the signal (i.e. actual number of counts) $\Psi(j, E_k)$. The inspection region is divided into cells $m = 1, 2, \ldots, N_x \cdot N_z$. The cells are rectangular and sized so that they are much less than 1 mean free path thick in either dimension. Beyond that requirement, the cells can be made even smaller to provide a finer grid to reduce error in the integration. Calculation of $I(j, E_k)$ involves summing the contributions from every cell in the inspection region to the signal in the energy bin E_k of detector j. ScatGram performs this summation as follows.

$$I(j, E_k) = \sum_{m=1}^{N_x \cdot N_z} P_{CS}(m, j) \cdot a_{in}(m, j) \cdot a_{out}(m, E_k, j) \cdot \sum_{q=1}^{N_E} \Theta(Z_m, E_k, \theta_q) \cdot \Lambda(m, \theta_q, j) \qquad (2\text{-}6)$$

An explanation follows for each term in Equation (2-6).

The term $P_{CS}(m, j)$ represents the probability, integrated over all scattering directions, that a photon emitted from the isotropic source (in source position j) that passes through cell m will Compton scatter in the cell.

$$P_{cs}(m, j) = \frac{\Omega_v(m, j)}{4\pi} \left[1 - \exp\left[-\sigma(m, E_0) \cdot \rho(m) \cdot L(m, j) \right] \right] \qquad (2\text{-}7)$$

Here $\Omega_v(m, j)$ represents the solid angle in steradians subtended by cell m relative to the source position j, $\sigma(m, E_0)$ is the Compton scatter partial interaction coefficient (cm^2/g) at energy E_0, of the material in cell m. This value is interpolated from tabulated values (Berger, 1987) that give the interaction coefficient integrated over all scattering angles. The mass density in cell m is denoted $\rho(m)$. There are many possible trajectories that originate at source position j and pass through cell m. $L(m, j)$ is the average pathlength

through cell m of trajectories that originate at the source position j and pass through the cell m. For cells that are much thinner than 1 mean free path, an alternative is to calculate P_{cs} using the first terms of the Taylor series expansion in $L(m, j)$ about zero to obtain

$$P_{cs}(m,j) = \frac{\Omega_v(m,j)}{4\pi}\sigma(m,E_0) \cdot \rho(m) \cdot L(m,j).$$

(2-8)

Using this approximation makes the probability of scatter in any cell proportional to its density, and will allow the linear system of Equation (1-12).

The P_{cs} term neglects the presence of all cells between cell m and the source. Inclusion of the $a_{in}(m, j)$ factor accounts for radiation attenuation along the path from the source to the center of cell m,

(2-9)

$$a_{in}(m,j) = \sum_{n=1}^{N_x \cdot N_z} \exp\left[-\rho(n) \cdot \mu^{tot}(n,E_0) \cdot x^{in}(m,n,j)\right]$$

where $\mu^{tot}(n,E_0)$ is the total attenuation coefficient (cm²/g) of the material in cell n at energy E_0, and $x^{in}(m,n,j)$ is the pathlength through cell n along the line containing the source and the center of cell m. The j index is required because the source position may change with detector position. Most $x^{in}(m,n,j)$ will be zero, so the algorithm only computes the nonzero paths.

The term $a_{out}(m, k, j)$ accounts for attenuation of the scattered radiation from scattering point to detector,

(2-10)

$$a_{out}(m,E_k,j) = \sum_{n=1}^{N_x \cdot N_z} \exp\left[-\rho(n) \cdot \mu^{tot}(n,E_k) \cdot x^{out}(m,n,j)\right],$$

where $x^{out}(m,n,j)$ is the pathlength through voxel n from the center of voxel m to the center of the detector j. Most $x^{out}(m,n,j)$ will be zero, so the algorithm only computes the nonzero paths. To avoid calculating the exact pathlengths for every combination of m, k, and j, all scatters from within the isogonic region prescribed by k′ and j are approximated as having traveled from the center of the voxel m to the center of detector j. This reduces the problem to one of calculating the pathlengths for every combination of (m, n, j) rather than for every combination of (m, n, j, k). In reality, not all photons scattered from voxel m will travel precisely the same path to the detector window, since a range of scattering angles may intercept the window. Care must be taken to ensure that detectors are not placed very close to regions of high attenuation, in which case this approximation may produce large errors in the a_{out} term.

The purpose of the $\Theta(Z_m, E_k, \theta_q)$ term is to distribute the radiation scattered from each voxel in both angle and energy. The Klein-Nishina equation with the incoherent scattering function dictates how the scattered gammas are distributed in angle. Then for every scattering angle, the impulse approximation dictates how those gammas are distributed in energy. This approach is both computaionally convenient and self-consistent, as the impulse approximation integrated with respect to energy is equivalent to a Klein-Nishina distribution as described in Chapter 1. The value of $\Theta(Z_m, E_k, \theta_q)$ represents the superposition of these two distributions.

$$\Theta\left(Z_m, E_k, \theta_q\right) = \frac{\left[\dfrac{d\sigma}{d\Omega}\left(\theta_q, Z_m\right)\right]_{KN} \dfrac{S\left(\theta_q, Z_m\right)}{Z_m} \Omega_q}{\displaystyle\int_0^\pi \left[\dfrac{d\sigma}{d\Omega}\left(\theta, Z_m\right)\right]_{KN} d\theta} H(E_k, \theta_q, Z_m) \tag{2-11}$$

The quotient in the first term is responsible for distributing the scattered gammas in angle per the Klein-Nishina and Incoherent Scattering functions. The normalized distribution is required because the total Compton scattering cross section is taken from tabulated data (Berger, 1987) and included in the P_{CS} (m) term of Equation (2-8). The atomic number of the material in cell m is denoted Z_m as a reminder of the material-dependence. Normalizing the incoherent scattering function by Z_m assumes it is tabulated as in Hubbell, et al. (Hubbell, 1975). The second term distributes the gammas scattered at a given angle across the range of energies according to the impulse approximation.

$$\mathbf{H}\left(E_k, \theta_q, Z_m\right) = \frac{\left[\dfrac{d^2\sigma_s}{d\Omega dE'}\left(E_k, \theta_q, Z_m\right)\right]_{IA} \delta E'}{\left[\dfrac{d\sigma_s}{d\Omega}\left(\theta_q, Z_m\right)\right]_{KN}} \tag{2-12}$$

This should be recognized as the (k,q) entry in the $\mathbf{H}$ matrix of Equation (2-3), evaluated for the material in cell m (with atomic number Z_m).

The spectrum is discretized into finite-sized bins, so any angle θ_q resides within a bin whose boundaries may be called θ_{min} and θ_{max}. The solid angle subtended by this range of angles in steradians is

$$\Omega_q = 2\pi\left(\cos\theta_{min_q} - \cos\theta_{max_q}\right). \tag{2-13}$$

The window of detector j as viewed from voxel m will subtend none or some of the Ω_q solid angle. Only a fraction of the bin's solid angle will intersect the detector, and only part of the detector window may fall within the bin boundaries. The $\Lambda(m,\theta_q, j)$ term represents the fraction of Ω_q which intersects the detector window. It is important to recognize that Λ is unitless, and only represents the fraction of the scattering angle bin's solid angle Ω_q that intersects the detector window. The angle bin solid angle Ω_q has units of steradians.

One might suggest as an alternative computing Ω_d, the solid angle of the detector window relative to cell m, and using it to replace Ω_q in Equation (2-11). That method ignores the possibility that photons scattered into the angle bin θ_q may not intersect the detector. Indeed, most Ω_q do not intersect Ω_d resulting in a Λ of zero. It also fails to recognize that only a fraction of the Ω_q may actually intersect the detector window, as illustrated in Figure 2-2. Using the intersection of these two solid angles is how ScatGram incorporates the effects of finite-sized detectors.
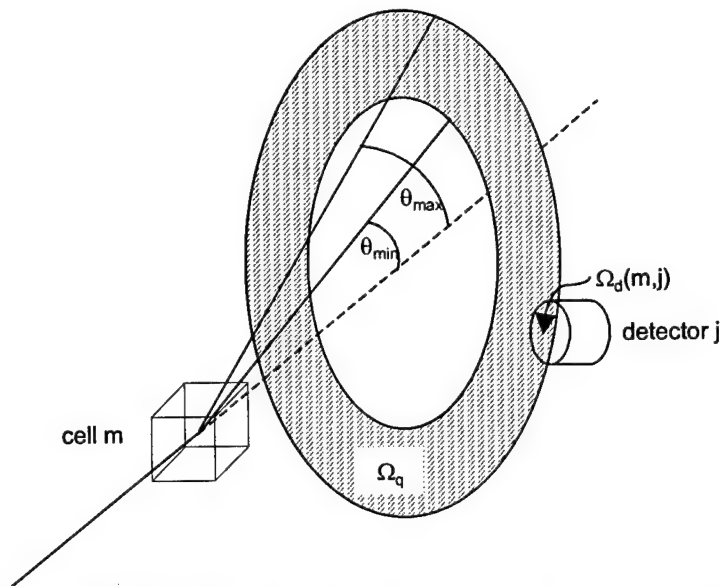
Figure 2-2. Factors in the Λ Term. The value of Λ is the fraction of the angular bin solid angle Ω_q that intersects the detector window with a solid angle of Ω_d.

ScatGram simulates an extended source by simulating multiple point sources within the volume defined by the parameters given in the SourceSpecs namelist of the geometry file (see Table 2-1). For each position of the extended source, ScatGram calculates NXsrc * NZsrc (see Table 2-1) point source contributions to the signal. The entire calculation of Equation (2-6) is repeated NXsrc * NZsrc times, each

time with a point source at a new location within the extended source volume. The average of the values of $I(j,E_k)$ over all simulated point sources approximates the response from an extended source.

2.4. Incorporating Detector Properties

ScatGram calculates I, a relative energy distribution of gammas scattered once from the target, and into the detector window. The actual energy spectrum recorded in the laboratory will differ because each bin will contain an integer number of detected events. There will also be multiple scatter events, photons that deposit only a fraction of their energy in the detector (resulting in a peak-to-total ratio less than one), background counts, and statistical noise. Furthermore, the energy resolution of the detector and the variation in detector peak efficiency with energy and incident angle will affect the energy specta. Multiple scattering and peak-to-total response do not lend themselves easily to analog modeling. Selecting the right combination of source energy and detector minimizes the effects of the peak-to-total response, but multiple scatter remains untreated in the ScatGram model. With the exception of statistical noise, the remaining factors are unique to the particular detector system and must be experimentally characterized if they are to be included in the simulation.

2.4.1. Detector Intrinsic Peak Efficiency

The inclusion of detector intrinsic peak efficiency is straightforward. An additional term $\varepsilon(j,E_k)$ representing the intrinsic peak efficiency in detector j at energy E_k inserted in Equation (2-6) compensates for the efficiency of detection across the range of energies. Inclusion of this term leads to

$$I(j,E_k) = \sum_{m=1}^{N_x \cdot N_z} P_{CS}(m,j) \cdot a_{in}(m,j) \cdot a_{out}(m,E_k,j) \cdot \varepsilon(j,E_k) \cdot$$
$$\sum_{q=1}^{N_E} \Theta(Z_m,E_k,\theta_q) \cdot \Lambda(m,\theta_q,j) \tag{2-14}$$

The values used here for $\varepsilon(E)$ should be based on measurements taken with radiation incident on the detector axis, along the normal to the detector aperture. This is presumably the configuration with greatest efficiency.

2.4.2. *Oblique Angle Effects*

For many semiconductor detectors the incident angle of radiation with respect to the detector aperture normal can have a serious effect on the quality and efficiency of the signal recorded. Variations may be caused by several factors, but can be especially severe if the available pathlength through the active semiconductor volume varies significantly with incident angle, or if the entrance aperture contains absorptive material. The response may differ between similar detectors in an array and may also vary with energy.

As presented so far, the ScatGram algorithm calculates the intensity of particles crossing the detector aperture, so the correction for oblique incidence must still be incorporated if the variation is significant. This correction cannot be accomplished in a post-processing step because the spectral data contain no information concerning the incidence of photons. Instead it must be embedded within the calculations. A function $\eta(\phi)$ is needed whose values are the peak efficiency as a function of the oblique angle ϕ, defined as the angle between the detector aperture normal and the incident photon direction. Incorporating this effect into the calculations means adding another factor within the kernel of Equation (2-14) as follows.

$$I(j, E_k) = \sum_{m=1}^{N_x \cdot N_z} P_{CS}(m, j) \cdot a_{in}(m, j) \cdot a_{out}(m, E_k, j) \cdot \varepsilon(j, E_k) \cdot \eta(\phi(m, j)) \cdot \sum_{q=1}^{N_E} \Theta(Z_m, E_k, \theta_q) \cdot \Lambda(m, \theta_q, j) \tag{2-15}$$

The angle ϕ is a function of both the detector and scatter cell location, so it is written as a function of m and j. The $\eta(\phi)$ function is normalized to have a maximum value of unity so that the efficiency correction provided by $\varepsilon(E)$ is not duplicated. The efficiency $\varepsilon(E)$ should be measured at the incident angle of maximum efficiency, which should typically be $\phi = 0$.

It is important to realize that this treatment presumes efficiency as a function of energy, $\varepsilon(E)$, and efficiency as a function of incident angle, $\eta(\phi)$, are separable so the efficiency at any combination of energy and angle is just the product $\varepsilon(E)\eta(\phi)$. If this were not a reasonable assumption, the code would require a two-dimensional function that might be written $\varepsilon(E,\phi)$. Chapter 4 will show how this seperability assumption was valid for the demonstration MCST system.

2.4.3. Detector Resolution

To simulate the effect of detector resolution, a linear operator acts on each spectrum in the data set $I(j,E_k)$ individually. This operator constitutes a shift-variant blurring much like the Doppler-broadening operator $\mathbf{H}$ developed earlier. In multiple detector arrays it may be necessary to develop an operator unique to each detector element because of disparate resolutions. Begin with the assumption that the recorded energy distribution for an energy E follows a Gaussian distribution $G(E', E)$ with a FWHM dependent on E, denoted $\Delta E(E)$. This Gaussian assumption is well established in radiation detection (Knoll, 1986).

$$G(E',E) = \exp\left(\frac{-\pi(E'-E)^2}{(1.065 \cdot \Delta E(E))^2}\right) \qquad (2\text{-}16)$$

Considering a single energy distribution $I(E)$, we return to a linear superposition integral of the form

$$f(E') = \int_0^\infty I(E)G(E',E)dE \cdot \qquad (2\text{-}17)$$

Discretizing the equation above leads to

$$f(E_i) = \sum_{k=1}^{N_E} I(E_j)G(E_i,E_j)dE_j \qquad (2\text{-}18)$$

suggesting the linear operation

$$\mathbf{f} = \mathbf{DI} \qquad (2\text{-}19)$$

where $\mathbf{D}$ embodies the Gaussian $G(E_i,E_j)$ as

$$D(E_i,E_j) = \frac{G(E_i,E_j)}{\sum_{j=1}^{N_E} G(E_i,E_j)} \qquad (2\text{-}20)$$

and the denominator is a normalization to preserve the number of counts. The detector resolution matrix $\mathbf{D}$ may be more conveniently incorporated into the kernel of the ScatGram algorithm, and doing so produces the following, as suggested by Equation (2-19).

$$I(j,E_n) = \sum_{k=1}^{N_E} D(E_n, E_k, j) \cdot \begin{bmatrix} \sum_{m=1}^{N_x \cdot N_Z} P_{CS}(m,j) \cdot a_{in}(m,j) \cdot a_{out}(m,E_k,j) \cdot \varepsilon(j,E_k) \cdot \eta(\phi(m,j)) \\ \cdot \sum_{q=1}^{N_E} \Theta(Z_m, E_k, \theta_q) \cdot \Lambda(m, \theta_q, j) \end{bmatrix} \quad (2\text{-}21)$$

The j index has been added to $D(E_n, E_k)$ to acknowledge that different detectors will have different energy-dependent resolutions.

2.4.4. _Background Counts and Poisson Random Noise_

The values $I(j,E_k)$ computed by ScatGram represent the distribution of singly-scattered photons that can be expected across the energy bins. To simulate an actual collected signal, this distribution must be converted to an absolute number of counts. The random nature of radiation detection and counting statistics, however, will cause random variations about the expected distribution (Knoll, 1986). A post-processing feature can randomize the ScatGram output to simulate the measurement noise. This is useful for testing the robustness of spectral processing and image reconstruction algorithms since actual measured data will inevitably contain random noise. The first step is to multiply the ScatGram output $I(j,E_k)$ by the factor N_γ so that the magnitude of each entry represents the expected number of counts in that bin. This will produce the spectrum of mean scattergram values $\overline{\Psi}(j, E_k)$.

$$\overline{\Psi} = \mathbf{I} N_\gamma \quad (2\text{-}22)$$

If counts resulting from background radiation will be significant during the measurement, they will add another source of variance, even if the mean background is subtracted away. In that case a set of background counts $\overline{b}(j, E_k)$ should be considered, each element of which contains the expected (mean) background intensity in energy bin k at detector position j for the duration of the modeled counting time. Each measurement in both $\overline{\Psi}$ and $\overline{b}$ may be assumed an independent Poisson random variable. For a mean greater than about 10, the Poisson distribution is well approximated by a Gaussian, or normal, distribution, where the variance in each measurement is equal to its mean (Knoll, 1986). It follows that the standard deviation in each measurement should equal the square root of the mean. To simulate statistical noise in the signals, both the expected scattered photon counts $\overline{\Psi}$ and the expected background $\overline{b}$ must be randomized with statistical noise. The two signals are added together and randomized, then the mean

background $\overline{b}$ is subtracted away. This presumes the expected background is accurately known. It is usually possible to obtain a good estimate of the mean background from an extended background count. The randomized version of $\overline{\Psi}$ is

$$\Psi(j, E_k) = \overline{\Psi}(j, E_k) + R_{norm}\sqrt{\overline{\Psi}(j, E_k) + \overline{b}(j, E_k)}$$ (2-23)

where each R_{norm} represents a different selection from normally-distributed random numbers with zero mean and variance of one. For measurements with mean greater than 10, the normal distribution is a good approximation for the Poisson distribution (Knoll, 1989). Each value in Ψ represents a number of counts in that energy bin.

2.5.   EZScat Code

A closely related code named EZScat was developed in FORTRAN 90 to handle limited target geometries with greater computational speed. The speed advantage comes from avoiding calculation at every cell of the incident and scattered radiation pathlengths through all the other cells. The user may specify a limited geometry consisting of three regions within the inspection plane. The first region is defined as a rectangle bounded by two x and two z values. This region is intended to contain the aluminum sample under inspection. Another region, which may be contained within the boundaries of the first, is also rectangular, but defined by specifying its center and its height and width. This region is useful for adding a low-density inclusion to the sample to simulate corrosion within the sample. The remaining region, meant to be the air surrounding the object, is reserved for parts of the inspection plane that are not otherwise assigned. Each of the three regions may be assigned any mass density, but density within any region is uniform. The user may choose to model the inclusion region as either aluminum or gibbsite. For every cell EZScat must only calculate 3 pathlengths, one for each region, of the inbound photon. For every cell and detector combination EZScat must only calculate three pathlengths for the outbound scattered photon. Equation (2-9) is replaced with

$$a_{in}(m, j) = \sum_{r=1}^{3} \exp\left[-\rho_r \cdot \mu_r^{tot}(E_0) \cdot x_r^{in}(m, j)\right]$$ (2-24)

where r = 1, 2, 3 sums over the three regions. Likewise Equation (2-10) is replaced with

$$a_{out}(m, E_k, j) = \sum_{r=1}^{3} \exp\left[-\rho_r \cdot \mu_r^{tot}(E_k) \cdot x_r^{out}(m, j)\right].$$ (2-25)

Figure 2-3 gives an illustration of the box-in-box sample geometry that is possible in EZScat. Additional input parameters in the geometry input file define the EZScat geometry. These are listed in Table 2-2.
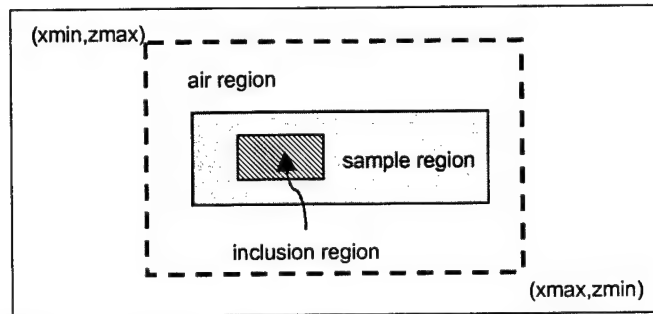
Figure 2-3. The Box-In-Box Sample Geometry of the EZScat Code.

Table 2-2. Additional Geometry Parameters for EZScat Code

NAMELIST	PARAMETER	DESCRIPTION
SampleData	bAlTop	Maximum z-value of sample region (cm).
	bAlBot	Minimum z-value of sample region (cm).
	AlLeft	Minimum x-value of sample region (cm).
	AlRight	Maximum x-value of sample region (cm).
	xCorr	X-coordinate of inclusion region center (cm).
	zCorr	Z-coordinate of inclusion region center (cm).
	DxCorr	½ Width (x-direction) of inclusion region (cm).
	DzCorr	½ Height (z-direction) of inclusion region (cm).
	densAir	Density (g/cm^3) of air region.
	densCorr	Density (g/cm^3) of inclusion region.
	densAl	Density (g/cm^3) of sample region.

2.6. A^0 System Mapping

Both the ScatGram code and EZScat code can produce a binary file which contains all the (j, E_n) summations in Equation (2-19) without the ρ-dependent terms. This matrix of values called $\mathbf{A}^0$. The values stored in $\mathbf{A}^0$ are of no apparent significance, except that storing them avoids the computational expense of recomputing those terms during image reconstruction.

Before discussion of the $\mathbf{A}^0$ matrix proceeds, a new convention for organizing the data must be established. Consider the central MCST equation, Equation (1-12). To remain consistent with that nomenclature and to keep the system two-dimensional, the energy spectra $\Psi(j, E_k)$ are resorted into a vector $\mathbf{\Psi}$ of length $N_d N_E$ where again N_d is the number of detector positions and N_E is the number of energy bins used. The nth energy bin in the jth detector now corresponds to the ith element of $\mathbf{\Psi}$ where $i = (j-1)N_E + n$.

The set of voxel densities is again represented by the vector ρ of length $N_X N_Z$ where again N_X is the number of voxels in the x-direction and N_Z is the number of voxels in the z-direction.

$$A^0(j, E_n, m) = A^0(i, m) \qquad (2\text{-}26)$$

A^0 can be considered a mapping of the voxel densities ρ to the energy spectra Ψ that neglects all attenuation in the sample and assumes that Compton scatter is the only interaction. Unlike $A(\rho)$, A^0 is not a function of ρ. A^0 is an $N_d N_E$ by $N_X N_Z$ matrix whose entry $A^0(i,m)$ is

$$A^0(i,m) = A^0((j-1)N_E + n, m) = N_\gamma \frac{\Omega_v(m,j)}{4\pi} L(m,j) \cdot \sigma_S(m) \cdot$$
$$\sum_{k=1}^{N_E} D(E_n, E_k, j) \varepsilon(j, E_k) \cdot \eta(\phi(m,j)) \cdot \sum_{q=1}^{N_E} \Theta(Z_m, E_k, \theta_q) \cdot \Lambda(m, \theta_q, j) \qquad (2\text{-}27)$$

Note that $A^0(i,m)$ contains all the ρ-independent terms from the mth summation in Equation (2-21). Since these values will be used for image reconstruction with little a priori knowledge of the sample, each voxel must be assumed to be composed of a default material, aluminum, for example. Therefore the material-dependent terms $\sigma_s(m)$ and $\Theta(Z_m, E_k, \theta_q)$ are always computed from the default material regardless of what the user-supplied input files may reveal about the sample. The approximation for P_{cs} given by Equation (2-8) is now critical since it allows the entire system to be linearized. Comparing the terms outside the summations of Equation (2-27) to Equation (2-8) reveals that, aside from the scalar value N_γ, multiplication by $\rho(m)$ makes them equivalent to P_{cs}. The linear approximation in Equation (2-8), therefore, will allow us to use a linear systems solution to solve $\Psi = A \cdot \rho$.

2.7. Stochastic MCST Modeling

MCNP (Monte Carlo N-Particle) Version 4B is a well-established radiation transport code that can be used for neutron, photon, electron, or coupled neutron/photon/electron transport. MCNP was contributed by the Radiation Transport Group at Los Alamos National Laboratory and is distributed by the Radiation Shielding Information Center (RSIC) at Oak Ridge National Laboratory. The user specifies a radiation source and an arbitrary three-dimensional geometry of material cells bounded by surfaces. Unlike deterministic methods such as the ScatGram code or discrete ordinates, the Monte Carlo method obtains answers by simulating individual particles and recording aspects, called tallies, of their average behavior

(LANL, 1997). MCNP, like the ScatGram code, can predict the energy-distribution of scattered photons. MCNP would be impractical to use in lieu of the ScatGram code for analysis of an MCST system because of the computational time required to simulate an adequate number of particles. It can, however, provide an independent check of the answers provided by the ScatGram code. As such, it is a useful tool to benchmark the ScatGram code on test cases.

Another useful feature of MCNP is the ability to filter singly-scattered photons from multiply-scattered using the FTn INC special tally treatment. This feature provides a prediction of the multiple scatter contribution to the signal with an accuracy that is sufficient to at least judge the magnitude of the multiple scatter problem. Coherent scatter is also included in the photon physics of MCNP, so any discrepancy caused by ignoring coherent scatter in the ScatGram model should be manifest in the difference between the two solutions. The contribution from coherent scatter may be observed as single or multiple scatter tallies at the source energy. If a coherent scatter is followed by a Compton scatter then the series of events is tallied as multiple scatter at the final energy.

MCNP is a 3-dimensional model, whereas ScatGram assumes all interactions take place in a 2-D array of cells. MCNP also provides a check of the 2-D assumption to verify that it agrees well with the 3-D reality. This is accomplished by modeling a 3-D imaging volume in MCNP whose third dimension is the tomographic slice thickness defined by the divergence of the fan beam from an ideal plane.

2.7.1.   MCNP Benchmarking of ScatGram Code

Doppler broadening is not included in the photon physics of MCNP as it is distributed by RSIC. Compton scatter is assumed to follow the stationary electron model of the Compton equation (LANL, 1997), therefore it is appropriate to compare the spectra predicted by MCNP to the ScatGram model results without Compton broadening and without the effects of detector resolution. This approach is equivalent to benchmarking ScatGram's computation of the scattering angle distributions, and still provides a good check of nearly all aspects of the code, excluding only the Compton profiles. The MCNP F1 tally was invoked to approximate photon current across a surface with shape and position identical to the detector window in ScatGram. Source photons were biased to begin their flight in directions toward the sample to improve the efficiency of computation.

Test Case A. The Geometry for test case A is illustrated in Figure 2-4. Two aluminum targets measuring 6.35 x 6.35 x 10.0 mm were illuminated with a source producing 88 keV gammas. Four detectors having an entrance window radius of 4.0 mm were positioned 40 mm above the target center at various scattering angles as shown. This test is intended to gauge whether ScatGram is properly calculating the angular distributions of singly-scattered photons. Each aluminum target contributes a unique angular distribution to each detector, resulting in a unique energy distribution. Using multiple detectors allows the test to be conducted simultaneously over a broad range of scattering angles. Figure 2-5 compares the results from both the MCNP and ScatGram simulations for singly-scattered photons only. The MCNP results include error bars.
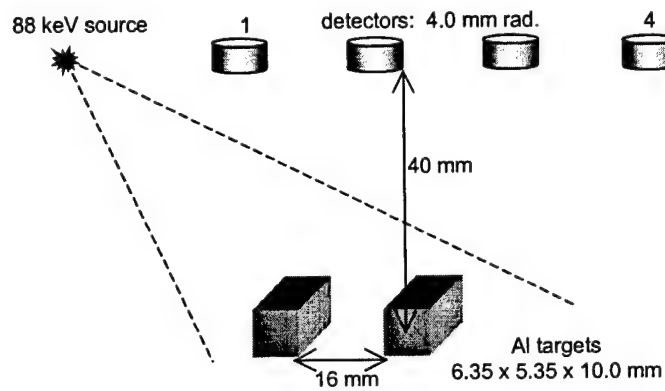
Figure 2-4. Geometry for Test Case A

For computational efficiency, source photons in the MCNP simulation are biased to travel initially into a narrow range of angles in the direction of the sample. Therefore, the magnitude of the energy distribution per source photon will not match the magnitude of the ScatGram distribution. A scalar factor must be applied to the results to make them match in total number of counts, and the scalar factor is constant across all four detectors.

The results agree remarkably well with respect to spectral shapes and relative intensity between detectors, indicating that ScatGram is properly modeling the angular distribution of singly-scattered gammas. Figure 2-6 shows the tallies of multiple-scatter events superimposed on the single-scatter tallies, as provided by MCNP. While multiple scatter contributes a relatively flat background compared with the single-scatter signal, it can certainly not be considered negligible, and it can be expected to increase in larger volume targets (Arendtsz, 1995b)
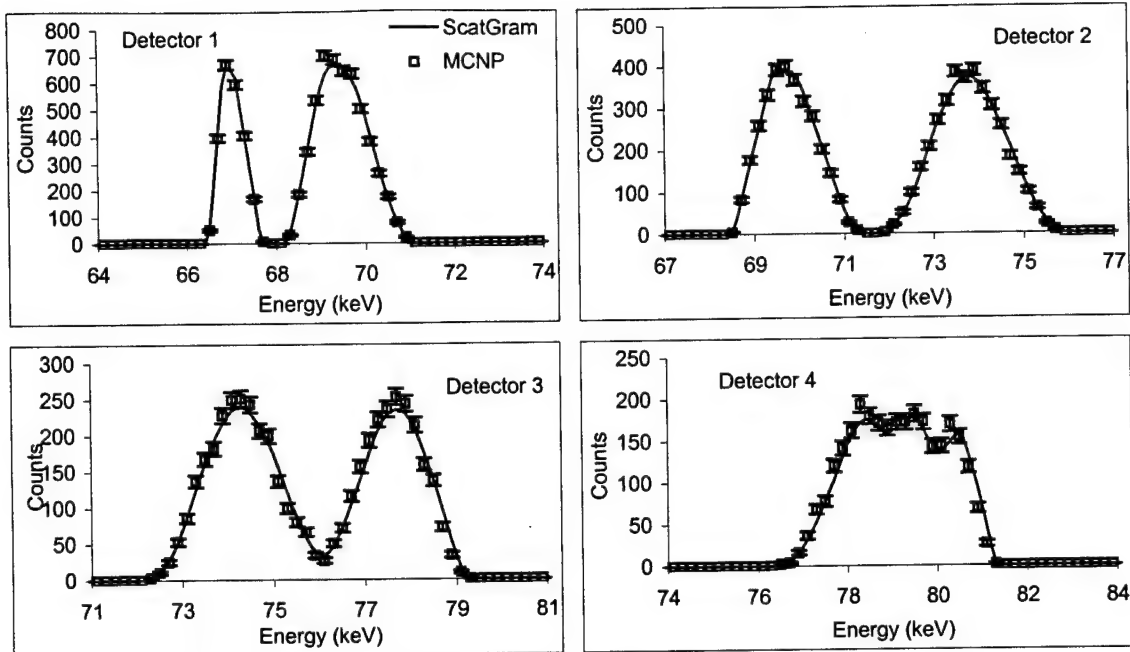
Figure 2-5. ScatGram and MCNP Single-Scatter Results for Test Case A.
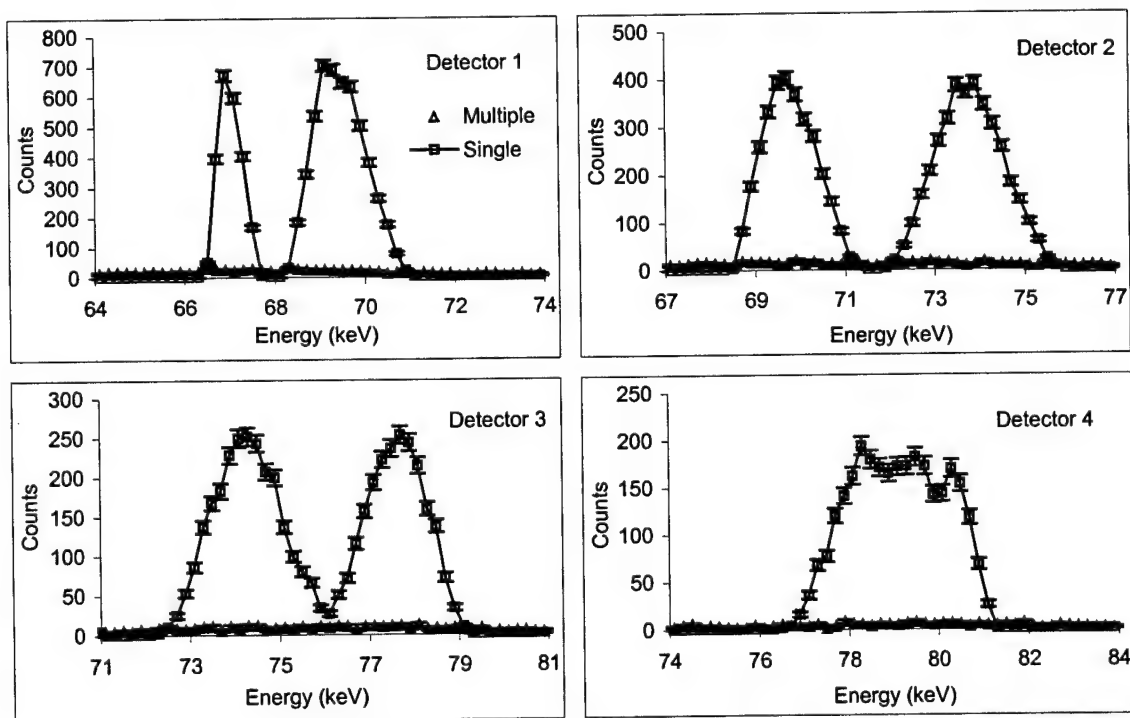
Figure 2-6. Multiple Scatter Contribution in Test Case A.

Test Case B. Test case B is checks that ScatGram is properly treating the attenuation of source radiation at 88 keV before it reaches a scattering site. The geometry for test case B is illustrated in Figure 2-7. Any gammas which scatter in the aluminum block on the right must first pass through the aluminum block on the left, which will attenuate about half the source gammas along its 15 mm length. Consequently the relative heights of the peaks produced by each target will be dissimilar, and both should agree with the MCNP results provided ScatGram treats this attenuation properly. Inspection of Figure 2-8 reveals that this is indeed the case. The ScatGram results match those of MCNP in both spectral shape and intensity.
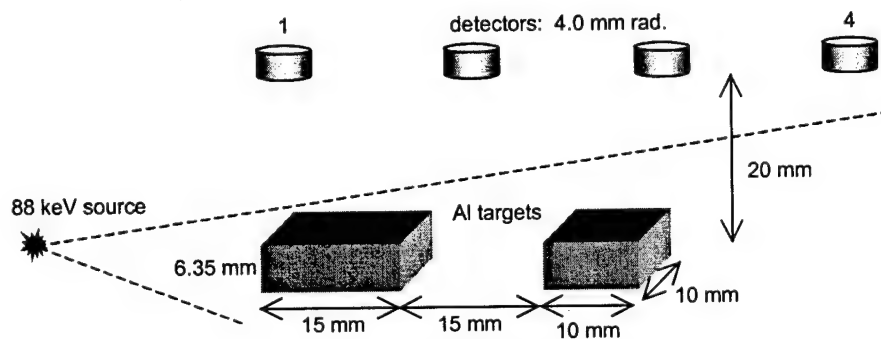
Figure 2-7. Geometry for Test Case B.
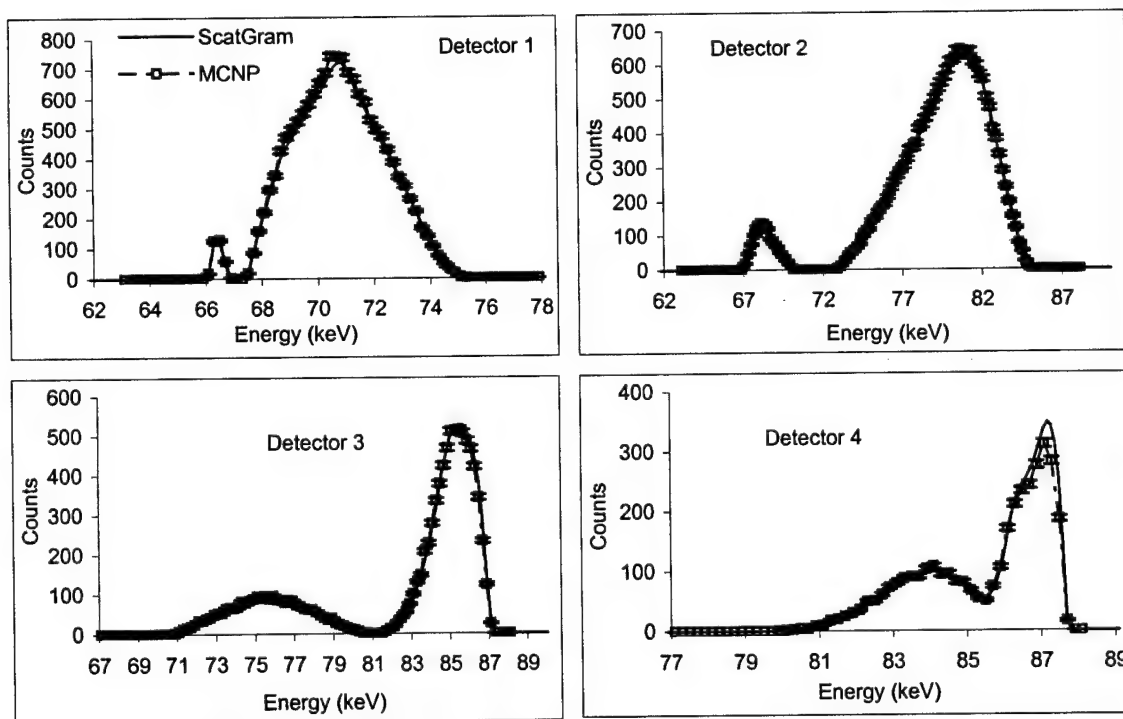
Figure 2-8. Comparison of ScatGram and MCNP Results for Test Case B.

Test Case C. The geometry for test case C is illustrated in Figure 2-9. Unlike the previous test cases, this one has only one detector location but has three different source locations. This test case is intended to check ScatGram's treatment of the outbound attenuation along the path from the scattering site to the detector. The source is collimated to illuminate only the smaller aluminum target, so all the scattered gammas must pass through the 15 mm target before detection. The attenuation is energy-dependent, and therefore scattering angle-dependent, so the three source locations allow testing over a range of angles. The relative height of the peaks predicted by ScatGram should agree well with the MCNP results and scale consistently across the three source locations, provided Scat Gram is treating the attenuation correctly. The results as shown in Figure 2-10 indicate that this is indeed the case.
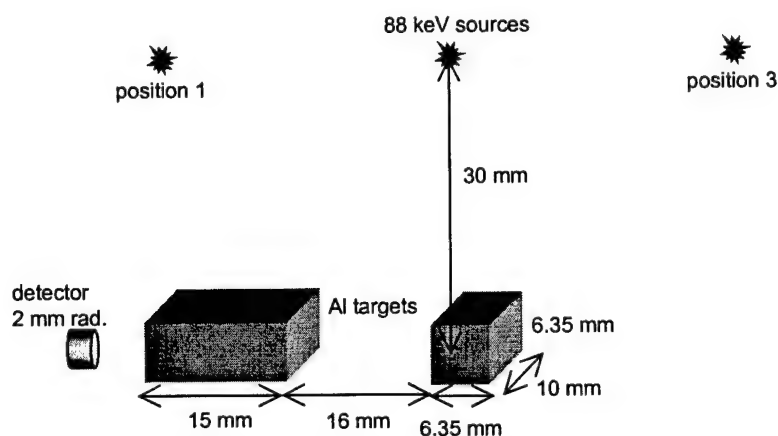
Figure 2-9. The Geometry for Test Case C.

2.7.2. *MCNP Study of Multiple and Coherent Scatter*

The ScatGram code incorporates the possibility of three series of interactions within the target:

1) photoabsorption of the incident gamma ray,

2) transmission of the incident gamma ray

3) Compton scatter of the incident gamma ray then escape of the scattered photon from the sample,

4) Compton scatter of the incident gamma ray followed by photoabsorption of the scattered photon within the sample.

ScatGram assumes the signal collected in the instrument is composed exclusively of interactions of the third type. The model of the MCST system response used for image reconstruction is founded on the same assumptions inherent in the ScatGram code. If series of interactions other than these form a non-negligible
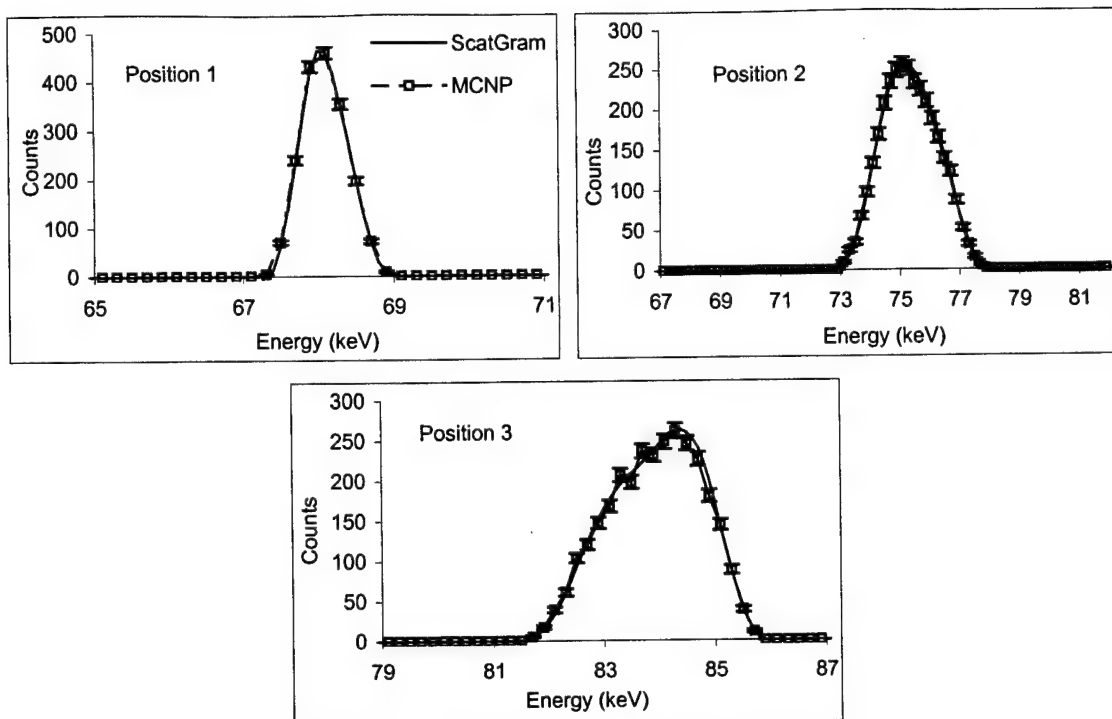
Figure 2-10. Results of Test Case C.

part of the signal, it may lead to poor image quality and greater instability of iterative reconstructions. Of particular concern are multiple Compton scatters and coherent (Rayleigh) scatters because they are the most probable neglected interactions in aluminum at the energies considered here. MCNP's statistical photon transport simulates multiple Compton scatters and incoherent scatter, unlike the ScatGram code. Several MCNP test cases were developed to study the validity of the assumption that the MCST signal is composed predominantly of singly Compton scattered photons.

Multiple Scatter Simulation. A photon which Compton scatters twice or more and is subsequently detected represents a signal contaminant because it has undergone two energy losses at two scattering locations. When it is assumed to have scattered only once, its final energy carries incorrect information about its scattering angle and thus its range of possible scatter locations, the isogonic region. It is impossible to distinguish many multiply scattered photons from singly scattered ones because they have similar energies. To minimize the number of multiply scattered photons detected, the MCST relies on the fan-beam collimation to image a thin tomographic slice. This approach makes use of the notion that a photon is unlikely to scatter twice in a direction that lies within the thin tomographic plane, but such events are still possible.

A series of simulations tested the ratio of single Compton scatter counts to multiple scatter counts collected in a typical MCST configuration. It is already known that the ratio of single to multiple scatter counts can be improved by reducing the volume of sample in the imaging region (Arendtsz, 1995b). These simulations gauge the extent to which volume changes in an aluminum sample will corrupt the single-scatter spectrum in the MCST system. To this end, two parameters in the simulation were varied, the tomographic slice thickness of the fan beam collimation and the sample thickness.

Figure 2-11 illustrates the geometry of simulation in which the fan beam slice thickness is varied. The imaging volume defined by the intersection of the source and detector fan beams will be a narrow tomographic slice of the sample which is treated ideally as a 2-dimensional plane. Slice thickness refers to the dimension of the imaging volume in the third, narrow, dimension. The source illuminated a 6-cm-long slice of a 2-cm-thick aluminum block, and the scattered flux was recorded by four detectors whose field-of-view was varied to change the thickness of the tomographic slice. A narrow slice thickness provides good spatial resolution because a small (thin) volume is inspected with each acquisition. It also provides a high ratio of single Compton scatter counts to total counts because the likelihood is low that secondary scatter events will be directed back into the narrow detector fan beam. However data throughput with narrow slices is poor because it is also unlikely that even first scatters will be directed into the detector fan beam. A thin tomographic slice thickness also benefits the image resolution, because it really represents the size of a voxel along the thickness direction. On the other hand, a thicker fan beam increases the amount of signal collected, but accepts more multiply scattered events and blurs the resolution. Figure 2-12 gives examples of the MCNP output, showing the intensity of the multiple-scatter spectrum compared to that of the single-scatter spectrum. There is a tradeoff between data throughput versus signal quality and image resolution. Figure 2-13 plots how the signal intensity improves, but the signal quality degrades as the slice thickness is increased from 1 mm to 2.5 cm. The signal quality is measured as the ratio of singly-Compton scattered photons (the useful signal) to all the photons detected (the total signal). Multiply-scattered photons are tallied outside the energy range for singly-scattered photons, so the ratio is a conservative estimate of the multiple-scatter photon contamination. Nevertheless, it provides a metric for evaluating its intensity. The ratio is averaged across the 4 detectors simulated.
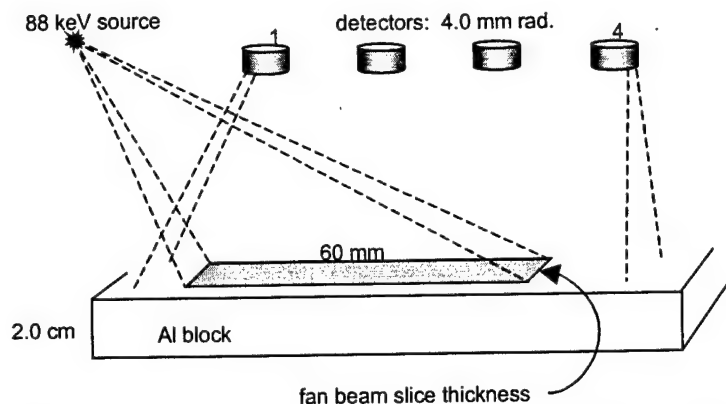
Figure 2-11. Tomographic Fan Beam Slice Thickness Simulation in MCNP
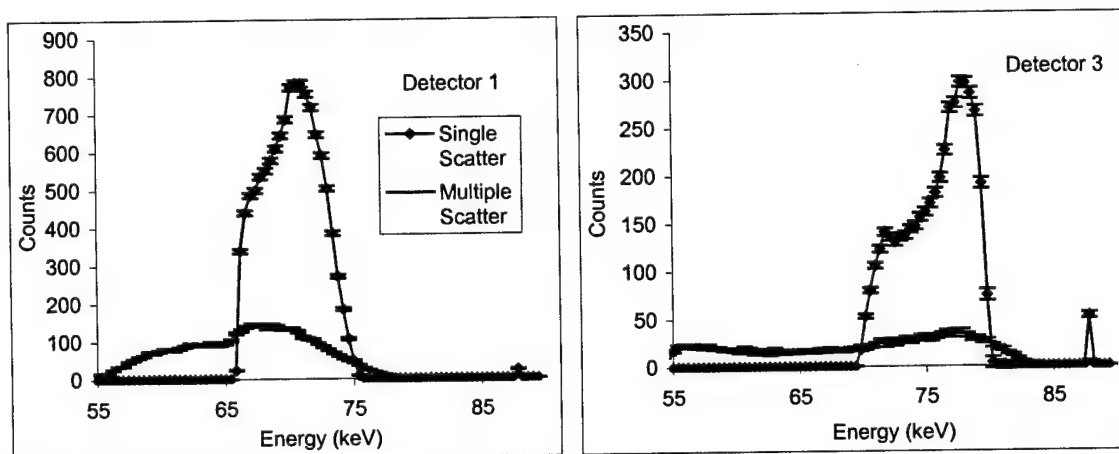
Figure 2-12. Examples of MCNP Output Comparing Single to Multiple Scatter. The simulation's configuration is shown in Figure 2-11. Tomographic slice thickness is 2.0 cm.
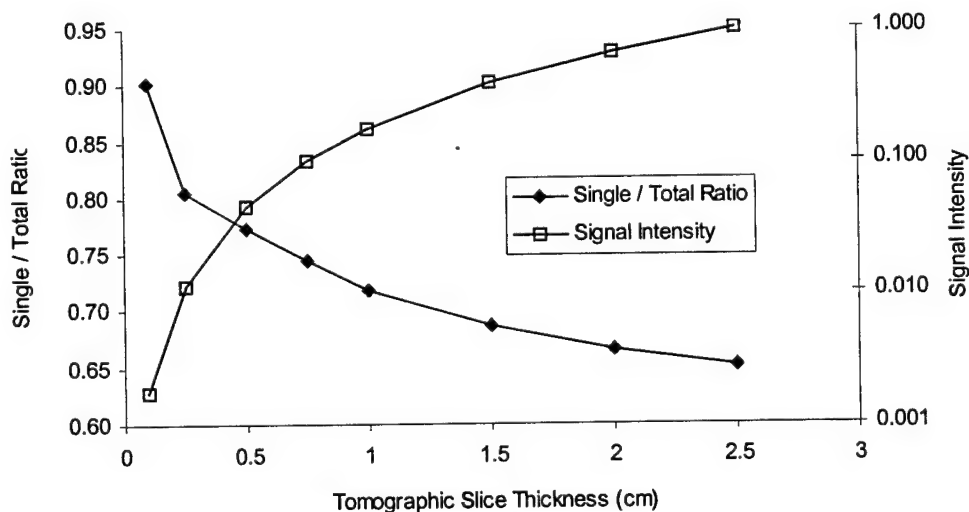
Figure 2-13. Single Scatter to Total Ratio and Signal Intensity vs. Slice Thickness. Results of MCNP simulations on a 2-cm-thick aluminum block.

The quality of the signal collected, as measured by the ratio of singly-scattered to total gammas recorded, is also a function of the sample thickness. MCNP was again used to simulate the signal collected in an MCST system where the thickness of the aluminum block sample was varied from 0.25 cm to 3.0 cm. Figure 2-14 illustrates the geometry of these simulations. A tomographic slice thickness of 1.0 cm was simulated for this study. The single-to-total ratio was averaged over the 4 detectors and Figure 2-15 plots the results as a function of sample thickness. As expected, the thicker targets allow a greater opportunity for multiple scatter, and thereby produce a lower single-to-total ratio.
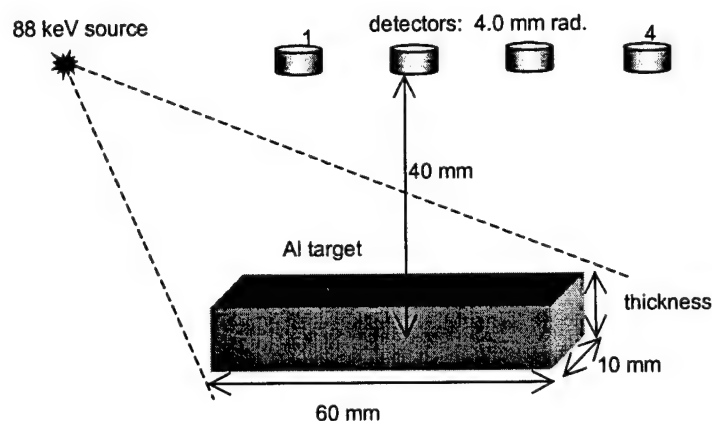
Figure 2-14. Geometry for the MCNP Study of the Effects of Sample Thickness.
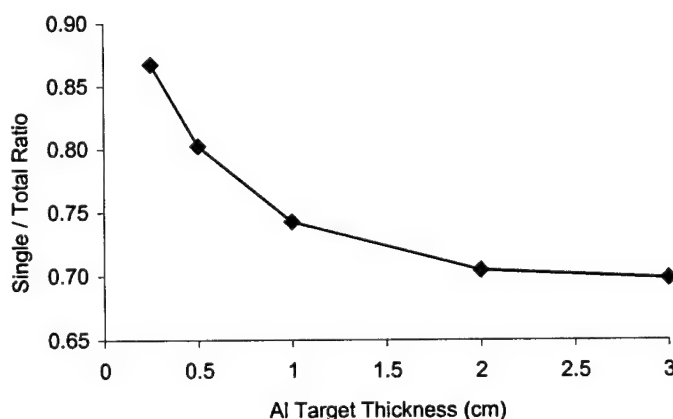
Figure 2-15. Single-to-Total Ratio vs. Aluminum Target Thickness. The data is for a tomographic slice thickness of 1 cm.

The results of the multiple scatter study indicate that multiple scatter will indeed be a significant component of the signal, unless the tomographic slice thickness can be reduced using very strong sources. This will not be possible in the demonstration MCST system, so a significant multiple scatter

contamination should be expected in the signals, and will represent a significant source of error between the recorded signals and the signals modeled with ScatGram.

Coherent Scatter Study. Coherent (or Rayleigh) scattering is the physical process whereby a photon-electron collision produces a scattered photon with no energy shift, but with a trajectory deflected from the incident direction. Figure 1-7 shows that the coherent scattering cross section in aluminum at energies just below 100 keV is comparable (within a factor of 1.5 to 3) to that of photoabsorption. Coherent scattering is most probable at small scattering angles, and is especially forward-biased for low-Z materials (Evans, 1965).

Although the degradation caused by coherent scatter is tempered by the forward-scatter bias, the series of interactions potentially detrimental to the MCST signal are coherent followed by Compton or Compton followed by coherent scatter. A series of multiple coherent scatters is unlikely to reach the detectors because of the forward-scattering bias. Even so, the final photon would not exhibit any shift in energy and would be discarded from consideration. Coherent scatter of an incident photon could cause ambiguity in the incident photon direction because it results in a photon with energy E_0 that is not propagating in a direction away from the source. Coherent scatter of a previously Compton scattered photon will result in a photon which retains the energy E', but has not retained the scattering angle θ between incident and final trajectories.

The feature which makes MCNP a useful tool for gauging the severity of coherent scatter in the MCST signal is the NOCOH option on the PHYS:P card (LANL, 1997). With the NOCOH option set to 1, the code simulates the photon physics without coherent scattering. This resembles the ScatGram treatment, except that multiple scatter is included and Doppler broadening is not. The default, NOCOH=0, includes coherent scatter in the computations. Comparison of a test case run with and without coherent scattering provides insight into how severely coherent scattering affects the signal.

To place an upper bound on the severity of the coherent scattering problem, a test case was devised that exacerbates the prevalence of coherent scatters beyond those expected in the typical MCST geometry. A row of four 8mm x 8mm x 10mm aluminum blocks was simulated with an 88 keV gamma source incident on one end of the row. An array of four 3.0mm-radius detectors tallies the scattered photon signal as illustrated in Figure 2-16. This arrangement encourages forward-biased coherent scatters from
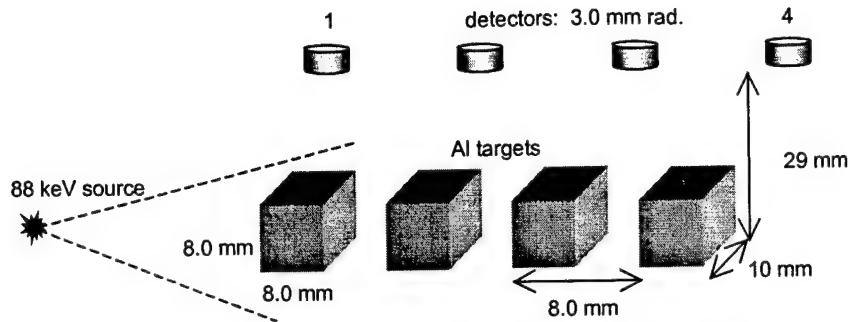
Figure 2-16. Geometry for the Coherent Scattering Test Case.

one block to enter the next block downstream. If coherent scatter is an important phenomenon, one should expect the downstream blocks to provide a greater response with coherent scattering than they would without it. This geometry should be affected more severely by coherent scatter than the typical MCST arrangement (as shown in Figure 2-11 and Figure 2-14) where little of the thin sample lies in a forward-scatter direction from any given scattering point.

Figure 2-17 shows the results of this simulation. The presence of photons tallied at the source energy, 88 keV, in the simulation that included coherent scatter (NOCOH = 0) and the absence of those photons in the spectra tallied without coherent scatter (NOCOH = 1) is the only observable difference between the two sets of spectra. Considering the statistical error in each spectrum, the results should be considered identical. Again, the MCNP simulations do not include Doppler broadening, but appreciable effects of coherent scattering would nevertheless be manifested as differences in the idealized spectra. These results suggest that coherent scattering in the sample will not provide a significant source of error between the measured spectra and the spectra modeled by ScatGram.
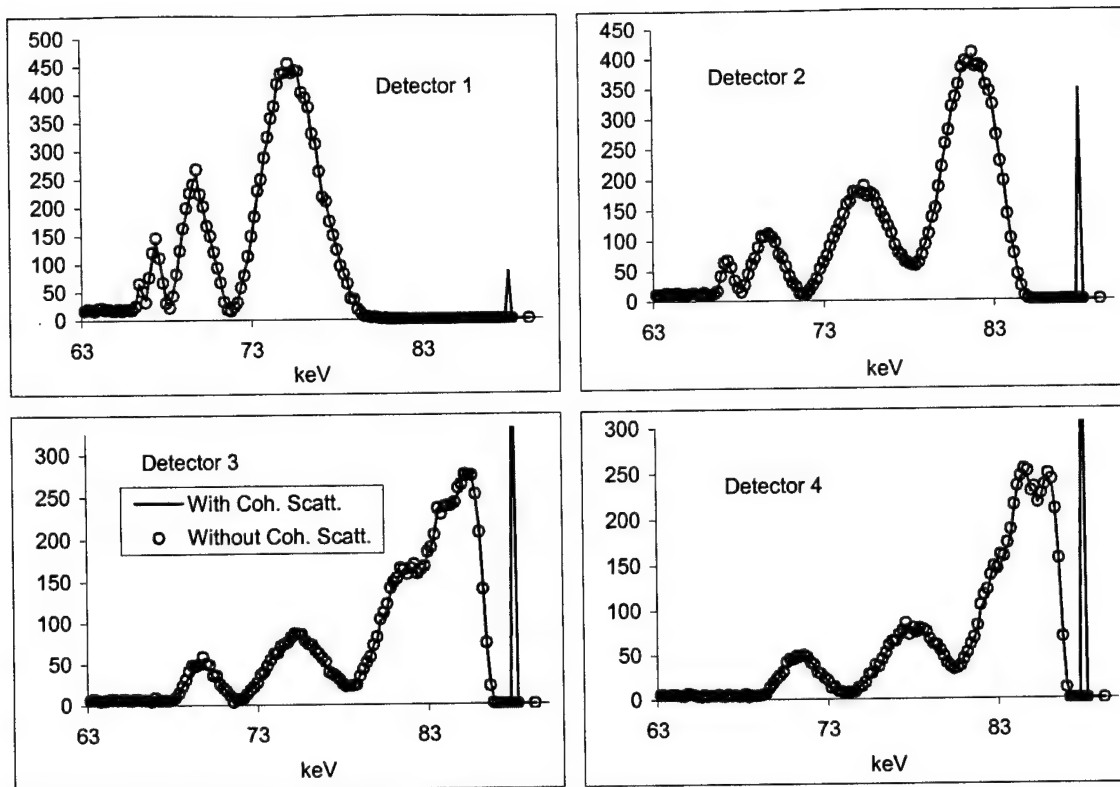
Figure 2-17. Results of the Coherent Scattering Test.

2.8. Summary of MCST Modeling

The ScatGram code calculates an estimate of the single-scatter gamma-ray spectra recorded in an MCST system. It uses a deterministic algorithm to integrate over the volume of a user-defined sample. A flexible geometry definition allows the user to specify the nature and locations of the sample, source, and detectors. ScatGram incorporates the important effects of Doppler broadening and finite source and detector sizes. The code has been benchmarked against an established Monte Carlo transport code, MCNP Version 4B, with good results.

Multiply-scattered photons may be significant in the actual MCST energy spectra. Their intensity will depend on factors such as the sample volume and thickness of the tomographic slice.

The system model embodied in the ScatGram code forms the foundation needed to produce electron density images from a recorded scattergram. The process of producing such images is called image reconstruction.

III. Image Reconstruction

Image reconstruction in Compton scatter tomography means building a spatial map of the sample's density from the energy spectral data, either simulated or measured with real detectors. The problem may be thought of as inverting the central MCST equation, Equation (1-12), to approximate the set of voxel densities ρ given the set of energy spectral measurements Ψ. Although the signal is related to the electron density, the reconstructed image may not represent the spatial distribution of the sample's electron density *per se*. Instead, it may give visual information on the homogeneity of the sample, in which changes in density may be manifested as discernible features. Thus it provides qualitative, but not necessarily quantitative information about the sample. Images are reconstructed as 2-dimensional cross sections that approximate the density distribution within the fan beam. As in conventional CT, three-dimensional images could be compiled by stacking two-dimensional slices (Barrett and Swindell, 1981).

Two approaches are used here, filtered backprojection (FBP), and an iterative technique called penalized weighted least squares (PWLS) image reconstruction. The discussion begins with a section on spectral deconvolution, because it is a necessary step for filtered backprojection.

3.1. Spectral Deconvolution

The purpose of spectral deconvolution is to unfold a scattering angle distribution from a recorded scattered photon energy distribution. It is the reverse of the operation indicated in Equation 2-4, because the objective is to recover the angle spectrum $f(\theta)$ from the recorded energy spectrum $g(E)$. This deconvolution step is needed to preprocess the data before filtered backprojection. Why? Because backprojection is performed along isogonic regions defined by their scattering angles as given in Equations (1-2) and (1-3), thus angular data must be used for backprojection. As explained in Chapter 1, the spectral broadening caused by detector resolution and Doppler broadening corrupts the relationship between scattered photon energy and scattering angle, so that backprojection of energy spectral data is not appropriate.

Equation (2-4) suggests this step could be accomplished by simply inverting the **H** operator. One finds, however, that the poor conditioning of this matrix and the presence of Poisson random noise in the measurement combine to create a numerically unstable system. Solution by inversion or by unregularized

linear methods such as Gauss-Siedel is not possible. Using wider energy bins improves the conditioning of the system, but the coarser sampling this entails degrades image resolution by increasing the areas covered by each isogonic region. Fourier transform techniques such as the Wiener filter are not useful because both the Doppler broadening and detector resolution represent a shift-variant point spread function, and the Weiner filter assumes shift-invariance (Gonzalez and Woods, 1992). Instead we turn to some iterative techniques developed primarily for two-dimensional image reconstruction that have been adapted here for one-dimensional spectral information.

Each collected energy spectrum of gross counts $\mathbf{g}$ is assumed to contain a spectrum of background counts $\mathbf{b}$. Of course randomness makes the precise values of $\mathbf{b}$ impossible to know, so the expected, or mean, number of background counts based on the collection time of $\mathbf{g}$ must be used. These values are determined by collecting background spectra over extended counting times to reduce the error in the predicted mean. Knoll suggests using comparable background and signal counting times to optimize the signal variance (Knoll, 1989), but this assumes a given time period to collect both signal and background for a single measurement. If the same background is to be used for multiple signal measurements, a better estimate of the mean background acquired over long counting times (possibly when the instrument is not being used for inspection) is preferable. This extended background is labeled $\mathbf{B}$ and T_g and T_B are the counting times for $\mathbf{g}$ and $\mathbf{B}$, respectively. Thus $(T_g/T_B) \cdot \mathbf{B}$ gives an estimate of $\mathbf{b}$. Recall the linear operator $\mathbf{H}$ converts the single-scatter angular distribution $\mathbf{f}$ to the Doppler-broadened energy distribution. The signal model can be written as

$$\mathbf{g} - \mathbf{b} - \mathbf{n}_g - \mathbf{n}_b = \mathbf{Hf} \qquad (3\text{-}1)$$

where $\mathbf{n}_g$ and $\mathbf{n}_b$ represent the unknown random noise in the gross counts and background, respectively. This equation ignores the effect of detector resolution broadening as defined by the matrix operator $\mathbf{D}$ from Equation 2-21. It may be included by operating on the Doppler-broadened energy distribution as

$$\mathbf{g} - \mathbf{b} - \mathbf{n}_g - \mathbf{n}_b = \mathbf{D}(\mathbf{Hf}) = \mathbf{DHf}. \qquad (3\text{-}2)$$

For compactness only the $\mathbf{H}$ operator is shown in the algorithms below, but $\mathbf{DH}$ may always be substituted for $\mathbf{H}$ to unfold the detector broadening effects simultaneously. To remove the detector's intrinsic peak efficiency $\varepsilon(E)$ during deconvolution, every row i of $\mathbf{D}$ is simply multiplied by the efficiency $\varepsilon(E_i)$.

3.1.1. Constrained Least-Squares Algorithm

The constrained least squares restoration maximizes the smoothness of the solution f' while also constraining it so the solution's residual matches the noise in the signal as follows (Gonzalez and Woods, 1992).

$$\|\mathbf{g} - \mathbf{b} - \mathbf{H}\mathbf{f}'\|^2 = \|\sigma_{g-b}\|^2 \tag{3-3}$$

The central difference approximation for the second derivative gauges the smoothness of the solution by providing a measure of the solution oscillations,

$$\frac{\partial^2 f(x)}{\partial x^2} \approx f(x+1) - 2f(x) + f(x-1), \tag{3-4}$$

which is given in matrix operator form as (Gonzalez and Woods, 1992)

$$
\mathbf{C} = \begin{bmatrix}
1 & & & & & & \\
-2 & 1 & & & & & \\
1 & -2 & & & & & \\
& 1 & \ddots & 1 & & & \\
& & & -2 & 1 & & \\
& & & 1 & -2 & & \\
& & & & 1 & &
\end{bmatrix}. \tag{3-5}
$$

In order to both satisfy Equation (3-3) and maximize smoothness, the method of Lagrange multipliers is used. This means minimizing the criterion function F(f') combining the oscillation measure and the residual with the parameter α.

$$F(\mathbf{f}') = \|\mathbf{C}\mathbf{f}'\|^2 + \alpha\left(\|\mathbf{g} - \mathbf{b} - \mathbf{H}\mathbf{f}'\|^2 - \|\sigma_{g-b}\|^2\right). \tag{3-6}$$

Differentiating with respect to $\mathbf{f}'$ and setting the result equal to zero yields (Gonzalez and Woods, 1992)

$$\mathbf{f}' = \left(\mathbf{H}^T\mathbf{H} + \gamma\mathbf{C}^T\mathbf{C}\right)^{-1}\mathbf{H}^T(\mathbf{g} - \mathbf{b}). \tag{3-7}$$

The Lagrange multiplier γ, equal to $1/\alpha$, is adjusted iteratively until Equation (3-3) is satisfied, successive solutions converge, or γ converges to within some tolerance. Currently a successive bisection algorithm finds the optimum γ. In some cases γ must also be constrained to remain above a judiciously selected minimum value so that the poorly conditioned $\mathbf{H}^T\mathbf{H}$ term in Equation (3-7) does not dominate the quantity under inversion. Components of the signal are assumed to be independent Poisson random variables with variance equal to their mean.

$$\left\| \sigma_{g-b} \right\|^2 = \left\| \sqrt{\sigma_g{}^2 + \sigma_b{}^2} \right\|^2 = \left\| \sqrt{g + \left(\frac{T_g}{T_B}\right)^2 B} \right\|^2 = \sqrt{g + \left(\frac{T_g}{T_B}\right)^2 B}^{\,T} \sqrt{g + \left(\frac{T_g}{T_B}\right)^2 B} \qquad (3\text{-}8)$$

3.1.2. *Maximum Likelihood Algorithm*

This technique is based on the expectation maximization (EM) technique used in SPECT and PET imaging (Shepp and Vardi, 1982). Instead of solving for an unknown distribution of emission densities as in emission tomography, we solve for an unknown angular distribution represented by f'. The transition matrix $p(b,d)$ in emission tomography which represents the probability that a photon emitted in voxel b is detected in detector d is analogous to our operator $H(E_i, \theta_j)$ which represents the probability that a detected photon scattered into angle bin θ_j falls in the energy bin E_i. Unlike the constrained least-squares algorithm, the solution itself is iterated, with each successive estimate of f' calculated as

$$f'^{k+1}(n) = f'^k(n) \sum_{i=1}^{N} \frac{H(i,n) \cdot [g(i) - b(i)]}{\sum_{m=1}^{N} H(i,m) \cdot f'^k(m)}, \qquad (3\text{-}9)$$

where k is the iteration number. A flat spectrum with uniform intensity over all bins serves as the initial guess f'^0.

Shepp and Vardi showed that for Poisson random variables the likelihood of each iteration in the ML algorithm is strictly increasing (Shepp and Vardi, 1982). It should be noted that while the background subtraction provides an unbiased estimator of the mean number of scattered photons, the data no longer has Poisson variance.

3.1.3. *Penalized Weighted Least Squares Algorithm*

This technique is essentially a one-dimensional version of the penalized weighted least squares algorithm used in 2-D image reconstruction (Fessler, 1994). More information about that algorithm is available in Section 3.3.3. The PWLS algorithm, like CLS, seeks a solution that most closely matches the data by minimizing the squared error as measured by the residual. There is no constraint, however, on the solution residual. Instead, each measurement is weighted by its variance, and a penalty function or prior is incorporated into the objective function. This penalty is used to force the solution to posses certain properties that are assumed from prior knowledge or assumptions about the solution.

The objective function PWLS seeks to minimize is (Fessler, 1994)

$$F(\mathbf{f}') = \frac{1}{2}(\mathbf{g} - \mathbf{b} - \mathbf{Hf}')\Sigma^{-1}(\mathbf{g} - \mathbf{b} - \mathbf{Hf}') + \beta R(\mathbf{f}') \cdot$$

(3-10)

The first term in Equation (3-10) constitutes a weighted measure of the residual. The weights come from the diagonal matrix Σ whose element Σ_{nn} is a measurement of the variance in channel n of the signal $g(E_n)$ – $b(E_n)$. Assuming Poisson statistics leads to

$$\Sigma_{nn} = \sigma^2_{g(n)-b(n)} = g(E_n) + \left(\frac{T_g}{T_B}\right)^2 B(E_n) \cdot$$

(3-11)

The second term in Equation (3-10) is the penalty term. To reduce large oscillations between neighboring bins, the penalty function $R(\mathbf{f}')$ uses the same smoothness measure of Equation (3-4).

$$\beta R(\mathbf{f}') = \beta \sum_{n=2}^{N_\theta - 1} f'(n-1) - 2f'(n) + f'(n+1)$$

(3-12)

The parameter β is adjusted to vary the amount of smoothing. Noisier measurements will require larger values of β to keep the solution stable, but sacrifice sharpness.

Fessler uses a successive over relaxation technique to minimize the objective function of Equation 3-10. This leads to (Fessler, 1994)

$$f'^{k+1}(n) = \omega \frac{\mathbf{H}_n{}^T \Sigma^{-1} \mathbf{r} + s(n) f'^k(n) + \beta R(\mathbf{f}'^k)}{s(n)} + (1-\omega) f'^{old}(n)$$

(3-13)

where $\mathbf{r}$ is the latest residual,

$$\mathbf{r} = (\mathbf{g} - \mathbf{b}) - \mathbf{Hf},$$

(3-14)

$\mathbf{H}_n$ denotes the nth column of $\mathbf{H}$, and

$$s(n) = \mathbf{H}_n{}^T \Sigma^{-1} \mathbf{H}_n \cdot$$

(3-15)

The algorithm used here starts with a flat spectrum as the initial guess $\mathbf{f}^0$.

3.1.4. Spectral Deconvolution Performance

Tests to compare the performance of the different spectral deconvolution tools were conducted on hypothetical energy spectra having 100 eV energy bins. The spectra were assumed to contain photons scattered once from aluminum with $E_0 = 88$ keV and recorded in a high purity germanium (HPGe) detector having an energy resolution of 500 eV across the energy range considered, 55 keV to 90 keV. The

spectrum in Figure 3-1 with sharp features represents the hypothetical angular distribution f(θ) used for these tests, but for better comparison it is plotted in the energy domain according to the simple one-to-one transformation $f_E(E)\delta E = f(\theta)\delta\theta$ provided by the Compton equation. $f_E(E)$ is termed the ideal energy spectrum. As suggested by Equation 3-2, corrupted spectra **g** were constructed by performing the operation **DHf**. Then a background with a uniform intensity was added across the spectrum, and the result randomized with statistical noise. Thus **g** contains the simulated effects of Doppler broadening, detector resolution, random noise, and background counts. In these simulations it was assumed that $T_B \gg T_g$. An example of a noisy g(E) is also shown in Figure 3-1.
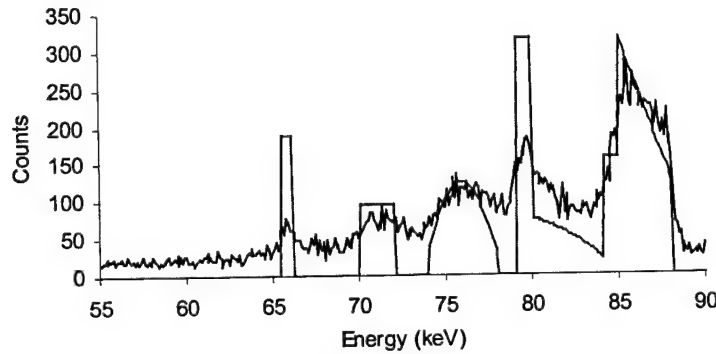
Figure 3-1. Hypothetical Test Spectra. An example of the hypothetical ideal spectrum $f_E(E)$ and its noisy counterpart g(E) with background added.

The error in deconvolved spectra was investigated for the three techniques as a function of the signal to noise ratio (SNR) using the hypothetical ideal spectrum plotted as f_E in Figure 3-1. The SNR is defined as

$$\text{SNR} = \frac{1}{N_E} \sum_{n=1}^{N_E} \frac{g(n) - b(n)}{\sqrt{\left(\sigma_{g(n)}\right)^2 + \left(\sigma_{b(n)}\right)^2}} = \frac{1}{N_E} \sum_{n=1}^{N_E} \frac{g(n) - \dfrac{T_g}{T_B} B(n)}{\sqrt{g(n) + \left(\dfrac{T_g}{T_B}\right)^2 B(n)}} \tag{3-16}$$

so the SNR may be varied by adjusting the intensity of background counts in **b** or scattering events in **g - b**.

Figure 3-2 shows how the error for each method changed when the ratio of background counts to total counts was held at 0.1, but the SNR was increased by increasing the total number of photons collected. This increase simulates longer counting times and reduces the relative variance in the measurements. CLS appears to be the most stable algorithm at low SNR, and as the Figure 3-2 shows, even converged in a
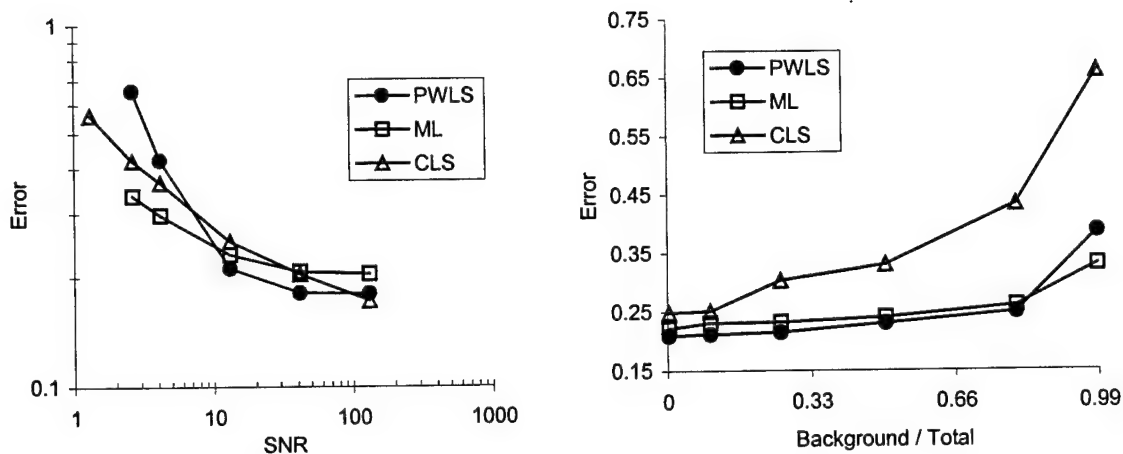
Figure 3-2. Performance of the Unfolding Algorithms vs. Noise.

region of very low SNR where the others did not. At lower SNR, the PWLS algorithm requires a high value of the regularization parameter β to maintain a stable solution. This accounts for its high error at low SNR where the strong penalty function tends to over-regularize the solution. ML works well in this region, but is unfortunately the slowest of the three algorithms to converge. As SNR increases, the three algorithms converge to similar performance.

Next the total number of scattered photons simulated was held at 1×10^5, but simulating a more intense background decreased the SNR. Thus the intensity of **g-b** remained constant, but the statistical noise in **g-b** increased as the background intensity increased. Figure 3-2 shows how the error increased for all three methods with increasing background intensity. The ML and PWLS algorithms are relatively unaffected by the additional variance until the background level becomes very high. In contrast, the error in the CLS algorithm grows steadily with increasing background level. This should come as no surprise since the basic precept of the CLS algorithm involves matching the noise in both the signal and background to the solution residual per Equation (3-3). The solution is intentionally oversmoothed to induce a large error, which will match the constraint.

3.1.5. *Demonstration with Hypothetical Data*

Figure 3-3 gives some examples of the deconvolution of hypothetical spectra that produced the results shown in Figure 3-2. The first plot shows the hypothetical ideal spectrum used for the following examples. The **H** operator constructed from the Compton profile of aluminum with $E_0 = 88$ keV combined with the **D** operator for a detector with a uniform resolution of 500 eV blurred the ideal spectrum. The
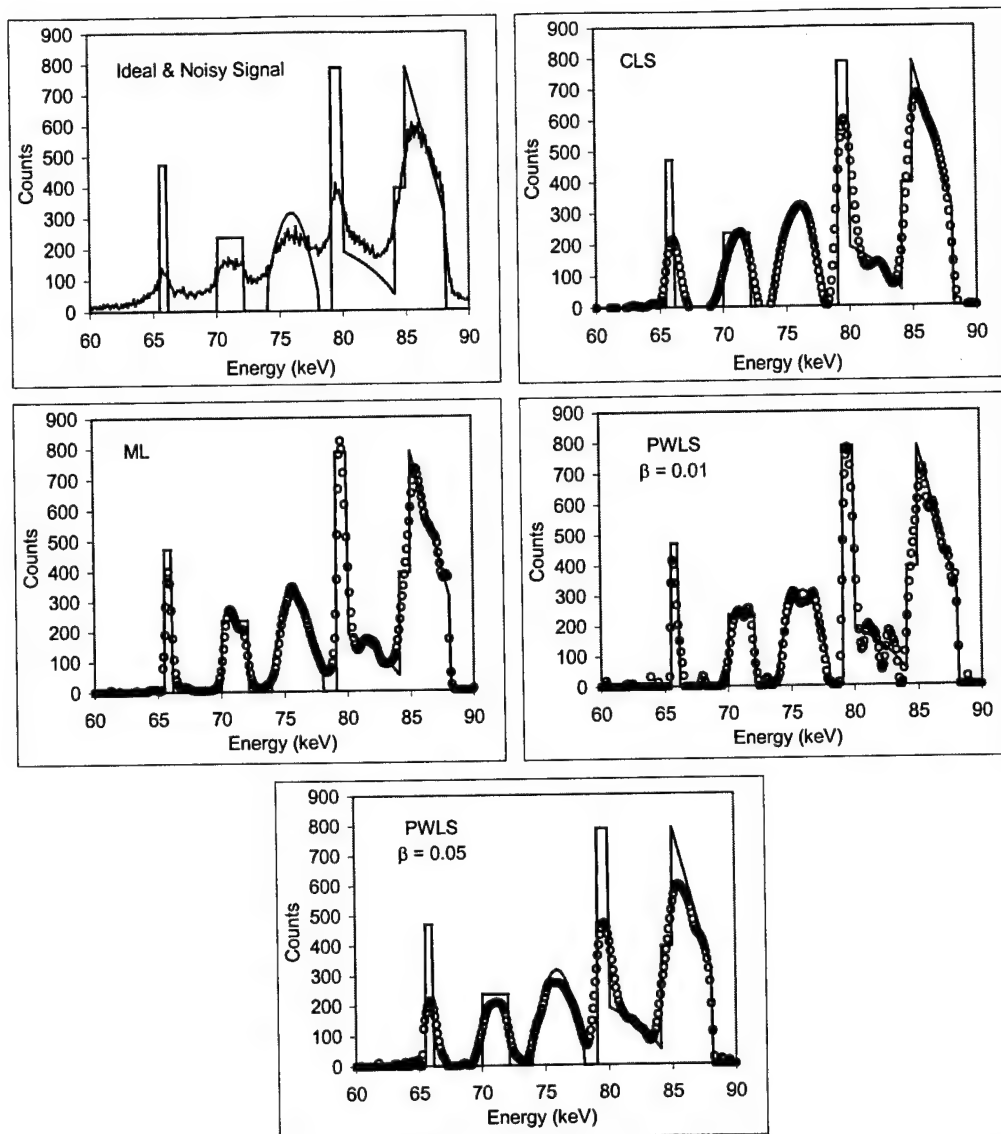
Figure 3-3. Demonstration of Spectral Deconvolution on Hypothetical Data. Top left: original noisy signal and ideal signal. Others: spectra recovered from CLS, ML, and PWLS algorithms.

addition of background counts and statistical noise provided a spectrum with an SNR of 8.9 and a background-to-total ratio of 0.1. This noisy spectrum is also displayed in the first plot labeled "ideal and noisy signal." The remaining plots of Figure 3-3 show the spectra recovered from the various deconvolution algorithms and how they compare with the ideal. Iteration continued with each technique until successive approximations converged to within 0.1 percent. The initial guess was a flat spectrum with 150 counts in each channel. The constrained least squares (CLS) deconvolution converged in only 8 iterations to a final value of $\gamma = 3.8$. The maximum likelihood (ML) deconvolution converged in 50 iterations. Two penalized weighted least squares algorithms ran for 30 iterations each with different values

of the regularizing coefficient β. The solution with β = 0.01 recovers the amplitude and shape in the spectral features well, but suffers from severe oscillations between 80 and 85 keV. Increasing β by a factor of 5 dampens the oscillations at the expense of losing some shape and amplitude

3.1.6. *Demonstration on Measured Data*

What follows are examples of the deconvolution of measured scattered gamma ray spectra collected from a known sample. The sample consisted of two 6.35 mm x 6.35 mm square aluminum rods. Using *a priori* knowledge of the sample, ScatGram calculates a true angular distribution of scattered photons $f(\theta)$ for comparison to the deconvolved approximations. Figure 3-4 compares the associated ideal spectrum $f_E(E)$ with the noisy and blurred measured signal. This energy spectrum has an SNR of 4.37 and a background-to-total ratio of 0.2373. The measured spectrum shown has background subtracted. Figure 3-4 shows the resulting approximations to $f_E(E)$ provided by the CLS, ML, and PWLS algorithms. The
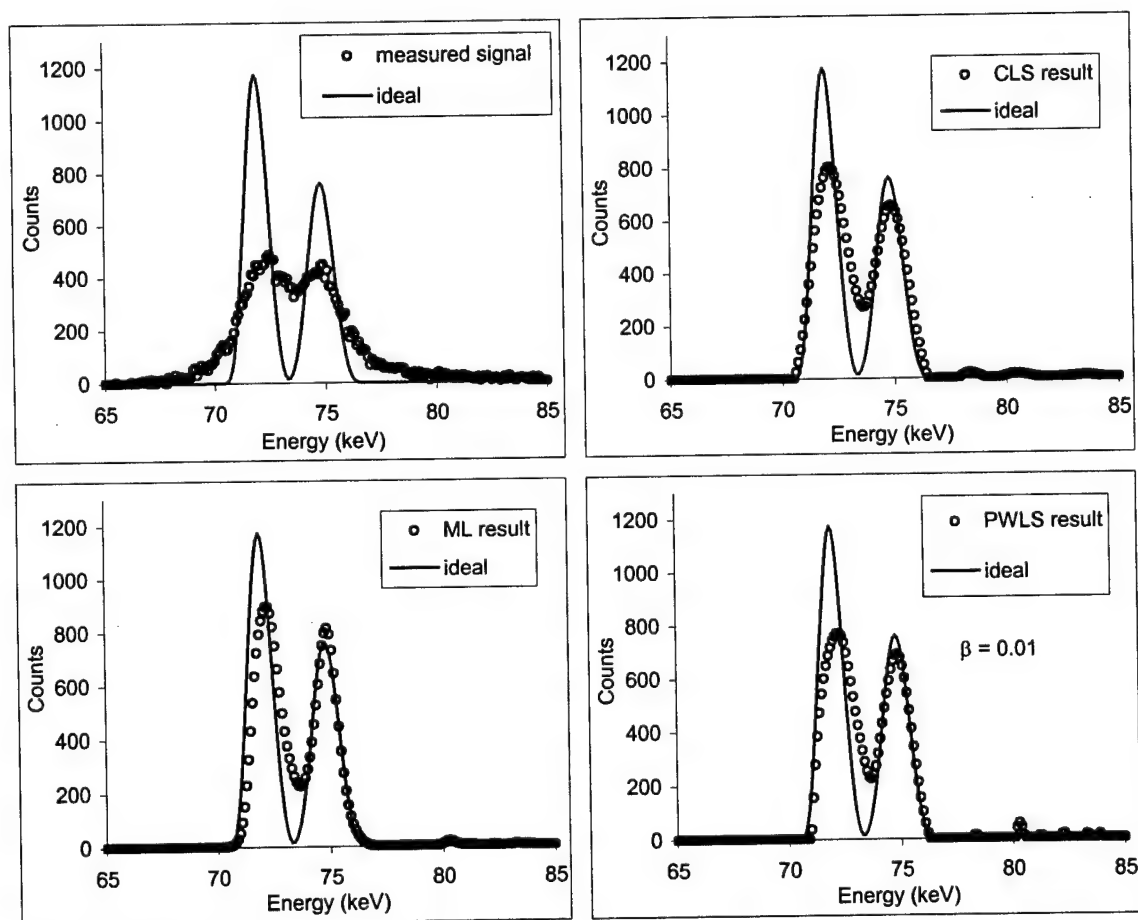
Figure 3-4. Demonstration of Spectral Deconvolution with Measured Data. Top left: original noisy signal and ideal signal. Others: spectra recovered from CLS, ML, and PWLS algorithms.

CLS algorithm converged to $\gamma = 6.78$ in 12 iterations. The ML algorithm converged to the solution shown in 61 iterations and the PWLS algorithm converged to the solution shown in 37 iterations. The results for each technique are similar, as can be expected considering the SNR and background/total conditions and Figure 3-2.

## 3.2.   Filtered Backprojection

Norton proved that the image reconstruction problem in Compton scatter tomography has an analytical solution given the ideal conditions of an infinite line detector providing continuous position and energy data (Norton, 1994). The derivation also assumes that Compton scatter is the only interaction, and that the energy-angle relationship obeys the Compton equation. While these conditions are not realistic, his derivation at least provides the framework and equations that underlie a plausible mode for MCST image reconstruction. The reconstruction Norton derives is similar in many ways to the filtered backprojection technique widely used in transmission CT. Whereas in CT the backprojection is performed along the straight lines of transmission, here a weighted backprojection is performed along the isogonic scattering lines (Norton, 1994). The solution contains the same frequency ramp filter used in CT.

The filtered backprojection reconstruction technique developed for the MCST system is based on the equations presented by Norton. The relatively large sizes of the MCST detectors required adaptation of the technique to perform weighted backprojection within the curved isogonic regions described in Chapter 1. The code, developed in Fortran90, makes use of the same namelist formatted files used by the ScatGram code to read the geometry specifications including the locations, sizes, and orientations of sources and detectors.

The first step is to preprocess the energy spectral data $\Psi(j,E_k)$ to unfold an approximation to the angular data $f(j,\theta_q)$ using one of the deconvolution schemes. Doppler broadening and detector resolution nullify the one-to-one realtionship between energy and scattering angle so that the scattered energy distribution does not represent the scattering angle distribution. The deconvolution is necessary because the isogonic regions along which backprojection takes place are truly defined by scattering angle, not energy. Each backprojection should be weighted by the number of photons that scatter at each angle.

The next step is to divide the image region into a rectangular grid of m = 1…M voxels then compile a summation image b(m) by performing a weighted backprojection of the scattering angle distribution f(j,q) over the image region. Backprojection is performed for every nonzero angle bin q = 1…N_θ in every detector j = 1…N_d. It includes only those voxels which lie within the isogonic region defined by j and q. The summation image value for voxel m is

$$b(m) = \sum_{j=1}^{N_d} \sum_{q=1}^{N_\theta} \frac{1}{W(j,q)} \frac{f(j,q)}{w(m,j,q)} \cdot \qquad (3\text{-}17)$$

The weighting factor w(m,j,q) is needed to account for the variation in distance of each voxel m from the source, distance of each voxel m from the detector j, and the probability for scattering in angle bin q.

$$w(m,j,q) = \frac{\Omega_v(m,j)}{4\pi} L(m,j) \cdot \left[\frac{d\sigma}{d\Omega}(\theta_q, Z) \right]_{KN} S(\theta_q, Z) \cdot \Omega_q \cdot \eta(\phi(m,j)) \cdot \Lambda(m,j,q) \qquad (3\text{-}18)$$

The terms here are similar to those developed in Chapter 2. Here $\Omega_v(m)$ is the solid angle subtended by the cell of voxel m as viewed from the source. L(m, j) is the average pathlength through cell m of paths that originate at the source position j and pass through the cell. The term in brackets represents is the Klein-Nishina differential cross section. S(θ, Z) is the incoherent scattering function, Ω_q is the solid angle of scattering bin q, and Λ(m,n,q) is the fraction of the scattering solid angle of bin q subtended by the window of detector j. The detector's oblique angle efficiency is accounted for with the η(φ) factor, but the intrinsic full-energy efficiency as a function of energy ε(E) should accounted for during the deconvolution step. A value for Z must be assumed for all voxels in the backprojection. Doing otherwise would imply some *a priori* knowledge of the sample. The W(j,q) factor is used to normalize each backprojection so that any particular isogonic region is not overrepresented or underrepresented in the summation image. Various normalizations were investigated, but the following yielded the best (and comparable) results:

$$W(j,q) = \frac{1}{\sum_{m=1}^{M} w(m,j,q)} \qquad (3\text{-}19)$$

$$W(j,q) = \frac{1}{N_p(j,q)} \qquad (3\text{-}20)$$

where $N_p(j,q)$ is the number of voxels in the isogonic region (j,q).

The final image is obtained by convolving a ramp filter function with the summation image. The summation image, as in transmission CT, is the object convolved with a 1/r point spread function (Norton, 1994). For the 2-dimensional filtering step it is more useful to consider the one-dimensional array of voxel values b(m) as the two dimensional image array of voxels b(x,y) = b(r). The final image I(r) is

$$I(r) = b(r) * * q_2(r) \tag{3-21}$$

where

$$q_2(r) = \mathcal{F}^{-1}\{\delta \cdot a(\delta)\} \qquad \delta = \sqrt{\xi^2 + \eta^2} \tag{3-22}$$

and where ** represents a two-dimensional convolution and $\mathcal{F}$ represents a 2-dimensional Fourier transform. This is equivalent to applying an apodized ramp filter to the Fourier transform $B(\xi, \eta)$ of b(x,y).

$$I(\xi, \eta) = B(\xi, \eta) \cdot \delta \cdot a(\delta) \qquad I(x, y) = \mathcal{F}^{-1}\{I(\xi, \eta)\} \tag{3-23}$$

Many choices are available for the apodizing function $a(\delta)$ but its primary purpose is to attenuate high frequency noise. The Shepp-Logan filter (Barrett and Swindell, 1981) was used predominantly in the MCST image reconstructions. The Shepp-Logan filter is

$$a_{SL}(\delta) = \pi \cdot \text{rect}\left(\frac{\delta}{2\delta_{max}}\right) \cdot \text{sinc}\left(\frac{\delta}{2\delta_{max}}\right) \tag{3-24}$$

where

$$\text{sinc}(x) = \frac{\sin(\pi x)}{\pi x} \tag{3-25}$$

and

$$\text{rect}\left(\frac{x}{b}\right) = \begin{cases} 1, & |x| \leq b/2 \\ 0, & |x| > b/2 \end{cases} . \tag{3-26}$$

and δ_{max} is a maximum cutoff for frequencies passed by the filter.

Comparison of Equation (3-18) and Equation (2-6) reveals that the attenuation terms given by Equation (2-9) and Equation (2-10) are not accounted for during the backprojection. Attenuation effects cannot be included because they would require prior knowledge of the sample being imaged. Consequently, the regions of the sample which suffer significant attenuation of the incident and scattered photons will be significantly underweighted during backprojection, and will appear disproportionately dim

in the image. As such, filtered backprojection does not give any quantitative information on the density of the sample, only on its spatial distribution. Further image processing could presumably correct for this effect by correcting the brightness of voxels based on their location within the reconstructed object. Another possibility is difference imaging where the image of an unknown sample is subtracted from that of a known homogeneous control sample to highlight regions of possible defects. Nevertheless, the effects of attenuation will vary smoothly within a homogeneous region of the object so sharp features may still be discernible as intensity variations against a smoothly varying background.

3.3. Iterative Image Reconstruction

Iterative image reconstruction for the MCST system involves solving a large system of non-linear equations to approximate the unknown set of electron densities (the image) given the recorded signal. This system of equations is none other than the central MCST equation from Chapter 1,

$$\Psi = \mathbf{A}(\rho) \cdot \rho \tag{1-12}$$

where Ψ represents a set of measured energy spectra (the signal), ρ represents the set of sample densities, and $\mathbf{A}$ is a matrix that represents a mapping of the densities to the spectra (Arendtsz, 1995a). The equations developed in Chapter 2 for the ScatGram code also form the basis for constructing the system mapping $\mathbf{A}(\rho)$. The inverse problem that must be solved is finding the solution for ρ which best matches Ψ. The solution is iterative in the sense that an initial guess for ρ is repeatedly refined until some convergence criteria are met.

During iterative reconstruction an estimate of the sample density is available which may be incorporated into the equations to correct each voxel for attenuation of source and scattered photons. The mapping $\mathbf{A}(\rho)$ is written as a function of ρ to demonstrate that, because of this attenuation correction, $\mathbf{A}$ is indeed density-dependent. This makes the system implicit and nonlinear so that solving by linear inversion of $\mathbf{A}$ is not possible. Whereas backprojection suffers from nonuniform response through the sample depth caused by attenuation, the problem is alleviated in iterative reconstruction by correcting for the attenuation.

The effects of Doppler broadening and of detector resolution can be included into the set of equations defining the system mapping $\mathbf{A}$. This eliminates the need for the spectral deconvolution required for filtered backprojection. Instead, iterative techniques can use unfiltered energy spectra.

The primary disadvantages of iterative reconstruction are greater computational effort and potential instability caused by poor conditioning of the mapping **A**, or inexact characterization of the system response.

3.3.1. *Previous Work in Iterative Reconstruction*

The work of Arendtsz most closely resembles the reconstruction problem here (Arendtsz, 1995a; Arendtsz, 1995b). The reconstruction problem in Prettyman's dual-mode transmission and scattering problem, despite many parallels, is somewhat different due to the availability of transmission measurements to estimate the linear attenuation coefficients within the sample. Arendtsz successfully demonstrated iterative image reconstruction for energy-dispersive Compton scatter tomography with both simulated and experimental data. In these experiments she collected scattered gamma-ray spectra at positions surrounding the phantom, so the problem was not one-sided.

As explained in Chapter 2 the mathematical modeling of Arendtsz treats the detectors as ideal points, but this treatment is compensated for with an experimentally measured detector response function whose purpose is to incorporate the effects of detector size and resolution. The response of the actual detector at several energies was measured by scattering from small targets, and the response at intermediate energies interpolated from the results. She used a 662 keV source that creates a significant Compton continuum in the detector response. Although Doppler broadening is not specifically mentioned, it would also be included in the detector response function. Arendtsz uses the ideal point detector model as the mapping **A**, and consequently must unfold the detector response function from the measured data to estimate a point detector response to use with **A** for image reconstruction. Prettyman uses a similar approach to unfold scattering projections from measured scattered energy spectra. This step is similar to the spectral unfolding used in the MCST system to estimate a scattering angle distribution from a scattered energy distribution – a necessary step for filtered backprojection image reconstruction. The MCST algorithms, however, do not need to correct for the finite size of the detectors since their size is considered during backprojection. They only unfold the effects of Doppler broadening and energy resolution.

In contrast to Arendtsz's point detector model and Prettyman's scattering projection model, the MCST system mapping considers source size, detector aperture size, detector resolution and Doppler broadening. Deconvolution of a detector response function is therefore avoided for iterative reconstruction.

Working at 88 keV with adequately large detectors allows the MCST model to ignore the effect of the Compton continuum that is negligible at this lower energy.

3.3.2. Implicit Mapping

Computing the implicit mapping $A(\rho)$ involves modification of the A^0 matrix to account for the attenuation of incident and scattered radiation. Recall that the ρ-independent terms of the forward model are precomputed and stored in A^0, so computation of $A(\rho)$ entails the inclusion of these terms as follows For energy bin n in detector position j and voxel m, the system matrix is computed

$$A(\rho)(j, E_n, m) = A(\rho)(i, m) = A^0(i, m) \cdot a_{in}(\rho, j, m) \cdot a_{out}(\rho, j, m, n) \qquad (3\text{-}27)$$
$$i = (j-1)N_E + n$$

$$a_{in}(\rho, j, m) = \sum_{n=1}^{N_X \cdot N_Z} \exp\left[-\rho(n) \cdot \mu^{tot}(E_0) \cdot x^{in}(m, n, j)\right] \qquad (3\text{-}28)$$

$$a_{out}(\rho, j, m, n) = \sum_{p=1}^{N_X \cdot N_Z} \exp\left[-\rho(p) \cdot \mu^{tot}(p, E_n) \cdot x^{out}(m, n, j)\right] . \qquad (3\text{-}29)$$

Now all the terms in the forward mapping of Equation (2-21) except $\rho(m)$ are included in the matrix $A(\rho)$. Recall from Chapter 2 that $I(j, E_k)$ is represents a probability, per source photon, of observing a count in energy bin E_k of detector j, and that N_γ is a factor to scale those probabilities into an expected number of counts $\overline{\Psi}$. $A(\rho)$ is ordered so that when multiplied by the column vector ρ, product is $\overline{\Psi}$.

$$A(\rho) \cdot \rho = N_\gamma I \approx \Psi \qquad (3\text{-}30)$$

Use of scattering and attenuation cross sections for a single material such as aluminum implies that if the sample were composed strictly of that material, then the reconstruction would represent the mass density of the sample, which is related to the electron density through a scalar factor. The material could also be a compound with a homogeneous composition. When other materials are present, this scalar relationship is lost. The Compton scatter cross section is directly proportional to Z (Evans, 1965), so the intensity of scattered photons in each voxel will always be proportional to the voxel's electron density independent of the type of material. The assumption of a constant macroscopic scattering cross section therefore, should not be of concern. In the absence of attenuation the reconstructed image would still represent the relative electron density of the sample. More difficult to predict is the error resulting from

calculation of total attenuation through unknown materials with the assumed (incorrect) cross sections because total attenuation is not directly proportional to Z.

The Compton profile of the assumed material is embedded in the mapping through the Doppler broadening matrix **H**. This provides another inconsistency if the sample contains unknown materials because the Compton profile is a nonlinear function of Z. As with the scattergram code, the results of background, multiple scatter and the detector's peak-to-total ratio (i.e. the Compton continuum) are not included. While background can be removed to some extent through simple subtraction, these other two phenomena are not as straightforward. Numerical stability of the iterative reconstruction must rely on these factors being negligible.

3.3.3. *Penalized Weighted Least-Squares Algorithms*

To reiterate, the objective of iterative reconstruction is to solve Equation (1-12) to find the set of densities ρ that best match the signal Ψ. Penalized weighted least-squares (PWLS) is the method selected to accomplish this in the MCST system.

The penalized weighted least-squares method belongs to a broad class of image reconstruction methods known as Statistical Image Reconstruction (SIR) (Fessler, 1994; Sauer and Bouman, 1993). Statistical methods seek a solution that best matches the random and probabilistic nature of the data. This is in contrast to such deterministic iterative algorithms as the algebraic reconstruction technique (ART) which may be unsuited for situations in which the data is very noisy, the system is underspecified, or the numerical system is poorly conditioned (Sauer and Bouman, 1993). Even familiar statistical methods such as maximum likelihood (ML) may select the solution that most closely matches the available data, but the closest solution, while it fits the data quite well, may be highly oscillatory and not represent a reasonable image of the sample. This was indeed the case when ML was investigated for use in the MCST system. Bayesian estimation in statistical image reconstruction incorporates a Bayesian prior or penalty that dictates, based on some prior beliefs or assumptions about the sample, the types of solutions deemed acceptable as estimates of the electron density image (Sauer and Bouman, 1993).

The penalized weighted least squares technique is a statistical image reconstruction with Bayesian priors. It was developed for positron emission tomography (PET) imaging by Fessler (Fessler, 1994). In PET, the positron-annihilation distribution is reconstructed from a data set consisting of the number of

coincidence measurements in N detector pairs. In MCST we seek to reconstruct the electron density distribution from the data set $\Psi(j,k)$ consisting of the number of Compton scattered photons recorded in each bin of each detector.

PWLS requires a system model that relates the unknown image to the expectation value of each detector measurement. In PET, this model is embodied in a system matrix $\mathbf{P}$, whose element $P(i,m)$ denotes the probability that an annihilation in the jth voxel is detected by the ith detector pair. The need for such a system matrix is generally true for all iterative reconstruction techniques. To use PWLS in the MCST system, we must construct the $\mathbf{A}(\rho)$ mapping whose element $A(i,m)$ relates the density in voxel m to the measurement $\Psi(i)$ – the number of counts in a single energy bin of a single detector.

PWLS also requires an estimate of the variance in each measurement. Recall that Ψ is obtained by computing the difference between two Poisson random variables: the raw counts $\mathbf{g}$ and the expected background $\mathbf{b}$ so that $\Psi = \mathbf{g} - \mathbf{b}$ and

$$\sigma_{\Psi}^2 = \sigma_{\mathbf{g}}^2 + \sigma_{\mathbf{b}}^2 \tag{3-31}$$

$$\sigma_{\Psi(i)}^2 = g(i) + \left(\frac{T_g}{T_B}\right)^2 B(i) \tag{3-32}$$

The PWLS method finds a weighted least-squares solution which matches the recorded data while regularizing the solution so that it remains well-behaved. The regularization incorporates a quadratic smoothness penalty or prior to ensure the solution avoids high-frequency oscillations. The method of Fessler is based on minimizing following penalized weighted least-squares objective function:

$$\Phi(\rho) = \frac{1}{2}(\Psi - \mathbf{A}\rho)^T \Sigma^{-1}(\Psi - \mathbf{A}\rho) + \beta R(\rho) \tag{3-33}$$

where Σ is the diagonal matrix with $\Sigma_{ii} = \sigma_{\Psi(i)}^2$. The first term of the objective function is the least squares similarity measure. The residual $(\Psi - \mathbf{A}\rho)$ terms are weighted with the inverse variance so that the weighting reflects the relative information in each measurement. The purpose of this first term is to encourage agreement between the image and the measured data. $R(\rho)$ is the regularizing penalty function. The purpose of this term is to discourage oscillatory solutions by reducing intensity variations between

neighboring voxels. The regularization parameter β controls the tradeoff between the two. For particularly

noisy measurements β must be increased to affect a stable solution at the expense of image sharpness.

The penalty function presented by Fessler and used here is the quadratic smoothness penalty

$$R(\rho) = \frac{1}{2} \sum_{m=1}^{N_X N_Z} \sum_{n \in N_m} w_{mn} \frac{1}{2} (\rho(n) - \rho(m))^2$$

(3-34)

where N_m is the set of eight neighbors of voxel m. Horizontal and vertical neighbors of m are given a

weight of 1, diagonal neighbors are given a weight of $2^{-1/2}$ and voxel m is given a weight of 0. Figure 3-5

illustrates the weights of surrounding voxels.

				$\frac{1}{\sqrt{2}}$	1	$\frac{1}{\sqrt{2}}$
	voxel m			1	0	1
				$\frac{1}{\sqrt{2}}$	1	$\frac{1}{\sqrt{2}}$

Figure 3-5. Weighting of Neighboring Voxels in the Penalty Function.

Unlike the PET reconstruction problem, the MCST system matrix is dependent on the solution as

suggested by Equation (1-12). This means that not only must the solution ρ converge, but the system

matrix $A(\rho)$ must also converge before a solution is accepted. Such implicit dependence requires two

levels of iteration. An inner iteration repeats until ρ converges to a solution based on the current estimate

of A. Then the system mapping A is updated based on solution for ρ, comprising one outer iteration step.

Every time an outer iteration step is performed and A gets updated, the inner iteration is repeated until ρ

converges again.

To minimize the objective function the successive overrelaxation (SOR) method of Fessler is used

during the inner iteration. Starting with an initial guess for the density ρ^0, Figure 3-6 outlines the PWLS

algorithm. The symbol a_m denotes the mth column of A. The relaxation constant ω controls the

convergence rate of the solution. Fessler suggests iterating initially with $\omega < 1$, which will converge the

lower-frequency components, then using $\omega = 1$ to resolve the higher-frequency components of the solution.

The amount of regularization is primarily noise-dependent and is adjusted with β. As suggested by Fessler,

the algorithm reverses the order in which the voxels are processed, i.e. the scan direction for every inner

iteration. This reduces the likelihood of artifacts resulting from one particular scan direction.

Outer Iteration

$$\boldsymbol{\rho} = \boldsymbol{\rho}^0$$
$$\boldsymbol{A} = \boldsymbol{A}(\boldsymbol{\rho}) \quad \text{(update nonlinear } \rho \text{ dependencies)}$$
$$\boldsymbol{r} = \boldsymbol{\Psi} - \boldsymbol{A}\boldsymbol{\rho}$$
$$s(m) = \boldsymbol{a}_m^T \boldsymbol{\Sigma}^{-1} \boldsymbol{a}_m \qquad m = 1,\dots,N_X N_Z$$
$$d(m) = s(m) + \beta \sum_{n \in N_m} w_{mn} \qquad m = 1,\dots,N_X N_Z$$

Inner Iteration

yes

$$\boldsymbol{\rho}^{old} = \boldsymbol{\rho}$$

$$\rho^{new}(m) = \frac{\boldsymbol{a}_m^T \boldsymbol{\Sigma}^{-1} \boldsymbol{r} + s(m)\rho^{old}(m) + \beta \sum_{n \in N_m} w_{mn}\rho^{old}(m)}{d(m)}$$

$$\rho(m) = \max\left\{0, (1-\omega)\rho^{old}(m) + \omega\rho^{new}(m)\right\}$$

$$\boldsymbol{r} = \boldsymbol{r} + \boldsymbol{a}_m\left(\rho^{old}(m) - \rho(m)\right)$$

no

ρ Converged ?
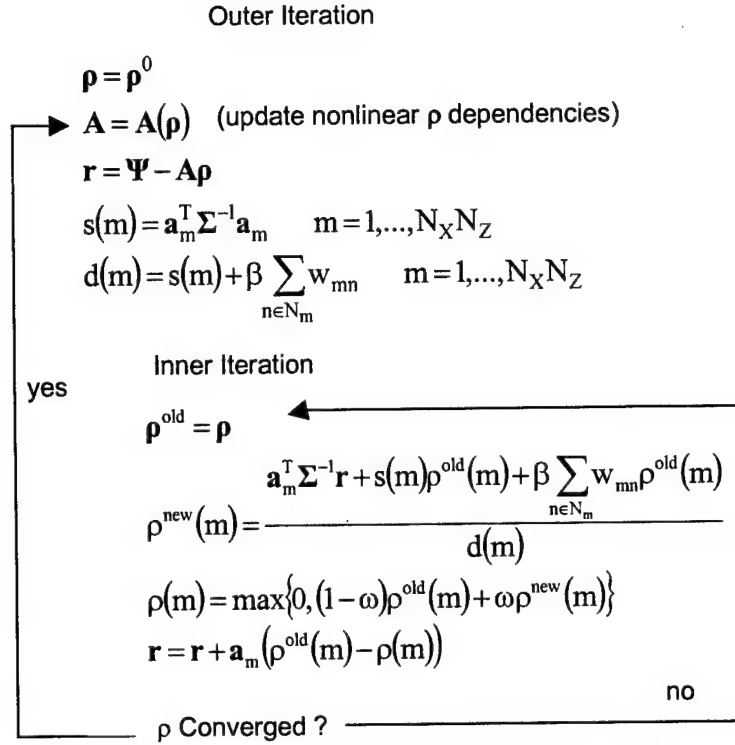
Figure 3-6. PWLS Algorithm for Image Reconstruction.

Now the advantage of the $\boldsymbol{A}^0$ matrix should be apparent. Using $\boldsymbol{A}^0$ and the Equations (3-27) through (3-29) avoids computation of the ρ-independent terms of the model at each outer iteration.

The quadratic penalty function incorporates an assumption about the solution, it's assumed smoothness, to regularize the solutions within the inner iteration, but it is also possible to use some prior knowledge of the sample to constrain the solution at each outer iteration. For instance, if there is a known maximum density ρ_{max} for any voxel, then the values exceeding that maximum can be reset to the maximum ρ_{max} before proceeding with the next outer iteration. Likewise, if it is known the sample is composed primarily of material at density ρ_{max} with possible low-density anomalies, then all voxels within a certain tolerance of ρ_{max} may be reset to ρ_{max}. Sauer and Bouman suggest an intriguing prior that presumes each voxel has one of a fixed number of known densities (Sauer and Bouman, 1993). They suggest that this approach is better conditioned than continuously-valued reconstructions under low signal-to-noise conditions.

3.4. Comparison of Reconstruction Techniques

A direct comparison of filtered backprojection and PWLS iterative reconstruction is difficult because the data appropriate to reconstruct with one technique is not appropriate for the other technique. For example, to produce a reasonable image with filtered backprojection, a large quantity of data is needed to provide adequate angular and spatial sampling. Because each data point is considered and backprojected independently, this extensive data set does not present computational difficulties. With iterative reconstruction, however, each voxel must be mapped simultaneously to each measurement, creating a large system that must be stored and manipulated within the computer's memory. For example, a typical problem considered in this project involved a 21 x 84 image and 20 detector positions with 176 energy bins in each detector. This creates a 1764 x 2816 system matrix. It requires nearly 50 MB to store one such array in double-precision arithmetic, and the iterative nature of the algorithm requires storage of two such arrays simultaneously. Clever programming could allay some of this difficulty, but iterative reconstruction will remain more computationally demanding than backprojection. Fortunately, iterative reconstruction generally requires less data to produce a reasonable image.

The demonstration MCST system introduced in Chapter 4 must rely on iterative reconstruction because it is severely limited in angular sampling and because collection of data is an arduous process.

Figure 3-7 illustrates the steps involved in reconstructing an image, either with simulated spectra or spectra measured in the laboratory. The boxes shaded in gray represent information that must be provided by the user. To simulate an MCST image, the ScatGram code produces the $I(j,E_n)$ data as described in Chapter 2. The ScatGram code needs information about the sample (sample info.) such as its material and density distribution and location. Also required is specific information about the MCST system (system info.) for instance the source and detectors' sizes and positions, and the detectors' efficiencies, and resolutions. The energy distributions are then corrupted with Poisson noise and noisy background counts $b(E)$ to produce a simulated energy spectra $\Psi(E)$. In the case of measured data, $\Psi(E)$ and $b(E)$ are recorded directly in the laboratory, and nature provides the random noise. From this point the simulated and measured data are treated precisely the same. To proceed with filtered backprojection, one of the spectral deconvolution algorithms must extract an approximation for $f(\theta)$ from $\Psi(E)$. Backprojection
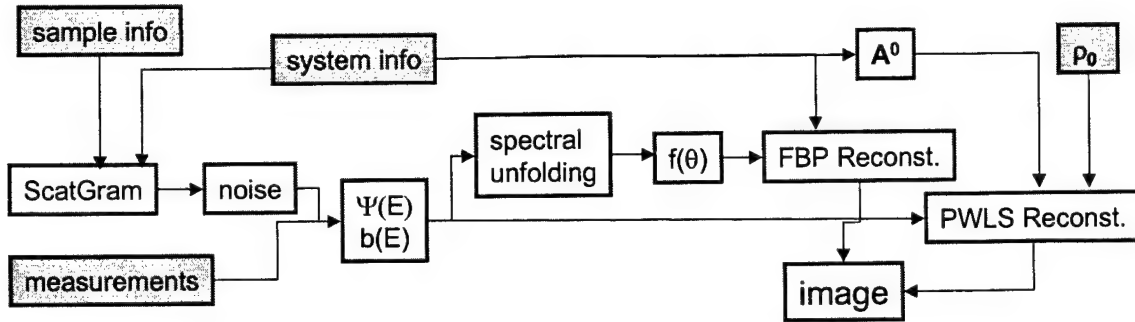
Figure 3-7. Steps in Measured and Simulated Image Reconstruction.

and filtering of f(θ) proceeds as described above. PWLS iterative reconstruction, on the other hand, accepts

the raw spectra Ψ(E) and b(E) without spectral unfolding. It also requires the A^0 matrix which uses only

system information. No *a priori* knowledge of the sample is embodied in A^0. Also required for iterative

reconstruction is a first guess of the sample density ρ_0. A reasonable guess for ρ_0 does embody some *a*

priori assumptions about the sample; for instance ρ_0 could be the electron density image of a clean sample.

The problem illustrated in Figure 3-8 demonstrates the image reconstruction algorithms. The

ScatGram code simulated the scattered energy spectra collected from a 4.0 cm x 1.0 cm aluminum target

with a 1.4 cm x 0.5 cm void on the top surface. Two source / detector configurations simulate the source to

the left and right of the phantom, with the detectors positioned as shown. Note the symmetry with respect

to the center of the sample. Spectra from 60 detectors total (30 in each source / detector configuration)

comprise the data set used for filtered backprojection reconstruction, and spectra from 30 detectors (15 in

each source / detector configuration) comprise the data set used for penalized weighted least squares

reconstruction. Initially, statistical noise was not included in the simulations to isolate the reconstructions

from its effects. The resulting reconstructions represent ideal results and may be considered a theoretical

best possible solution for the data set. The filtered backprojection result is reconstructed directly from the

scattering angle distributions; error caused by spectral deconvolution on noisy data will blur the image by

backprojecting an imprecise angular distribution.
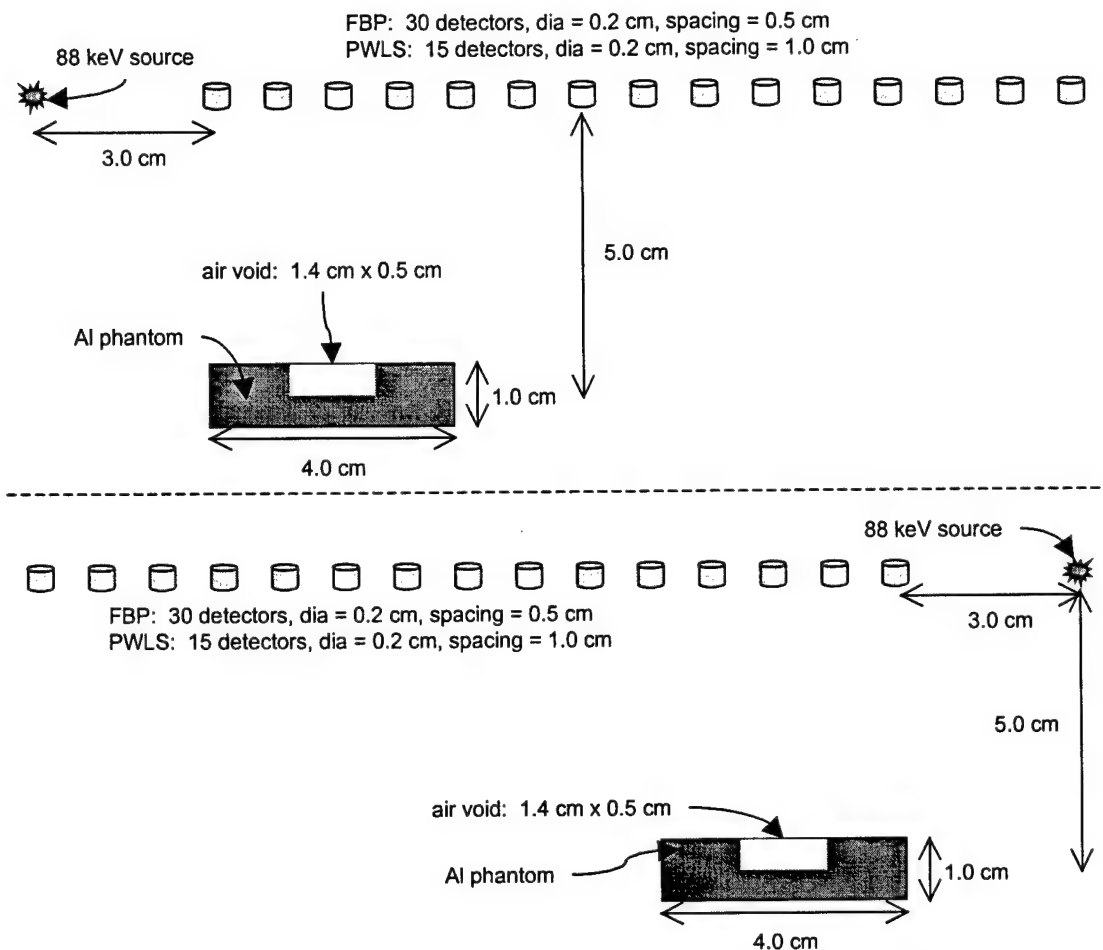
Figure 3-8. Configurations Used To Demonstrate the Reconstruction Codes.

Figure 3-9 shows the results of a filtered backprojection reconstruction using 60 spectra sorted into 100 eV-wide bins. A Shepp-Logan function was used to apodize the ramp filter (Cho, 1993) when applied to the summation image. The resulting image clearly suffers from blurring and artifacts caused by the non-uniform and incomplete backprojection. In transmission CT this problem is ordinarily overcome by rotating the sample with respect to the source and detectors (Barrett and Swindell, 1981). Rotation is also used in Prettyman's combined transmission/scatter technique to provide more uniform sampling. This luxury is not available in one-sided tomography, so the presence of such artifacts seems unavoidable. Nevertheless, the void anomaly is recovered in the final image. This method provides qualitative information about the sample's density distribution, so a relative density scale is appropriate.

phantom

FBP summation image

FBP image reconstruction
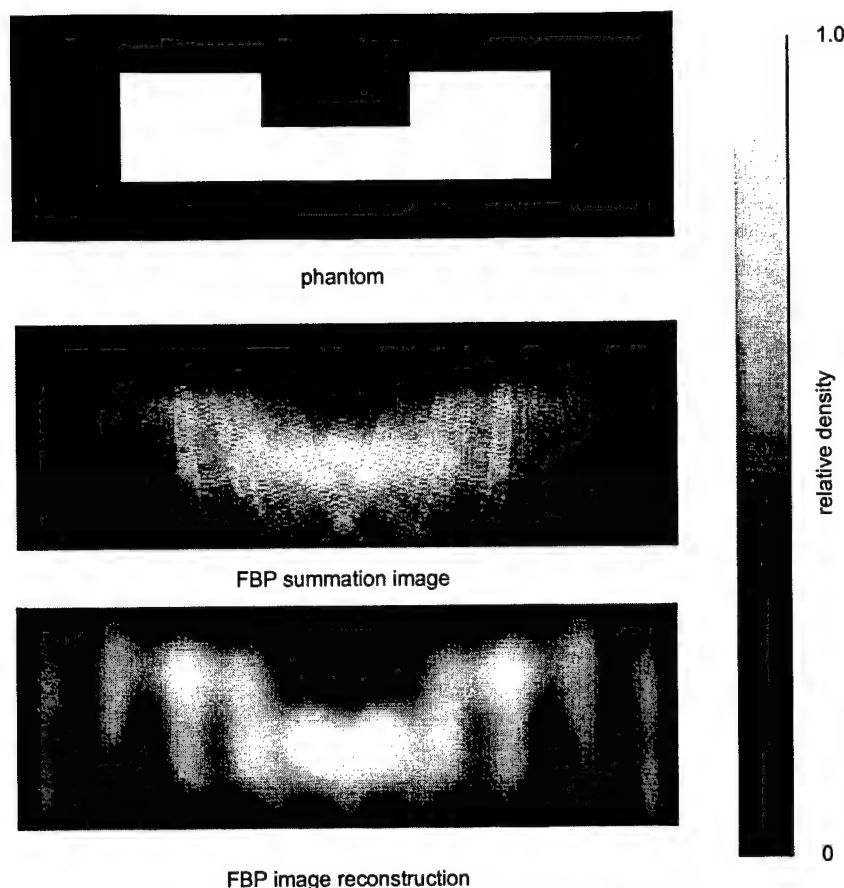
Figure 3-9. Results of the Filtered Backprojection Reconstruction.

Figure 3-10 shows the results of the PWLS iterative reconstruction using 30 spectra sorted into 200-eV-wide bins. The phantom density cross section is shown, along with the initial guess ρ_0 supplied to the algorithm. This initial guess assumes the resulting image was recovered in 6 outer iterations, two with $\beta = 0.5$ and $\omega = 0.5$, then two with $\beta = 0.2$ and $\omega = 0.8$, then two with $\beta = 0.15$ and $\omega = 0.8$. All voxels with densities greater than 2.50 g/cm^3 were reassigned the density of aluminum metal, 2.702 g/cm^3, at every outer iteration. Despite the coarser energy bins and half as many spectra, the phantom density distribution is recovered with better fidelity than with filtered backprojection. The image does not suffer from artifacts of nonuniform backprojection. Perhaps the one disadvantage of the iterative method is the coarseness of the image that results from the larger voxel size. Iterative reconstruction requires a larger voxel size to keep the number of voxels in the image tractable. As more voxels are added the problem becomes poorly conditioned and the sizes of the matrices become unwieldy.

phantom

initial guess ρ_0

PWLS reconstruction
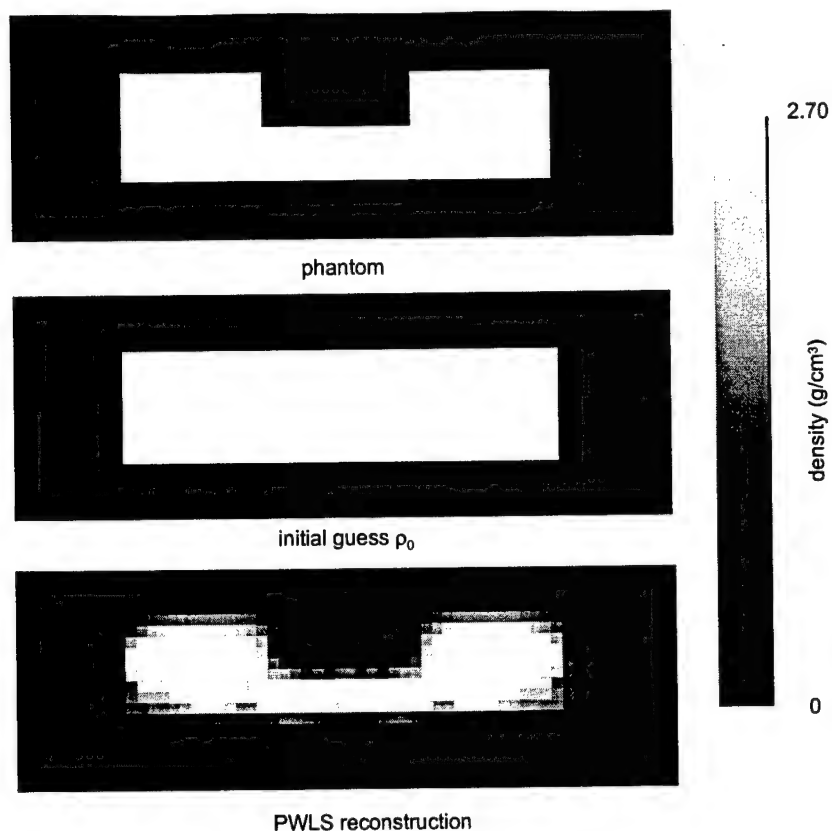
Figure 3-10. Results of the PWLS Iterative Reconstruction.

Several factors make iterative reconstruction the method of choice for the MCST system. The one-sided geometry limitation makes complete and uniform angular sampling impossible, and that is an enormous liability for filtered backprojection, as the artifacts in Figure 3-9 testify. These results were computed assuming the detectors had a wide field-of-view. The detectors acquired for the demonstration MCST system, however, have a relatively narrow field-of-view, providing far greater restrictions on the angular sampling. This restriction will be covered in greater detail in Chapter 4. The other major factor working against FBP is the large amount of data required. The demonstration system has poor efficiency and requires hours of measuring time to collect reasonably well-defined spectra. Any technique that reduces the amount of data required presents a distinct advantage.

Both the images reconstructed with perfect symmetry in the x-direction because of the symmetry in the sample, the symmetry in the acquisition configurations, and the symmetry in the ideal noise-free data sets. The addition of random noise to the data would produce an asymmetric data set, and the same image symmetry would not be expected.

IV. The Demonstration MCST System

The primary components of the demonstration MCST system are the high purity germanium (HPGe) detector array, the [109]Cd radionuclide source, radiation collimators, pulse-shaping electronics, data acquisition system, and the positioning system.

4.1. Fan Beam Collimators

The fan beam collimators are a critical part of the inspection system because their purpose is to narrow the inspection volume to a plane-like region of the sample. To do so, the collimators provide fan-beam collimation of the source illumination and of the detector field-of-view. The inspection volume is the region of space where the source illumination fan beam and detector field-of-view fan beam intersect. In practice, the fan beams will not be truly planar, but will exhibit some widening with distance from the source and detectors. This width is referred to as the tomographic slice thickness and represents the divergence of the beam from an ideal plane.

An important aspect of collimator design is selection of the collimating material. A material is needed which can be machined to the desired shape and has sufficient radiation attenuation to provide effective collimation. Many radiological imaging instruments take advantage of the exceptional attenuation properties of lead, but the choice of 88 keV gamma rays for the source prohibits the use of lead for this application. Lead has a K x-ray absorption edge just below the 88.03 keV source energy. Consequently, source gamma rays incident on a lead collimator have a high probability of removing a K-shell electron. The characteristic x-rays emitted as the resulting vacancy is filled would be indistinguishable from gamma rays scattered from the sample because the lead K_α x-ray is 75 keV. Furthermore, these x-rays would act as an extended and unwanted source. The energy of the K edge decreases with atomic number, but any alternative collimator material needs high enough Z to provide photoabsorption without low scatter. Steel, another popular collimating material made primarily made of iron (Z = 26), was investigated in some early experiments, but judged inadequate because of the appreciable scattering it produced. Copper (Z = 29), Cadmium (Z = 48), Tungsten (Z = 74), and Tin (Z = 50) were also considered. Tin was eventually selected because it provided the best combination of absorption, machinability, and cost.

Early attempts at collimator design for this system involved two parallel metal plates. The same two plates provided the source fan beam collimation and also restricted the detector field of view to a similar fan beam. This design concept is referred to as the horizontal plate design and is illustrated in Figure 4-1. A few experiments with this configuration revealed that the photons reaching the detector were overwhelmingly scattered from the collimating plates. Any photons that had scattered from the sample into the detectors were buried underneath the contaminating events from the collimator plates. The problem arises because large areas of the plates are directly exposed to source gammas and also lie in the detectors' field of view. The intensity of primary scatters from these areas can overwhelm the scatters coming from the sample. Some modifications on the design attempted to correct the problem. Sections of the plates judged inessential for the collimation were removed, and the detectors were shielded from those areas of the plates nearest the source. Nevertheless, it remained difficult to discern signal from the sample from the background of signal from the collimators. Although these preliminary designs were constructed from steel plates, there was little reason to believe that tin would provide a significantly better signal. Experiments showed that, although tin provided much greater attenuation for a given thickness, the intensity of radiation scattered from tin was reduced by less than a factor of 10. It became evident that a new design was needed. A primary objective of the new design would be the minimization, if not elimination, of collimator area exposed simultaneously to source photons and the detector field of view.

The next design iteration is referred to as the vertical plate design and consists of two pairs of vertical tin plates with lengthwise continuous horizontal apertures drilled out. The first pair of plates collimates the source to a fan beam volume. The second pair of plates reduces the detector field of view to a fan beam volume. Figure 4-2 illustrates the positions of these collimator plates, as well as typical source,
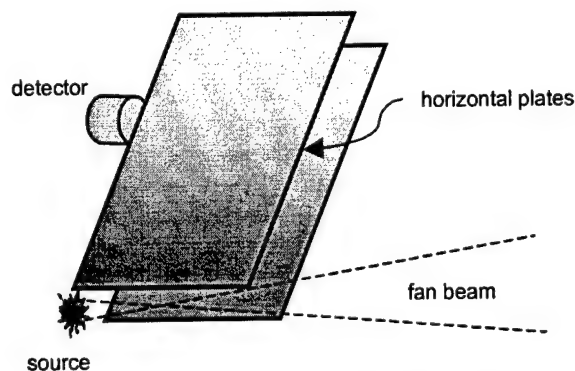

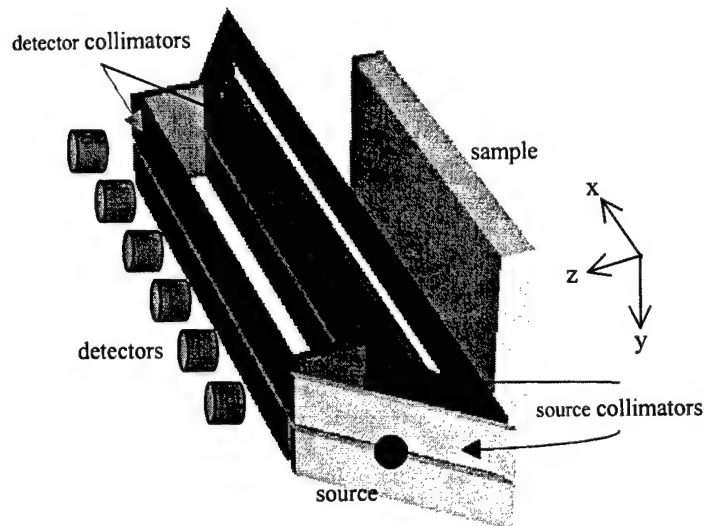Figure 4-1. Horizontal Plate Collimators. An ill-conceived concept

Figure 4-2. The Vertical Collimator Plates. This perspective drawing was rendered from the MCNP input file using SABRINA (Van Riper, 1993). Possible sample and detector locations are shown.

sample, and detector locations. Additional material shields the detectors from direct source gammas. The plates are held in place above and below by steel frames. Both sets of collimators contain 0.1-inch apertures. Another longer tin plate has a 3/8-inch aperture. The purpose of this plate is to further collimate the source beam, but the aperture is wide enough that the tin is not exposed to the narrower detector fan beam. Ideally, nothing should lie within the intersection of the source and detector fan beams except the sample. More detailed drawings of the final collimator design are given in Appendix A.

4.1.1.   Calculation of Tomographic Slice Thickness

To aid in the design of this collimator assembly, an algorithm developed in Mathematica can calculate the intensity of the source and detector fan beams at any position in the inspection volume. The inspection volume is defined by the intersection of the source and detector fan beams. Parameters specified by the user include the positions of all components, including a source and single detector, plate thickness, and aperture widths. The code produces a schematic drawing of the component positions as a visual verification that the user-defined geometry parameters are correct.

Barrett and Swindell show the equivalence between two separate apertures, like the ones in the pairs of collimator plates, and a single bore collimator with bore length equivalent to the distance between the apertures (Barrett and Swindell, 1981). The notebook uses their derivation for the point response of such a collimator, but because of the non-symmetric configuration of the collimator plates, the equivalent bore lengths vary with position in the fan beam. The equivalent source bore and detector bore length must

therefore be calculated for every point in the inspection region. The notebook then determines if the particular point lies in the umbra or penumbra region of the source fan beam, and likewise for the detector fan beam. The intensity of detector response is weighted accordingly. A simple correction to account for septal penetration is used which simply decreases the modeled bore length by one mean free path in tin (Barrett and Swindell, 1981)

The user specifies an inspection depth defined by a plane normal to the z-axis (see the coordinate system shown in Figure 4-2). The notebook calculates how the fan beam intensity varies at with x and y across that inspection depth. Figure 4-3 provides an example output for a typical inspection. The notebook provides a visual aid to ensure that the geometry is properly defined. It shows the locations of source, detector, inspection depth, and collimator plates in a simple drawing. The other output shows the intensity of the fan beam plotted as a function of x and y position (in cm) at the inspection depth shown. Note that the tomographic slice thickness should be considered less than 1 cm because its intensity is very low at y =
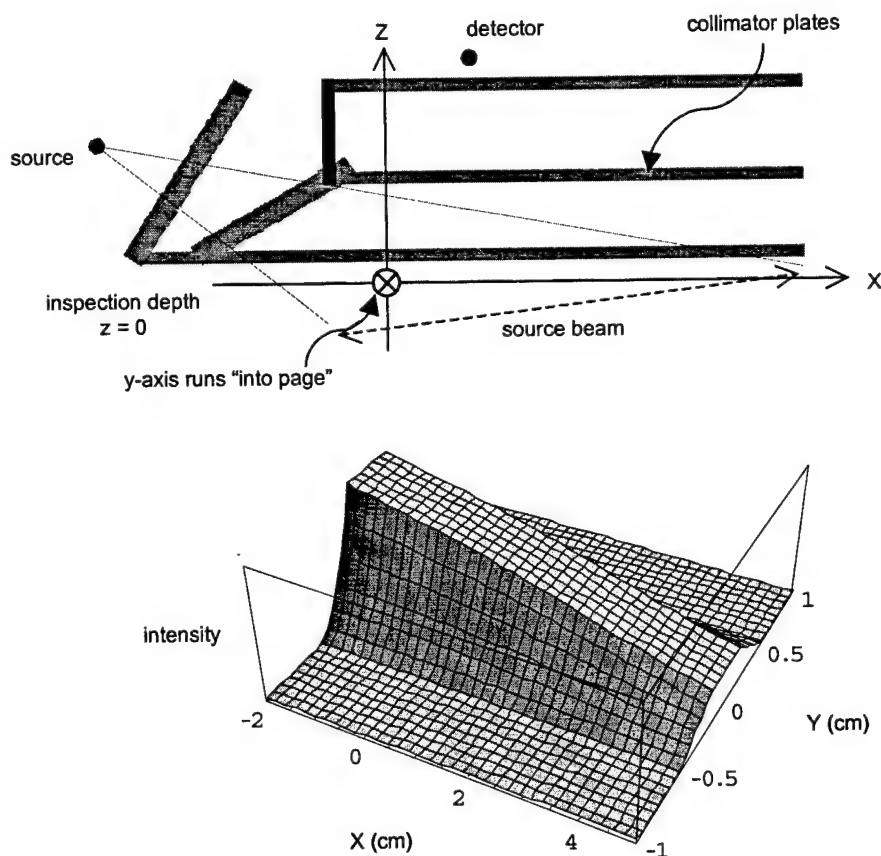

Figure 4-3. Example Output From The Mathematica Fan Beam Model. The axes units are cm.

4-4

±0.5 cm. This tomographic slice intensity profile is typical of the eventual collimator design that was adopted. This Mathematica code was a valuable tool in designing the collimators.

4.1.2.   MCNP Modeling of Collimator Assembly

Monte Carlo simulations were used to study the viability of the vertical plate design, particularly to ensure that the prevalence of detected photons scatter from the sample and not the collimator components. The cell flagging option in MCNP Version 4b tallied the contributions to detectors from cells representing the sample and components of the collimator assembly (LANL, 1997). The simulated sample was 2 cm-thick aluminum. The source and detectors were placed in positions typical of those used in the demonstration MCST system. MCNP binned each count according to the component in which the last collision occurred in that particle history. The drawing in Figure 4-4 labels the components that contributed the highest number of scores to the detector tally. This drawing and Figure 4-2 were generated by the RSIC software package SABRINA from the MCNP input file (Van Riper, 1993). Although not shown in Figure 4-4, the steel framework supporting the tin collimator plates was included in the geometry. Part B of Figure 4-4 plots the number of detector scores for each component. Unlisted components, including the steel framework, made negligible contributions.

Results of these MCNP simulations provided evidence that the collimator design was sound, at least from the aspect of increasing the prevalence of photons scattered from the sample and reducing the intensity of those scattered from parts of the collimator. The results indicate that for the geometry modeled, 99.6 percent of the detected photons experienced their last collision in the sample.
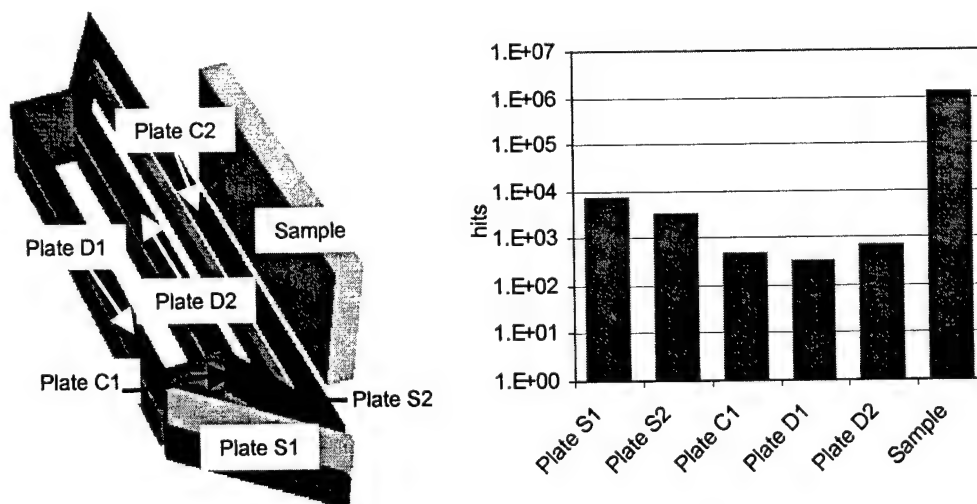

Figure 4-4. MCNP Modeling of Scattering Contributions from Collimator Components.

MCNP provides a good tool for modeling the intensity of the source fan beam within the imaging region. The algorithm in ScatGram computes the source beam intensity at any point in the imaging region assuming an isotropically emitting point source. Simulating an extended source with ScatGram involves simulating multiple point sources. The effects of the tin collimator plates and the tin source container are neglected in the ScatGram algorithm. The tin source container, however, does contain an aperture that may mask some of the source volume at certain positions in the imaging region. The apertures in the collimator plates may also partially mask the source at certain positions in the imaging region because the slits do not extend to the ends of the plates. MCNP has the capacity, however, to simulate the precise geometry of the collimator plates, the source, and the source container. An MCNP input deck was constructed to model the source, source container (including the aperture), and collimator plates with high fidelity. The source container was placed in a configuration typical of that used in the demonstration system. MCNP tallied the flux of photons across a relatively small surface and that surface was moved along the x-axis as shown in Figure 4-5. The variation in the intensity of the photon flux across the tally surface provides an estimate of the source beam intensity as a function of x. Figure 4-6 compares the source beam intensity provided by MCNP to the intensity calculated according to the ScatGram model. The two curves are normalized so the source beam intensity is 1.0 at x = 0.0, the center of the intended imaging region. The MCNP tally falls off below x = -4.0 because the source is partially obscured by the apertures, and ScatGram does not fall off because it does not take this effect into account. The results match more closely in the positive x direction. These results verify that the ScatGram models the source beam intensity reasonably well, and identifies the regions of the image plane that should be avoided.
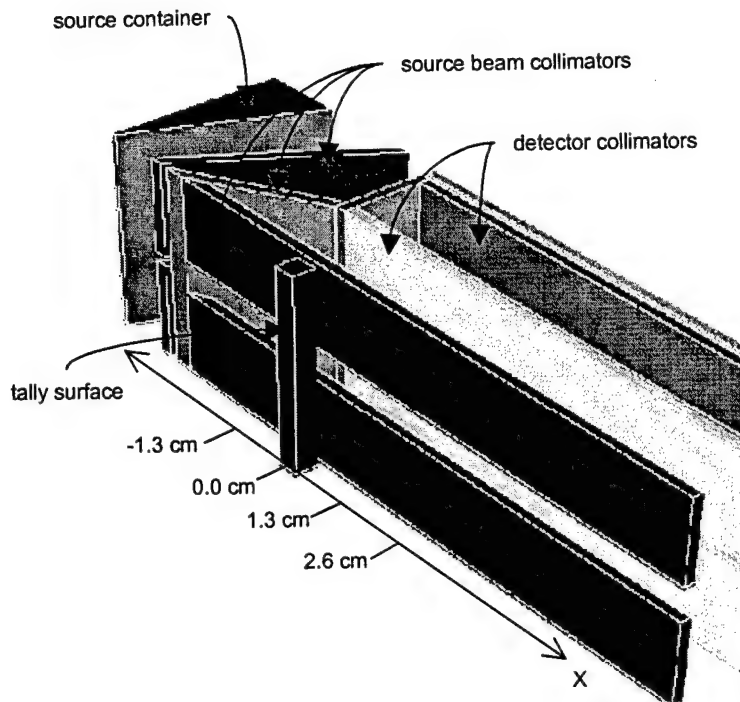
Figure 4-5. Investigating the Source Beam Intensity.
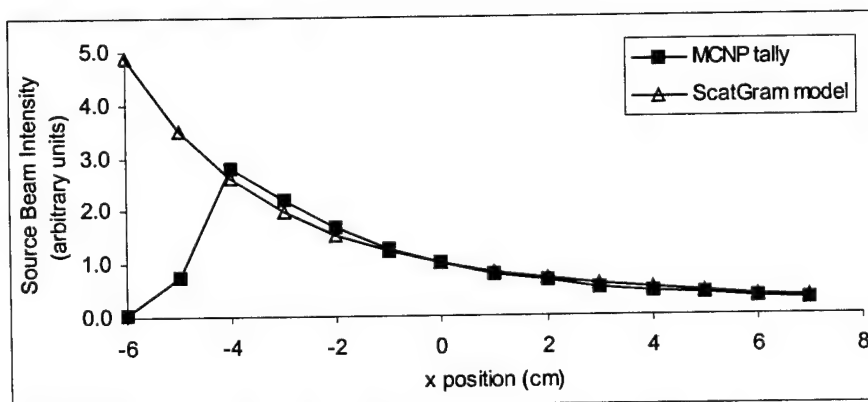
Figure 4-6. Variation in Source Beam Intensity with Position.

4.2.   HPGe detector array

The high purity germanium (HPGe) detector array consists of 6 detector elements, each of which is a planar p-type intrinsic germanium crystal with an active diameter of 10 mm and active depth of 10 mm, though the size of the complete crystal is somewhat larger. The elements are arranged in a linear array with a 9.5-mm center-to-center spacing and housed in a single aluminum cryostat with a diameter of 14 cm. Princeton Gamma Tech, Inc. of Princeton, NJ manufactured the detector. The cryostat endcap contains six circular holes of 10.69-mm diameter behind which the elements are located. A beryllium entrance window

covers each hole. The distance from the window to the detector crystal is 5.94 mm. Figure 4-7 shows the cryostat dimensions and how a germanium crystal is positioned within the cryostat.

To reduce the effective size of each detector element, each element is masked off at its beryllium window with a tin mask. The mask is a 0.125" thick tin sheet containing six tapered holes of diameter 0.20" at the entrance window side and 0.63" on the outer side. This tapering is designed to reduce the effective detector area by nearly a factor of 2.5 to provide finer sampling while not further restricting the field of view beyond the limitations already imposed by the endcap holes. Figure 4-8 provides an illustration. Another important function of this detector mask is that it shields the aluminum endcap from exposure to radiation. The low-Z material in the endcap is prone to scatter gamma rays that might be subsequently recorded as noise in the detectors. Experiments indicated that the presence of the tin mask improved the peak-to-total ratio significantly.
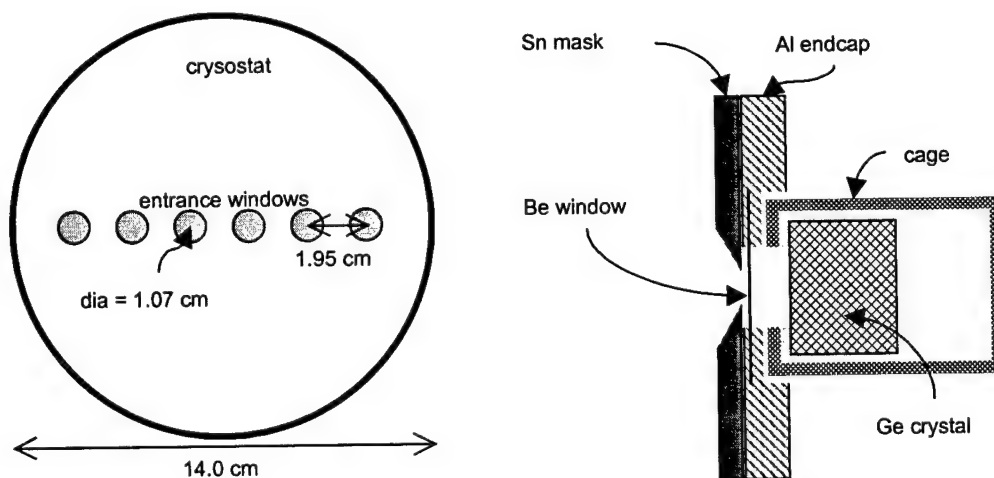

Figure 4-7. Critical Detector Array Dimensions. Left: The dimensions of the cryostat and the entrance windows. Right: a cutaway perspective showing the position of a detector crystal behind the endcap. The Tin mask is also shown.
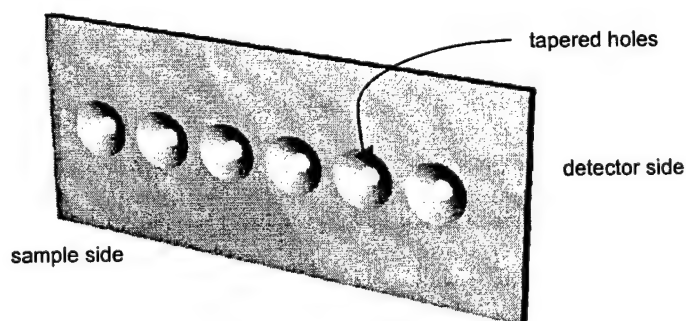
Figure 4-8. Tin Endcap Mask

4.3. Data Acquisition

Signals from the detector are processed with analog pulse shaping electronics and digitized in a multichannel CAMAC standard CAEN C420 ADC. Figure 4-9 gives a schematic of one detector's signal processing. A Wiener, Plein & Baus CC16 CAMAC crate controller interfaces the ADC to a personal computer running Weiner's multiparameter data acquisition software named Multi. Unfortunately the use of analog pulse-shaping electronics hampered the accuracy of the system as a whole because the amplifiers tended to drift in calibration over many hours of data acquisition. The need to stop periodically for recalibration of the system also made it impossible to achieve the level of automation that the computer-controlled positioning table was intended to provide.
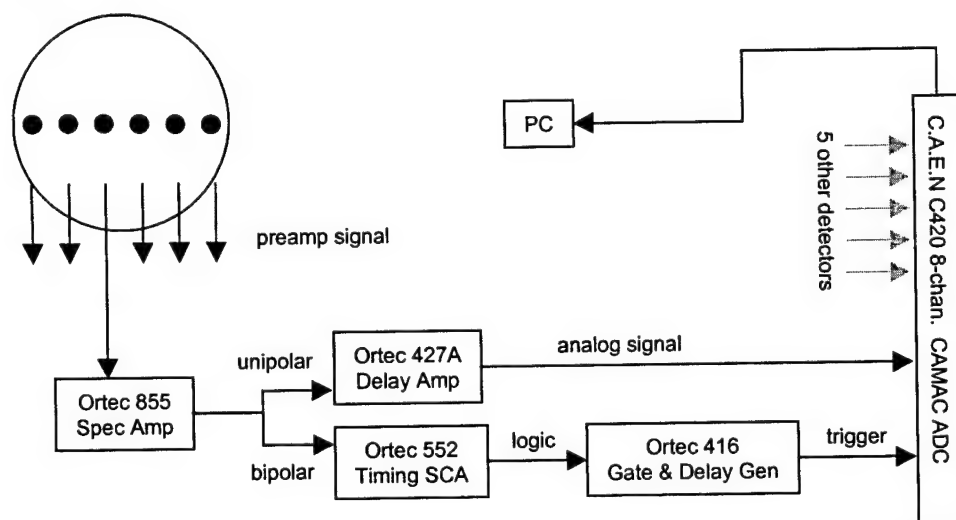
Figure 4-9. Signal Processing for One of Six Channels. Signal path for the other five channels is identical.

Care was taken to characterize the detector array response at the energies of interest in this project. The detector characteristics studied included intrinsic peak efficiency, energy resolution, and peak-to-total ratios. Efficiency and peak-to-total ratios were studied as a function of the angle of incident radiation and a function of energy.

4.4. Detector Response

4.4.1. Energy Resolution

The total overall FWHM resolution of the detector system is the quadrature sum of individual sources of fluctuation in the signal chain. The predominant components are the statistical fluctuation in the

number of charge carriers generated for a fixed incident energy, and the fluctuations due to electronic noise (Knoll, 1989).

$$\left(\text{FWHM}\right)^2_{\text{system}} \approx \left(\text{FWHM}\right)^2_{\text{statistical}} + \left(\text{FWHM}\right)^2_{\text{noise}} \qquad (4\text{-}1)$$

Replacing the detector with a precision pulse generator to eliminate the statistical term provides an estimate of the noise contribution. This exercise reveals that the system resolution is dominated by the statistical contribution and that the noise contribution remains independent of the signal amplitude. The statistical fluctuations result from the Poisson-distributed number of charge carriers generated in the detector crystal per event. Since the variance in this distribution depends on the mean number of particles generated, the system resolution is energy-dependent. Figure 4-10 shows the resolution measured in the laboratory of each of the six detectors in the array. The resolutions were measured at 22.16 keV (^{109}Cd), 59.54 keV (^{241}Am), 88.03 keV (^{109}Cd), 122.06 keV (^{57}Co), and 136.48 keV (^{57}Co). A second-order polynomial fit to these data points constitutes the $\Delta E(E)$ detector resolution correction in ScatGram.

All the resolutions are comparable except for detector 6, which has much poorer resolution at the lower end of the energy range. The problem probably stems from leakage current. All semiconductor detectors will show some conductivity driven by the extreme bias, -1500 V in this case, applied across the active volume, resulting in a steady-state leakage current. Random fluctuations that occur in this current leakage current provide a contribution to the noise term of Equation (4-1). It is likely that detector 6 has a greater leakage current than the other five resulting in extra electronic noise.

A more extreme problem develops when gasses that intrude into the cryostat condense on the cold
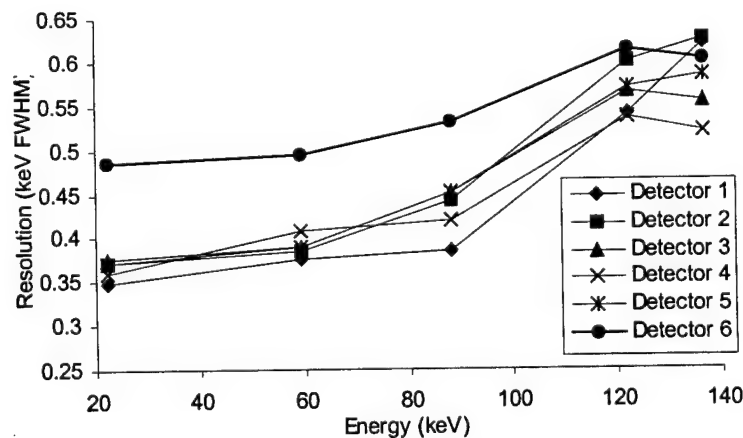

Figure 4-10. FWHM Energy Resolution of the Detector Array.

detectors. The condensate can provide a breakdown current path across the face of the detector crystal, destroying the resolution with an enormous electronic noise term. This particular detector array was returned to the manufacturer after four of the six detectors developed a breakdown current problem. Even after the repair, detector 2 has been known to develop this problem periodically.

4.4.2. Efficiency

The relative peak efficiency of each detector was measured at 22.16 keV (^{109}Cd), 30.80 keV (^{133}Ba), 59.54 keV (^{241}Am), 80.10 keV (^{133}Ba), 88.03 keV (^{109}Cd), 122.06 keV (^{57}Co), and 136.48 keV (^{57}Co). These efficiencies were determined with the radionuclide sources positioned on the detector axis, meaning they were aligned directly in front of the detector windows to achieve maximum intrinsic efficiency. Figure 4-11 shows the relative efficiency of each detector as a function of energy. Second-order polynomial fits to these data points provide the efficiency corrections $\varepsilon(E)$ for the ScatGram code, however the two high-energy points at 122.06 keV and 136.48 keV were not included in the polynomial fits because they are not relevant for the energy range considered and would only cause additional error in the fits.
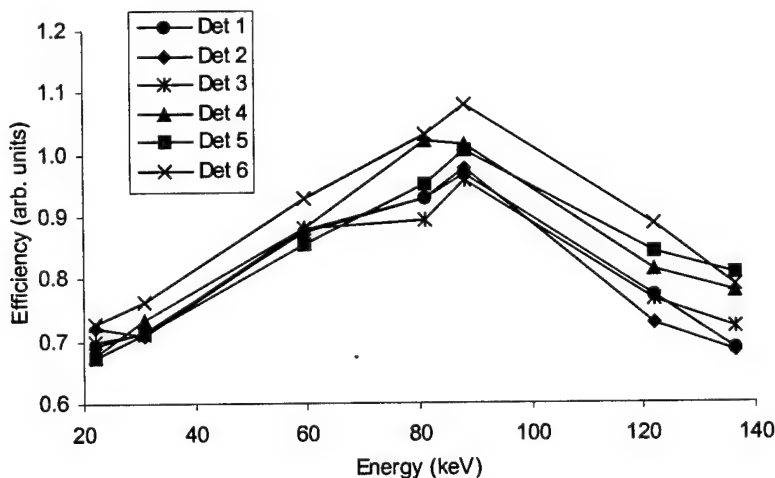
Figure 4-11. Relative Peak Efficiency of the Detectors. The values are normalized so the mean efficiency at the source energy 88.03 keV is unity.

4.4.3. Detector Response as a Function of Incident Angle

The position of the germanium crystals within the cryostat (as illustrated in Figure 4-7) and the endcap's circular entrance windows combine to significantly limit each detector's field-of-view. The aperture created by the circular entrance window or tin mask, if it is in place, constrains each detector's

field of view when combined with the 6 mm offset from the crystal to the beryllium window. The setup is problematic because the projection of the aperture onto the detector crystal varies significantly with the position of the radiation source. Figure 4-12 illustrates this concept. For a source directly on the detector axis, the projection of the aperture passes through the center of the detector, providing a long pathlength through the active volume along which the incident radiation is likely to be fully absorbed. This condition provides good efficiency and a good peak-to-total ratio. On the other hand, radiation incident at an oblique angle creates an aperture projection passing through only a corner of the active volume. The short pathlength through the active volume makes it much less likely that radiation will be fully absorbed, leading to lower efficiency and a reduced peak-to-total ratio. Furthermore, incomplete energy deposition is more likely to occur due to scattering from other components of the detector array exposed at these angles, such as the cage or the inactive regions of the germanium crystal.

Clearly placing the aperture much closer to, if not in contact with, the active detector volume as shown in Figure 4-12 under improved configuration could reduce the deleterious effects of the aperture projection. Such a configuration would probably involve placing the mask within the cryostat and replacing the round endcap holes with a long, continuous slit. The improvement would cause the projection of the aperture onto the face of the crystal to change minimally with the incident angle. The pathlength would also vary less severely with angle, leading better efficiency and cleaner spectra over a wider range of angles. A detector crystal with a greater radius relative to its depth would further improve the pathlength for oblique angles. The current design is clearly not ideal for the MCST application because it runs counter to the fundamental MCST concept of using wide field-of-view detectors to interrogate extended regions of the sample simultaneously.
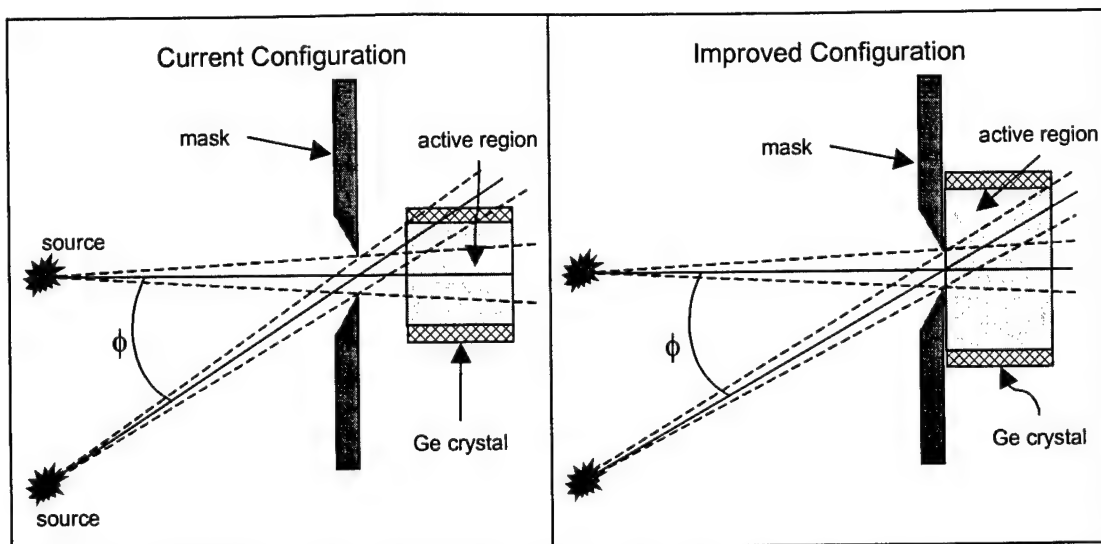
Figure 4-12. Current and Improved Detector Configurations. The improved configuration is a suggestion for improving detector response at oblique angles.

Yet another problem arises as a result of the window-to-detector distance. It is possible for radiation to enter through one detector's aperture at a sufficient angle to intercept a neighboring detector and be recorded there. This can cause significant position error during imaging because it is assumed that any events recorded in a particular detector are photons passing through its aperture. Instead the position of the aperture through which the radiation passed is ambiguous. This effectively limits the size of the sample that can be used for the demonstration MCST system to several centimeters in width. Longer samples would require masking off the aperture of some detectors. Eliminating the aperture-to-crystal distance will solve this problem. An improved configuration may also include shielding around the circumference of the detector crystals to ensure that only radiation passing through the correct aperture is detected.

4.4.4. Peak Efficiency as a Function of Incident Angle

To investigate the peak efficiency as a function of angle, ^{109}Cd and ^{241}Am radionuclide sources were placed at various positions relative to detectors 2, 3, and 5 and the intensity of the 88.0 keV (^{109}Cd) and 59.5 keV (^{241}Am) lines was observed. The purpose of this exercise was to measure $\eta(\phi)$ described in Chapter 2 for inclusion in the ScatGram code. Figure 4-13 shows how the peak intensity varied with angle. The angle is measured between the normal to the aperture provided by the tin mask and a vector from the source to the center of that aperture. The data from the separate series of measurements are combined here as mean values for each value of ϕ and normalized so the efficiency at 0 degrees is unity. Each data point
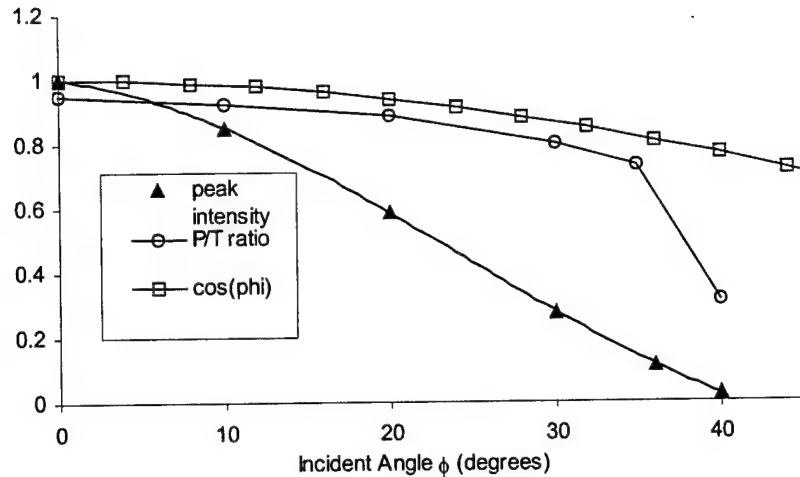
Figure 4-13. Peak Intensity and Peak-to-Total Ratio as a Function of Incident Angle.

is corrected for the source distance from the aperture. A least-squares quadratic fit is drawn through the data. This fit is the function used in ScatGram for $\eta(\phi)$. The energies used (59.5 keV and 88.0 keV) effectively bound the energy range of interest here, but there is no consistent or appreciable difference between them with respect to the behavior of the peak intensity with angle. This result is important because it makes viable the assumption of seperability between $\varepsilon(E)$ and $\eta(\phi)$ discussed in Chapter 2.

The severity of the oblique angle effects are apparent when one considers the type of peak intensity response that could be expected from a detector with a mask placed very near the active volume. If the detector is large enough compared to the mask aperture, the pathlength should always be large enough to provide nearly 100 percent absorption of the incident gamma at these energies. In such a configuration one could reasonably expect the efficiency due to oblique angle to fall off as the cosine of ϕ, the angle between the normal and incident vector. The $\cos(\phi)$ curve is plotted in Figure 4-13.

4.4.5. *Peak-to-Total as a Function of Incident Angle*

The same set of measurements used to characterize $\eta(\phi)$ provided the data needed to investigate the peak-to-total ratio as a function of ϕ. As expected, the ratio of peak counts to total counts decreases as incident angle increases. The peak-to-total ratio decreases at the oblique angles because all the possible interaction positions within the crystal are close to a crystal surface. It is much more likely that secondary radiation like scattered photons will escape the detector from these positions. The peak-to-total ratio decreases only slightly from 0 to 35 degrees, after which it falls precipitously. Figure 4-13 shows the average measured

peak-to-total ratio for each value of ϕ. It is noteworthy that at angles where the peak-to-total ratio becomes dismal, the total efficiency is also low.

4.5. Other Components

4.5.1. ^{109}Cd Radionuclide Source

The ^{109}Cd source had an initial activity of 75mCi when delivered on January 1, 1998. Isotope Products Labs of Burbank, CA manufactured it. The radioactive element is Cadmium metal deposited on a ceramic matrix. It is sealed within a stainless steel capsule (IPL model 3205) with a 0.04" beryllium window. The diameter of the radioactive region is 5.08 mm.

For safety the capsule is housed within a special tin shielding that was designed for the MCST system. The shielding has a tin door that swings open to expose the source when it is installed in the system. When the door is secured closed the source is safe to handle by personnel. The door can be manipulated from behind so that exposure to the hands and whole body is minimized.

Unfortunately, the source was delivered with a significant contamination by the radionuclide ^{153}Gd which emits gammas at 69.7 keV (2.42%), 83.4 keV (0.21%), 97.4 keV (29.5%), and 103.2 keV (21.1%). Figure 4-14 shows a spectrum collected from the source through 0.25" of tin shielding. The difference in attenuation between the three energies amplifies the intensity of 97.4 keV and 103.2 keV counts relative to the 88.0 keV counts. This spectrum was collected on a large coaxial HPGe detector so the resolution is lower but efficiency is greater than that of the 6-element planar detector array. Correcting for the attenuation using cross section data (Berger, 1988) reveals that at energies of 88 keV and higher the ratio of contaminant gammas to ^{109}Cd gammas emitted by the source is 2.1 percent. The total activity of ^{153}Gd is 0.15% the activity of ^{109}Cd. The source does not meet the spectral purity specifications required from the supplier, which stated that radioactive impurities must emit gamma rays with intensities less than 0.2% of the 88 keV gamma ray line intensity. Time constraints made the return and replacement of the source impractical. The half-life of ^{153}Gd (242 days) is shorter than that of ^{109}Cd (1.27 years) so the spectral purity will improve with age as shown in Figure 4-14, where spectral purity is measured as the ratio of 88 keV emissions to total emissions at or above 88 keV.
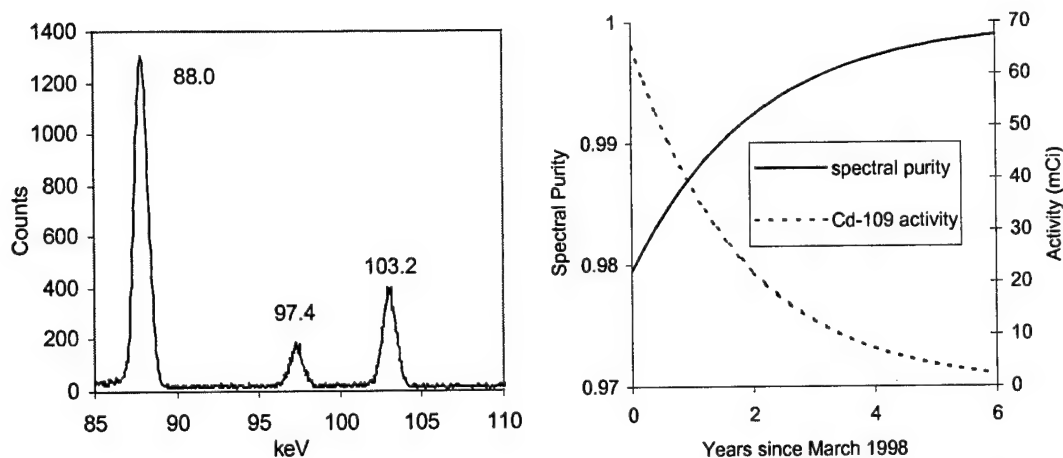
Figure 4-14. Spectral Purity of the ^{109}Cd Source. Left: Source emissions collected through 0.25" of tin. Right: Spectral purity and activity versus time.

4.5.2.   Positioning System

The purpose of the positioning system is to position the source and phantom relative to the detector array with reasonable accuracy. The primary component of the positioning system is an automated linear translation table that moves the source and sample horizontally while the detector array stays stationary. This allows translation of a consistent source and phantom geometry to simulate an array with more than six elements. The table is a Velmex Unislide model driven with a Velmex NF90 stepper motor controller interfaced to a personal computer. A code written for the MCST demonstration system allows the user to program, via the computer, predetermined displacements of the table at predetermined times. This works by sending commands to the stepper motor controller through the computer's serial port. There are 4000 steps per centimeter, so the precision provided by the translation stage is 0.00025 cm – much better than required considering the resolution of the imaging system.

The translation table is mounted on a heavy-duty laboratory jack. Moving the jack up and down provides vertical positioning. This adjustment is made less frequently than horizontal movements, and is really only needed to align the collimators, source, and phantom vertically with the detector array.

One intended purpose of the positioning system was to provide automated repositioning during an extended data acquisition. Later the data would be sifted to separate those events recorded at different positions. An unexpected complication, however, resulted from the instability of the analog pulse-shaping electronics purchased for this system. They exhibit significant gain drift over the period of hours during

which each spectrum is collected. That made it necessary to stop the acquisition periodically to recalibrate, and the intended automation was not needed.

4.5.3. Radiation Shielding

For safety of personnel, the detectors, positioning system, and collimators are housed in a shielded box constructed of a layer of 0.125" thick tin surrounded by a layer of 0.150" thick steel. When the source is exposed within the box, no dose above background levels is measured. Pass-throughs are provided for the cryostat and cables.

4.5.4. System Photographs

Figures 4-15 through 4-17 provide photographs of the demonstration MCST system with major components labeled.
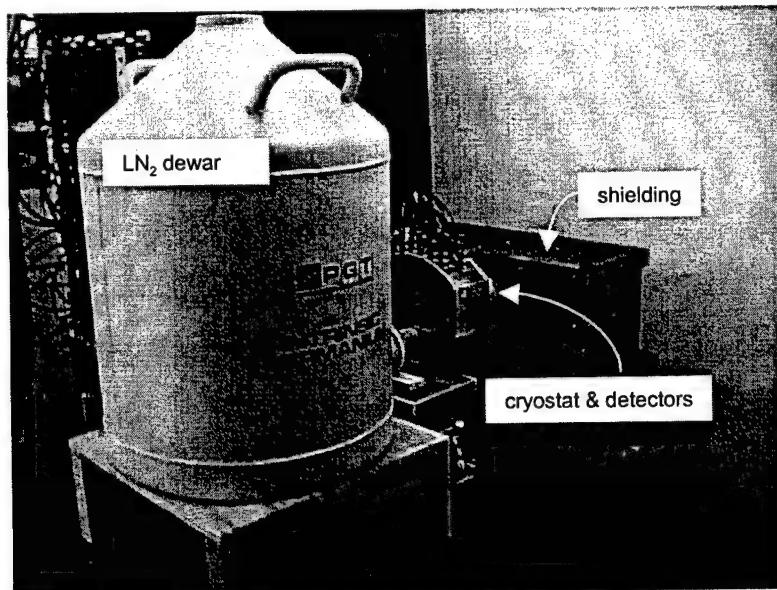
Figure 4-15. MCST System.
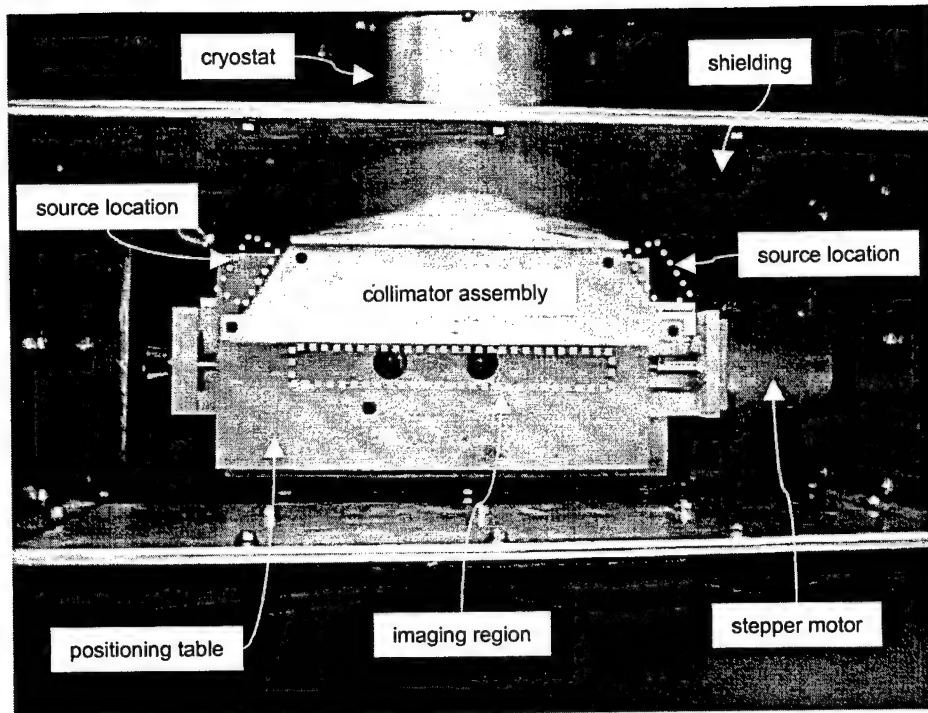
Figure 4-16. MCST System--Top View With Shielding Open.
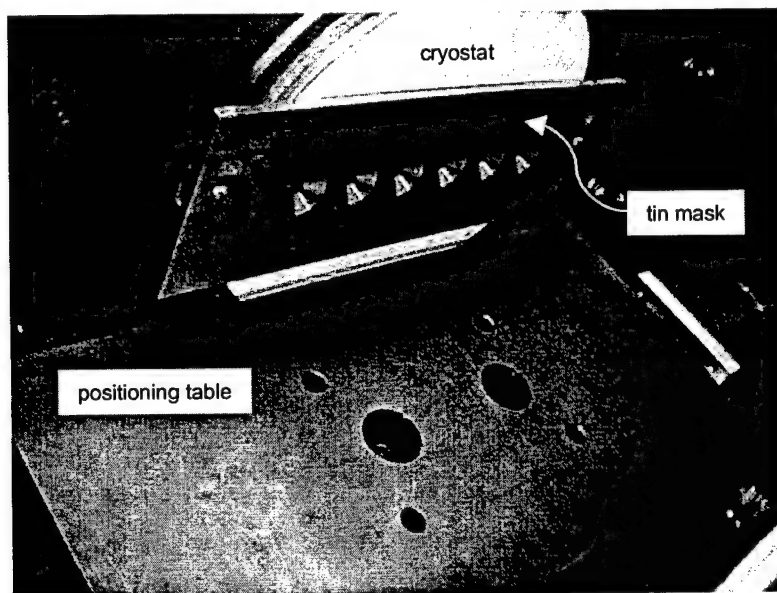
Figure 4-17. MCST System--View from Within the Shielding.

4.6. Angular Uncertainties in the Demonstration MCST System

Distortion in the reconstructed image results from ambiguity in determining the scattering angle and scattering location for any detected photon. Geometric factors such as the size of the source and the size of the detector aperture spread the idealized isogonic line for a given scattering angle into an isogonic region as shown in Figure 1-4, increasing uncertainty in the scattering location for any precisely known

scattering angle θ. Energy factors such as Doppler broadening and detector energy resolution lead to an uncertainty in scattering angle for any precisely known scattered photon energy E'. This creates uncertainty in identifying the isogonic region that the photon scattered from. The relative importance of these uncertainties is not uniform within the imaging region, and not consistent between detectors. However, the imaging region is long (in the x-direction) and shallow (in the z-direction) as shown in Figure 4-16, and the uncertainties are dependent most strongly on the x-position. To investigate the relative importance of the angular uncertainties, a particular system geometry must be established and each detector must be considered individually. Because of the strong x-dependence, it is most useful to consider the variation with position along the x-axis within the imaging region while fixing the z-position in the center of the image.

Consider a highly idealized MCST system that uses a point source and point detector with perfect energy resolution. In this idealized system there is no Doppler broadening. Compton scattering physics follows the Compton equation, Equation (1-1), to establish a one-to-one correspondence between the scattered photon energy E' and θ. Under these conditions any scattering location (x_S, z_S) in the imaging region exactly defines an incident and a scattered photon trajectory, and exactly defines a scattering angle θ_C. The Compton equation and the assumption of perfect energy resolution also mean that the scattered photon energy E' is precisely known. The angular uncertainties in a realistic system can be considered deviations from this ideal system. For any scattering location (x_S, z_S) the geometric factors will cause uncertainty in the photon trajectories as shown in Figure 4-18. The angular uncertainty about the incident photon trajectory caused by the extended source is labeled $\Delta\theta_S$. The angular uncertainty about the scattered photon trajectory caused by the extended detector aperture is labeled $\Delta\theta_d$. The energy factors will cause uncertainty in the scattering angle θ_C as shown in Figure 4-19. The angular uncertainty about the scattering angle caused by the imperfect energy resolution of the detector is labeled $\Delta\theta_E$ and the uncertainty about the scattering angle caused by the Doppler broadening is labeled $\Delta\theta_{DB}$. In both Figures 4-18 and 4-19, the sizes of the components have been exaggerated to make the illustrations more legible. All these angular uncertainties contribute to the error in properly locating the correct scattering point (x_S, z_S) from a given detected event.
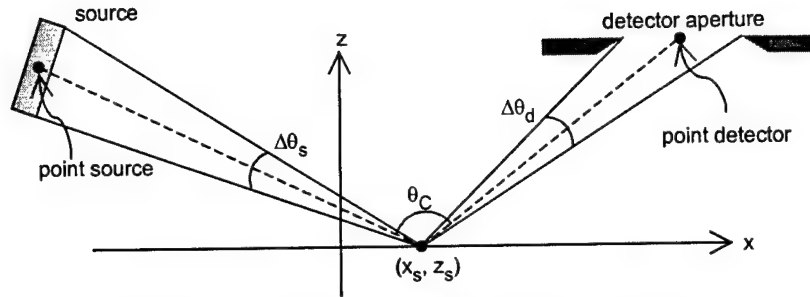
Figure 4-18. Geometric Factors in Angular Uncertainty.
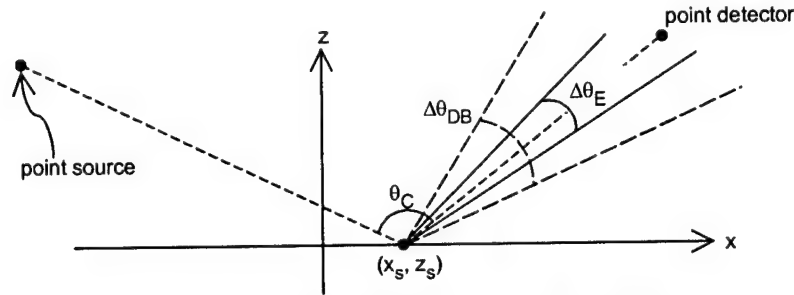
Figure 4-19. Energy Factors in Angular Uncertainty.

Computing the geometric uncertainties is simply a matter of taking the dot product of the trajectory boundaries shown in Figure 4-18. This technique gives an extreme estimate of $\Delta\theta_S$ and $\Delta\theta_d$ because the most extreme trajectories are used. Relative to each other, the values of $\Delta\theta_S$ and $\Delta\theta_d$ provide a fair comparison.

To compute $\Delta\theta_E$, the energy-dependent energy resolution of the detector must be known. The uncertainty $\Delta\theta_E$ is computed as

$$\left(\Delta\theta_E\right)^2 = \left(\frac{d\theta}{dE'}\left(E_C\right)\right)^2 \left(\Delta E\left(E_C\right)\right)^2 \tag{4-2}$$

where $d\theta/dE'$ is computed from Equation 1-1. Every position (x_S, z_S) will have a central angle θ_C as illustrated in Figure 4-18. The derivative of Equation (4-2) is evaluated at the energy $E'=E_C$ given by the Compton equation for angle θ_C. The FWHM of the photopeak at energy E_C, denoted $\Delta E(E_C)$, is used as a measure of the detector resolution.

To compute the angular uncertainty due to Doppler broadening $\Delta\theta_{DB}$ at a scattering position (x_S, z_S), the extent of the Doppler broadening must be quantified. The FWHM of the Doppler-broadened angular distribution of gammas that scatter with energy E_C provides an estimate of this angular uncertainty.

However, the FWHM criterion underestimates the severity of the Doppler broadening because the Compton profile of aluminum is heavily weighted in the tails as shown in Figure 1-11. The standard deviation of the distribution is larger relative to its FWHM than it would be for a Gaussian distribution. Nevertheless, this criterion is convenient and has been used by others to quantify Doppler broadening (Matschenko, 1989; Ordonez, 1997) with the acknowlegement that the broadening is actually more severe than this criterion might suggest. The component momentum p_z at which the aluminum Compton profile falls to half its maximum value is $p_z = \pm 0.5411$. Substitution into Equation 1-9 yields

$$\pm 0.5411 = \frac{137}{511} \frac{E_0 E_C (1 - \cos\theta) - 511(E_0 - E_C)}{\sqrt{E_0{}^2 + E_C{}^2 - 2E_0 E_C \cos\theta}} \tag{4-3}$$

then solving for θ leads to $\Delta\theta_{DB}$. This parallels Matschenko's calculation for the FWHM energy broadening about $p_z = 0$ (Matschenko, 1989), but solves for the broadening in angle rather than energy.

To investigate the angular uncertainties in the demonstration MCST system, a typical system configuration will be considered. Figure 4-20 provides an illustration of such a configuration showing a typical source configuration and three typical detector positions. The imaging region is centered at the origin of this coordinate system. The [109]Cd source with a 2.54 mm radius is rotated 71 degrees from horizontal and the center is positioned as indicated. Corrected for septal penetration, the detector apertures have a radius of 3.2 mm.
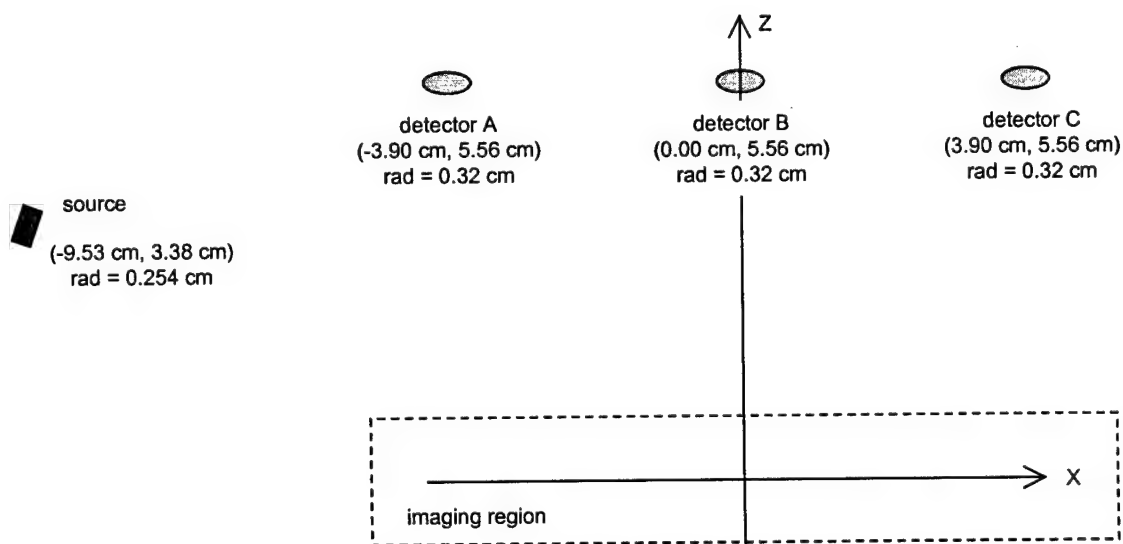
Figure 4-20. Configuration to Investigate Angular Uncertainties.

Figure 4-21 shows the angular uncertainties for each of the three detectors. They are evaluated along z=0 and plotted as a function of x. The plot for $\Delta\theta_S$ is labeled "source," $\Delta\theta_d$ is labeled "aperture," $\Delta\theta_E$ is labeled "E resolution" and $\Delta\theta_{DB}$ is labeled "Doppler." Comparing the two geometric uncertainties reveals that in most circumstances the aperture size has a greater effect than the size of the source, except in regions near the source and distant from the detector. This suggests that the source could be placed closer to the sample to improve efficiency, but that would result in less uniform illumination of the sample. Alternatively, the radius of the detector aperture could be reduced, but that would come at the expense of signal intensity. In the current configuration, however, the size of the source does not affect the image resolution as significantly as the size of the detectors does.

Comparing the energy-dependent uncertainties $\Delta\theta_E$ and $\Delta\theta_{DB}$ reveals that the Doppler broadening is always responsible for a greater angular uncertainty than the detector's energy resolution by a factor of at least 1.5, even with the conservative FWHM criterion used to quantify the Doppler broadening. Thus it can be concluded that the energy resolution of the planar HPGe detectors is certainly adequate for the application.

Figure 4-21. Angular Uncertainties in the Demonstration MCST System.

V. Experimental Results

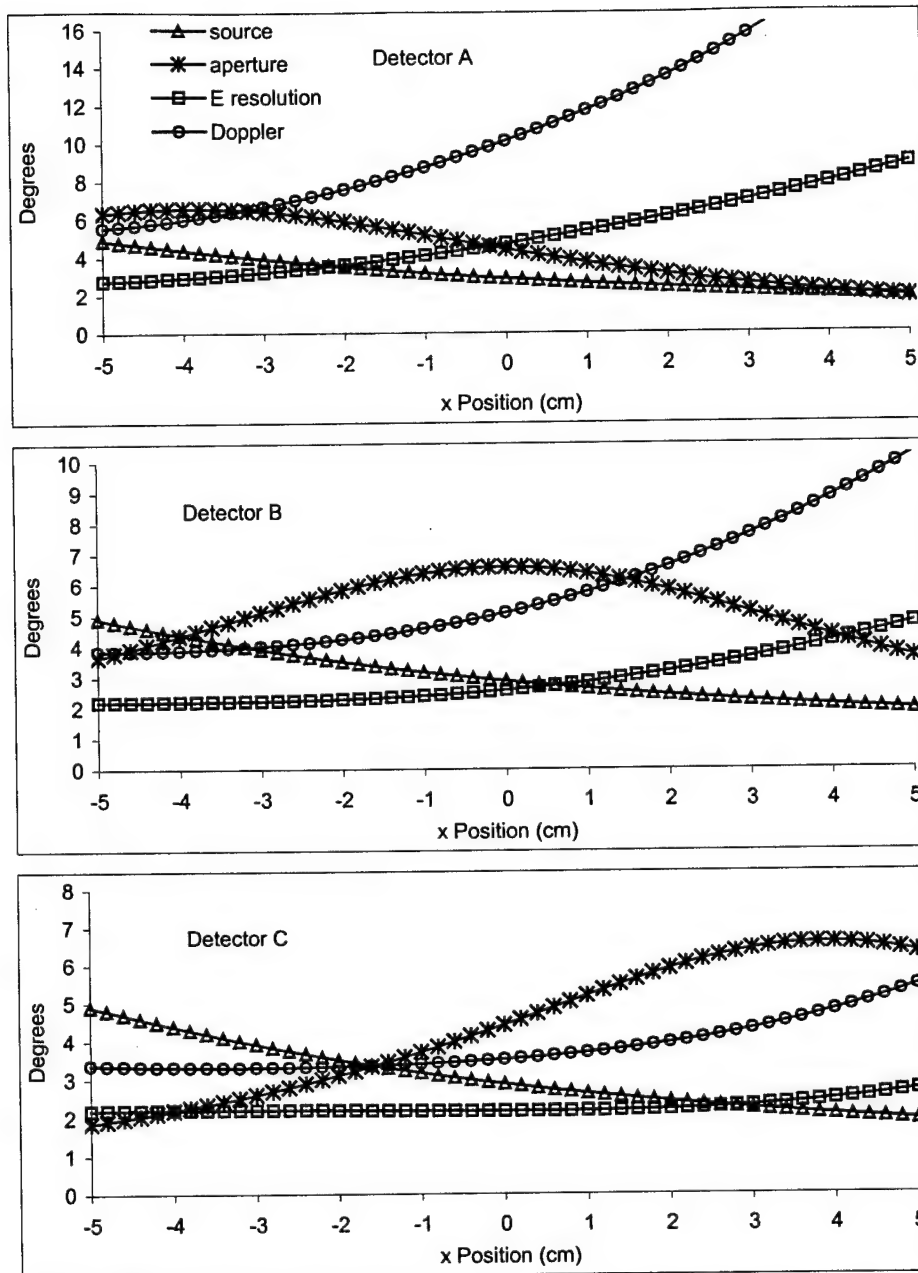Despite its limitations, the demonstration MCST system is capable of imaging simple high-contrast aluminum phantoms. Doing so helps validate the ScatGram model and PWLS image reconstruction algorithm. It also demonstrates the feasibility of single-sided MCST in general. Several phantoms were chosen from which the demonstration MCST system collected scattered photon spectra. Then the PWLS image reconstruction algorithm produced estimates of their electron density image from the set of measured spectra. In the case of pure aluminum phantoms, the electron density is directly proportional to the mass density.

5.1   Measurement of Point Response

In many imaging applications the response of the system to a delta function or point input is used to characterize the performance of the system (Barrett and Swindell, 1981). Although the delta function can be treated mathematically, in the laboratory the point response must be measured using a very small source to approximate the delta function. Even this approximation presents problems in the MCST application because, to first order, the signal intensity is proportional to the sample volume. The consequences of using a very small scattering sample to measure the point response would be very low data throughput. A compromise was required to strike a balance between the size of the point-like scattering sample and reasonable data throughput.

The point-like sample used for the MCST system consisted of 6.35 mm x 6.35 mm x 40 mm rectangular aluminum rods. The sample was constructed from 1100 series aluminum that is 99.9% pure and contains very few alloying metals. The 6.35 mm x 6.35 mm cross section was positioned parallel to the fan beam so the system would image the smallest cross section, as illustrated in Figure 4-5. Figure 5-1 illustrates the positions of the sample and system components for this experiment. The figure shows two cross-sectional diagrams of the experiment corresponding to two separate locations of the source. The ^{109}Cd source is located in the center of the tin shielding represented by the item marked "source container." Sample positions 1-3 were collected with the source at the left, as in the top diagram. Sample positions 4-6 were collected with the source at right, as in the bottom diagram. The large trapezoidal object is the fan beam collimator assembly housing the source and detector collimators. The
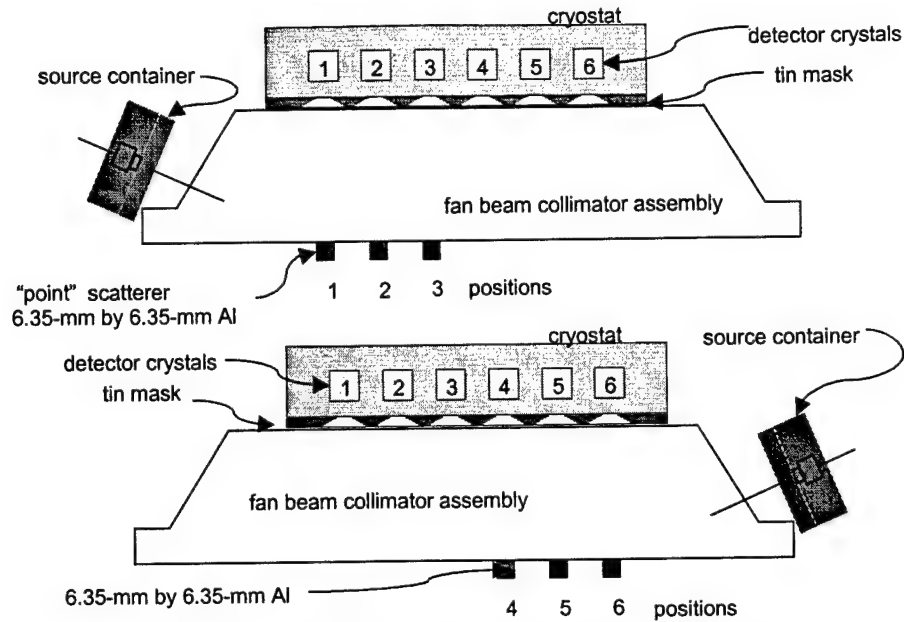
Figure 5-1. Configurations for Measuring Point Responses.

positions of the six detector crystals are shown within the cryostat at the top of each diagram. The tin mask with tapered holes is also shown between the cryostat and collimator assembly.

Figure 5-2 shows the resulting point response energy spectra recorded in each detector for the sample positions labeled 1-3 in Figure 5-1. Figure 5-3 shows the point response energy spectra for the sample positions labeled 4-6 in Figure 5-1. The spectra shown include those detectors for which each sample position was within the detector's field-of-view. Plotted with the recorded energy spectra is the ScatGram output without statistical noise, $\mathbb{I}N_\gamma$. A single scaling factor N_γ is applied consistently to all the modeled results.

The agreement between the recorded spectral shapes and the modeled results is good. In some cases the magnitude of the model prediction does not match the magnitude of the experimental data, but shapes of the modeled and experimental spectra do match. The good agreement in the spectral shapes indicates that the ScatGram computation of the scattering angle distribution converging on the finite-sized detectors works well. This was already verified computationally, however, by benchmarking against MCNP as discussed in Chapter 2.

Figure 5-2. Point Responses for Positions 1-3.

Figure 5-3. Point Responses for Positions 4-6.

The more important result provided by this set of experimental data is that the impulse approximation accurately predicts the energy distribution of the scattered photons. The shapes of the spec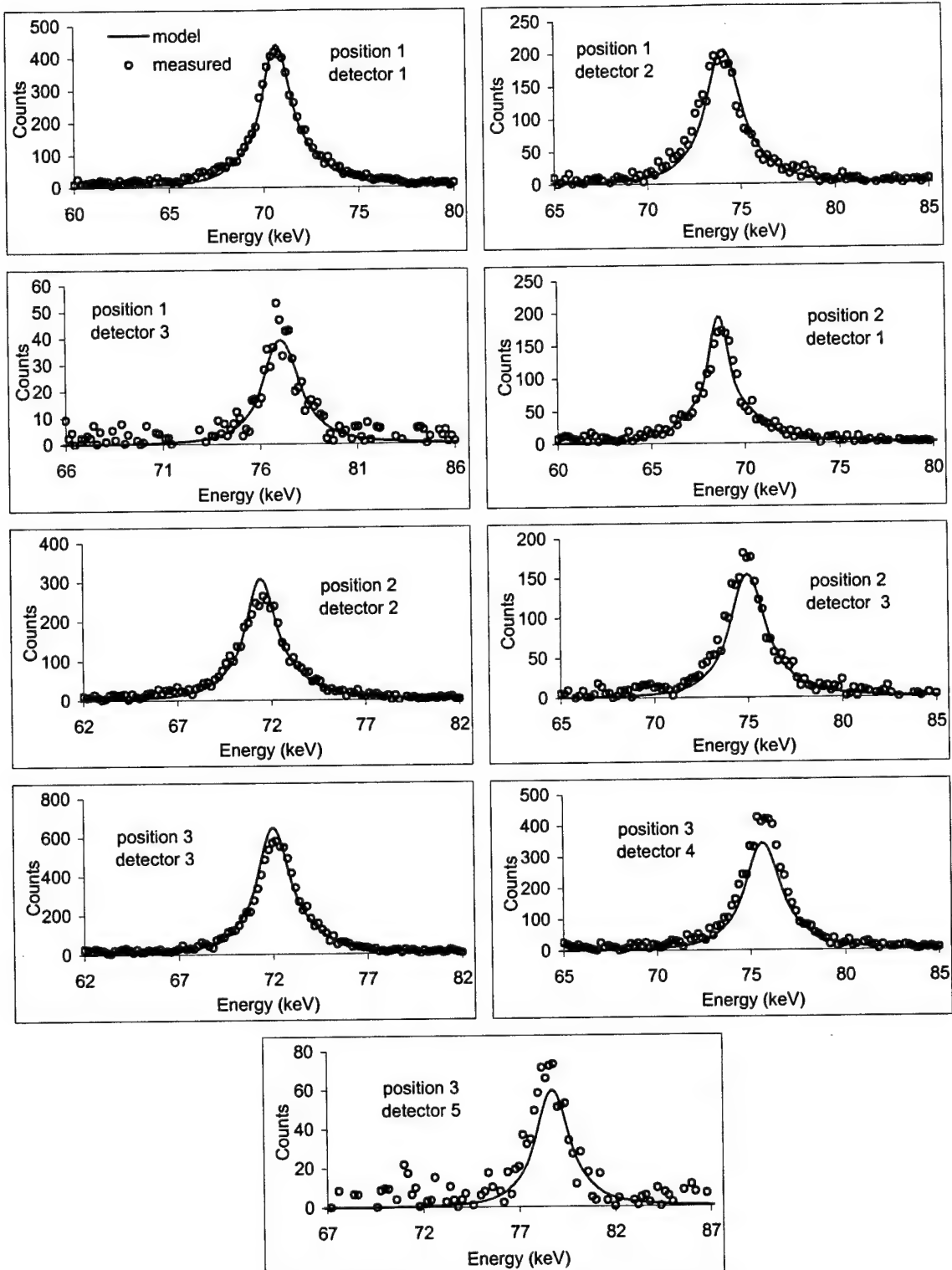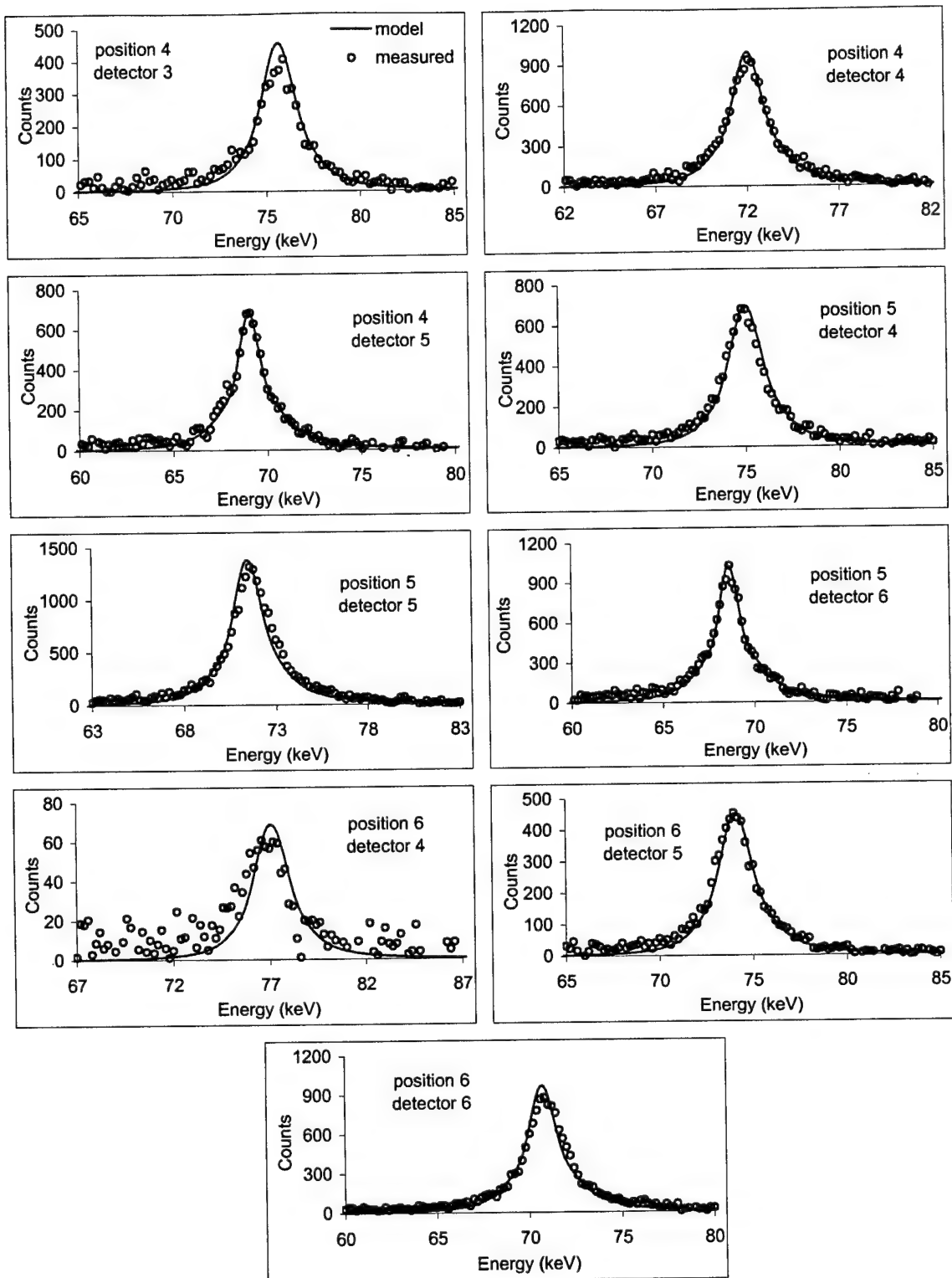tra are distinctive and dominated by Doppler broadening because they represent a narrow range of scattering angles. The impulse approximation has been correctly implemented in the advanced system model. This represents the first implementation and verification, to the author's knowledge, of Doppler broadening in a deterministic photon transport code.

There is excellent agreement in the magnitude of the models and recorded spectra for those configurations in which the sample is placed directly in front of the detector: position 1, detector 1; position2, detector 2; etc. These configurations are relatively unaffected by the accuracy of the oblique angle efficiency function $\eta(\phi)$ because the scattered photons enter the detector aperture along the path of greatest efficiency, $\phi = 0$. Moreover, the solid angle of the detector aperture as viewed from the sample is identical for this set of spectra, so these configurations are also relatively unaffected by the accuracy of the Λ calculation. Recall from Section 2.3 that Λ represents the fraction of the bin solid angle Ω_q intercepted by the detector aperture. The universal N_γ scaling factor was selected to make the composite of all the $\phi = 0$ spectra agree with the model as closely as possible. This result indicates that ScatGram does an accurate job predicting the variation in intensity of the source fan beam across the imaging region. Disagreement in the magnitudes of the recorded and modeled spectra may be attributed to several inaccuracies in the model, or imprecision in the experiment. An inaccurate characterization of the function $\eta(\phi)$ of Equation (2-21) is the most obvious culprit, but inaccuracies in $\varepsilon(E)$ and the calculation of Λ may also be to blame.

Alternatively, imprecision in the experiment can also cause these errors. Misalignment of the tin plates in the collimator assembly caused gross errors in some early experiments before the problem was identified. The symptoms were very similar – agreement in the spectral shapes but disagreement in magnitude. Machinists corrected the problem to the greatest extent possible, and the repairs resulted in a significant improvement. Measurable misalignment still persists, however, and may be part of the problem. Misalignment of the collimator assembly, detector mask, and detector crystals relative to each other may cause similar problems. Care was taken to align these components as well as possible with the available resources, which are admittedly crude. The system should not be as sensitive to misalignment of the source, since its size is large relative to the precision with which it may be positioned. Moreover, source

misalignment would likely have a uniform effect across all spectra. An experimental error that is undoubtedly present is the drift in energy calibration caused by the analog pulse-shaping electronics which are poorly suited for the long count times required here. As discussed in Chapter 4, these electronics regularly drift in calibration over a 12-hour period by amounts greater than the FWHM energy resolution of the detectors.

An important feature of all the spectra is the multiple scatter contamination evident at lower energies. The ScatGram results do not predict this component of the signal. Multiple scatter appears to provide a fairly uniform contribution at energies below the peaks. On the higher-energy side of the peaks it seems to provide little or no contribution. The ScatGram results and measured data agree better in those higher-energy regions. These results are not surprising considering a photon will lose some energy with each Compton scatter. Indeed the MCNP simulations discussed in Chapter 2 verify that the multiple scatter signal is expected predominantly at energies below the peak. They also suggest the somewhat uniform multiple scatter contribution is also present underneath the peak center, but is dominated by the single scatters.

The spectra with fewer counts such as position 1, detector 3; position 3, detector 5; and position 6 detector 4 suffer from very low signal-to-noise ratio due to their low intensity and the strong background subtracted from them. Further contamination of these spectra results from collection at higher values of oblique angle ϕ where the peak-to-total ratio is low. The breakdown current problem in detector 2, which was described in Section 4.4.1, appeared during the acquisition and ruined the spectrum for position 3, detector 2

5.2   Simple Phantom

Two of the 6.35 mm x 6.35 mm square aluminum targets were combined to form a simple phantom for verifying the validity both of ScatGram and the reconstruction codes. Figure 5-4 provides a diagram of the experimental configuration used to measure this simple phantom. Unlike the diagrams of Figure 5-1, both square scattering targets were in place simultaneously. Detectors 3-6 recorded spectra in position A, and also in position B. The geometry of position B is not ideal in the sense that the source is not pointed at the center of the phantom as in position A. The position B configuration was chosen because
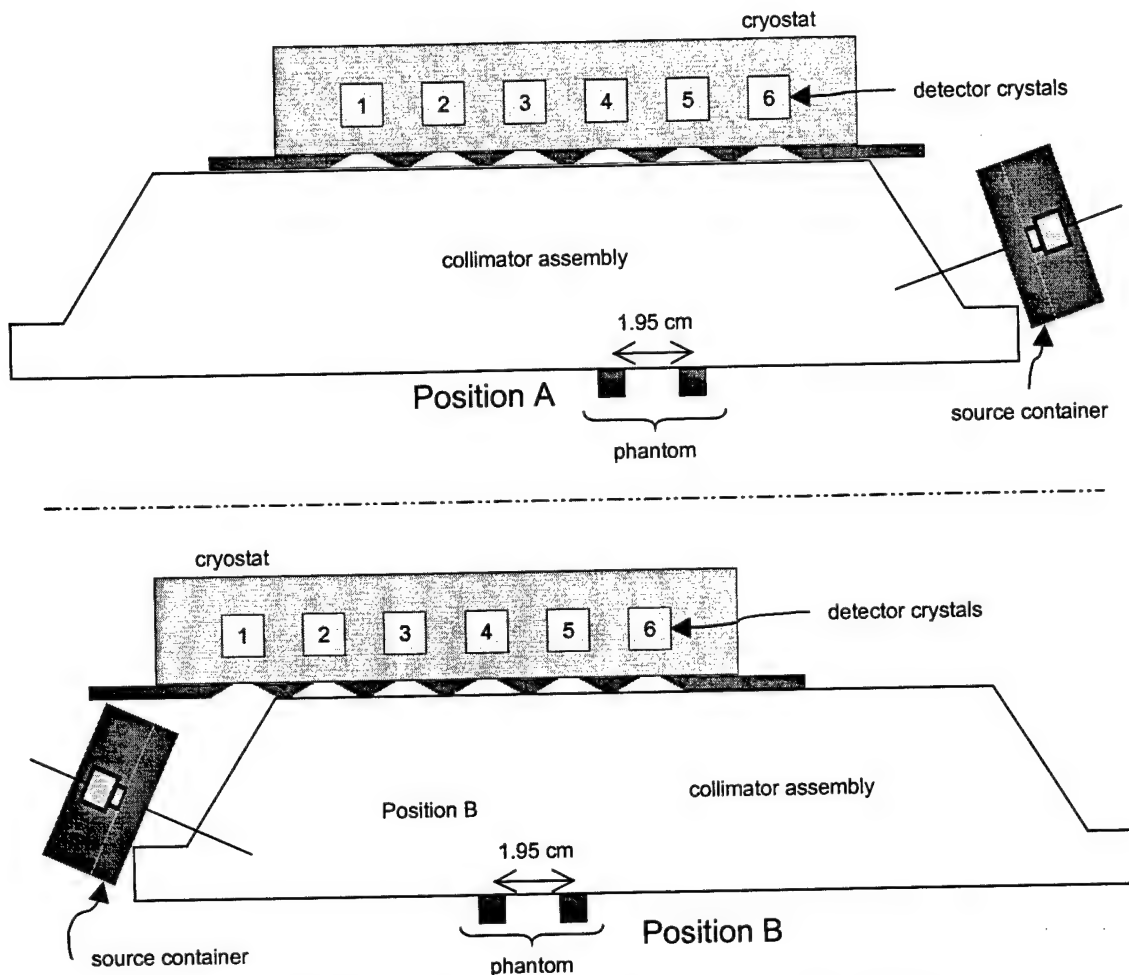
Figure 5-4. System Configuration for Imaging the Simple Phantom.

it illuminates the phantom from the left without relying on detector 2 where the breakdown current problem may occur. Figures 5-5 and 5-6 show the resulting spectra collected in positions A and B, respectively. ScatGram predictions of the spectra are plotted for comparison, but without noise so the model curve is the expectation value IN_γ. The scaling factor N_γ was selected by matching the experimental data to model as closely as possible for the composite of position A, detectors 4 and 5; and position B, detectors 2 and 3.

Again the symptom of incorrect amplitudes is evident in the results despite good modeling of the spectral shapes. The problem is more severe than should be expected from the results of the point response measurements, particularly for detector 3. This suggests that there is an inconsistency in the experimental system. The equations included in the model remain constant. If there were not an experimental inconsistency, the results would be comparable to those of the point response measurements.

Figure 5-5. Simple Phantom Spectra from Position A.

Figure 5-6. Simple Phantom Spectra from Position B.

The most probable experimental inconsistency is alignment of the fan beam collimators, mask, and detector crystals. The system is evidently more sensitive to these factors than anticipated.

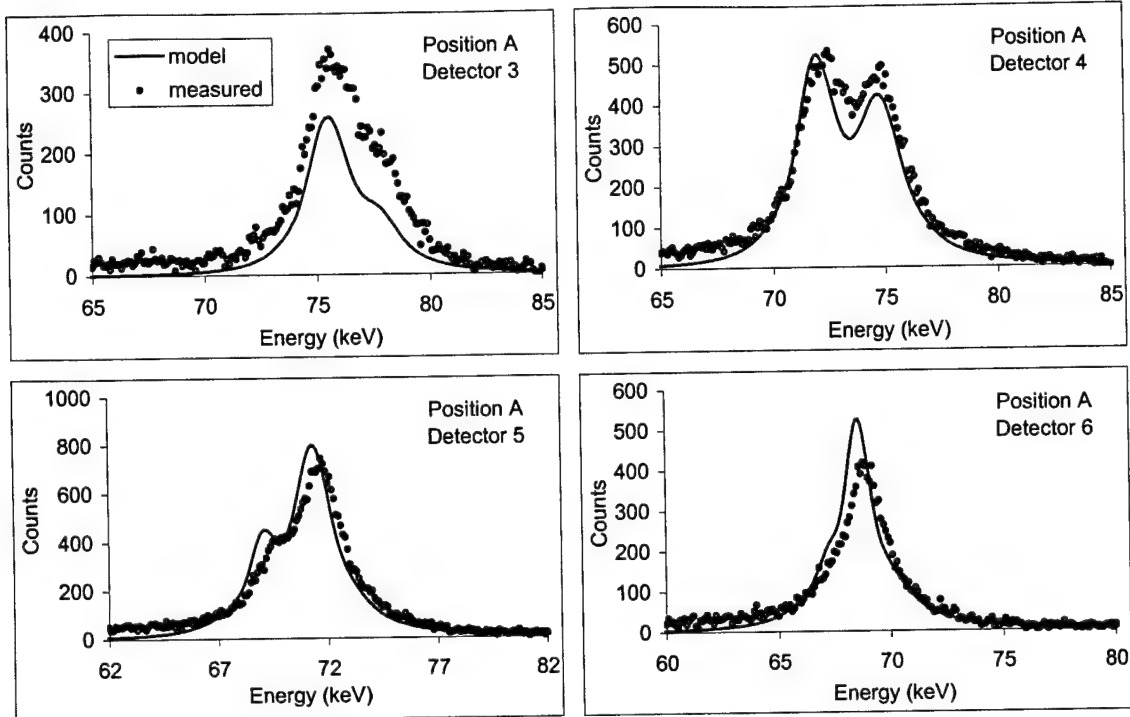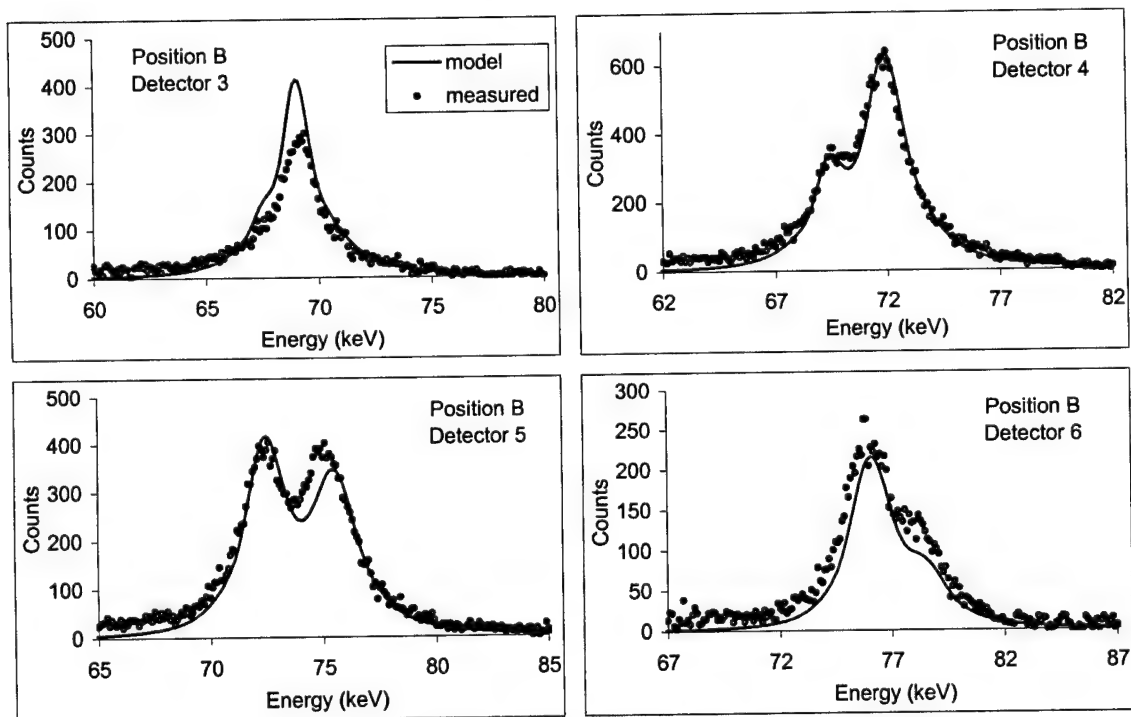Perhaps the most obvious feature of these spectra compared to those of Figure 5-2 and Figure 5-3 is the increased intensity of multiple scatter contamination at energies below the peaks. The larger volume sample produces more multiple scatter, as expected.

The eight spectra shown in Figure 5-5 and Figure 5-6 were used to reconstruct the simple phantom with the PWLS iterative reconstruction algorithm. Figure 5-7 shows the results. The set of eight spectra does not provide enough data for filtered backprojection reconstruction. The density cross section of the phantom is shown, as is the initial guess ρ_0 supplied to the PWLS algorithm, a larger aluminum block of uniform density. An image formed from noisy modeled data is shown to provide a best possible reconstruction for comparison. The data was corrupted with background and noise comparable to that of the measured data, which has an SNR of 4.92 as determined using Equation (3-16). The differences between the model and actual measurements are responsible for the distortion seen in the image constructed from measured spectra. The blurring, however, is due in part to the solution regularization imposed by the penalty function. Even in the ideal image reconstructed from model spectra, the blurring is evident. These images were reconstructed in six outer iterations, two with $\beta = 5.0$ and $\omega = 0.5$, then two with $\beta = 4.0$ and $\omega = 0.65$, then two with $\beta = 3.0$ and $\omega = 0.75$. Recall from Section 3.3.3 that β is the regularization coefficient that controls the strength of the penalty function, and ω is the relaxation parameter that controls the convergence rate of the solution. The image constructed from model spectra would converge with less regularization, but consistent values were used for a fairer comparison with the measured image. Voxel densities were bound at 2.70 g/cm^3 at each outer iteration, and all densities greater than 2.50 g/cm^3 were reset to 2.70 g/cm^3. Even in the modeled image, the sizes of the two blocks seem underestimated because of their blurred edges. However if the full width at half maximum (FWHM) of the blocks in the reconstructed image is taken as a measure of their height and width, their sizes are approximately 6.2 mm square, which is comparable to the 6.35 mm square phantom. Their positions are shifted to the center where the detectors sample the voxels more strongly than they sample the voxels near the edges of the image. Such artifacts are expected when reconstructing from a very limited data set of only eight spectra. In can be shown that, despite these distortions, the PWLS reconstruction has accomplished its task of

phantom

initial guess ρ_0

reconstruction from noisy models

reconstruction from measured spectra
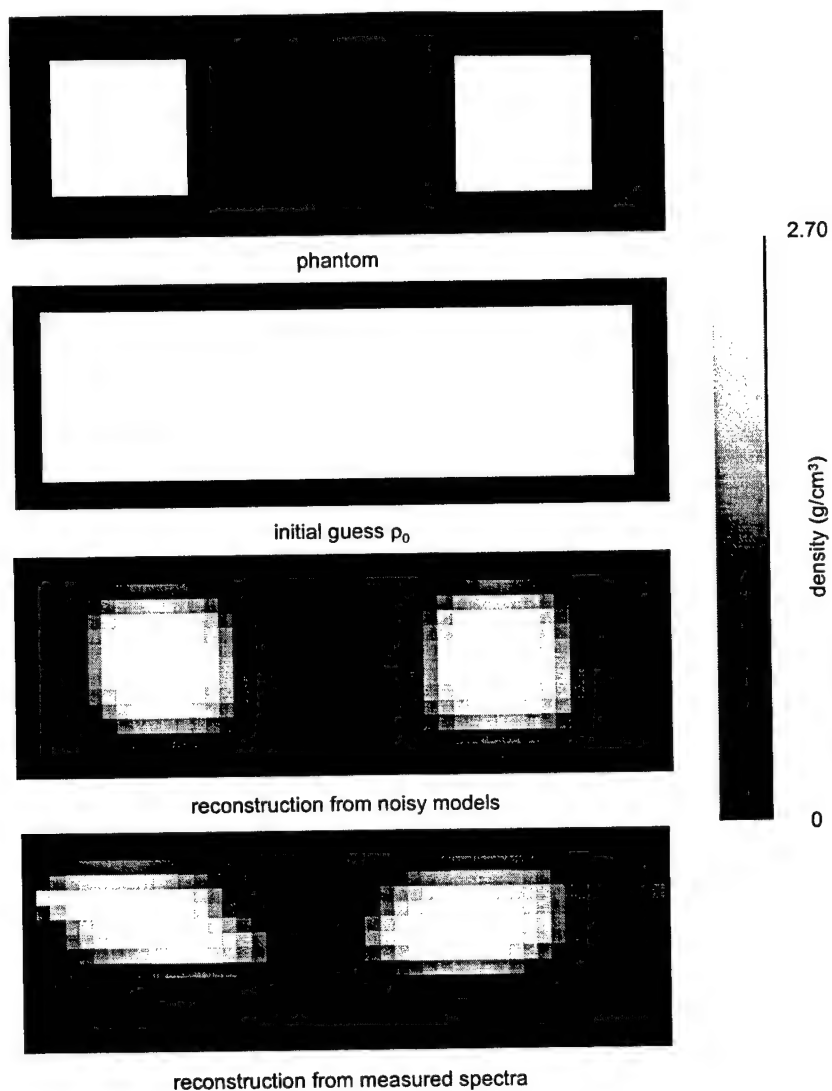
Figure 5-7. Reconstruction of the Simple Phantom.

finding a set of densities that matches the eight input spectra while retaining properties in the image demanded by the penalty function.

The measured image in Figure 5-7 is the algorithm's estimate of the voxel densities that will produce a spectrum matching the measured spectra Ψ. Labeling the set of densities estimated by the reconstruction as $\hat{\rho}$, a set of solution spectra $\hat{\Psi}$ may be calculated as

$$\hat{\Psi} = \mathbf{A}(\hat{\rho}) \cdot \hat{\rho}. \tag{5-1}$$

The implicit mapping based on the latest density estimate is stored within the computer's memory. After every outer iteration the PWLS reconstruction code writes out the set of solution spectra $\hat{\Psi}$. When the solution has converged, $\hat{\Psi}$ should resemble Ψ within the limits imposed by the penalty function. It can be

instructive to inspect these solution spectra for comparison against the measured spectra.Figure 5-8 and

Figure 5-9 show the solution spectra with their respective measured spectra.

Figure 5-8. The Solution Spectra Compared with the Input Spectra for Position A.

Figure 5-9. The Solution Spectra Compared with the Input Spectra for Position B.

The voxel densities that produced the solution spectra are the same shown in the measured image of Figure 5-7. This comparison helps illustrate the power of using bayesian priors with statistical image reconstruction techniques. It allows a solution that is clearly not the best fi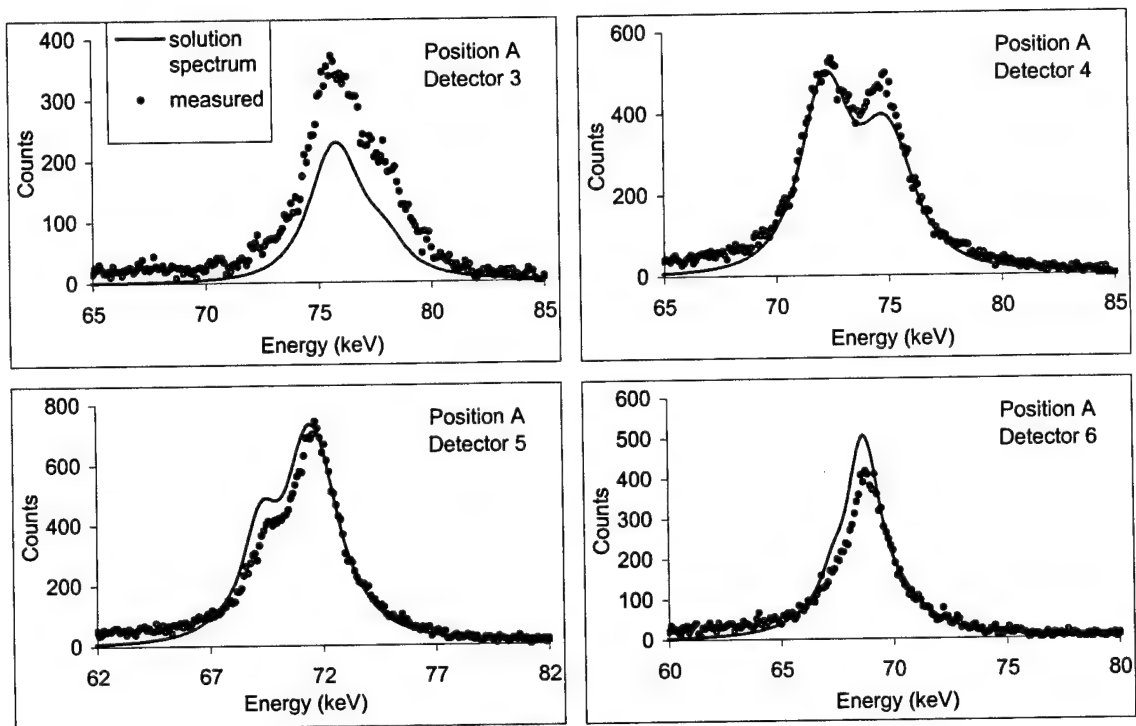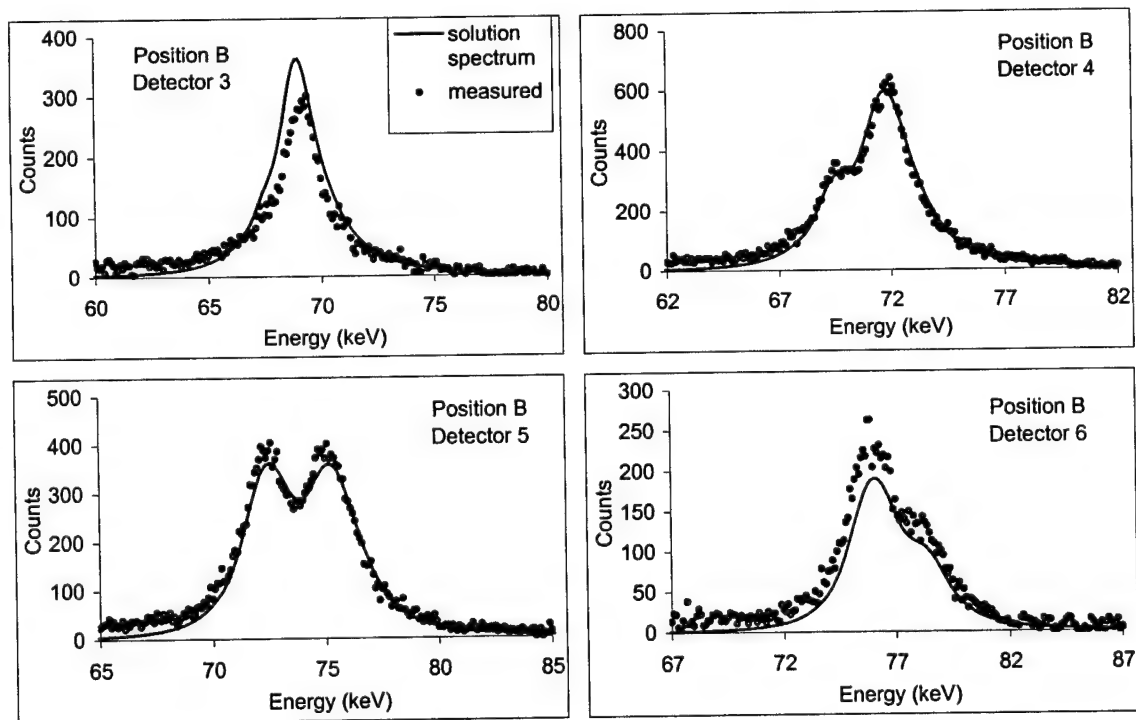t to the data, particularly in the case of position A, detector 3. An unregularized technique such as algebraic reconstruction or maximum likelihood would find a solution $\hat{\rho}$ that produces solution spectra $\hat{\Psi}$ most closely matching the noisy corrupted input data Ψ. The result would be an unrealistic set of voxel densities.

The quality of the reconstruction cannot be improved using the same number of spectra unless the model agrees more closely with the recorded data. There appear to be two factors preventing closer agreement between the modeled data and the recorded spectra. The first is the presence of multiple scatter contamination, and the second is the inconsistent agreement from detector-to-detector between the model amplitude and the amplitude of the recorded signal, despite the good agreement in spectral shape.

Simulations in MCNP such as those discussed in Section 2.7 provide a guideline for developing an *ad hoc* estimate of the multiple scatter intensity. One can expect it to provide a nearly flat, uniform contribution to the spectra below and under the peak, and fall off gradually toward the higher-energy regions of the peak. It is important to remember that the MCNP simulations did not include Doppler broadening. This effect will cause energy broadening, making the multiple scatter contribution at low and intermediate energies even more uniform than the simulations suggest, and providing a more gradual multiple scatter rolloff at higher energies than the simulations suggests. With this in mind, a simple algorithm was developed to estimate the multiple scatter contribution in the spectra recorded from the simple phantom. Figure 5-10 provides some examples of the original spectra displayed with the multiple scatter estimates. The algorithm computes the mean counts in an energy region well below the peak, and assumes the multiple scatter intensity is that mean value for most of the spectrum. At higher energies, however, the algorithm assigns a diminishing multiple scatter intensity based on a weighted sum of exponential and quadratic terms. The rolloff begins at an energy selected based on the shape of the high-energy tail and the location of the peak's maximum intensity. This correction is admittedly crude and based on intuitive guesses about the behavior of the multiple scatter contribution. Unfortunately there is presently no available model (short of MCNP) for predicting the multiple scatter spectrum. Research is underway at AFIT with the goal of producing such a model for use a next-generation MCST system (Gerts,
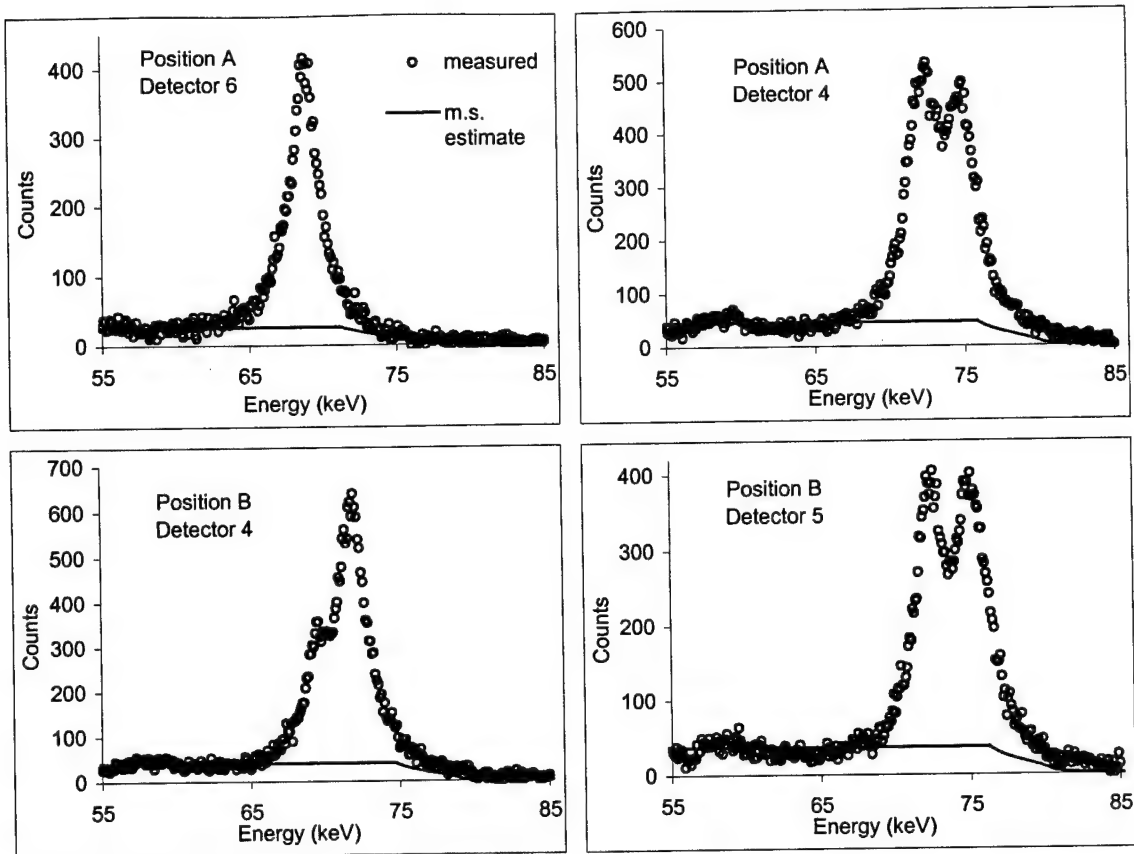
Figure 5-10. Examples of the Multiple Scatter Estimate.

1999). Another option, as suggested by Figure 2-13, is to narrow the tomographic slice thickness at the expense of the system's efficiency. The estimated single-scatter to total ratio in this set of signals is 0.69.

The inconsistency between the amplitudes of modeled and recorded spectra is straightforward to correct -- each modeled spectrum is adjusted by a scale factor. For each individual spectrum the factor is selected that provides the least-squares error between the data and model. This correction takes place after subtraction of the multiple scatter estimate, and only uses counts under the peaks when computing the least-squared error. Figures 5-11 and 5-12 compare the corrected model with the recorded spectrum for positions A and B, respectively. Comparison with Figure 5-5 and Figure 5-6 shows that the agreement is improved. The relative error introduced by the multiple scatter estimate will be greatest where the ratio of multiple scatter to single scatter events is highest. This occurs around the low energy tails of the peaks.
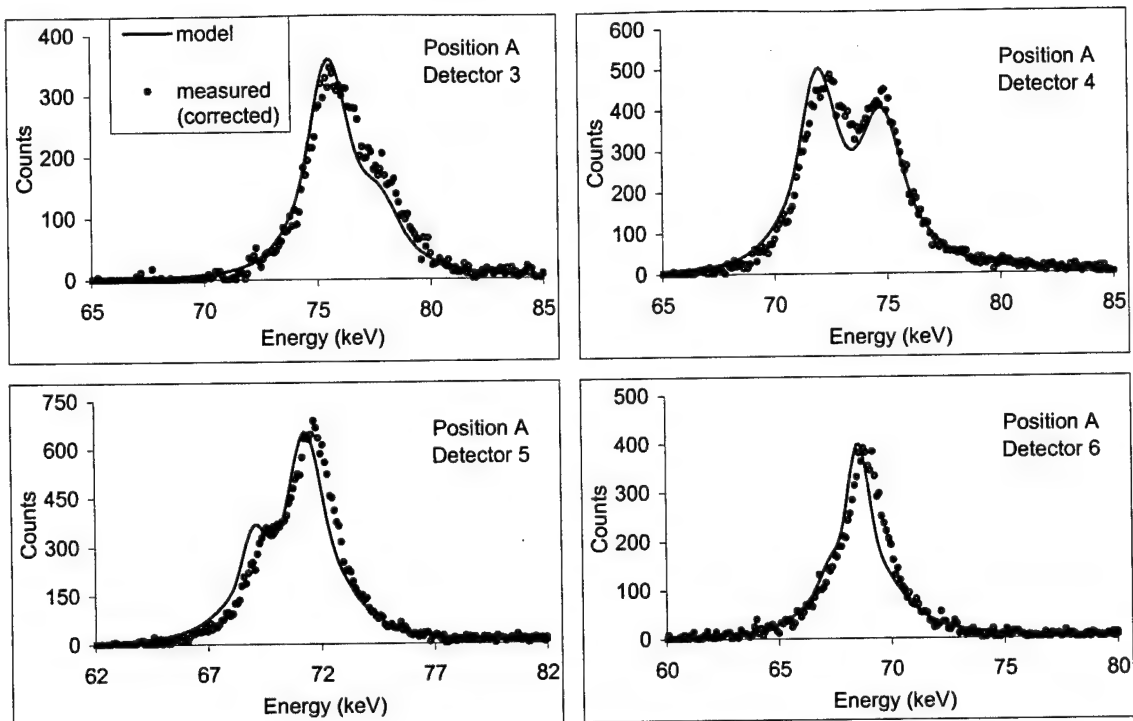
Figure 5-11. Comparison of the Multiple-Scatter Corrected Spectra and Scaled Model for Position A.
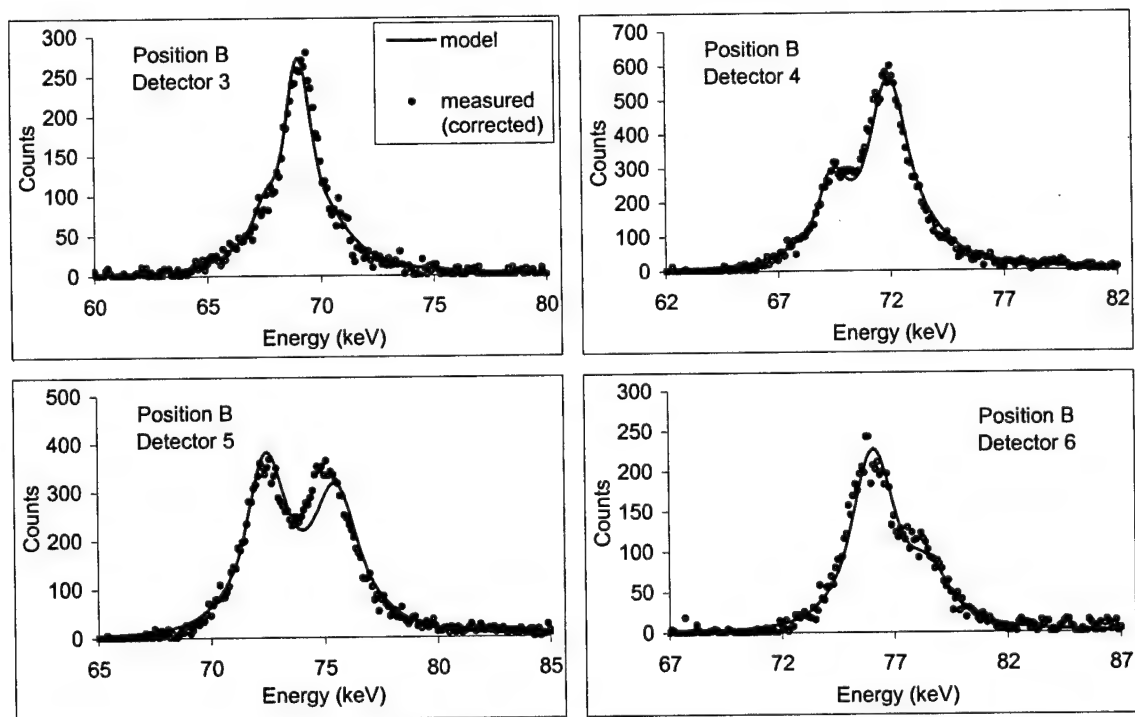
Figure 5-12. Comparison of the Multiple-Scatter Corrected Spectra and Scaled Model for Position B.

Now that the spectra agree more closely, an improved reconstruction can be expected. Indeed, Figure 5-13 shows the improved reconstruction resulting from the multiple scatter correction compared to the reconstruction from uncorrected spectra shown in Figure 5-7. More of the phantom's high-density regions are recovered. The image is less distorted, although the blurring is still present. The solution regularization imposed by the penalty function is responsible for much of the blurring. The new images was produced in six outer iterations, two with $\beta = 3.0$ and $\omega = 0.5$, then two with $\beta = 1.0$ and $\omega = 0.80$, then two with $\beta = 0.8$ and $\omega = 0.9$. The corrected spectra required less regularization (smaller β) to converge the image than did the untreated spectra. Voxel densities greater than 2.50 g/cm^3 were reset at each outer iteration to 2.70 g/cm^3. The same initial guess shown in Figure 5-7 was used for ρ_0. While the image is a distorted version of the actual sample density, the image reconstruction recovered the essence of the phantom, two distinct similarly-shaped high-density regions, from the initial guess of a large uniform block of aluminum.

phantom

reconstruction from uncorrected measured spectra

reconstruction from corrected measured spectra
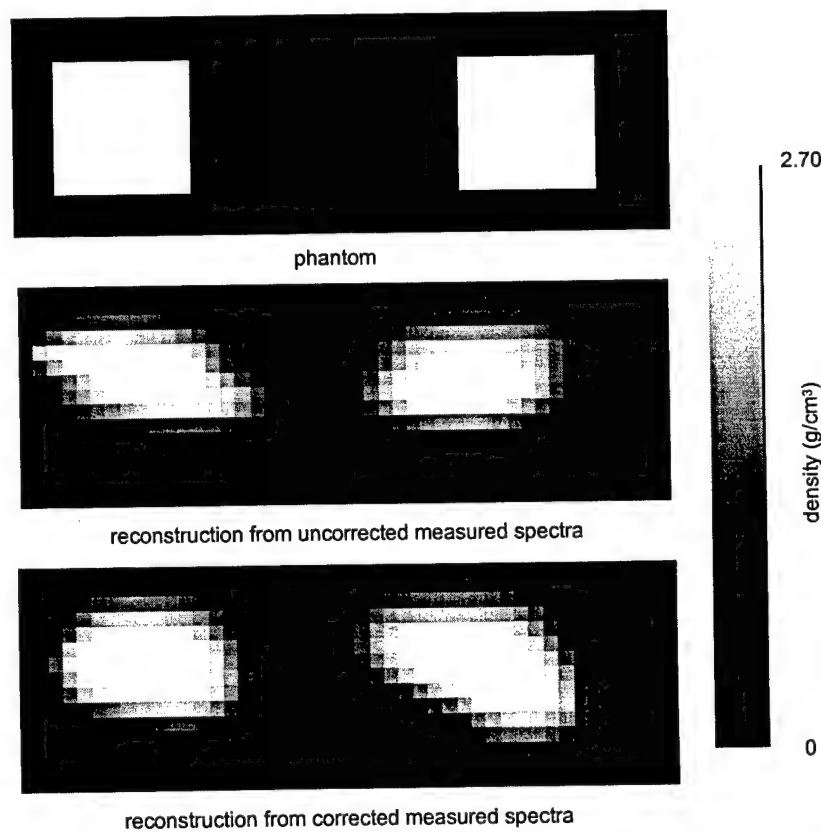
Figure 5-13. Comparison of Reconstructions from the Corrected and Uncorrected Spectra.

5.3 Void Phantom

The next phantom considered is a 30 mm x 8 mm aluminum phantom with 20 mm x 4 mm void in the center. The purpose of this phantom is to demonstrate MCST's ability to resolve a hidden low-density region included within a sample. Spectra collected in four source/detector array configurations comprised the data set for this experiment. Each source and detector configuration produced four spectra. Figure 5-14 shows diagrams of these configurations, and Figure 5-15 shows the recorded spectra compared with the models. Just as in Figure 5-11 and 5-12 the recorded spectra have been corrected with the multiple scatter estimate and the model had been scaled to match the measurements by individually selecting N_γ to minimize the least-squares error between the model and measured data. Compared to the simple phantom, this larger volume phantom provided better data throughput for comparable counting times, but the fraction of events due to multiple scatter was greater. The agreement between the model and corrected spectra is
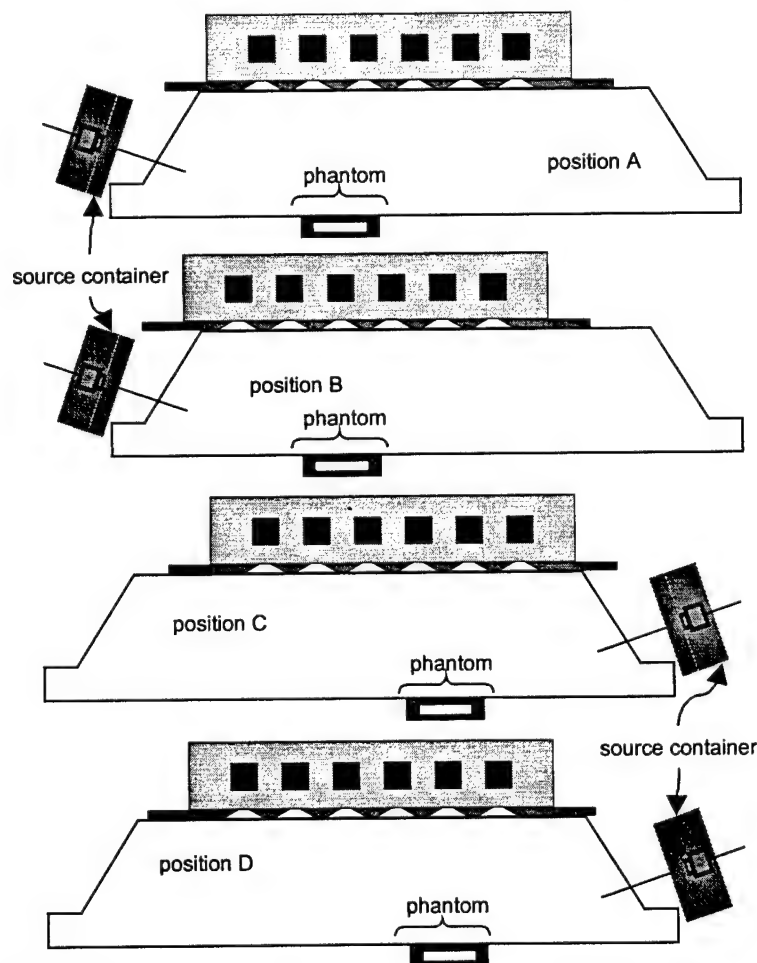
Figure 5-14. Experimental Configurations to Measure the Void Phantom.

good in most cases with a few exceptions, particularly detector 3 in positions C and D. These are spectra collected at the most extreme oblique angles where the detector response is poor both with respect to the efficiency and peak-to-total ratio. However, it should be noted that detector 4 in position A and detector 5 in position B had symmetric geometries with respect to the source and sample, and the model agrees better with the measured data in those cases. This suggests an experimental anomaly in detector 4 for positions C and D. An energy calibration error is the expected culprit. A positioning error is unlikely since it would have produced comparable results in the other detectors.

Figure 5-19 provides the results of the reconstructed images. The phantom density cross section and the initial guess provided to the PWLS algorithm are shown. To produce the first reconstruction, 16 spectra provided by the ScatGram model were corrupted with background counts and statistical noise comparable to that in the measured data. The measured data in this experiment has a signal-to-noise ratio of 6.47 and an estimated single-scatter-to-total ratio of 0.67. This reconstruction from modeled data presents a best case benchmark that can be considered the best reconstruction possible under the circumstances. The reconstruction from measured spectra was produced from the 16 measured spectra shown in Figures 5-15 through 5-18, with the exception of those for position C, detector 3 and position D, detector 3. These two spectra were rebinned with a new calibration that made them more closely match the model. The two images were reconstructed in eight outer iterations, two with $\beta=0.7$ and $\omega = 0.7$ then two with $\beta=0.5$ and $\omega = 0.8$, then two with $\beta = 0.4$ and $\omega = 0.8$, then two with $\beta = 0.3$ and $\omega= 0.9$. Only voxels with calculated densities greater than 2.70 g/cm^3 were reset to a density of 2.70 g/cm^3 after each outer iteration. Arguably these two images are comparable in quality. The true size of the void is recovered better in the modeled image, but in both cases the vertical side walls are poorly resolved. Nevertheless, the presence of the void is unmistakable in both images. The modeled image has better symmetry than the measured image, as one would expect considering the modeled data is nearly symmetric. For instance the spectrum modeled for position A, detector 1 is similar to the spectrum modeled for position C, detector 6. It is important to remember that the modeled spectra shown in the figures represent the noise-free expectation values IN_γ. Each modeled spectrum is randomized independently before it is used for reconstruction, so the noise in the similar spectra is different, and the similar spectra are not truly identical. This asymmetric noise causes the asymmetry in the modeled image.
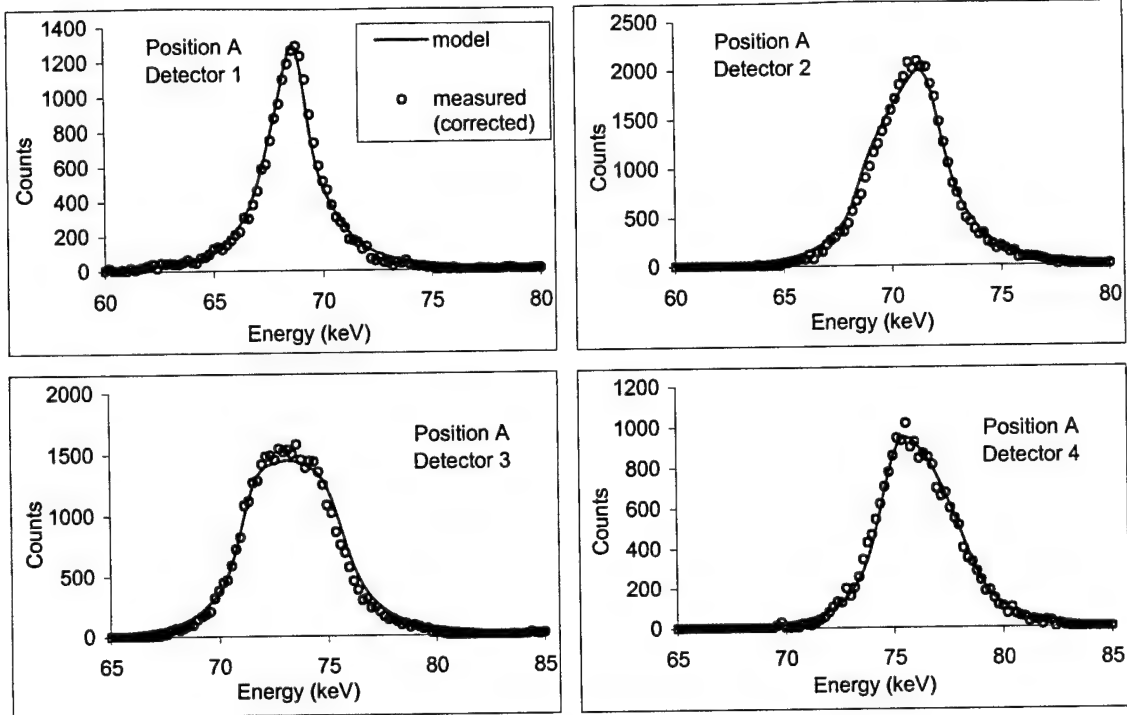
Figure 5-15. Void Phantom Modeled and Measured Spectra for Position A.
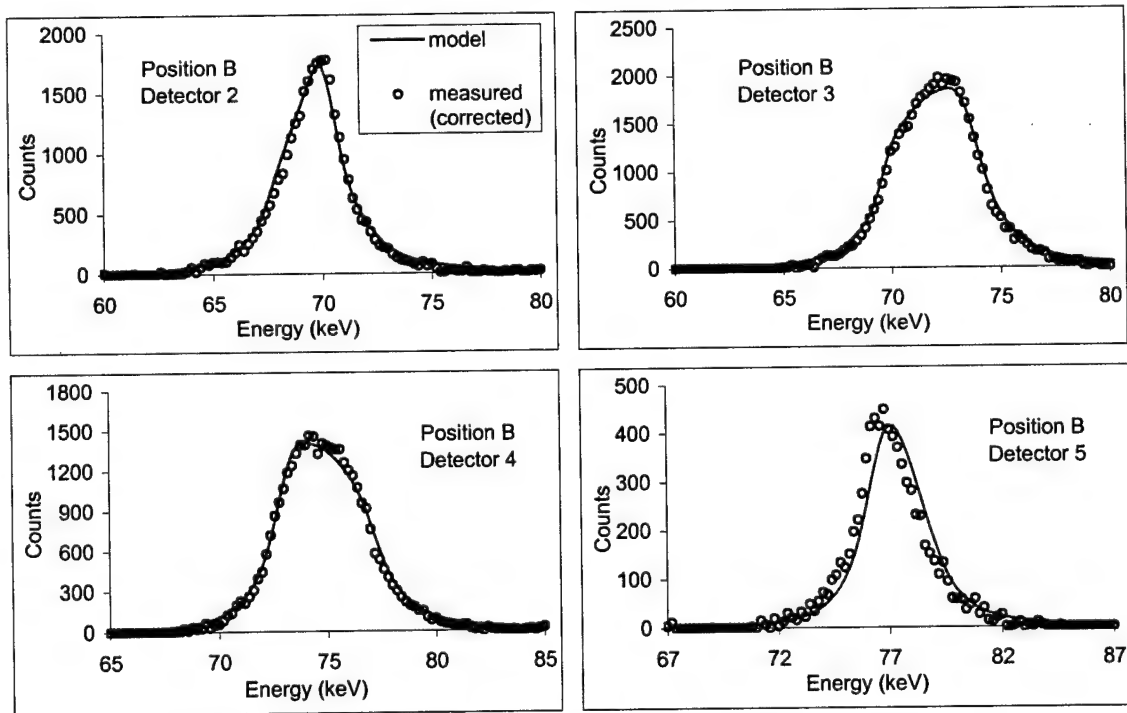
Figure 5-16. Void Phantom Modeled and Measured Spectra for Position B.
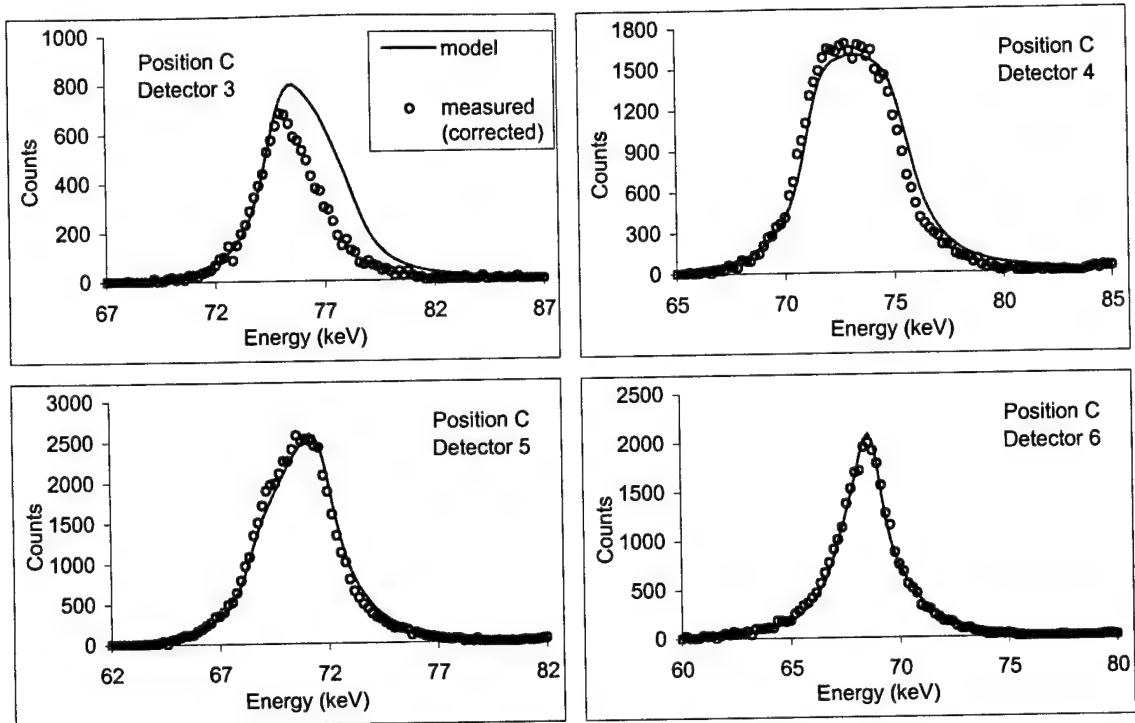
Figure 5-17. Void Phantom Modeled and Measured Spectra for Position C.
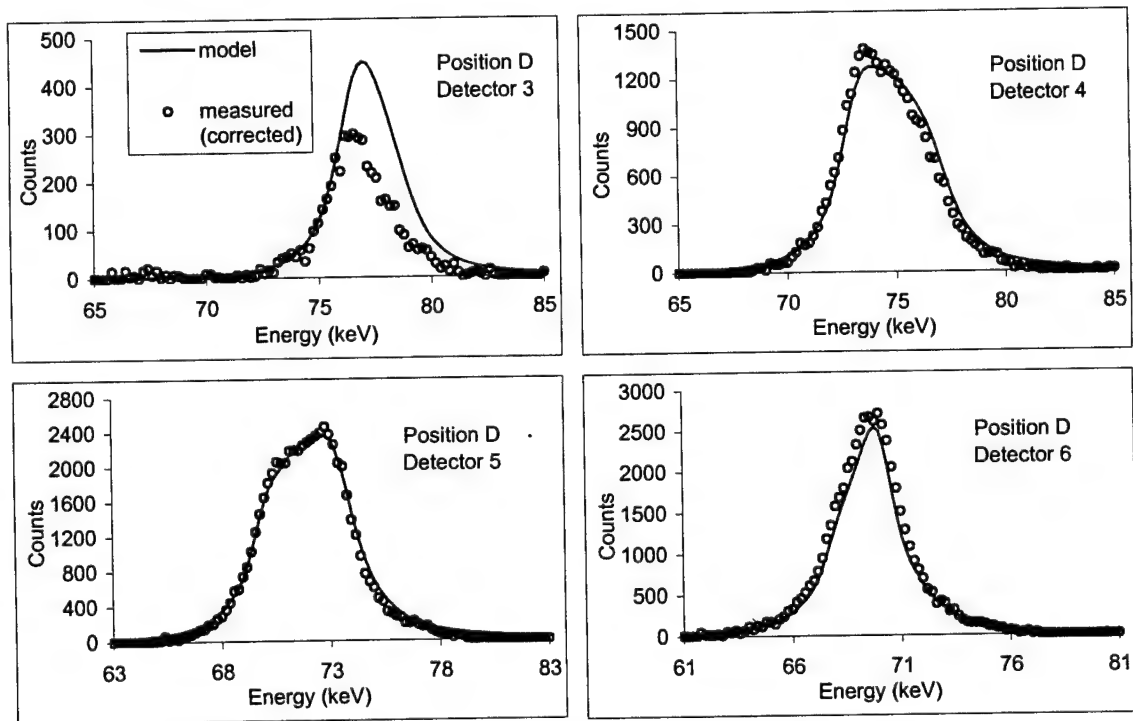
Figure 5-18. Void Phantom Modeled and Measured Spectra for Position D.

phantom density

initial guess ρ_0

reconstruction from modeled spectra

reconstruction from measured spectra
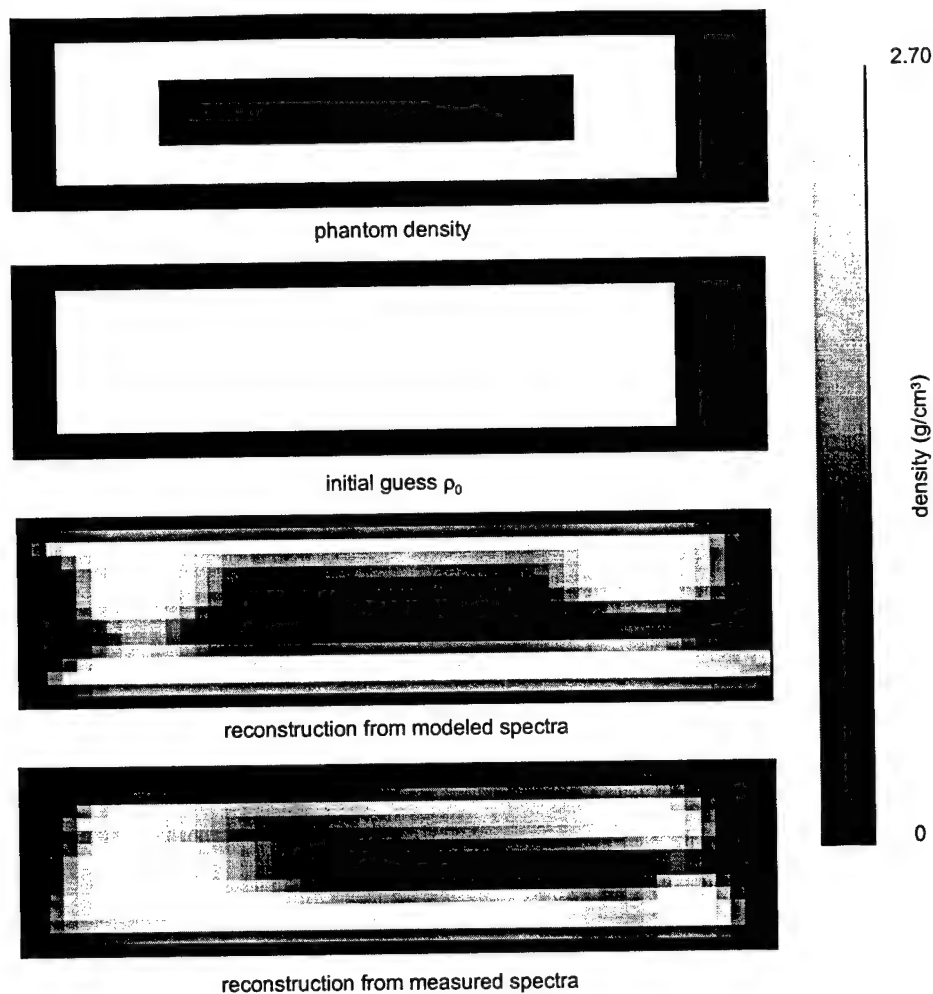
Figure 5-19. Void Phantom Reconstructions.

5.4 U-Shaped Phantom

The U-Shaped phantom experiment is designed to demonstrate the MCST system's ability to locate a loss of density hidden on the inaccessible side of a thick sample. The aluminum phantom is 10 mm thick and 40 mm wide. The void is on the opposite side of the sample relative to the source and detectors and measures 10 mm wide and 3 mm deep. Figure 5-20 shows the experimental configuration. During this experiment, detector 2 failed catastrophically with breakdown current across the crystal. This made it impossible to collect good data in detectors 1-4 with the source positioned at left as in positions A and B. Instead, exploiting the symmetry in the phantom and using detectors 3-6 with the source on the right simulated collection in positions A and B. Thus position C, detector 6 simulates position A, detector 1; position D, detector 5 simulates position B, detector 2, etc. Despite only two separate configurations, four separate acquisitions were taken to avoid correlated noise in the data. During image reconstruction the four

configurations shown in Figure 5-20 were assumed. Figure 5-21, 5-22, 5-23, and 5-24 show the spectra collected for positions A, B, C, and D, respectively. The numbers in parentheses for positions A and B indicate the actual experimental configuration under which that spectrum was collected for simulation. The measured spectra are corrected using the *ad hoc* multiple scatter estimates. For each energy spectrum, the model is scaled with separate values of N_γ to minimize the least-squares error between modeled and measured spectra. The charts also display each modeled spectrum from ScatGram for comparison.

Again the largest errors between modeled and measured spectra occur for forward-scattered gammas where the oblique angle ϕ into the detector is large. This error is rather consistent between position A, detector 4; position B, detector 4; position C, detector 3; and position D, detector 3. The problem does not appear to reside in $\eta(\phi)$ because backward-scattered spectra with similar ϕ such as position A, detector 1 agree well with the model. It is noteworthy that each of these spectra has the fewest counts in its respective position by several factors. Their estimated single-to-total ratio is also lowest by several factors. While the error is not as severe as it was in the case of the void phantom, the nature of the error suggests that either the *ad hoc* multiple scatter estimate may be too intense at the high-energy part of the peak. All four of these poorly-matching spectra were actually recorded in detector 3, so it's possible that detector 3 experienced some energy calibration or breakdown current problems. Other alternatives include a consistent misalignment of the system components. The results from the Simple Phantom in position B, detector 6; and position A, detector 3 as well as results from the Void Phantom in position A, detector 4; and position B, detector 5 indicate that ScatGram treated the most forward-scattered photons properly in those experiments. That is further evidence that an experimental error like component misalignment is to blame.

Figure 5-25 shows the images reconstructed from the experimental spectra. The spectra have a signal-to-noise ratio of 10.85. It also gives an image reconstructed from the modeled spectra corrupted with a similar amount of noise for a best possible image for comparison. The true phantom density and the initial guess ρ_0 supplied to the PWLS algorithm are also shown. This image was the slowest to converge of the samples imaged thus far. The images shown were produced in 17 outer iterations all with $\beta=2.0$ and $\omega = 0.8$. This phantom has more attenuation than the others considered, and the extensive attenuation corrections probably account for the slow convergence. The vertical features are better resolved in the
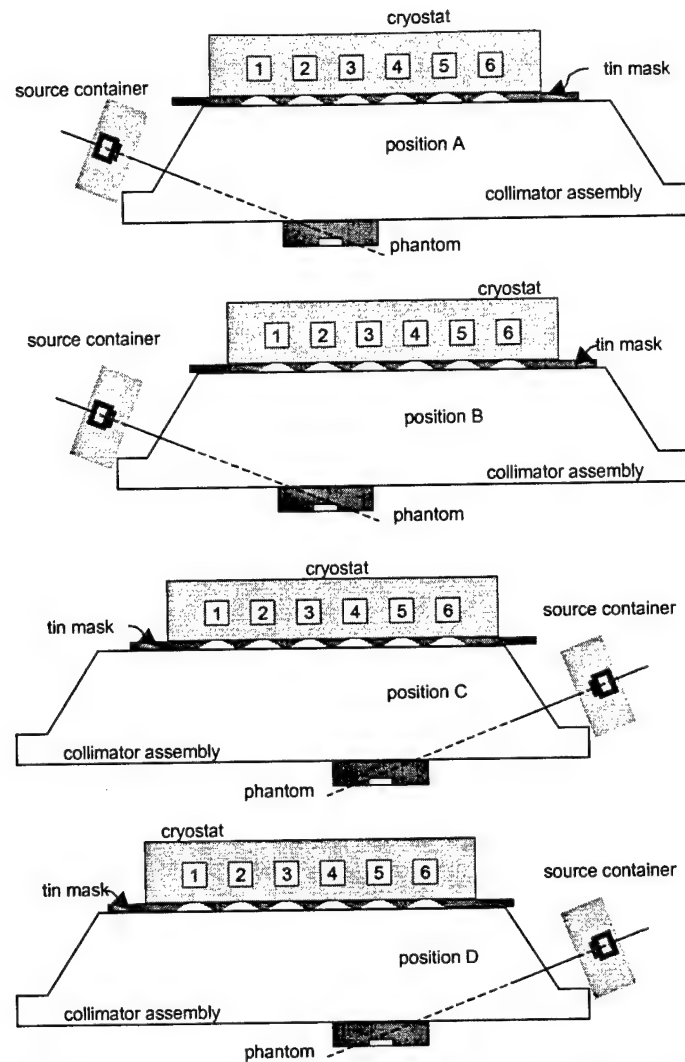
Figure 5-20. Experimental Configuration for Imaging the U-Shaped Phantom.

model image, but even so the left and right boundaries of the phantom are not recovered well. However, even the measured image recovers the hidden void.
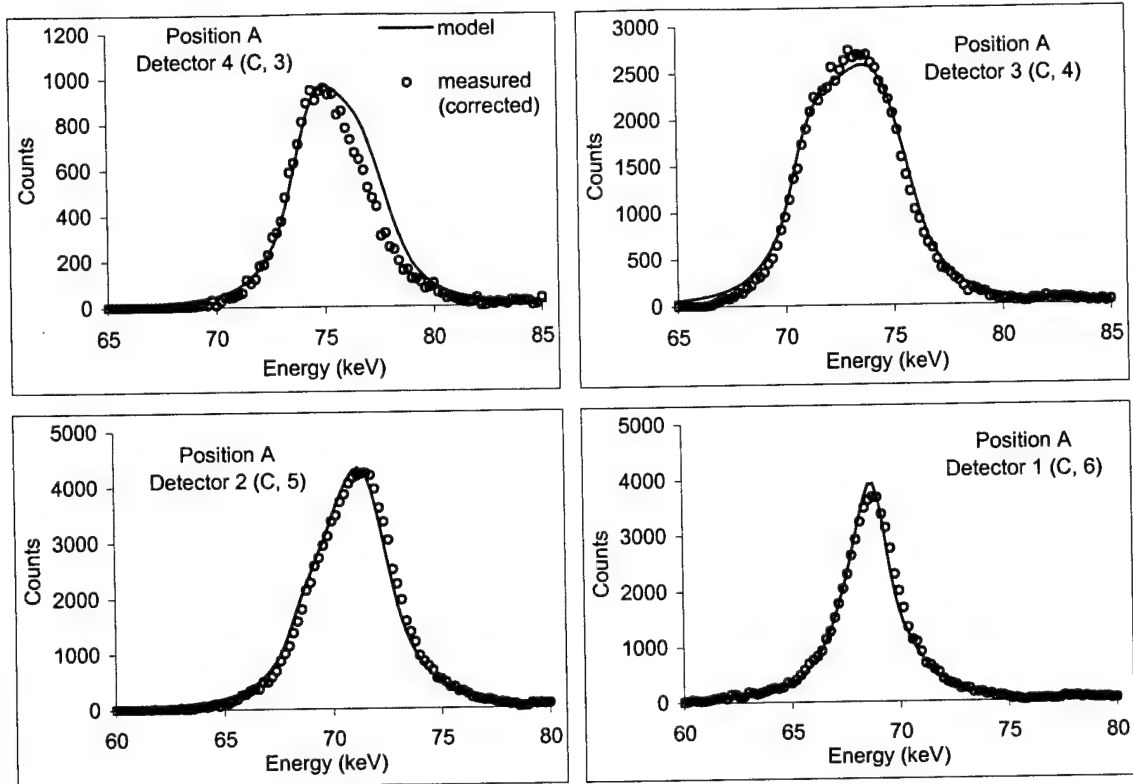
Figure 5-21. Spectra from U-Shaped Phantom, Position A.
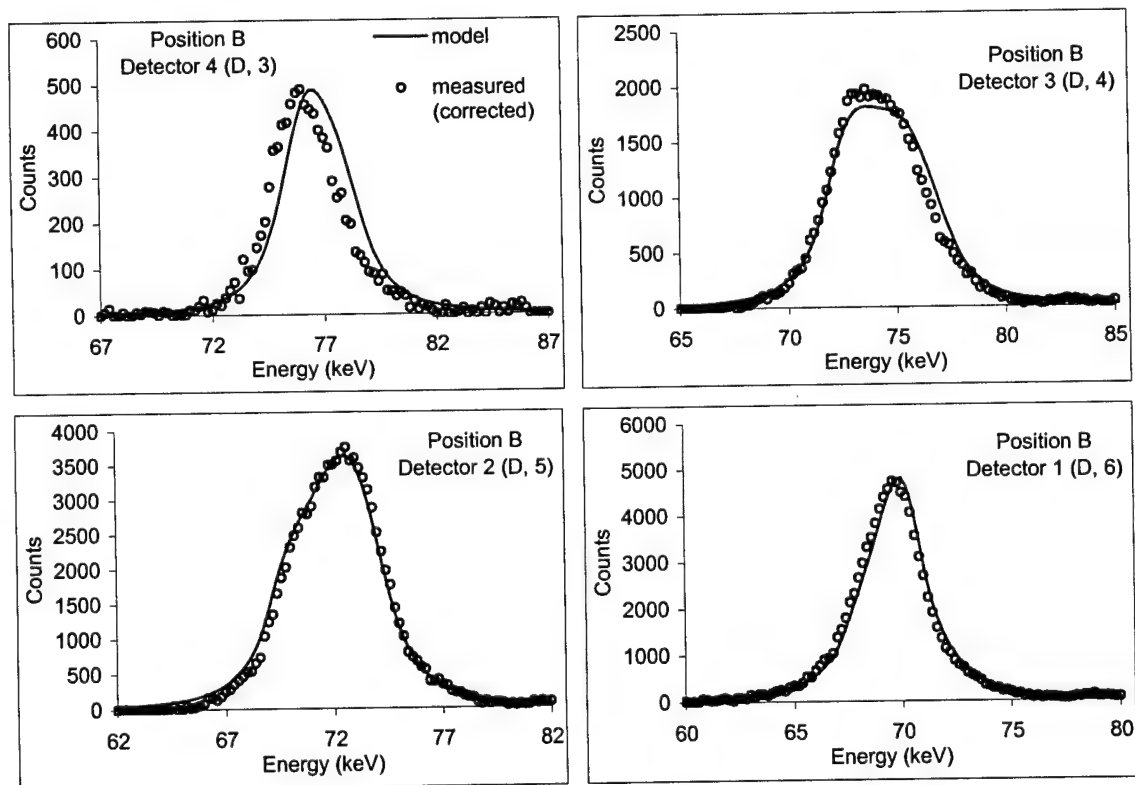
Figure 5-22. Spectra from U-Shaped Phantom, Position B.
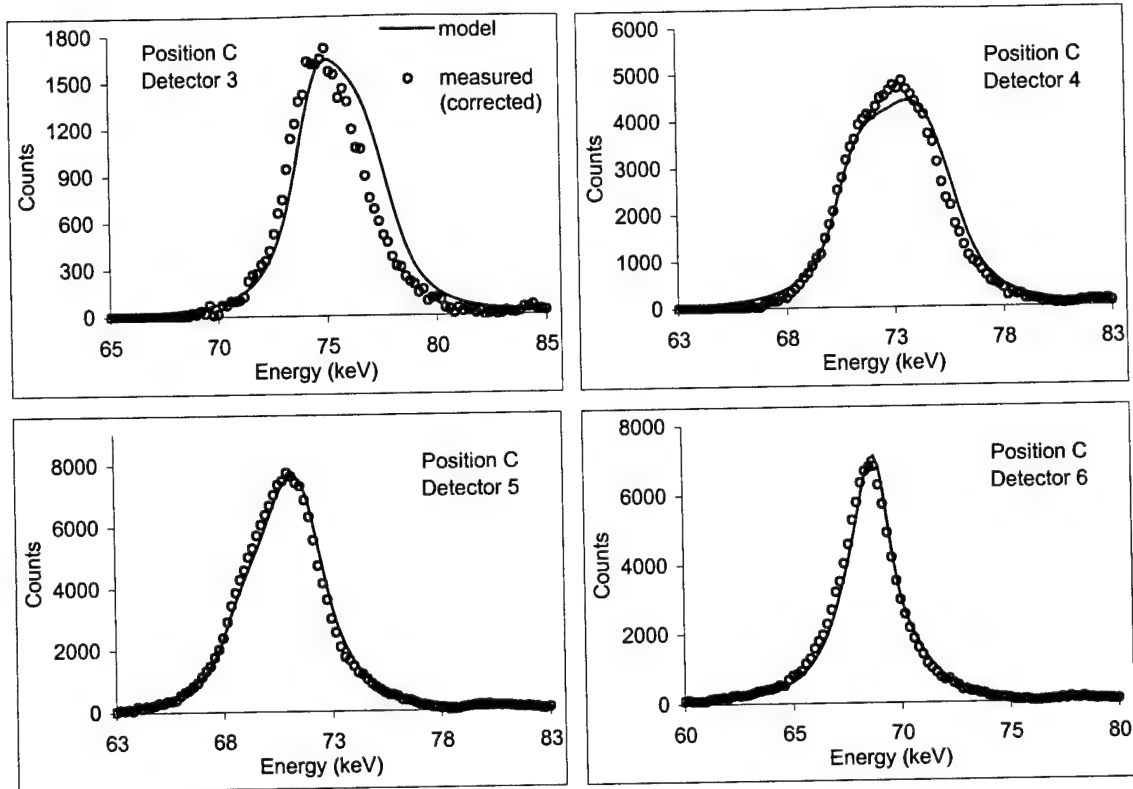
Figure 5-23. Spectra from U-Shaped Phantom, Position C.
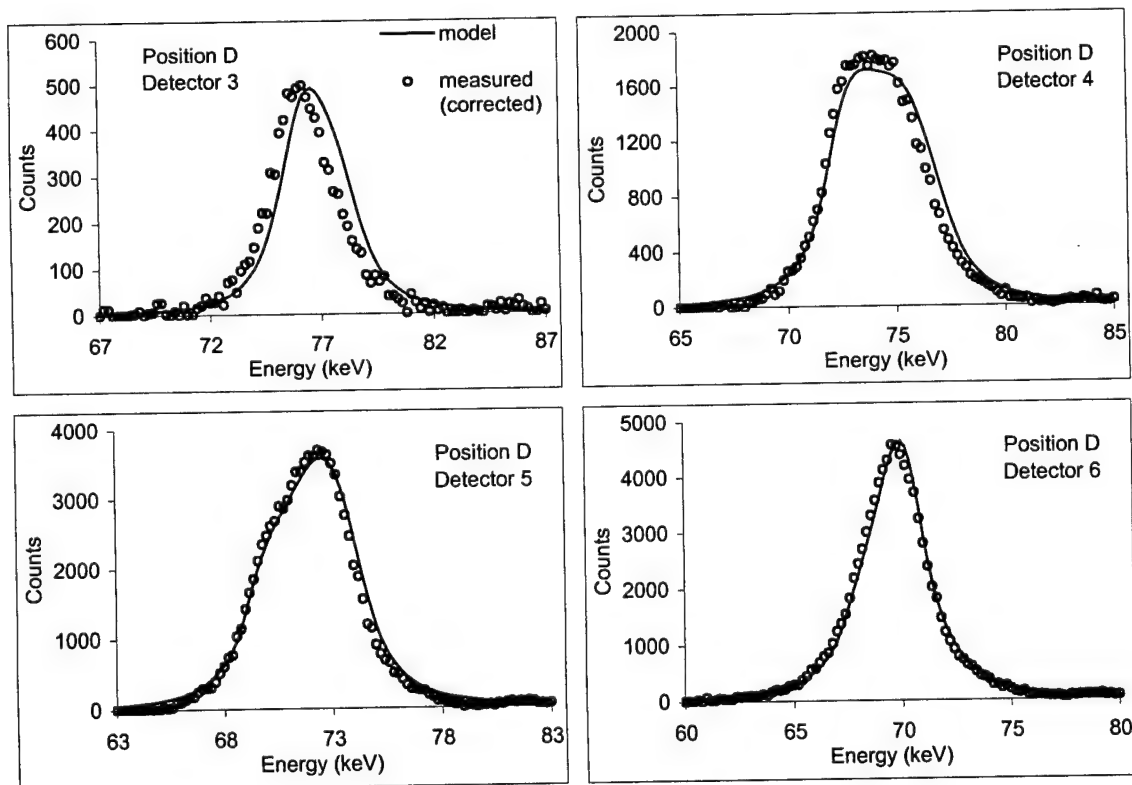
Figure 5-24. Spectra from U-Shaped Phantom, Position D.

phantom density

initial guess ρ_0

reconstruction from model spectra

reconstruction from measured spectra
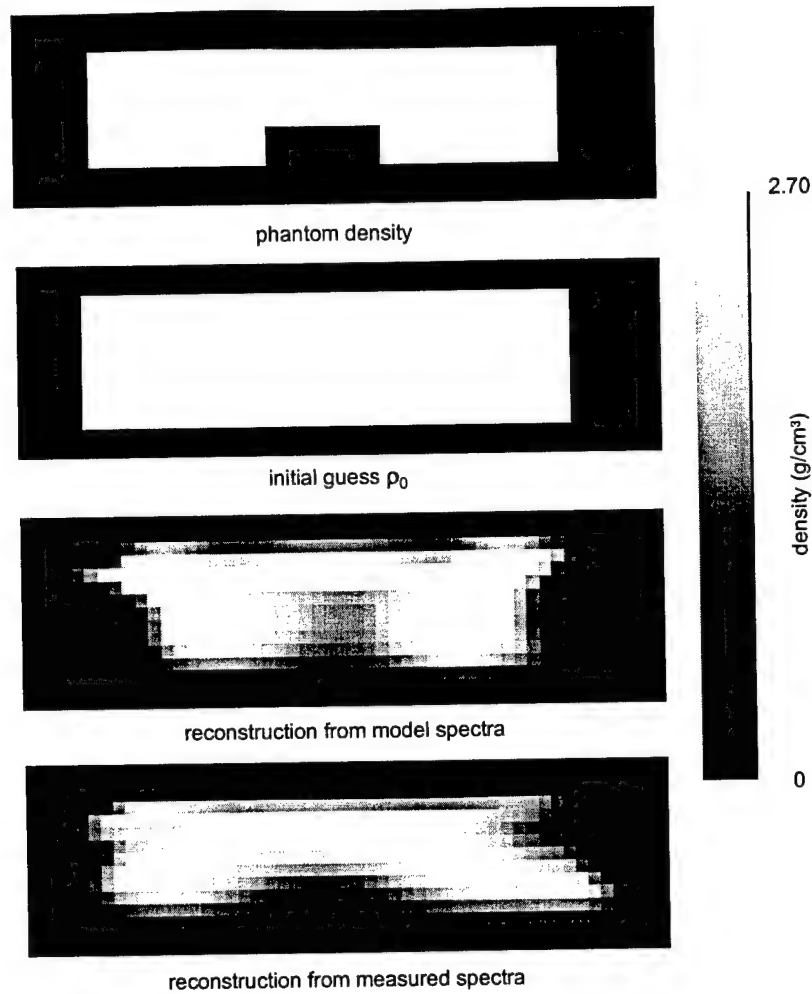
Figure 5-25. Images of the U-Shaped Phantom.

5.5 Summary of Experimental Results

The experimental results verify the ScatGram deterministic photon transport model. In some cases, scalar adjustments were required to get the modeled responses (spectra) to match the measured responses (spectra). This adjustment can be considered an instrument calibration. Such calibrations are not uncommon in complex instruments and imaging devices. With only a few exceptions in the case of the lowest-intensity signals at highest scattering angles, the modeled and recorded spectral shapes match very well, validating the impulse approximation model of the Doppler broadening.

By imaging the aluminum phantoms with the demonstration MCST system, it has shown that MCST is a plausible mode of single-sided nondestructive inspection for the detection of hidden voids in aluminum. The application of PWLS image reconstruction to multiplexed Compton scatter tomography

has been demonstrated using data collected in the demonstration system. The samples inspected were idealized due to their high density contrast and their composition from nearly pure aluminum. The demonstration system had some shortcomings, particularly the restricted field-of-view provided by the detectors. This characteristic runs counter to the MCST concept of wide field-of-view detectors capable of wide angular sampling, and hampered the demonstration system's ability to image more complex samples.

The experimental results have verified that an important component of the signal collected in MCST is the energy spectrum of multiply-scattered photons. This component increases in magnitude with the volume of the sample as shown in Table 5-1. The multiple-scatter component remains untreated in the deterministic model except for an *ad hoc* estimate. Using this *ad hoc* multiple scatter estimate produces an estimate of the single-scatter component of the signal that is subject to errors in the multiple scatter estimate. Nevertheless, the multiple scatter estimate was an adequate correction for producing respectable images of the samples. Computing the multiple scatter estimate based only on the shapes of the recorded spectra was consistent with the concept of the reconstruction process being privy to no *a priori* information about the sample. The acquisition times listed in Table 5-1 are the total summed times for all the source and array positions, but do not include time for counting background spectra.

Table 5-1. Properties of the Experimental Spectra.

Experiment	Signal-to-Noise Ratio (SNR)	Single-Scatter-to-Total Ratio (Est.)	Background-to-Total Ratio	Acquisition Time
Simple Phantom	4.92	0.69	0.33	41 hours
Void Phantom	6.47	0.67	0.19	89 hours
U-Shaped Phantom	10.85	0.62	0.08	111 hours

It remains to be seen how the presence of lower-density aluminum and a corrosion product containing oxygen and hydrogen will affect the reconstruction where only aluminum is assumed in the sample.

VI. Simulations of an Advanced MCST System

6.1.   Simulation of Various Inclusions

The demonstration MCST system was used to image selected high-contrast aluminum phantoms, testing the validity of the system model and image reconstruction algorithms. Samples encountered in the field, however, may have lower contrast and contain materials other than pure aluminum, for instance the corrosion product gibbsite, $Al(OH)_3$. Such samples are beyond the capabilities of the demonstration system, so a series of simulations was accomplished to predict how well a more advanced MCST system might perform under these conditions. The ScatGram deterministic model provided a tool to simulate the system response.

The simulated system consists of a linear array of 15 detectors, each with an entrance aperture 2.0 mm in diameter. Each detector is separated by 1.0 cm. These detectors are modeled with a wide field-of-view, meaning $\eta(\phi) = 1.0$ for the range of ϕ used; however the detectors are arranged so they all face the center of the imaging region as shown in Figure 6-1. This arrangement means that radiation enters the detectors at incident angles near $\phi = 0$. This represents a reasonable approximation of what the next generation MCST system may look like. The source and array are positioned at two symmetrical configurations as shown in Figure 6-1, providing 30 simulated spectra in the scattergram. The simulations include the same intrinsic peak efficiency and detector resolution found in the demonstration system. Adequate space must be maintained between the detector array, source, and sample to provide room for the collimators. The detector array remains parallel to the surface because this configuration provides realistic geometry for uniform fan beam collimation similar to the plates used in the demonstration system. Simulations were performed in which the detector array was tilted so that it no longer remained parallel to the sample, but no particular advantage to that configuration was observed.

Instead of assuming a particular source activity for this simulated system, it is useful to consider both counting time and source activity in units of milliCurie·seconds (mCi·s). This approach avoids choosing arbitrary source activities and collection times because long counting time can compensate for low source activity. For instance, the void phantom from Chapter 5 was imaged on the demonstration MCST system using a 43 mCi source, and data was collected for an average of 80,100 seconds per position.
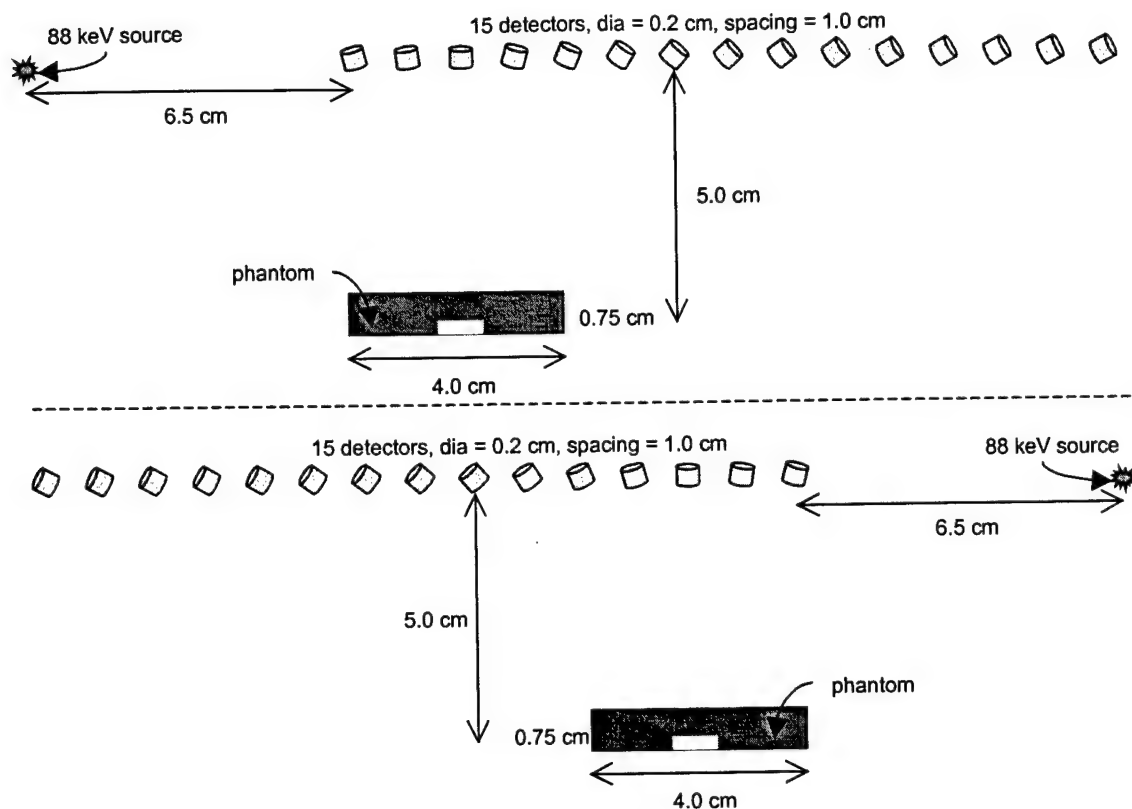
Figure 6-1. The Next Generation Configurations Simulated.

The data collected at each of the four positions, therefore, represents 3.4×10^6 mCi·s. The simulations presented below represent 4.3×10^6 mCi·s per position, but only 2 positions are needed, so there is actually about 37 percent less collection time for a given source. The intensity of background counts was chosen to simulate the background intensity found in the demonstration MCST system. The simulated spectra were randomized with statistical noise before using them in the PWLS image reconstruction, as suggested by Figure 3-7.

The sample considered measures 4.0 cm in length by 0.75 cm in height. It has 1.0 cm x 0.25 cm inclusion located at either the top or bottom surface. This inclusion is filled with air, reduced density aluminum, or the aluminum corrosion product gibbsite that is described in Section 1.5.1.

6.1.1.   Air Inclusion

This phantom is similar to those imaged with the demonstration MCST system, and establishes a baseline against which the proceeding simulations may be compared. Figure 6-2 gives the phantom density, the initial guess ρ_0 supplied to the PWLS algorithm, and the image reconstructed from the noisy
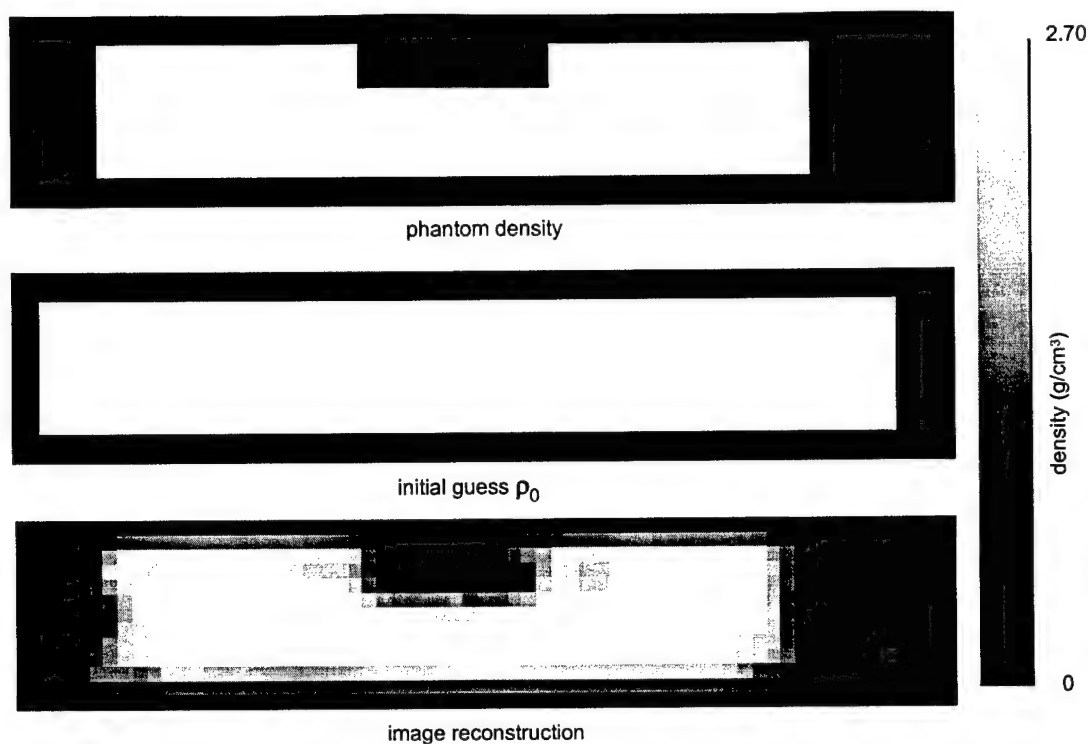
Figure 6-2. Air Inclusion at the Top Surface. 4.3 x 10^6 mCi·s per position.

spectra. The same initial guess ρ_0 will be used throughout this Section 6.1. The air inclusion is recovered

well because when it is located on the top surface near the detectors, it has a large influence on the scattered

energy spectra. Unless otherwise noted, the images in this chapter were reconstructed in 14 outer

iterations: two at $\beta = 1.0$ and $\omega = 0.8$, four at $\beta = 0.75$ and $\omega = 0.8$, four at $\beta = 0.4$ and $\omega = 0.85$, then four

at $\beta = 0.25$ and $\omega = 0.9$.

When the air inclusion is located on the side of the phantom hidden from the detectors, however, it

exerts a subtler influence on the spectra due to the attenuation of incident and scattered photons through the

sample bulk. Even though the reconstruction algorithm accounts for this attenuation, the signal is still

dominated by photons that scatter near the top surface, making spectral contributions from the bottom

surface difficult to discern. The reconstruction problem for inclusions on the bottom surface is ill posed

because large changes in the voxel densities cause small changes in the spectra. This makes it tougher to

recover features on the bottom surface with good fidelity. Figure 6-3 shows the phantom density and the

reconstruction obtained from the 30 noisy spectra. Indeed, even this high-contrast feature is not reproduced

with the same clarity as when it was located at the top surface.

phantom density

image reconstruction

2.70

density (g/cm³)

0
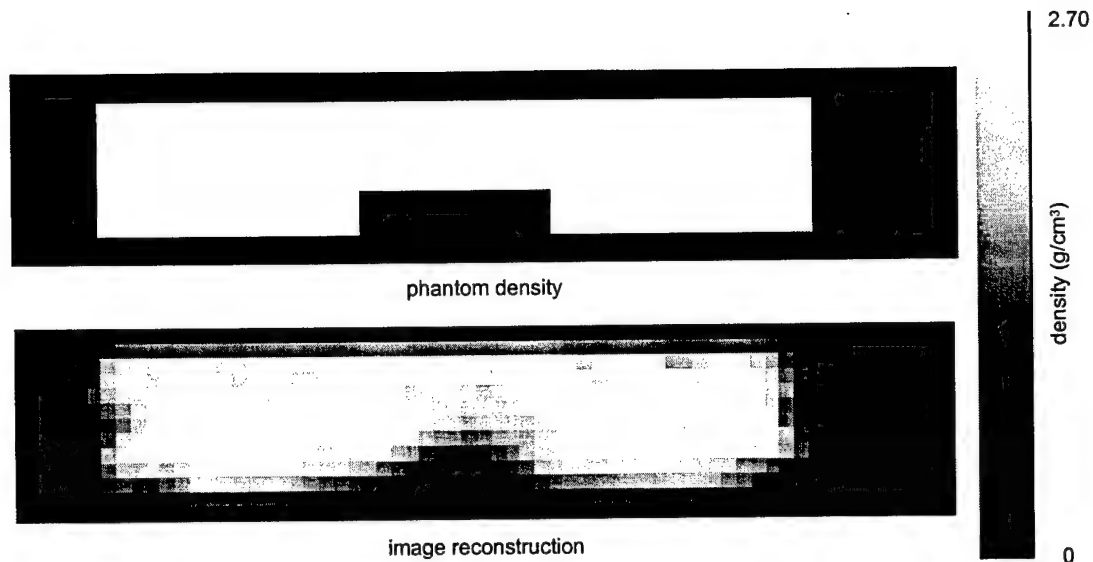
Figure 6-3. Air Inclusion at the Bottom Surface. 4.3 x 10^6 mCi·s per position.

6.1.2.   *Reduced-Density Aluminum Inclusion*

The next phantom considered has a region of aluminum with a density of 1.35 g/cm³, half the normal density of aluminum metal. This feature represents a primitive model of a corrosion anomaly. When this reduced-density inclusion is simulated on the top surface of the sample, the reconstruction shown in Figure 6-4 results. The reduced-density region is evident in the image, although its precise boundaries may not be discernible. Moving the reduced-density inclusion to the bottom surface of the phantom results in the reconstruction shown in Figure 6-5. There is an identifiable reduced density region on the lower surface of the reconstruction, but the shape and size are ambiguous.
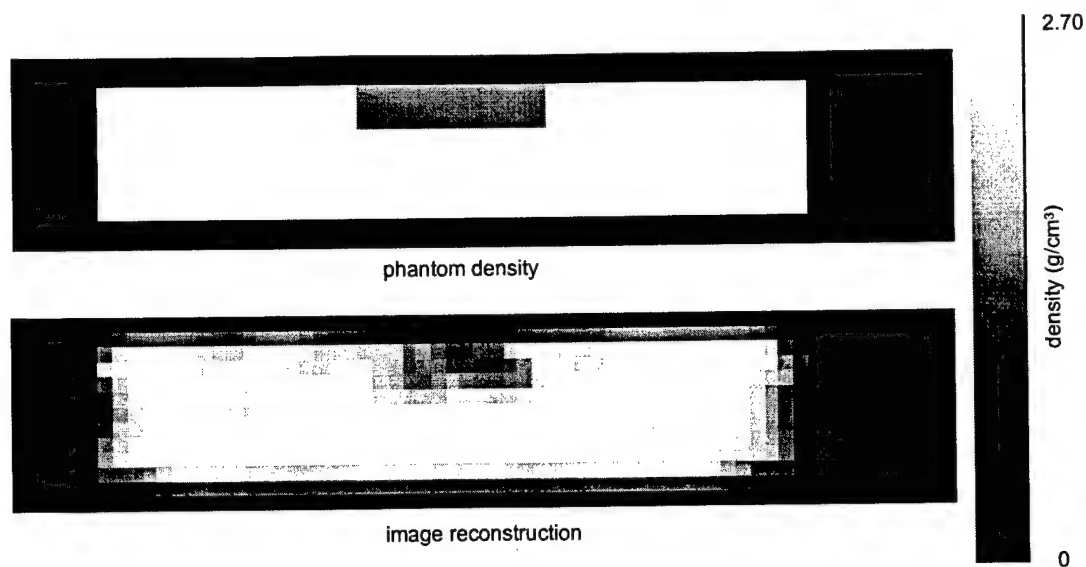
Figure 6-4. Reduced-Density Inclusion at the Top Surface. 4.3×10^6 mCi·s per position.
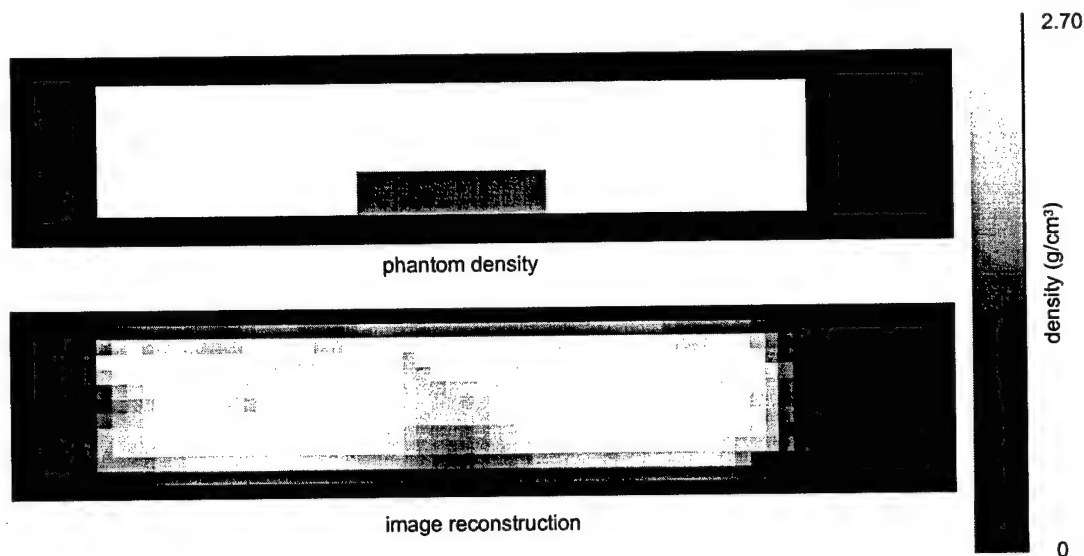
Figure 6-5. Reduced-Density Inclusion at the Bottom Surface. 4.3×10^6 mCi·s per position.

6.1.3.   Gibbsite Inclusion

Next the inclusion was modeled as the corrosion product gibbsite. It was also given a density of 1.35 g/cm³, half the density of normal aluminum metal. The density of the mineral gibbsite is slightly lower than that of aluminum, but we can expect the corroded regions to be composed of about 60 percent gibbsite and 40 percent air, by volume (Lawson, 1995). The gibbsite inclusion provides a higher-fidelity model of the composition of aluminum corrosion than the reduced-density aluminum inclusion provides.

Several important things set the gibbsite apart from the aluminum inclusion in the ScatGram code's photon transport simulation. First, the gibbsite is assigned a Compton scatter partial interaction coefficient of 0.153 cm^2/g, whereas the aluminum is assigned a coefficient of 0.142 cm^2/g (Berger, 1987). Second, attenuation of incident and scattered gammas through the gibbsite is calculated from different cross section data than the aluminum. Attenuation is based on polynomial interpolations of cross section data obtained from the XCOM cross section code (Berger, 1987). Finally, the Doppler broadening of gammas scattered in the gibbsite is not the same as those scattered in the aluminum. Photons scattered from oxygen or hydrogen atoms will have different energy distributions resulting from the different Compton profiles. As explained in Section 2.2.2, the Compton profile and incoherent scattering function of gibbsite is calculated as a weighted superposition of the Compton profiles and incoherent scattering functions of its three elements. Figure 6-6 compares the Compton profiles for aluminum, oxygen, and hydrogen. Although ScatGram includes gibbsite where appropriate, the reconstruction algorithm cannot have any *a priori* information about the sample's composition. Therefore, for the purpose of reconstruction, it must be assumed that the sample is composed entirely of aluminum. Despite the influence of gibbsite in the spectra, the PWLS reconstruction code calculates density and attenuation based entirely on cross sections of aluminum, and assumes the energy spectra contain Doppler broadening from aluminum only. This inconsistency will cause additional error and distortion in the image.

Figure 6-7 shows the results of simulating the gibbsite inclusion on the top surface. A lower-density region is recovered on the top surface, but its size is underestimated. Nevertheless, the differences
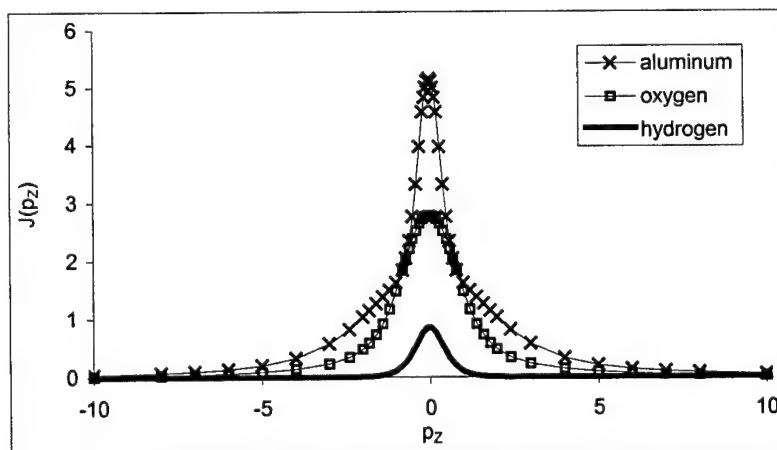
Figure 6-6. Compton Profiles for Aluminum, Oxygen, and Hydrogen.
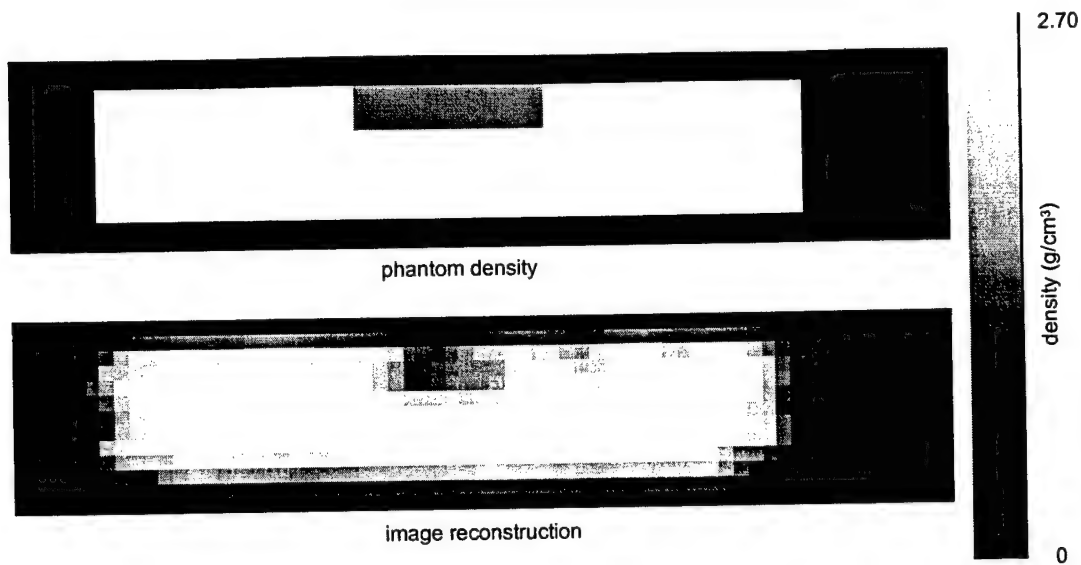
Figure 6-7. Gibbsite Inclusion at the Top Surface. 4.3×10^6 mCi·s per position.

in the energy spectra brought about by the gibbsite inclusion (as compared to the reduced-density aluminum inclusion) were not significant enough to cause complete failure of the reconstruction. Moving the gibbsite inclusion to the bottom surface leads to the results shown in Figure 6-8. This reconstruction is the most difficult to rectify with the original phantom density. Nearly all the contrast in the original phantom has been lost.
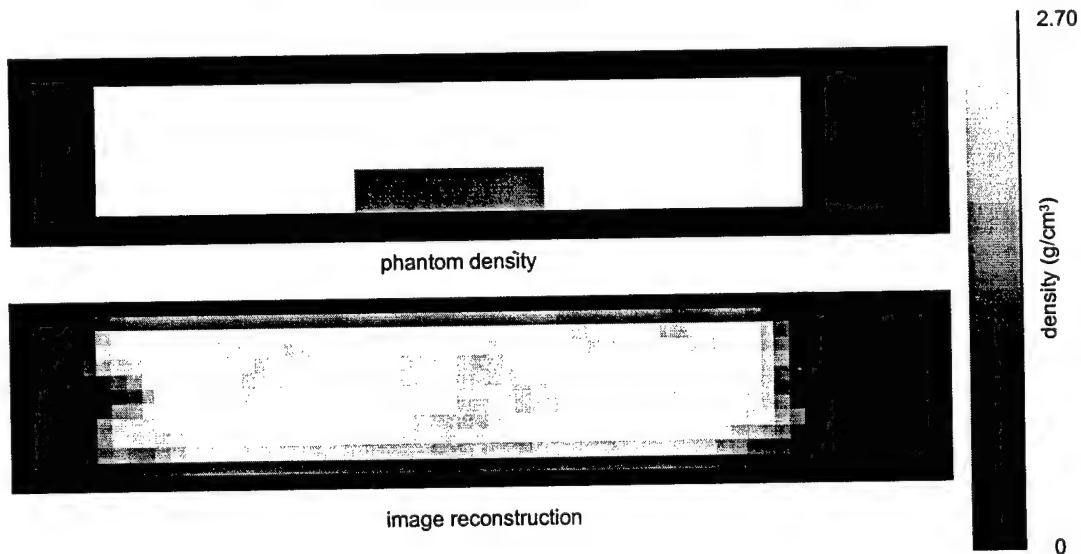
Figure 6-8. Gibbsite inclusion at the Bottom Surface. 4.3×10^6 mCi·s per position.

6.1.4. Contrast and Noise

Inspection of the simulated images reveals the presence of artifacts within the high density region that may be misidentified as lower density features. The artifacts are a result of the noisy data and the undersampling inherent in the MCST inspection scheme, but they are amplified when using the lower values of the parameter β during the later iterations. When β is reduced it sharpens the edges of the features because image smoothing is reduced and higher spatial frequencies are permitted in the solution. However, this comes at the expense of introducing higher-frequency noise artifacts. In many digital image processing applications, high frequency noise will take the form of granular noise (Gonzalez and Woods, 1992). Here the high-frequency artifacts do not appear as granular noise, but they are composed of the highest spatial frequencies allowed by the smoothing penalty. Thus there is a tradeoff between edge sharpness and noise. The parameters used here were selected to produce good contrast and edge sharpness in the images while accepting mild high frequency noise. Figure 6-9 shows the top surface air inclusion reconstruction that ended with $\beta = 0.25$ and a similar reconstruction performed by holding β at 1.0, thereby reducing the high-frequency noise at the expense of sharpness. The same noisy data at 4.3×10^6 mCi·s per position was used for both cases.
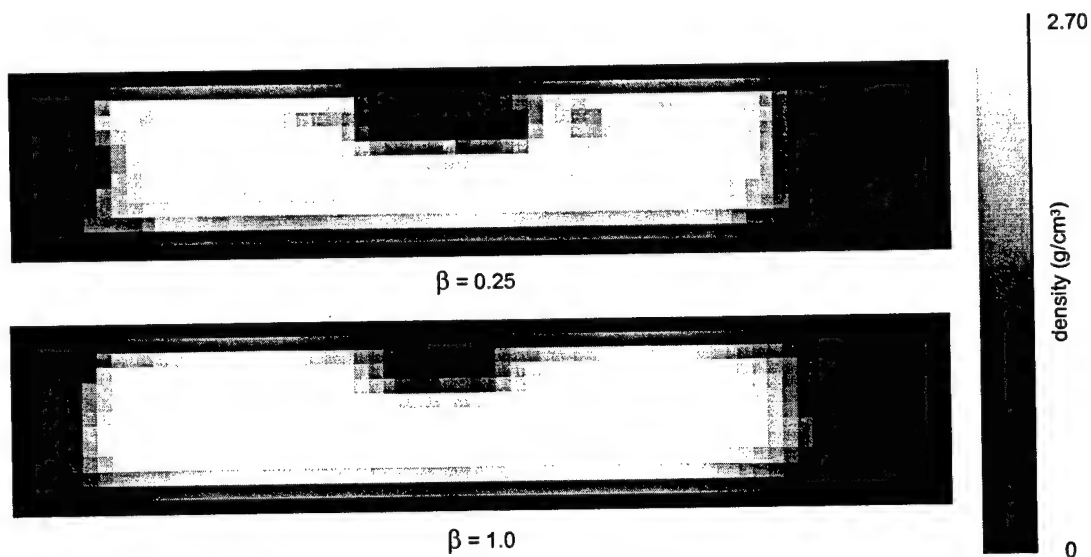
Figure 6-9. Reconstructions Comparing Two Values of β.

One way to quantify the quality of the reconstructed images is to calculate the contrast recovery. The contrast is defined as (Evans, 1998)

$$C = \frac{d_H - d_L}{d_H + d_L} \qquad (6\text{-}1)$$

where d_H and d_L are the mean density of the high-density and low-density regions, respectively. To calculate contrast in the reconstructed images, the mean densities in the regions corresponding to the phantom's actual high and low density regions are used. This approach to calculating contrast may provide a conservative figure compared to calculations that select the darkest and lightest fractions of the low-density and high-density regions. However, it provides a more consistent comparison between the actual phantoms and the recovered images. Table 6-1 gives the results.

Table 6-1. Contrast in the Simulated Images

Simulation	d_H	d_L	Contrast	Phantom Contrast	Contrast Recovery
Air Inclusion Top Surface	2.33	0.460	0.670	1.00	67.0 %
Air Inclusion Bottom Surface	2.30	1.06	0.368	1.00	36.8 %
Aluminum Inclusion Top Surface	2.39	1.64	0.184	0.333	55.3 %
Aluminum Inclusion Bottom Surface	2.37	1.82	0.132	0.333	39.6 %
Gibbsite Inclusion Top Surface	2.33	1.80	0.129	0.333	38.7 %
Gibbsite Inclusion Bottom Surface	2.38	2.24	0.030	0.333	9.0 %

The loss of signal from the bottom of the sample suggests that 88.03 keV is not penetrating enough to image samples as thick as those considered here. Table 1-1 lists $^{123}\text{Te}^m$, with a source energy of 159.0 keV, as a possible candidate. This energy would boost the mean free path of incident photons by about 37 percent and keep the energy of the scattered photons within a reasonable intrinsic peak efficiency for the detectors. This isotope is rather exotic and available in small activities in solution only. It is not clear, however, that a $^{123}\text{Te}^m$ cannot be manufactured with a higher specific activity to fit in a small-volume capsule. If such a source was developed, a dual-energy approach to MCST may be possible. The lower-energy source could be used to image the top regions of the sample, and the more penetrating source could be used to reach the bottom regions of the sample.

It is possible to reconstruct images using less intense signals than the ones modeled above. The phantom with the air inclusion on the top surface was reconstructed with several less intense, and therefore noisier, signals corresponding to 1.0×10^5 mCi·s, 3.0×10^5 mCi·s, and 1.0×10^6 mCi·s per position. These results may be compared against the 4.3×10^6 mCi·s per position results reported above. The noisiest signal corresponding to 1.0×10^5 mCi·s would not converge to a solution during reconstruction. Figure 6-10 shows the results for the other various levels, and Table 6-2 reports the contrast in the simulated images.

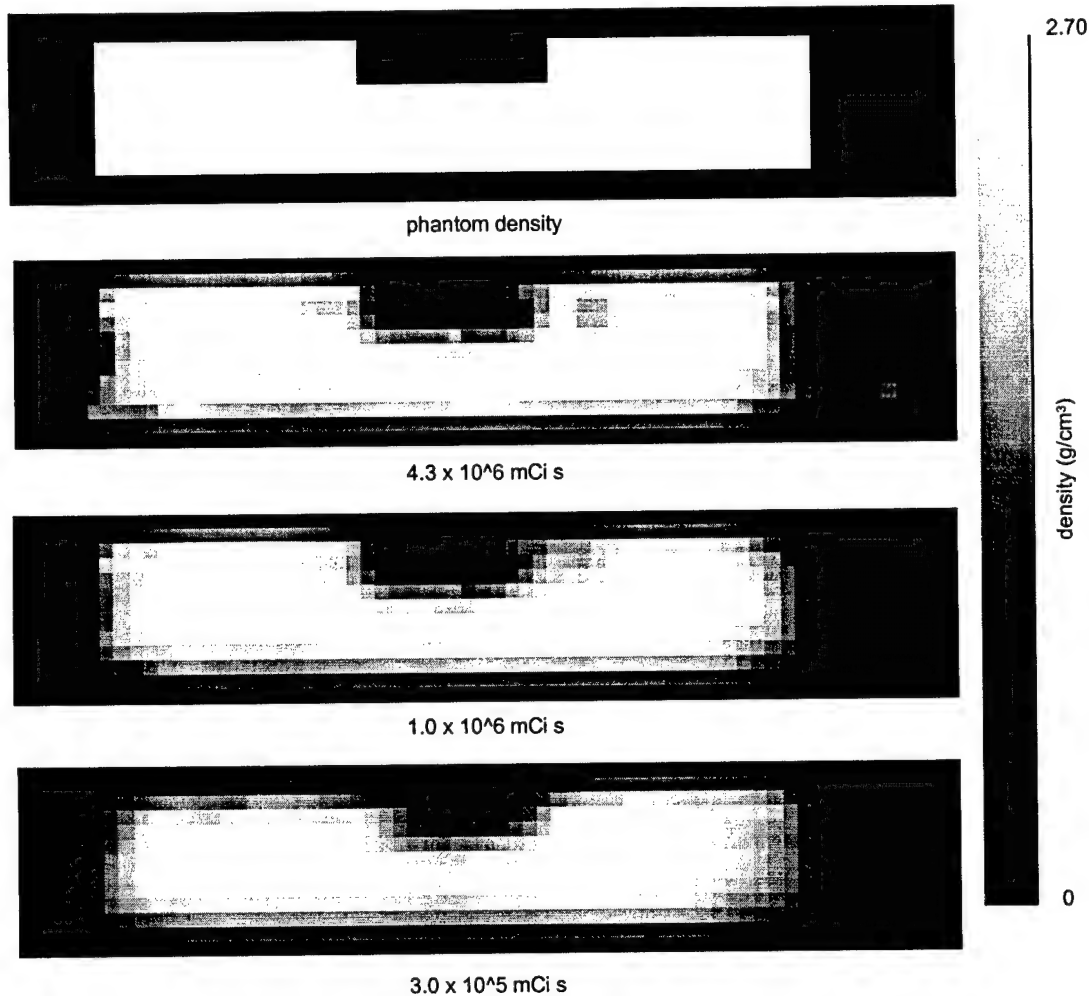Figure 6-10. Reconstructions at Various Levels of Signal Intensity.

Table 6-2. Image Contrast at Various Levels of Signal Intensity.

mCi·s	d_H	D_L	Contrast	Phantom Contrast
4.3×10^6	2.33	0.460	0.670	1.00
1.0×10^6	2.28	0.605	0.580	1.00
3.0×10^5	2.19	1.00	0.374	1.00

6.2. Scaling to Narrower Fan Beams

The next generation MCST system should move toward the capability of imaging the types of features important in the airframe inspection application. This application calls for resolutions on the order of a millimeter to detect important corroded regions. To resolve features this small, the fan beam's tomographic slice thickness must also be reduced to around 1 mm. Figure 2-13 illustrates the implications of this. While the prevalence of multiply-scattered photons will decrease, the signal intensity will fall dramatically. For instance, to maintain the number of counts collected in the demonstration MCST system, a system with a 2.5-mm wide tomographic slice would need to count approximately 10 times longer, and a system with a 1.0-mm wide tomographic slice would need to count approximately 60 times longer.

These dramatic numbers should be offset somewhat in the next generation system because it will collect more photons with its wide field-of-view detectors. The system should only have to collect in two positions per tomographic slice if a configuration like the one shown in Figure 6-1 is assumed. On the other hand, the detector apertures will probably be smaller to improve the spatial sampling, and that will decrease data throughput. Clever engineering of the fan beam collimators may allow the source and detectors to be placed closer to the sample, but one should keep in mind that placing the source too close to the sample causes the regions of the sample near the source to dominate the signal.

The simulations that produced the data shown in Figure 2-13 provide insight into how reducing the tomographic slice thickness will affect the number of mCi·s required per position. To maintain the image quality shown in Section 6.1 the signal intensity in terms of the number of counts must be maintained. Reducing the tomographic slice thickness to 2.5 mm will require a factor of 10 increase to 4.3 x 10^7 mCi·s per position, and reducing the fan beam intensity to 1 mm will require a factor of 60 increase to 2.6 x 10^8 mCi·s per position. Therefore, even if a 1 Curie ^{109}Cd source could be obtained for use an instrument having a 2.5-mm tomographic slice, it would still require 43,000 seconds (12 hours) per position to produce the images shown in Section 6.1.

6.3. Sources for an Advanced MCST System

An important liability for the overall efficiency of MCST is the 3.6% intensity of the 88 keV line from ^{109}Cd. If the next-generation MCST system could utilize an isotope with a single gamma emission of

85% intensity near 100 keV, it would represent a factor of 24 increase in the usable intensity. What took hours to acquire with a 1 Curie ^{109}Cd source would take only minutes with the new 1-Curie source. Furthermore, source energies in the 100-150 keV range would provide better penetration of thick samples than 88 keV, but still maintain good overall system efficiency. Unfortunately there are no radionuclides presently available in the marketplace with the desired properties and suitably high activity.

A search of radionuclides available from leading manufacturers uncovered two candidates that have relatively high-intensity emissions in the 100 keV region, ^{123}Te^m and ^{144}Ce. Both are free from higher-energy emissions that would contaminate the scattered gamma spectrum. They also have adequate half-lives that would allow source replacement on the order of months. They are both metallic elements, so their specific activity is theoretically high enough to manufacture a small-volume capsule provided enough radioactive material is available. The isotope ^{123}Te^m emits a 159.0 keV gamma at 85% intensity. It has a 119 day half life. The isotope ^{144}Ce emits a 133.5 keV gamma at 10.8% intensity, so the intensity advantage is not as compelling. It has a 285 day half-life.

Unfortunately, both of these isotopes are only available in microCurie quantities (ORNL, 1998). They are used primarily in mixed nuclide calibration sources. The isotope ^{123}Te^m is produced by neutron irradiation of separated ^{122}Te in a reactor. The difficulty in producing large quantities of ^{123}Te^m is its large thermal neutron cross section, 370 barns, relative to that of ^{122}Te at 2.4 barns (General Electric Co., 1996). Thus the ^{123}Te absorbs neutrons at a far greater rate than it is produced, resulting in large amounts of ^{124}Te and only small amounts of the desired isotope. Furthermore, the activity of the major impurity, ^{131}I, can be as much as 15% of the activity of ^{123}Te^m (ORNL, 1998) and it emits a 364keV gamma. The other candidate isotope, ^{144}Ce, is produced by neutron irradiation of separated ^{142}Ce in a reactor. The intermediate isotope, ^{143}Ce, has a short half life of 31 hours (General Electric Co., 1996), so very high neutron fluxes would be required to efficiently produce the ^{144}Ce. These difficulties explain why the two candidate isotopes are now only available in low activities.

6.3.1.   Polychromatic Sources

In this project the choice of isotopes was limited by the requirement for a single gamma emission (a monochromatic gamma source) near 100 keV. This was an important constraint for this project which sought to develop and demonstrate new system modeling and reconstruction codes. The constraint was

appropriate considering the primitive stage of MCST development. The development and verification of

the modeling and reconstruction tools was simplified by the fact that a single value for E_0 was considered.

It appears, however, that a monochromatic radioisotope may not be available with good intensity in the

optimal energy range. It may be possible, however, to use an isotope that has two gamma emissions near

100 keV in the next generation MCST system.

To treat the dual-energy source, the scattergram simulation will simply calculate two single-scatter

spectra, one for each of the gamma-ray energies, then superimpose them. The relative intensity of the two

component spectra will be calculated from the intensity of the corresponding emissions. Important

distinctions between the two emission energies must be maintained. For instance, each will require

separate attenuation calculations and the Compton scatter partial interaction coefficient σ in the P_{CS} term of

Equation (2-8) will change with source energy E_0. The E_0 dependence of Klein-Nishina (Equation (1-4)),

the incoherent scattering function, and the impulse approximation (Equation (1-7)) will require separate

$\Theta(Z_m, E_k, \theta_q)$ (Equation (2-11)) for each source energy. Two separate versions of the ρ-independent $\mathbf{A}^0$

system mapping must be calculated for each source energy per Equation (2-27) and stored as $\mathbf{A}^0_1$ and $\mathbf{A}^0_2$

for later use by the iterative reconstruction code. These two mappings must be stored separately because

the attenuation, which differs for each source energy E_0, is not a linear function of the voxel densities. The

deterministic system model still provides a mapping between the voxel densities and the scattergram

measurements. The role of image reconstruction remains solving the reverse problem of finding a set of

densities to match the scattergram measurements.

Recall that the PWLS image reconstruction code treats the system as explicit and linear within the

inner PWLS iteration, then updates the nonlinear ρ dependencies for each outer iteration. Therefore the

algorithm for the inner iteration will not change with a dual-energy source, but the matrix $\mathbf{A}$ will be updated

at each outer iteration based on both the $\mathbf{A}^0_1$ and $\mathbf{A}^0_2$ system mappings. Equation (3-27) is replaced with

$$
A(\rho)(j, E_n, m) = A(\rho)(i, m) \tag{6-2}
$$
$$
= \left[I_1 A_1^0(i, m) \cdot a_{in}\left(\rho, j, m, E_{0_1}\right) + I_2 A_2^0 \cdot a_{in}\left(\rho, j, m, E_{0_2}\right) \right]
$$
$$
\cdot a_{out}\left(\rho, j, m, E_n\right)
$$
$$
i = (j-1)N_E + n
$$

where E_{0_1} and E_{0_2} are the two source energies, and I_1 and I_2 are their relative intensities. This change is implemented on the second line of the algorithm outline shown in Figure 3-6.

With the addition of another source energy, however, the reconstruction problem becomes more poorly conditioned because the ambiguity of the scattered photon spectra will increase. There will be a range of energies for which any scattered photon's original energy E_0 will not be distinguishable, introducing another layer of complexity in the system model. Despite the greater difficulty in image reconstruction, a dual-energy source may be the best way to overcome the MCST efficiency problem that leads to long acquisition times with ^{109}Cd.

The ability to use a dual-energy source will make some appealing source isotopes available that are already widely used and commercially available in sealed capsules. The primary candidates are ^{57}Co and ^{153}Gd. The isotope ^{57}Co emits 122.06 keV gammas at 85.6% intensity, 136.47 keV gammas at 10.6% intensity. These energies will provide better penetration in aluminum for imaging thicker samples, but their energies are still low enough to provide good overall system efficiency in the planar HPGe detectors. The high intensity of these lines means about a factor of 27 improvement over ^{109}Cd in the number of useful photons per unit activity. It has a half-life of 272 days. ^{57}Co emits another gamma at 692.0 keV but only at 0.16% intensity. The other candidate isotope ^{153}Gd emits 97.43 keV gammas at 29.5% intensity and 103.18 keV gammas at 21.1% intensity. This isotope may be recognized as the one contaminating the demonstration system's ^{109}Cd source as described in Chapter 4. These energies are well suited for the application, but ^{153}Gd also emits some weaker gammas that may complicate the spectrum. It produces an 83.37 keV gamma at 0.21% intensity, and a 69.67 keV gamma at 2.42% intensity. The first of these may be weak enough to ignore. The second lies at the low-energy end of the single-scatter spectrum from the primary emissions, so it may also be of little concern. The ^{153}Gd radioisotope offers a factor of 14 advantage over ^{109}Cd in the number of useful photons per unit activity. Its half-life is 242 days.

Another appealing solution would be an energy-tunable x-ray tube that would be available in far greater strengths than radioisotopes. The x-ray source would also enjoy the significant safety advantage of having an on-off switch. Unfortunately x-ray tubes produce a continuous source energy spectrum that would need to be incorporated into the MCST system model – no small undertaking. The source spectrum

would introduce another source of error, and provide more ambiguity in the scattered spectra than even the

dual energy source would.

VII. Summary and Recommendations

7.1. Summary

The feasibility of a new imaging modality called multiplexed Compton scatter tomography (MCST) has been established for one-sided imaging of aluminum samples. Preliminary results are encouraging for the MCST technique as a noninvasive inspection tool for one-sided applications in which standard transmission tomography is not possible.

The new imaging modality represents an advance over Compton backscatter scanners that inspect small volumes independently and produce an image by compiling the individual measurements. MCST inspects extended regions simultaneously by multiplexing with multiple energy-discriminating detectors having comparatively wide fields-of-view. It exploits the relationship between a Compton-scattered photon's energy shift and its scattering angle to localize possible scattering locations. The primary components of an MCST system are a radioisotope source, an array of energy-sensitive photon detectors, and fan beam collimators that restrict the imaging region to a narrow tomographic slice.

This project has focused on the one-sided inspection of thin, low-Z samples, specifically aluminum. It was determined that the ideal source energy for this application is near 100 keV. This application posed new challenges not considered in previous Compton scatter tomography research. For instance, the application constrained all system components to lie on one side of the sample. The low energy of the gamma rays meant that the photon scattering physics was heavily influenced by the momentum distribution of atomic electrons.

A deterministic model was introduced to predict the spectra of singly-scattered photons collected in an MCST system. The model is embodied in a Fortran90 code called ScatGram. This model incorporates several effects not considered in deterministic (Arendtsz, 1995b) or probabilistic (Prettyman, 1991) models previously described for similar applications. It models the intensity of scattered photons incident on a finite-sized detector aperture, rather than treating detectors as points; and it allows the source to be modeled as a finite-sized object, rather than as a point. This is important because the dimensions of features in the sample are often on the order of these system components. The ScatGram code also allows various aspects of the detector response to be incorporated into the model such as efficiency, energy

resolution, and variation of detector efficiency with incident angle. Incorporation of these factors directly into the system response model avoids convolving ideally-modeled data with experimentally measured detector response functions. It gives the algorithm the flexibility to consider systems with hypothetical detector responses without actually having those detectors in the laboratory.

The most significant advancement in the deterministic model introduced here is the inclusion of Doppler broadening of the Compton scattered photons. Previous researchers in Compton Scatter tomography have assumed that the relationship between a Compton-Scattered photon's energy and scattering angle obeyed the one-to-one Compton equation, derived from a stationary-electron model (Arendtsz, 1995; Prettyman, 1991; Norton, 1994). In reality, the momentum distributions of atomic electrons give rise to a distribution in energies for any given scattering angle – the Doppler broadening phenomenon. The broadening shape is dependent on the scattering atom, and is particularly significant at the energies of interest here, below 100 keV.

The deterministic model does an impressive job predicting the shapes of the scattered photon spectra. This was verified by benchmarking against an accepted Monte Carlo radiation transport code, MCNP Ver. 4B, and by comparison with experimentally measured results. The ScatGram results matched those of MCNP almost perfectly. In the case of the experimental results, mild scalar adjustments were required to match the intensities of the model spectra to the data, but the spectral shapes generally matched quite well. This adjustment may be considered an instrumental calibration. A rudimentary estimate for the spectra of multiply-scattered photons was required to subtract this component from the measured spectra. It is important that the modeled spectra match the measured ones, because the deterministic model provides the foundation for reconstructing electron density images from the set of measured spectra.

Two image reconstruction methods were investigated for the MCST system: filtered backprojection and iterative image reconstruction. It became clear that iterative reconstruction was the only realistic choice considering the limited amount of data available from which to reconstruct an image.

A new algorithm for iterative reconstruction was introduced. The reconstruction problem in MCST is implicit and nonlinear, requiring two levels of iteration. The penalized weighted least squares (PWLS) algorithm of Fessler (Fessler, 1994) was used to find a solution assuming a linear system of equations. The latest solution estimates were then used to update the nonlinear dependencies in the system,

and the process repeated until both levels of iteration converged to a stable solution. The absolutely critical feature of the PWLS algorithm is the penalty function, or prior, that forces the solution to exhibit some assumed characteristics of the sample. The penalty function proved adequate to overcome the poor conditioning of the MCST reconstruction problem, but introduced some unavoidable blurring in the images. The advanced features incorporated in the deterministic system model allows measured energy spectra to be used directly for image reconstruction without first deconvolving them with a detector response function.

The first one-sided MCST system was assembled and used for this research. The central components were a 6-element array of planar high-purity germanium (HPGe) detectors, fan beam collimators, and radionuclide source. The demonstration multiplexed Compton scatter tomograph was successful in fulfilling its objective: to image simple high-contrast aluminum phantoms as a demonstration of the principles of multiplexed Compton scatter tomography. In the process, it helped validate the analytical model and image reconstruction codes. Unfortunately, many of the components of the demonstration system are not well suited to the MCST application. The detectors have a restricted field-of-view and the electronics are prone to drifting energy calibration. Two of the detectors suffer from poor energy resolution either from excess leakage current (detector 6) or periodic breakdown (detector 2).

The limitations of the demonstration MCST system described here will not be shared by the next generation MCST system designed from the ground up and built from components better-suited to the MCST application. Most importantly, a dedicated MCST system will have detectors with wider field of view, and digital signal processing that is not prone to drifting energy calibration. Preliminary modeling of a next-generation MCST system was performed to ascertain the effect of corrosion product in the sample. The spectral effects caused by the presence of oxygen and hydrogen were sufficient in some cases to make the reconstruction unsuccessful when the reconstruction algorithm assumed aluminum was the only material present.

Perhaps the most serious obstacle to developing a practical MCST device is the very poor efficiency, resulting in impracticably long counting times. Efficiency falls off rapidly as the tomographic slice thickness is narrowed to resolve smaller and smaller features. Efficiency of the detectors is already quite good, but stronger sources can help to a limited degree. The demonstration system uses only a 3.6%

intensity emission, the 88.0 keV gammas from [109]Cd. Using a more intense emission line will boost the efficiency. The penetrating power of 88.0 keV photons is not adequate to reliably recover features on the inaccessible side of an aluminum sample more than a few millimeters in thickness. A more energetic source is needed for thick samples. Unfortunately, a clear candidate isotope with a monoenergetic gamma emission does not exist. It may be possible to use a [57]Co source despite its two gamma emissions at 122 and 136 keV. This isotope provides much higher intensity and deeper penetrating radiation, but the dual energies will complicate the image reconstruction.

7.2.   Recommendations

A better approximation to the multiple scatter component of the signal must be developed to fully exploit the information in the MCST energy spectra. The multiple scatter approximation can be implemented as a correction to the raw energy spectra, as it was in this research. However the multiple scatter signal, like the single scatter signal, is a function of the unknown voxel densities. This suggests that a multiple scatter model could also be incorporated into both the scattergram simulation code and the image reconstruction algorithm. Preliminary work has begun on building a deterministic algorithm to calculate the multiple scatter signal in an MCST system (Gerts, 1999).

Questions remain about the impact of other materials in the aluminum sample such as paint, steel rivets, and corrosion. Preliminary modeling indicated that in some cases the presence of corrosion product could ruin the reconstruction. It should be possible to develop an adaptive reconstruction code that assigns different materials to suspect regions of the image.

The next generation of detectors used for MCST should be designed with the MCST application in mind. They must accept photons from a wide range of incident angles at similar efficiencies and similar peak-to-total ratios. Significant improvements can be made by designing detectors where the aperture is very close to the detector crystal as illustrated in Figure 4-12. A detector array should be designed so that all the detector apertures face the imaging region for maximum efficiency. The energy resolution of planar intrinsic high-purity germanium (HPGe) detectors is adequate for the 100 keV energy region, especially considering the width of the Doppler broadening overwhelms that of the detector resolution. Using germanium, however, limits one to using detectors with volumes similar to those used here in order to

maintain good intrinsic peak efficiency in the 100 keV energy region. This means that it will not be possible with germanium to place adjacent detectors closer than about 1 cm apart.

Some modifications to the existing detector array can improve its suitability for the MCST application. The most important modification is removing the round holes in the cryostat endcap that constitute a single-bore collimator in front of each detector element. Replacing the round holes with a continuous rectangular beryllium window as shown in Figure 7-1 will increase the detectors' fields of view. The tin mask will still be needed to prevent scatters in the aluminum endcap, but the tapered holes could be replaced with a long, continuous slit. Furthermore, the aluminum cages surrounding each detector crystal should be fabricated from a more absorbing, high-Z metal such as tin, tungsten, cadmium, etc. The close proximity of the cage to the germanium crystal combined with the endcap modification will allow a high-Z cage to act as the detector aperture without the 6 mm aperture-to-crystal offset that's responsible for the current field of view problems.
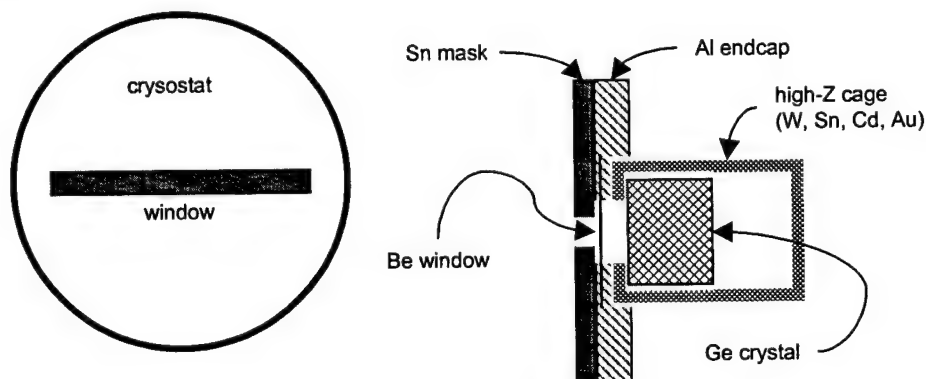

Figure 7-1. Recommended Modifications to Detector Array.

The volume of germanium needed to stop 100 keV photons may lead the designer of the next generation MCST system to consider cadmium-zinc-telluride (CdZnTe) detector crystals. The higher atomic number (Z) of CdZnTe means greater stopping power, so the volume of the detector crystal may be reduced significantly without sacrificing peak efficiency. More detectors could be packed together to improve spatial sampling. The bandgap of CdZnTe is wider than that of Ge, however, so fewer charge carriers are generated per keV, and consequently the energy resolution is poorer. The energy resolution also suffers from charge collection difficulties in this material stemming from differences in electron and hole mobility (Lund, 1996). The wide bandgap, on the other hand, means that the CdZnTe detectors can be operated at room temperature, which may have a logistical appeal to the designer. For instance, the

CdZnTe array could be hoisted on a robotic arm to inspect an aircraft wing without hoisting gallons of liquid nitrogen along with it; it could be flipped upside-down without concern of spillage, etc. When operated at room temperature the energy resolution is dominated by electronic noise, and not by the statistics of charge collection (Lund, 1996). Energy resolutions of 4.0 keV FWHM at 60 and 122 keV are reported for a 2 x 10 x 10 mm^3 CdZnTe detector operated at room temperature (Bertolucci, 1998). Improvements can be realized using miniature thermoelectric cooling to bring the operating temperature down to –45°C. Resolutions of 1.0 keV FWHM at 122keV and 2.5 keV FWHM at 662 keV have been reported in small-volume detectors operated this way (Khusainov, 1996).

Another detector possibility is the new generation of germanium strip detectors that can perform spectroscopy and register position of interaction along segmented germanium strips. One such detector has an active volume of 5.0 cm x 5.0 cm x 1.0 cm, which provides photopeak efficiencies of 80% to 90% for the range of energies in MCST (Inderhees, 1997). The energy resolution is about 1.5 keV FWHM at 59.5 keV (not as precise as the planar HPGe detectors), but position resolution is on the order of the 2-mm pitch of the individual strips (Kroeger, 1996). This position resolution would create finer spatial sampling than individual planar detectors could provide.

Nature has provided limited choices with respect to the available gamma ray emissions from radioisotopes. The [109]Cd source used in this project was selected because it was the only readily-available radioisotope with a single gamma ray emission in the energy region considered. It may be possible however, to use a [57]Co or [153]Gd source with two useful gamma emissions. These isotopes are widely available from commercial suppliers (Isotope Products Laboratories, 1995; Amersham Corp., 1994; North American Scientific, Inc., 1994). They offer much greater intensity of the useful gamma emissions and better penetration of the sample with higher-energy photons. One of these isotopes should be considered for the next generation MCST system.
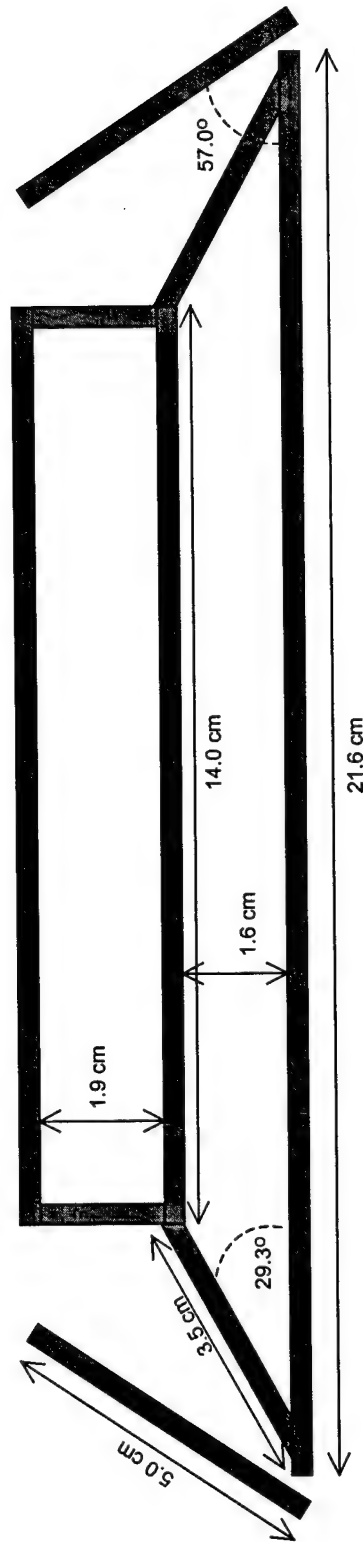
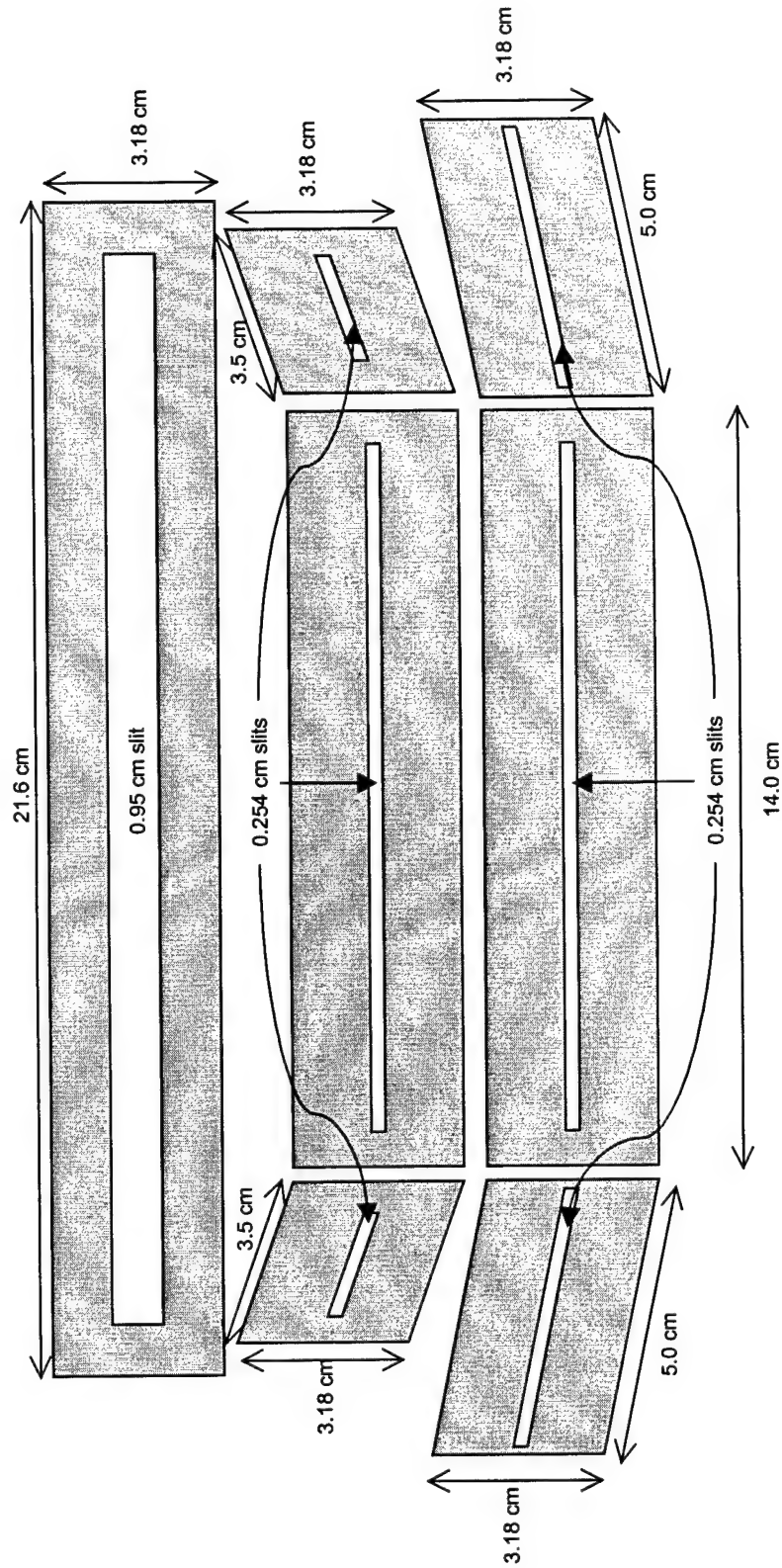Figure A-1. Relative Positions and Orientations of the Collimator Plates.

Figure A-2. Dimensions of the Collimator Plates. All plates are machined from tin sheet metal and are 0.3175 cm in thickness

Bibliography

Amersham Corp. <u>Radiation Sources for Industrial Gauging and Analytical Instrumentation</u>. Product Catalog. Arlington Heights, IL: Amersham Corp., 1994.

Arendtsz, Nina V. and Esam M. A. Hussein. "Energy-Spectral Compton Scatter Imaging; Part I: Theory and Mathematics, Part II: Experiments" <u>IEEE Transactions on Nuclear Science, Vol. 42, No. 6</u>: 2155-2172 (December 1995).

Arendtsz, Nina V. <u>Compton Scatter Tomography with Wide Field-of-View Energy-Discriminating Detectors</u>. The University of New Brunswick, Fredericton, New Brunswick, Canada, July 1995.

Barrett, Harrison H. and William Swindell. <u>Radiation Imaging; The Theory of Image Formation, Detection, and Processing</u>. New York: Academic Press, 1981.

Berger, M. J. and J.H. Hubbell. <u>XCOM: Photon Cross Sections on a Personal Computer</u>. Version 1.2. Gaithersburg, MD: National Bureau of Standards Center for Radiation Research, 1987.

Berstrom, P.M., Jr. and R.H. Pratt, "An Overview of the Theories Used in Compton Scattering Calculations," <u>Radiation Physics and Chemistry, Vol. 50, No. 1</u>: 3-29 (July 1997).

Bertolucci, E. and others. "Imaging Performance of Single-Element CdZnTe Detectors for Digital Radiography," <u>IEEE Transactions on Nuclear Science, Vol. 45, No. 3</u>: 406-416 (June 1998).

Biggs, F., L.B. Mendelsohn and J.B. Mann. "Hartree-Fock Compton Profiles," <u>Atomic Data and Nuclear Data Tables, Vol. 16, No. 3</u>: 202-222 (September 1975).

Bray, Donald E. and McBride, Donald. <u>Nondestructive Testing Techniques</u>. New York: John Wiley & Sons, 1992.

Cho, Z. H. and Joie P. Jones and Manbir Singh, <u>Foundations of Medical Imaging</u>. New York: John Wiley & Sons, 1993.

Cooper, Malcom J. "Compton Scattering and Electon Momentum Distributions," <u>Advances In Physics, Vol. 20, No. 86</u>: 453-491 (1971).

Cooper, Malcom J. "Compton Scattering and Electron Momentum," <u>Contemporary Physics, Vol. 18, No. 5</u>: 489-517 (1977).

Cooper, Malcom J., "Compton Scattering and the Study of Electron Momentum Distributions," <u>Radiation Physics and Chemistry, Vol. 50, No. 1</u>: 63-75 (July 1997).

Dix, E. H., Jr. "Corrosion of Light Metals (Aluminum and Magnesium)," in <u>Corrosion of Metals</u>. Ed. American Society for Metals. Cleveland: American Society for Metals, 1946.

EG&G Ortec, Inc. <u>Modular Pulse-Processing Electronics and Semiconductor Radiation Detectors</u>. Product Catalog. Oak Ridge, TN: EG&G Ortec, 1997.

Eisenberger, P. "Electron Momentum Density of He and H_2; Compton X-Ray Scattering," <u>Physical Review A, Vol. 2, No. 5</u>: 1678-1686 (November 1970).

Evans, Brian L., Martin, J. B. and L. W. Burggraf. "Nondestructive Inspection of Thin, Low-Z Samples Using Multiplexed Compton Scatter Tomography," <u>1997 Materials Research Society Symposium Proceedings</u>, Boston, MA; November 1997. 297-308.

Evans, Brian L., Martin, J. B., Burggraf, L. W., and M. C. Roggemann. "Nondestructive Inspection Using Compton Scatter Tomography," IEEE Transactions on Nuclear Science, Vol. 45, No. 3: 950-956 (1998).

Evans, Brian L., Martin, J. B., Burggraf, L. W., and M. C. Roggemann. "Nondestructive Inspection Using Compton Scatter Tomography," 1997 IEEE Nuclear Science Symposium, Albuquerque, NM; November 1997. 386-390.

Evans, Brian L., Martin, J. B. and M. C. Roggemann. "Deconvolution of Shift-Variant Broadening for Compton Scatter Imaging," Nuclear Instruments and Methods in Physics Research A: Vol 422, No. 1: 661-666 (1999).

Evans, Brian L., Martin, J. B., and L. W. Burggraf. "Characterization of a Multiplexed Compton Scatter Tomograph for Nondestructive Inspection of Thin, Low-Z Samples," 1998 IEEE Nuclear Science Symposium, Toronto, Canada; November 1998.

Evans, Robley D. The Atomic Nucleus. New York: McGraw-Hill, 1965.

Fessler, Jeffrey A. "Penalized Weighted Least-Squares Image Reconstruction for Positron Emission Tomography," IEEE Transactions on Medical Imaging, Vol. 13, No. 2: 290-300 (June 1994).

General Electric Company. Nuclides and Isotopes: Chart of the Nuclides, 15th Ed. San Jose, CA: General Electric Nuclear Energy, 1996.

Gerts, David. Double Scatter Spectrum for the Multiplexed Compton Scatter Tomograph. MS thesis, AFIT/GAP/ENP/99M-03. Graduate School of Engineering, Air Force Institute of Technology (AU), Wright-Patterson AFB, OH, January 1999.

Godard, Hugh P. and others. The Corrosion of Light Metals. New York: John Wiley & Sons, 1967.

Gonzalez, Rafael C. and Richard E. Woods. Digital Image Processing. New York: Addison-Wesley, 1992.

Harding, G. and Kosanetzky, J. "Scattered X-Ray Beam Nondestructive Testing," Nuclear Instruments and Methods in Physics Research, A280: 517-528, (1989).

Harding, G., "Inelastic Photon Scattering: Effects and Applications in Biomedical Science and Industry," Radiation Physics and Chemistry, Vol. 50, No. 1: 91-111 (July 1997).

Hubbell, J.H., and others. "Atomic Form Factors, Incoherent Scattering Functions, and Photon Scattering Cross Sections," Journal of Physical and Chemical Reference Data, Vol. 4, No. 3: 471-494 (1975).

Hubbell, J.H., "Summary of Existing Information on the Incoherent Scattering of Photons, Particularly on the Validity of the Use of the Incoherent Scattering Function," Radiation Physics and Chemistry, Vol. 50, No. 1: 113-124 (July 1997).

Inderhees, S. E., and others. "Spectroscopy, Imaging, and Compton-Scatter Polarimetry with a Germanium Strip Detector," IEEE Transactions on Nuclear Science, Vol. 43, No 2: 1467 (1996).

Isotope Products Laboratories. Radiation Sources for Research, Industry, and Environmental Applications. Product Catalog. Burbank, CA: Isotope Products Laboratories, January 1995.

Kane, P. P., "Experimental Studies of Inelastic X-Ray and Gamma-Ray Scattering," Radiation Physics and Chemistry, Vol. 50, No. 1: 31-62 (July 1997).

Knoll, Glenn F. Radiation Detection and Measurement, New York: Wiley, 1989.

Kondic, N., A. Jacobs and D. Ebert. "Three-Dimensional Density Field Determination By External Stationary Detectors and Gamma Sources Using Selective Scattering," Proceedings of the Second International Topical Meeting on Nuclear Reactor Thermal-Hydraulics: 1443 - 1455 (January 1983).

Kroeger, R.A., and others. "Spatial Resolution and Imaging of Gamma-Rays with Germanium Strip Detectors," SPIE Proceedings, Vol. 2518: 236-243 (1996).

Lale, P. G., "The Examination of Internal Tissues Using Gamma-Ray Scatter with a Possible Extension to Megavolt Radiography," Physics in Medicine and Biology, Vol. 4: 159-166 (1959).

Lawson, Larry. "Compton X-Ray Backscatter Depth Profilometry for Aircraft Corrosion Inspection," Materials Evaluation, August 1995: 936-941.

Los Alamos National Laboratory. MCNP—A General Monte Carlo N-Particle Transport Code. Version 4B. LA-12625-M, Version 4B Manual. March 1997.

Marcus, P. and Oudar, J. Corrosion Mechanisms in Theory and Practice. New York: M. Dekkar, 1995.

Matscheko, Georg, Gudrun Alm Carlsson and Roland Ribberfors. "Compton Spectroscopy in the Diagnostic X-ray Energy Range; II. Effects of Scattering Material and Energy Resolution," Physics in Medicine and Biology, Vol. 34, No. 2: 199-208 (1989).

Namito, Y., S. Ban and H. Hirayama. "Implementation of the Doppler Broadening of a Compton-Scattered Photon into the EGS4 Code," Nuclear Instruments and Methods in Physics Research A349: 489-494 (1994).

Namito, Y., and others. "Compton Scattering of 20- to 40- keV Photons," Physical Review A, Vol. 51, No. 4: 3036-3043 (April 1995).

North American Scientific, Inc. Radiation Sources and Standards for Instrument Calibration & Reference, Envioronmantal Analysis, Industrial Guaging, Nuclear Medicine. Product Catalog. North Hollywood, CA: North American Scientific, Inc., August 1994.

Norton, Stephen J. "Compton Scattering Tomography," Journal Of Applied Physics, Vol. 49, No. 1: 2007-2015 (August 1994).

Oak Ridge National Laboratory. "Isotope Production and Distribution Catalog." n. pag. WWWeb, http://www.ornl.gov/isotopes/catalog.htm. 22 December 1998.

Prettyman, Thomas H., Composition and Density Imaging of Industrial Samples by a Combination of Photon Transmission Tomography and Projective Compton Scatterometry. North Carolina State University, Raleigh, NC, 1991.

Prettyman, T.H., R.P. Gardner, J.C. Russ and K. Verghese. "A Combined Transmission and Scattering Tomographic Approach to Composition and Density Imaging," Applications of Radiation Isotopes, Vol. 4, No. 10/11: 1327-1341 (1993).

Ribberfors, R., "Relationship of the Relativistic Compton Cross-Section to the Momentum Distribution of Bound Electron States," Physical Review B, Vol. 12: 2067-2074 (1975)

Sands, Marc J. An Investigation into the Non-Invasive Assessment of Bone Density using Multiplexed Compton Scattered Tomography. MS thesis, AFIT/GAP/ENP/99M-10. Graduate School of Engineering, Air Force Institute of Technology (AU), Wright-Patterson AFB, OH, January 1999.

Sauer, Ken and Charles Bouman. "A Local Update Strategy for Image Reconstruction from Projections," IEEE Transactions on Signal Processing, Vol. 41, No. 2: 534-548 (February 1993).

Shepp, L.A. and Y. Vardi. "Maximum Likelihood Reconstruction for Emission Tomography," IEEE Transactions on Medical Imaging, Vol. MI-1, No. 2: 113-122 (October 1982).

Thoe, R.S. "High Resolution Low Dose Scattered Gamma Ray Tomography," Review of Scientific Instruments, Vol. 67, No. 1: 89-101 (January 1996).

Urban, J.P. and R. Hosemann. "The Compton Profile of Aluminum With Silver K-alpha Flourescence Radiation," Journal Of Applied Physics, Vol. 49, No. 1: 392-395 (January 1978).

Van Riper, Kenneth A. SABRINA Users Guide For SABRINA Version 3.54. Los Alamos National Laboratory, October 1993.

Yuasa, T. and others. "Incoherent-Scatter Computed Tomography with Monochromatic Synchotron X-Ray: Feasibility of Multi-CT Imaging System for Simultaneous Measurement of Flourescent and Incoherent Scatter X-Rays," IEEE Transactions on Nuclear Science, Vol. 44, No. 5: 1760-1769 (October 1997).

Zhu, P., P. Duvauchelle, G. Peix and D. Babot, "X-ray Compton Backscattering Techniques for Process Tomography: Imaging and Characterization of Materials," Measurement Science and Technology, Vol. 7: 281-286 (1996).

Vita

Capt. Brian L. Evans was born on 12 May 1969 at Roosevelt Roads U.S. Naval Air Station in Puerto Rico. He grew up in Fairfax, VA where he graduated from James W. Robinson High School in 1987. He entered undergraduate studies at Miami University in Oxford, Ohio in 1987 and graduated in 1991 with a Bachelor of Science degree in Engineering Physics. He received his commission as a second lieutenant in the United States Air Force through the Reserve Officer Training Corps (ROTC) on 12 May 1991.

In March 1992, he began his first assignment at Minot Air Force Base in Minot, North Dakota as an ICBM maintenance officer on the Minuteman III weapon system. In May 1994, he entered graduate studies in nuclear engineering at the Graduate School of Engineering, Air Force Institute of Technology. He earned a Master of Science degree in December 1995, after which he began studies toward the Doctor of Philosophy Degree in nuclear physics.

Mailing Address: 301 Hilton Head Dr.
Papillion, NE 68133-2874